NAVAL POSTGRADUATE SCHOOL
MONTEREY, CALIFORNIA

DISSERTATION

ON THE BARENTS SEA POLAR FRONT IN SUMMER AND INTERPRETATIONS OF THE ASSOCIATED REGIONAL OCEANOGRAPHY USING AN ARCTIC OCEAN GENERAL CIRCULATION MODEL

by

Arthur Rost Parsons

September, 1995

Dissertation Advisors: Robert H. Bourke
Albert J. Semtner

19960508 139

DTIC QUALITY INSPECTED 1

REPORT DOCUMENTATION PAGE

Form Approved OMB No. 0704-0188

Public reporting burden for this collection of information is estimated to average 1 hour per response, including the time for reviewing instruction, searching existing data sources, gathering and maintaining the data needed, and completing and reviewing the collection of information. Send comments regarding this burden estimate or any other aspect of this collection of information, including suggestions for reducing this burden, to Washington Headquarters Services, Directorate for Information Operations and Reports, 1215 Jefferson Davis Highway, Suite 1204, Arlington, VA 22202-4302, and to the Office of Management and Budget, Paperwork Reduction Project (0704-0188) Washington DC 20503.

1. AGENCY USE ONLY *(Leave blank)*	2. REPORT DATE September 1995	3. REPORT TYPE AND DATES COVERED Doctoral Dissertation

4. TITLE AND SUBTITLE On the Barents Sea Polar Front in Summer and Interpretations of the Associated Regional Oceanography using an Arctic Ocean General Circulation Model	5. FUNDING NUMBERS ONR N0001492AF00002

6. AUTHOR(S)
Parsons, Arthur, R.

7. PERFORMING ORGANIZATION NAME(S) AND ADDRESS(ES) Naval Postgraduate School Monterey CA 93943-5000	8. PERFORMING ORGANIZATION REPORT NUMBER

9. SPONSORING/MONITORING AGENCY NAME(S) AND ADDRESS(ES) Office of Naval Research , ONR 322, 800 N. Quincy Street, Ballston Tower One, Arlington, VA 22217-5660	10. SPONSORING/MONITORING AGENCY REPORT NUMBER

11. SUPPLEMENTARY NOTES The views expressed in this thesis are those of the author and do not reflect the official policy or position of the Department of Defense or the U.S. Government.

12a. DISTRIBUTION/AVAILABILITY STATEMENT Approved for public release; distribution is unlimited.	12b. DISTRIBUTION CODE

13. ABSTRACT *(maximum 200 words)*

In August 1992 a combined physical oceanography and acoustic tomography experiment was conducted to describe the Barents Sea Polar Front (BSPF) and investigate its associated mesoscale phenomena. The study area was an 80 by 70 km grid east of Bear Island where the front exhibits topographic trapping along the northern slope of the Bear Island Trough. CTD, current meter and ADCP data, combined with tomographic cross-sections, presented a highly resolved picture of the front in August. All hydrographic measurements were dominated by tidal signals with the strongest signatures associated with the M2 and S2 semidiurnal species. Tomographic cross sections indicated a high-frequency (~16 cpd) upslope motion of filaments of Norwegian Atlantic Water (NAW) origin at the front. Mean currents in the warm saline water to the south of the front, derived from a current meter mooring and ADCP data, were directed to the southwest and are associated with a barotropic recirculation of NAW within the Bear Island Trough. To examine the relation of BSPF to the regional oceanography, a high resolution (1/6° and 30 vertical levels) Arctic Ocean and Nordic Seas model was developed from the Semtner-Chervin General Circulation Model (GCM) with a free-surface. Three numerical experiments, annual mean forcing, annual mean forcing coupled with semidiurnal tidal forcing, and seasonal forcing, were conducted to simulate conditions in 1992. All three numerical experiments predicted the recirculation of NAW within Bear Island Trough supporting the observed conditions. The unique experiment with simulated tides indicated enhanced mixing on the slopes and shallow topography of the Barents Sea. Modeling predictions indicate that the coherent advection of Barents Polar Water (BPW) to the front summertime is contingent upon strong surface stratification of the upper layers from the summer ice melt.

14. SUBJECT TERMS Oceanography, Arctic Ocean, Fronts, Barents Sea, Modeling, Tides	15. NUMBER OF PAGES 196
	16. PRICE CODE

17. SECURITY CLASSIFICATION OF REPORT Unclassified	18. SECURITY CLASSIFICATION OF THIS PAGE Unclassified	19. SECURITY CLASSIFICATION OF ABSTRACT Unclassified	20. LIMITATION OF ABSTRACT UL

SN 7540-01-280-5500 Standard Form 298 (Rev. 2-89)

Prescribed by ANSI Std. 239-18 298-102

i

ON THE BARENTS SEA POLAR FRONT IN SUMMER AND INTERPRETATIONS OF THE ASSOCIATED REGIONAL OCEANOGRAPHY USING AN ARCTIC OCEAN GENERAL CIRCULATION MODEL

Arthur Rost Parsons
Lieutenant Commander, United States Navy
B.S., Duke University, 1981
M.S., Naval Postgraduate School, 1992

Submitted in partial fulfillment
of the requirements for the degree of

DOCTOR OF PHILOSOPHY IN PHYSICAL OCEANOGRAPHY

from the

NAVAL POSTGRADUATE SCHOOL
### September 1995
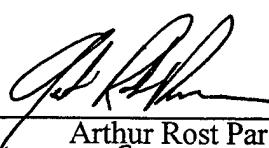
Author: _____
Arthur Rost Parsons

Approved by:
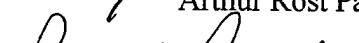
Robert H. Bourke
Professor of Oceanography

Albert J. Semtner
Professor of Oceanography
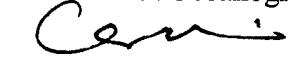
Ching-Sang Chiu
Associate Professor of
Oceanography
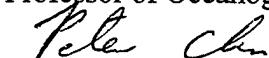
Peter C. Chu
Associate Professor of
of Oceanography

Kenneth L. Davidson
Professor of Meteorology
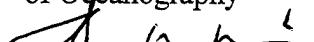
James H. Miller
Associate Professor
of Electrical
and Computer Engineering

Approved by: _____
Robert H. Bourke, Chairman, Department of Oceanography
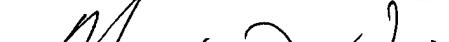
_____
Maurice D. Weir, Associate Provost for Instruction

iii

iv

ABSTRACT

In August 1992 a combined physical oceanography and acoustic tomography experiment was conducted to describe the Barents Sea Polar Front (BSPF) and investigate its associated mesoscale phenomena. The study area was an 80 by 70 km grid east of Bear Island where the front exhibits topographic trapping along the northern slope of the Bear Island Trough. CTD, current meter and ADCP data, combined with tomographic cross-sections, presented a highly resolved picture of the front in August. All hydrographic measurements were dominated by tidal signals with the strongest signatures associated with the M2 and S2 semidiurnal species. Tomographic cross sections indicated a high-frequency (~16 cpd) upslope motion of filaments of Norwegian Atlantic Water (NAW) origin at the front. Mean currents in the warm saline water to the south of the front, derived from a current meter mooring and ADCP data, were directed to the southwest and are associated with a barotropic recirculation of NAW within the Bear Island Trough. To examine the relation of BSPF to the regional oceanography, a high resolution (1/6° and 30 vertical levels) Arctic Ocean and Nordic Seas model was developed from the Semtner-Chervin General Circulation Model (GCM) with a free-surface. Three numerical experiments, annual mean forcing, annual mean forcing coupled with semidiurnal tidal forcing, and seasonal forcing, were conducted to simulate conditions in 1992. All three numerical experiments predicted the recirculation of NAW within Bear Island Trough supporting the observed conditions. The unique experiment with simulated tides indicated enhanced mixing on the slopes and shallow topography of the Barents Sea. Modeling predictions indicate that the coherent advection of Barents Polar Water (BPW) to the front summertime is contingent upon strong surface stratification of the upper layers from the summer ice melt.

TABLE OF CONTENTS

ACKNOWLEDGMENT

I would like to extend my appreciation to Anthony Craig of NCAR who not only provided the climatological data used in the ocean model initialization but generously shared his knowledge and experience throughout the modeling experiments. Additional thanks go to Steve Hankin and his colleagues at the NOAA Pacific Marine Environmental Lab, who provided "Ferret", an outstanding gridded data analysis software package, and many hours of technical assistance.

I would like to acknowledge the person who provided my original impetus to become an Oceanographer, Father Bertrand Dunegan, OSB. My parents love and continual belief in me provided the foundation for this effort -- thank-you Mom and Dad! **Finally and most of all, I extend from my heart my love and gratitude to the most wonderful wife in the world, Judith, for her love, patience, encouragement and support.**

Beyond the ken of mortal men, beneath the wind and waves,
There lies a land of shells and sand, of chasms, crags and caves,
Where coral castles climb and soar, where swaying seaweed grow,
And all around without a sound the ocean currents flow...

- Graeme Base, from **The Sign of the Seahorse**

I. INTRODUCTION

Our main object was to explore the unknown Polar Sea.

Fridtjof Nansen, 1902

The Barents Sea Polar Front (BSPF) is an oceanographic feature formed by the confluence of Arctic and Atlantic water masses north of Norway and is a perennial feature located along the bathymetric slope extending from Bear Island (Bjørnøya) eastward along the Bear Island Trough (Johannessen and Foster, 1978). (Figure 1). The study of the transition from Atlantic Water to Polar Water in the Barents Sea has been ongoing for almost a century (Nansen, 1902; see Figure 2). Hydrographic data from fishery surveys conducted during the late 1960's and early 70's identified the transition region, i.e., the Barents Sea Polar Front, as a permanent oceanographic feature and suggested its location was linked to the bathymetry near Bear Island (Johannessen and Foster, 1978; Dickson et al., 1970).

This study serves to examine and characterize the BSPF in the light of a new data set collected in summer of 1992. Model simulations, using a three dimensional Arctic Ocean and Nordic Seas General Circulation Model (GCM) developed as a part of this research effort, provide the spatial and temporal resolution necessary to examine the relationship of the BSPF to the regional oceanography.

A. THE POLAR FRONT

The Barents Sea is shallow in comparison to many of the world's seas with average depths ranging only from 100 - 300 m. It is slightly inclined from west to east with deeper values to the west. The topography is highly irregular with many shallow banks and deeper pockets scattered throughout (Perry, 1986). The circulation pattern is strongly influenced by the topography. Anticyclonic eddies are found following the topography around prominent bank features such as Central Bank and, in proximity to this experiment, Spitsbergen Bank (Loeng, 1991). In much of the literature depiction of

1
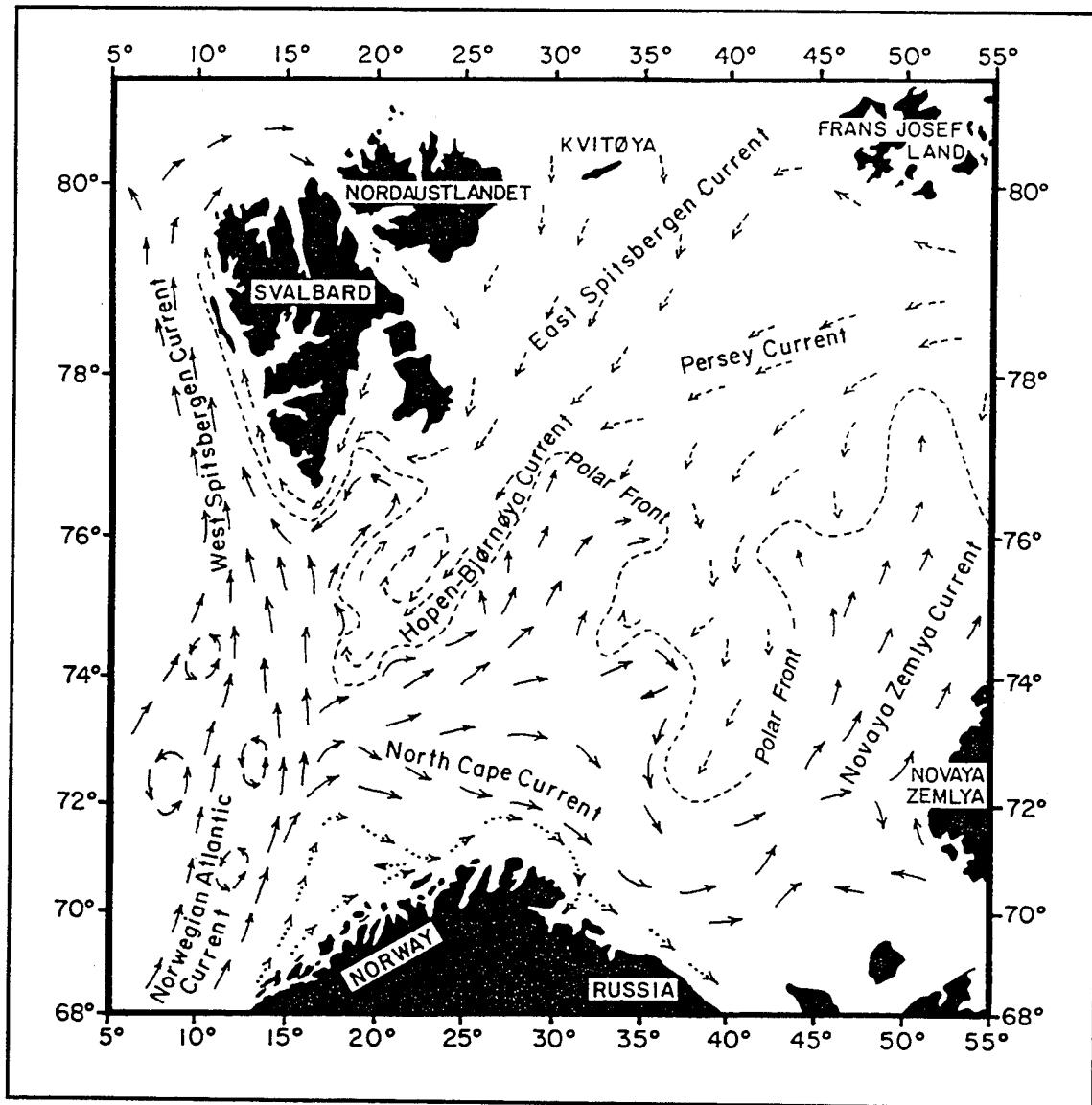
Figure 1. The surface circulation in the Barents Sea shows the major currents and their relation to the Polar Front. Dashed arrows indicate cold currents; solid arrows indicate warm currents. The hatched line indicates the position of the Polar Front (from Pfirman et al., 1994).

the overall circulation of the Barents Sea similar to Figure 1 can be traced to early works by Russian scientists (Tantsiura, 1959 and Novitskiy, 1961). Even today many of the details of the current system are poorly known with the southern section being the most intensively studied region (Midttun and Loeng, 1987).

2
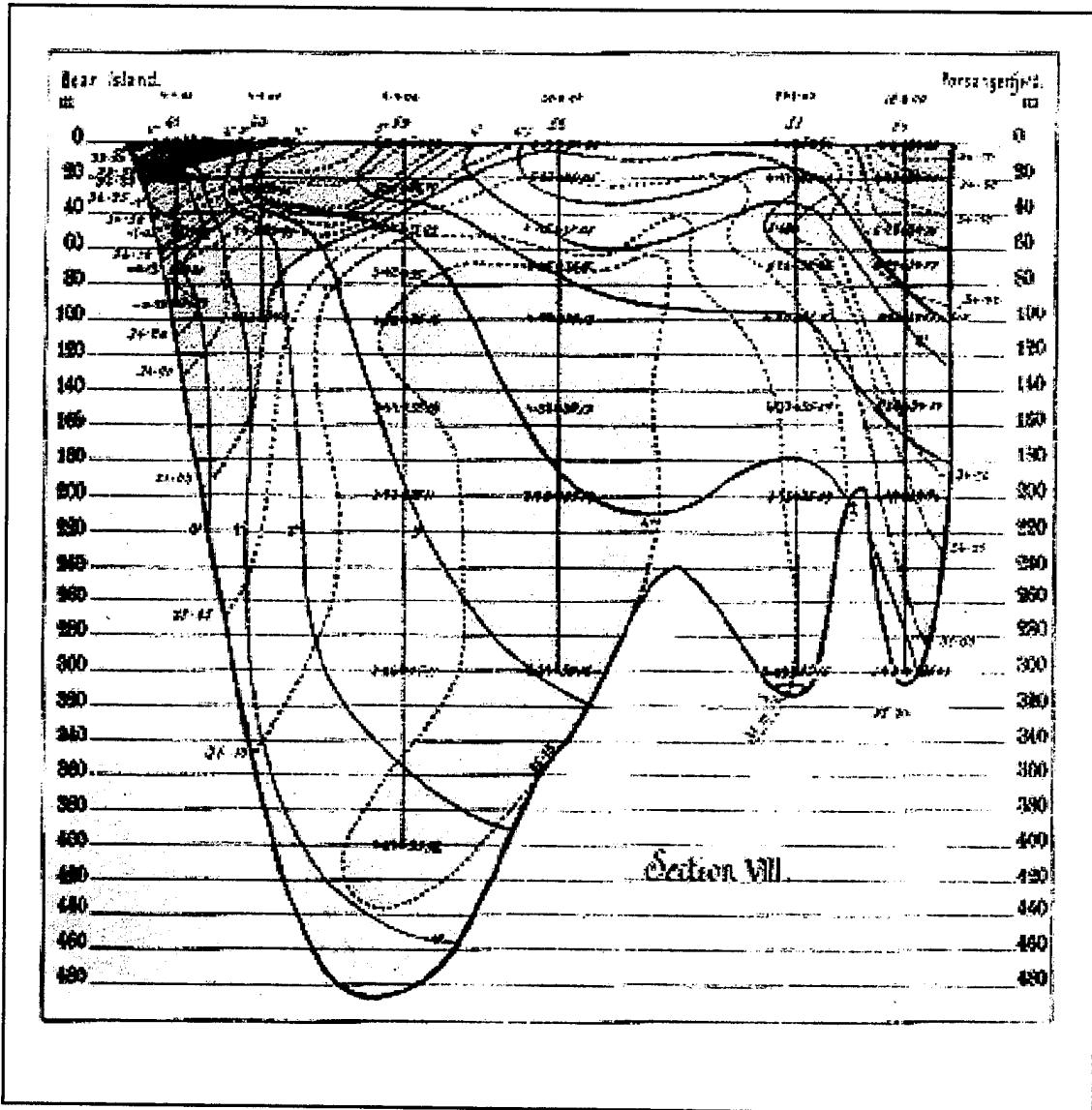
Figure 2. Section VIII from Plate 9 (Sections from the Barents Sea) depicts a cross section from Bear Island to Finmarken made in September 1900 (Nansen, 1902). From this section Nansen traced a warm saline core in the center of Bear Island Trough as well as the gradients marking the boundary of the "Gulf Stream" and the "polar water (coming from the Barents Sea)." The salinity ranged from 33.2 psu to 35 psu and temperature from 1°C to 6.5°C across the front.

The source waters which contribute to the BSPF and their circulation pattern within the shallow Barents Sea have been described by Loeng (1991). Cold, fresh Arctic Water enters the Barents Sea from the north as a surface or near-surface current between

3

Spitsbergen and Franz Josef Land via the East Spitsbergen Current and more significantly between Franz Josef Land and Novaya Zemlya via the Persey Current. Cold Arctic Water exits the Barents Sea via a branch of the Bear Island Current (a continuation of the east-to-west flowing Persey Current). Most of the cold Polar Water which enters the Barents Sea is thought to recirculated back to the Arctic Ocean (Novitskiy, 1961).

Warm, saline Atlantic Water flows into the Barents Sea via the North Cape Current (Nordkapp Current). A smaller and diluted Atlantic Water fraction also enters the Barents Sea as a subsurface flow (~200 m) between Kvitøya and Victoria Island and the Franz Joesef Victoria Trough. This fraction is carried northward by the West Spitsbergen Current of which a portion follows the topography around Svalbard (Rudels, 1987; Pfirman et al., 1994). Outflow of Atlantic Water occurs via the Bear Island Trough. This southwestward flow has infrequently been reported in the literature but is an inherent aspect to the observations discussed in this paper. Atlantic Water entering the trough from the south has been inferred by indirect hydrographic evidence to recirculate around the Bear Island Trough and exit the Barents Sea topographically trapped between the 150 - 300 m depth contours flowing parallel but southward of the cold Bear Island Current (Novitskiy, 1961; Pfirman et al., 1994).

The portion of Atlantic Water which enters the Barents Sea but is not recirculated is cooled and freshened as it moves eastward and northward. This water is believed to exit into the Kara Sea between Novaya Zemlya and Franz Joesef Land and then down the St. Anna Trough into the Arctic Ocean (Rudels, 1987). The water exiting through the St. Anna Trough has been termed the Barents Sea Branch and is believed to be an important source for the water of Atlantic origin which circulates througout the Central Arctic (Rudels et al., 1994, Figure 3).

Outflow from the Barents Sea through the Bear Island Trough also occurs as Bottom Water formed locally in the wintertime on Svalbard Bank through brine rejection (Midttun and Loeng, 1987). Its presence was not expected nor observed during this summertime experiment.

4

Estimates of the volume transport for the currents flowing into and out of the Barents Sea, derived from observations, are poorly known (Loeng, 1991). Table 1 summarizes some estimates of the transports found in the literature. Based on model studies, Loeng (1991) cautions on the interpretations of these transports since fluctuations due to wind forcing and remote forcing appear to be the same order of magnitude as the mean transports estimates themselves.

Study	Estimate (Sv)	Region	Source
Aagaard and Griesman, 1975	(a) 0.1 Sv (b) ~ 0.7 Sv	(a) Spitsbergen to Franz Joesef Land (summer) (b) Franz Joesef Land to Novaya Zemlya	Collation of historical observations and current charts
Rudels, 1987	1.2 Sv [0.8 Sv CW 0.4 Sv AW][1]	Net transport from the Norwegian Sea through the Barents Sea to the Arctic	Heat budget balance to match observed conditions
Blindheim, 1989	3.0 Sv -1.0 Sv	Norway to Bear Island	Current meter measurements
Loeng et al., 1993	(a) 2.1 Sv (b) 1.4 Sv (c) -2.0 Sv	(a) Norway to Bear Island (winter) (b) Norway to Bear Island (summer) (c) Franz Josef Land to Novaya Zemlya	Compilation of measurements

[1] CW is coastal water carried by the Norwegian Coastal Current; AW is Atlantic Water carried by the North Cape Current

Table 1: Estimates of transports for the Barents Sea derived from observations (units 1 Sv = 10^6 m^3 s^{-1}). Positive values are transports into the Barents Sea.

Tidal currents are important in the shallow Barents Sea and have speeds up to 1 to 1.5 m s^{-1} in the vicinity of Bear Island (Johannessen, 1986). Observations from 11 current meter moorings between northern Norway and Bear Island indicated that 77% of the total current variance was due to tidal forcing (Huthnance, 1981). Tidal models estimate the maximum amplitude of the M2 or principal lunar semi-diurnal sea level in the vicinity of this experiment is on the order of 30-40 cm while the amplitude of the K1 (principal lunisolar diurnal) sea level is on the order of 4 to 6 cm (Schwiderski, 1986; Gjevik et al.,

1994, Kowalik and Proshuntinsky, 1994). Gjevik et al. provide a model and observed M2 and K1 tidal ellipse parameters for several stations within the Barents Sea. For a station just south of the experimental area the major axis components for the M2 and K1 constituents are ~10 cm s^{-1} and ~ 3.5 cm s^{-1}, respectively, which is significantly smaller than the currents observed on the shelf and in closer proximity to Bear Island. Huthnance (1981) found from observations near Bear Island that over 90% of the M2 and K1 kinetic energy is barotropic. Another aspect of the tides within the region is that the M2 tidal period is identically equal to the inertial period at 74°28'N (or the critical latitude) and the two are indistinguishable in short-term current measurements. Nost (1993) found that the vertical structure of the tidal current at the critical latitude in the Barents Sea is very sensitive to the turbulence level and distribution of the eddy viscosity in the water column.

The Polar Front is the dominant mesoscale feature in the Barents Sea (Johannessen, 1986; Pfirman et al., 1994;). Though the existence of the BSPF has long been known and mapped via remote sensing, very few direct observations of the front immediately to the east of Bear Island have been reported (T. McClimans, personal communication, 1994). Johannessen and Foster (1978) provided the first detailed observations of the Polar Front in the vicinity of Bear Island based upon an XBT survey conducted in July 1974. They found the strongest surface temperature gradient was 0.15°C- km^{-1} and closely followed the 100 m isobath. The subsurface structure of the front was delineated best by the 3-4°C isotherms. Data from an airborne radiation thermometer survey (ART) and the XBT data indicated that the surface perturbations of the boundary laterally extended a maximum of 10 km and occurred over a semidiurnal tidal cycle.

Loeng (1991) provides a schematic of the summertime front which portrays several features of the inferred oceanography surrounding the front (Figure 4). A prominent feature is the northeastward flowing warm current on the slope-side of the front and an opposing cold current on the shelf-side of the front. The structure of the frontal
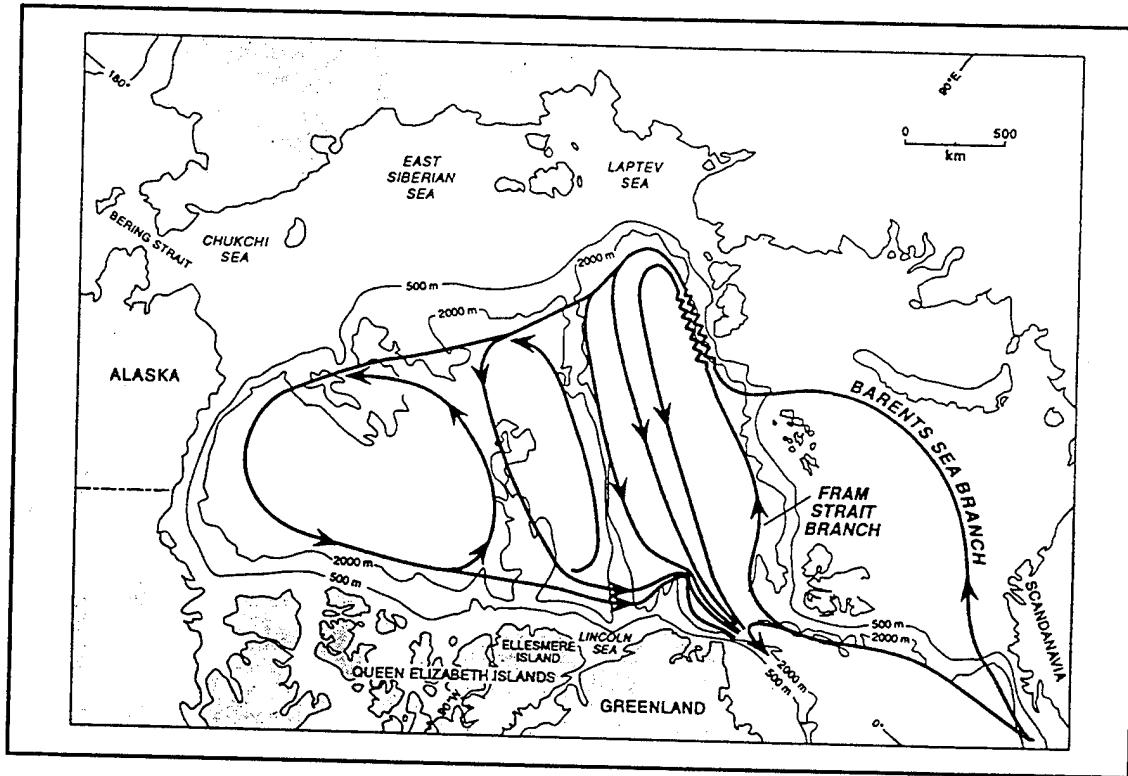
Figure 3. The schematic of routes of the Atlantic layer as it passes into and around the Arctic Ocean. A significant route is identified as the Barents Sea Branch which exits into the Kara Sea and down the St. Anna Trough (from Rudels et al., 1994).

isopleths are retrograde to the bathymetry. Additionally, the influence of the melt water on the water mass distribution during summer is seen with the establishment of a 'summer front' and a melt water surface layer.

From a consideration of its known characteristics (Johannessen and Foster, 1978; Loeng, 1991), the summertime BSPF may be representative of a shelf-slope frontal system (Mooers et al., 1978) though it may well possess some characteristics of a shallow sea front (Simpson, 1981) or topographic-circulatory front (Federov, 1983). The combined hydrographic-acoustic tomographic data set from the 1992 BSPF experiment have for the first time permitted the necessary resolution to discern the density and flow structure of the front to the east of Bear Island and to investigate its frontal characteristics in detail.

7

B. RECENT MODELING STUDIES OF THE BARENTS SEA REGION

Observational studies of the Barents Sea have historically either been spatially biased towards the southern area, temporally restricted to summer months for the northern regions or of generally coarse resolution. To further expand our understanding of this economically and environmentally important region, several other investigators have recently simulated the circulation and tides within the Barents Sea.

Slagstad et al. (1990) used a 20 km resolution baroclinic model of the Barents Sea to investigate the density circulation. With prescribed mass fluxes through the open boundaries and an initialization density field from interpolated autumn temperature and salinity observations (1988 and 1979), their model produced a current pattern similar to Figure 1 with an absence of direct wind forcing. However, most interesting to this investigation, was the presence of a large cyclonic eddy predicted in Bear Island Trough (Figure 5). Though the eddy is adjacent to a model closed boundary and the authors could not cite observations to support its existence, the circulation pattern is suggestive of southwestward flow bordering the BSPF. This southwestward flow along the front could be attributed to topographic recirculation within the Bear Island Trough.

Harms (1992), in contrast to the experiment above, used an homogenous environment to examine the barotropic circulation due to tidal and wind forcing. The model resolution was 18 km and incorporated forcing from geostrophic winds derived from the Arctic Drifting Buoy Program data and from the principal lunar semidiurnal tide (M2). He found that the polar frontal signature could be attributed to the interaction of the southwestward tidal residual flows on Svalbard Bank, the anticyclonic residual flow circulation around Bear Island, and a northeastward moving North Cape Current along the front. In simulations the weak residual flows, which define the front, could be disturbed by west or southwest winds but in calm periods the strong frontal signature returned.

In a laboratory model of the Barents Sea, McClimans and Nilsen (1993) point out that the typical scales of current numerical models of the region are too coarse to show details of jet currents and eddies, considering that a nominal baroclinic Rossby radius for

8
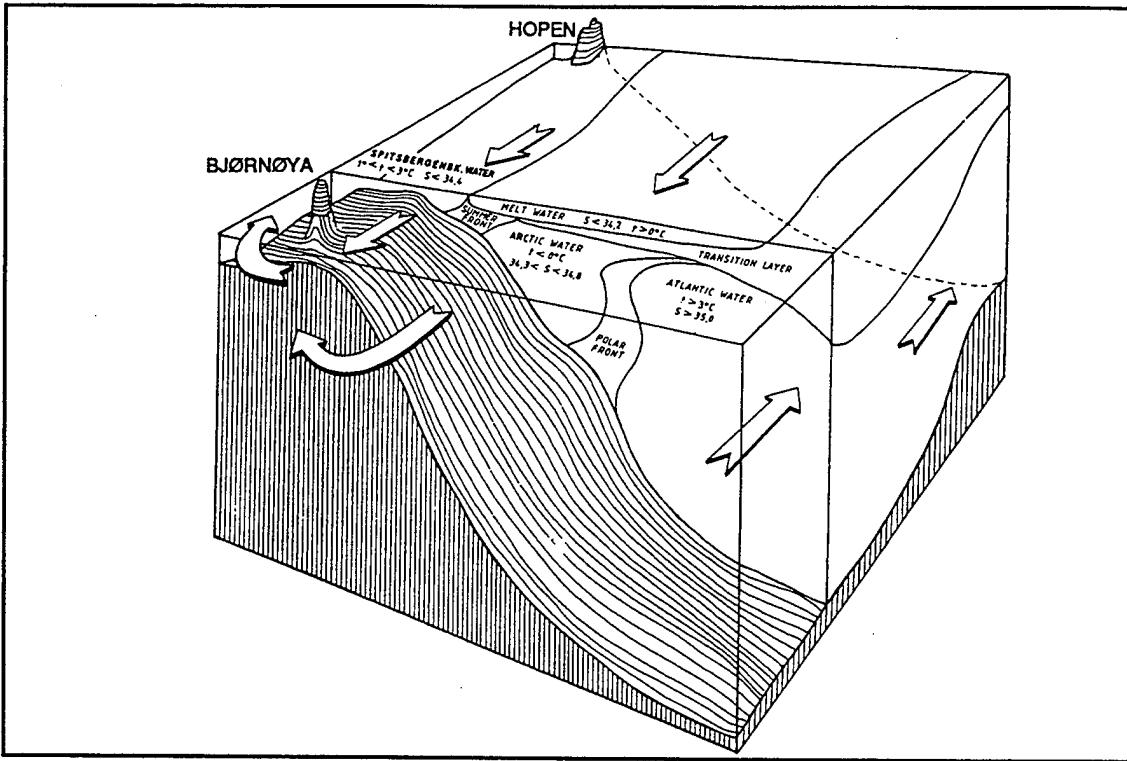
Figure 4: **A schematic diagram of the Polar Front from Loeng (1991) show the typical water mass distribution during summer as well as the principal current directions.**

the region is 5 km. Their rotating laboratory model provides an equivalent resolution of 2 km. Forcing of the model was achieved primarily through monthly prescribed inflows around the periphery of the Barents Sea. Additionally, the model vertical axis was tilted to roughly simulate diurnal tides The central findings germane to this study were: (1) a warm northeastward flow of Atlantic Water along Svalbard Bank and the BSPF and (2) a robust tidally driven circulation on Svalbard Bank and around Bear Island. They conclude that entrainment of Arctic Water with the northeastward moving Atlantic Water keeps the front sharp and modifies the Atlantic Water proceeding deeper into the Barents Sea. This description is consistent with Loeng (1991).

As previously cited, Gjevik et al. (1994) have developed a 2-D tidal model of the Barents Sea. With two resolutions (25 and 12.5 km) and four simultaneous forced tidal constituents (M2, S2, N2, and K1), their model provides a greatly enhanced depiction of

the tides within the Barents Sea as compared with those derived from global studies such as Schwiderski (1986). Similar to Harms (1992), significant topographically steered tidal residual flows (southwestward and parallel to the front) were predicted on Svalbard Bank as well as an anticyclonic circulation around Bear Island. Increasing the model resolution from 25 km to 12.5 km (and thus increasing the topographic resolution) greatly enhanced the residual flows (up to 10 times in the vicinity of Bear Island). The significance of these tidally generated flows adjacent to the front ($\sim$ 1.5 - 3 cm s^{-1}) warrants their inclusion in frontal simulations. They also conclude that the resolution of the semidiurnal tide in the Barents Sea is effected by the boundary conditions applied in the North Atlantic. Astronomical forcing alone in the region is insufficient to account for tidal amplitudes which are driven by the influx through the Norwegian and Greenland Seas.

Harms and Backhaus (1994) used a baroclinic model coupled to a dynamic-thermodynamic ice model to examine winter water mass formation in the Barents and Kara Seas. The model was initialized with climatological summertime temperature and salinity data (Levitus, 1982) and forced with daily ECMWF wind stress and air temperature data for September 1987 to March 1988. They noted that the BSPF is not apparent in the climatological fields used to initialize the model. However, from the wind and temperature forcing combined with the topographically guided circulation, the prognostic simulations create the temperature and salinity gradients associated with the front. Two other features of the front from their simulation are pertinent to this investigation. First, their model did not show a recirculation within the trough or a southwestward flow along the front (Harms, personal communication, 1994). Secondly, the model did produce strong salinity gradients at the surface which defined the front in the summer months (fresh Polar Water and salty Atlantic Water). However, by February in the simulated forcing, brine release from ice production had virtually eliminated the frontal salinity gradient. From their simulations, the character of the front is clearly influenced by the seasonal melting and formation of sea ice.
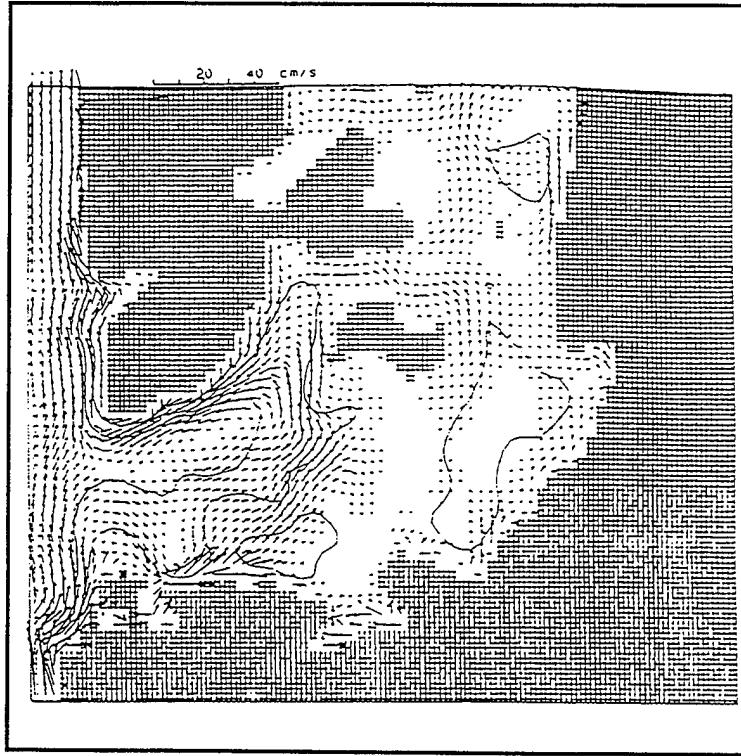
Figure 5: The simulated density currents between 200 and 300 m from Slagstad et al. (1990) show a cyclonic circulation within Bear Island Trough.

Finally, the degree to which the tides control the dynamics of the BSPF have recently been examined by other investigators. Calculations of the stratification parameter, given by Pingree and Griffiths (1978) for predicting the location of shallow-sea or tidal-mixing fronts, were conducted for the Barents Sea by Kowalik and Proshutinsky (1995) using their high resolution (~1.5 km) tidal model results. In the vicinity of Bear Island, the BSPF and the tidal mixing front are relatively coincident at the shelf break. Farther to the east, the Polar Front and the predicted tidal mixing front are disparate with the Polar Front remaining tied to the steep topography while the tidal mixing front is farther north on Svalbard Bank. They conclude that the generation and maintenance of the front near Bear Island could be explained by tidal mixing aside from the circulation patterns of Atlantic and Arctic waters. It is apparent from their work that the tides do not act uniformally in the dynamical balance of the BSPF along its breadth.

C. ARCTIC MODELING STUDIES

As the discussion of the currents in Section A revealed, though the Barents Sea is a very shallow shelf sea, it is not isolated from the surrounding deep circulation patterns of the Norwegian Sea and Arctic Ocean. The regional models discussed above are constrained in their accuracy by the prescribed boundary conditions of flow into and out of the Barents Sea. As will be further discussed in Chapter VI, the intent of this study was to simulate the circulation of waters in the Barents Sea and their relation to the Polar Front by first resolving the circulation of the Arctic Ocean and Nordic Seas. Several numerical modeling studies of the Arctic Region, including the Barents Sea, have been reported in the literature. A review of the pertinent details found in these articles follows.

1. Barents Sea Circulation

Semtner (1976) employed the first 3-dimensional numerical model driven by atmospheric forcing (derived annual mean geostrophic winds) to simulate the Arctic circulation. The model, based on the formulation of Bryan (1969), currently known as "Bryan-Cox", had a 1° horizontal resolution (~110 km) and 14 vertical levels. In examining the relationship of the predicted vertical motion fields to the horizontal velocity, a particle trajectory was traced for a particle originating in the Norwegian Sea. The particle traveled in the Norwegian Atlantic Current prior to rising and entering the Barents Sea. The particle made one cyclonic recirculation before exiting near Novaya Zemlya. This simulation demonstrated a connection through the Barents Sea to the Central Arctic (the Barents Sea Path) and the tendency for Atlantic Water to recirculate within the Barents Sea.

Semtner (1987) presented a coupled ice-ocean model of equivalent horizontal and vertical resolution to that of Semtner (1976). The model was forced with long-term monthly mean atmospheric fields. By using monthly forcing, the model was able to predict a seasonal cycle in transport of the cyclonic gyre predicted in the Barents Sea. The

cyclonic gyre was most intense in the period November through March (~7 Sv) while reaching a minimum in June (~ 1 Sv).

Holland and Mysak (1995) used an isopycnal model also with 1° horizontal resolution to investigate the Arctic circulation. The model forcing was based upon climatological monthly averages of wind stress, radiation, air temperature, humidity, rainfall, and cloud cover. The model did not reproduce an Atlantic Water recirculation in the Barents Sea. Predicted transports of Atlantic Water through the Barents Sea ranged from 2.0 Sv in summer to 4.0 Sv in winter.

Aukrust and Oberhuber (1995) also used an isopycnal model to investigate the circulation in the Greenland-Iceland-Norwegian (GIN) Sea. Their model has a resolution of ~ 1/4° in the horizontal with 9 vertical layers and was forced with monthly mean data. A recirculation of Atlantic Water in the Barents Sea is not supported in their depiction of the currents and a net transport of ~ 0.9 Sv through the Barents Seas into the Central Arctic is reported.

Depiction of finer features, such as the recirculation of Atlantic Water in the Barents Sea, in the large scale models presented above are believed to have suffered from the horizontal and vertical scales of the model. These investigations have generally been limited by computer size and speed. A motivation for this research was to investigate if the increased model resolution in a large scale model could improve the depiction of the circulation of the Barents Sea.

Many other studies have focused on modeling the sea ice cover and ice-ocean interactions (e.g., Hibler and Bryan, 1984; Ranelli and Hibler, 1991, Hakkinen and Mellor, 1992). Preller and Posey (1989) have formulated an ice-ocean model which is now routinely used in ice edge and thickness forecasting for the United States Navy. Of interest to this study is the generally good performance of these models near the BSPF. The strong tie of the winter ice edge to the BSPF suggests the dynamics of the circulation of the Atlantic Water is not a seasonal phenomenon but is perennial.

2. Tides

A recent study of the tides in the Arctic Ocean and Nordic Seas by Kowalik and Proshutinsky (1994) has demonstrated the importance of tides in many aspects of the Arctic circulation. Kowailk and Proshutinsky, using 14 km spaced grid, modeled four tidal constituents, the principal lunar semidiurnal (M2), the principal solar semidiurnal (S2), the luni-solar diurnal (K1), and the principal lunar diurnal (O1). Figure 6a and 6b shows the predicted M2 coamplitude and cophase charts from their solution which agrees well with observed tidal heights and altimetry data. Strong tidal currents were predicted in the shallow shelf regions of the Arctic and Nordic Seas. In the Barents Sea, particularly, maximum currents ranged from 30 cm s^{-1} to 130 cm s^{-1}. Additionally, residual tidal currents resulting from nonlinear interactions with the topography induced a weak motion which was shown to play a significant role in ice drift and the formation of polynas. Also, the effect of the tidal oscillations on the ice cover due to opening and closing small leads was predicted to account for 8 10^{11} m^3/year of ice production. Finally, the importance of tidal mixing over steep topograpahic features in the central Arctic was noted as a mechanism to transfer heat from the Atlantic layer to the surface layer. The opposite transfer of heat occurs in the Norwegian Sea and North Atlantic where warmer surface water overlies the cooler intermediate waters. From their work, it is apparent that future simulations of the Arctic and subpolar seas should include tidal forcing in order to fully account for the complex dynamics of the region.

14
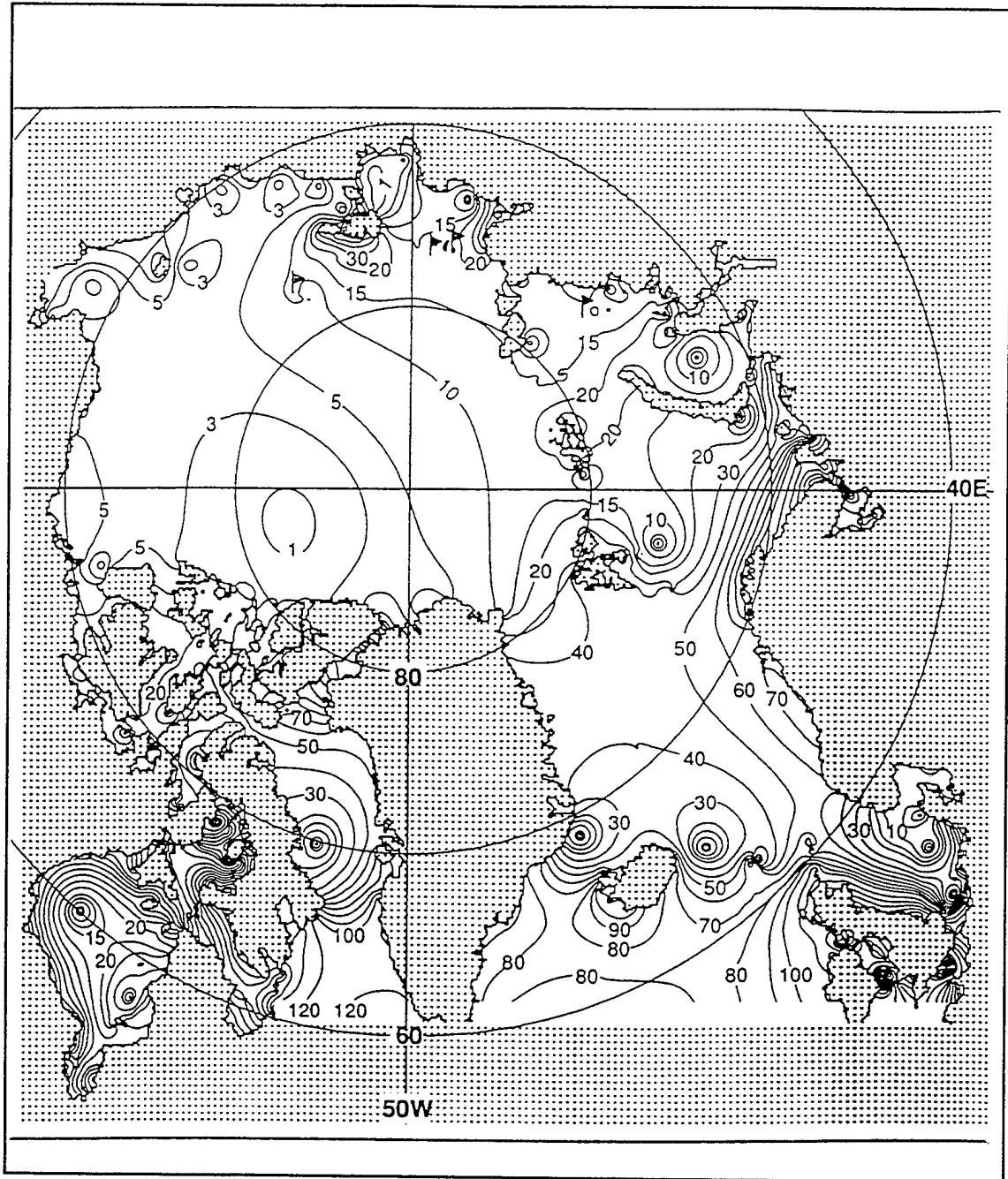
Figure 6a: Coamplitude of the M2 tide for the Arctic Ocean and Nordic Seas shows the large magnitude of this tidal constituent in the subpolar seas but decreased amplitude in the Central Arctic (from Kowalik and Proshutinsky, 1994).
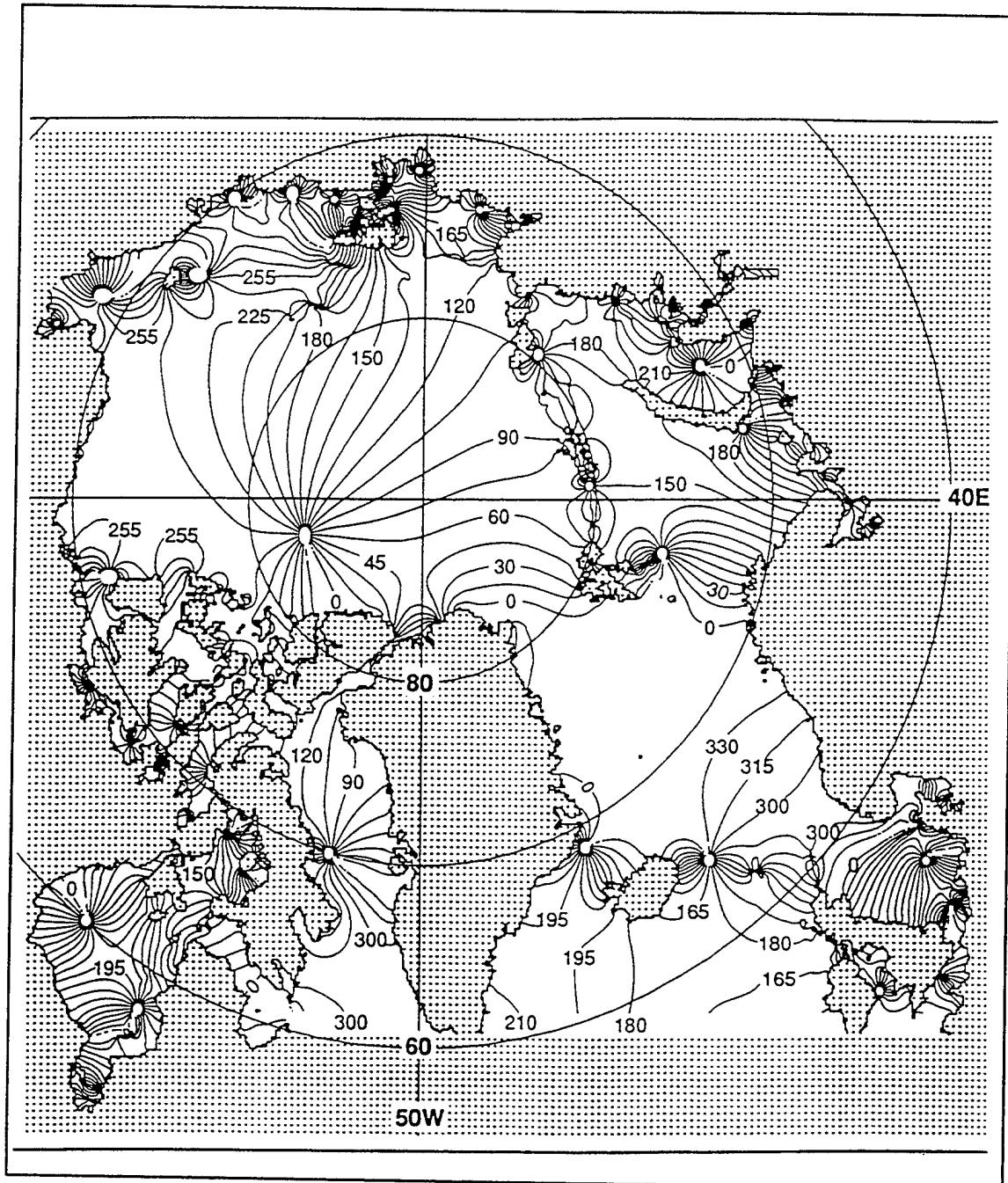
Figure 6b. The cophase chart of the M2 tide shows an amphidromic point in the Barents Sea to the southeast of Spitsbergen which defines the propagation of the M2 tide within the Barents Sea (from Kowalik and Proshutinsky, 1994).

II. THE FIELD PROGRAM

During the period 6 - 26 August 1992, an integrated physical oceanography and acoustic tomographic field experiment was conducted 60 km east of Bear Island in the Barents Sea to describe the BSPF, to investigate its associated mesoscale processes, to enhance the understanding of frontal dynamics and their impact on regional oceanography, and to assess the ability of acoustic tomographic methods to define frontal and mesoscale features (Figure 7). In an 80 x 70 km (Figure 8) experimental area, a total of 257 CTD stations were occupied during four runs of a 10 km-spaced grid by the USNS BARTLETT. Two of the CTD grid runs occupied all stations on the grid and many subgrid scale stations were taken during the experiment. A separate twenty-seven hour CTD time series was taken coincident with the strongest frontal signature location. Nine current meters and 8 temperature loggers on three moorings were deployed for approximately 10 days during the experiment. Two 400 Hz acoustic transceivers and a 224 Hz acoustic source were deployed on the three current meter moorings. A fourth mooring was set especially for a vertical hydrophone array. The acoustic source, transceivers and vertical array were deployed to obtain acoustic tomographic data. Unfortunately, one of the 400 Hz acoustic transceivers failed when deployed limiting the ability to invert current data from the measurements. Continuous ADCP data were recorded on the USNS BARTLETT during its occupation of the experimental area.

Measurements of conductivity, temperature and depth were made with a Neil Brown Instrument Systems Mark IIIB CTD. Sampling was conducted at a scan rate of 31.25 Hz with an average winch speed of 1.8 m s^{-1}. Nisken bottles, closed at the bottom of sixty casts, were used for post-cruise salinity calibration purposes. Pre- and post- cruise calibration residual analyses were within instrument accuracy (+/- .005 °C, +/- .005 mmho, and +/- 0.5 dbar). The CTD data were first treated for gross spikes in the recorded data and were then adjusted for post-cruise conductivity calibrations and a conductivity time-lag correction. As a last step, the data were pressure averaged to 1.0
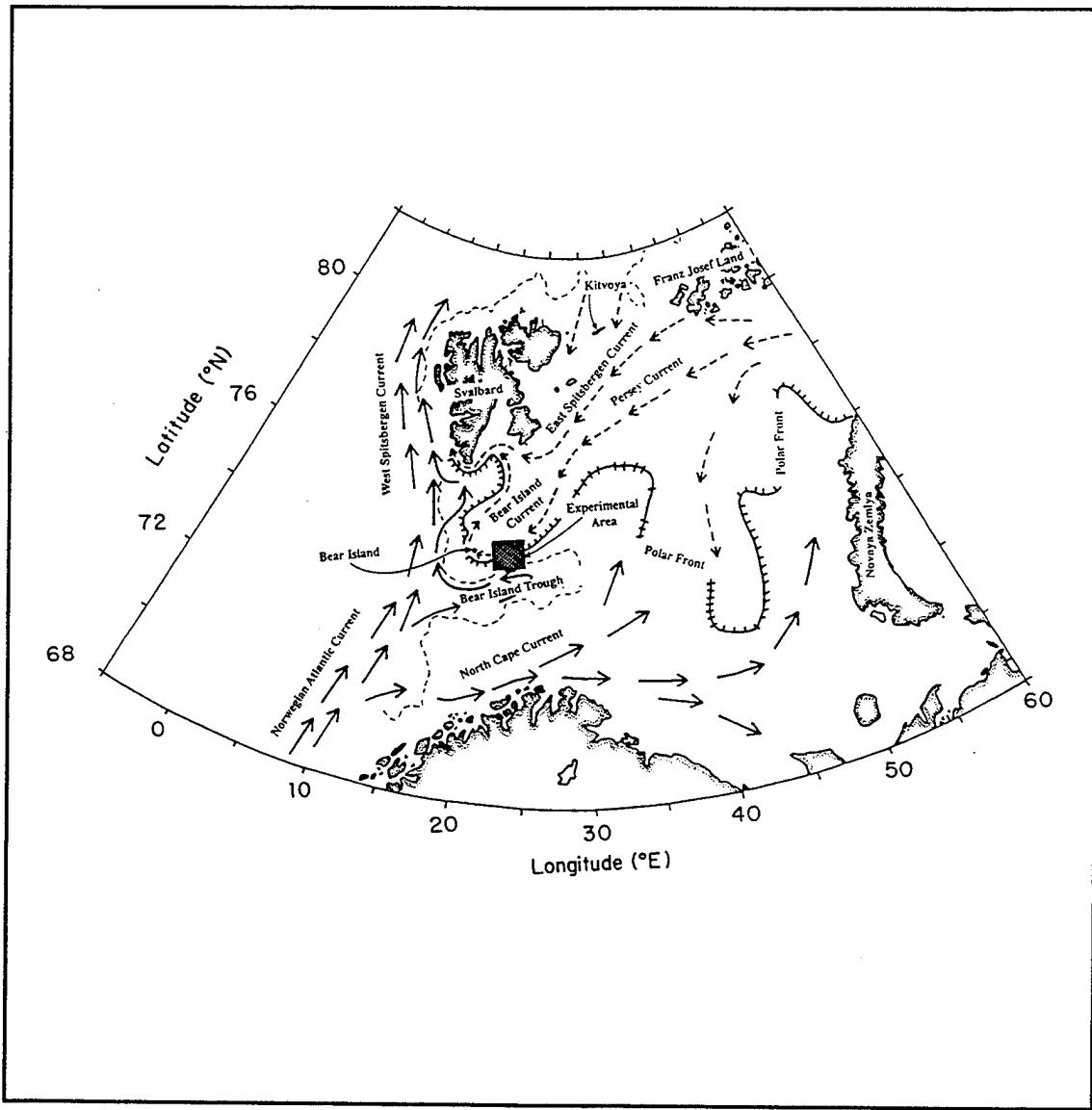
Figure 7. The surface circulation in the Barents Sea shows the major currents and their relation to the Polar Front. The dashed 400 m isobath is also displayed showing the outline of Bear Island Trough. The gray-shaded box depicts the experiment location on the northern side of Bear Island Trough. Dashed arrows indicate cold currents; solid arrows indicate warm currents. The hatched line indicates the mean frontal position adapted from Loeng (1991). This depiction differs from many seen in the literature (such as Johannessen , 1986 and Loeng, 1991) by suggesting a substantial recirculation entirely within Bear Island Trough. The major portion of the North Cape Current is portrayed flowing into the Barents Sea much closer to the Norwegian Coast. This depiction is based primarily on a Lagrangian drifter study by Poulain et al. (1995) and modeling studies by Gawarkiewicz and Plueddemann (1995).

18
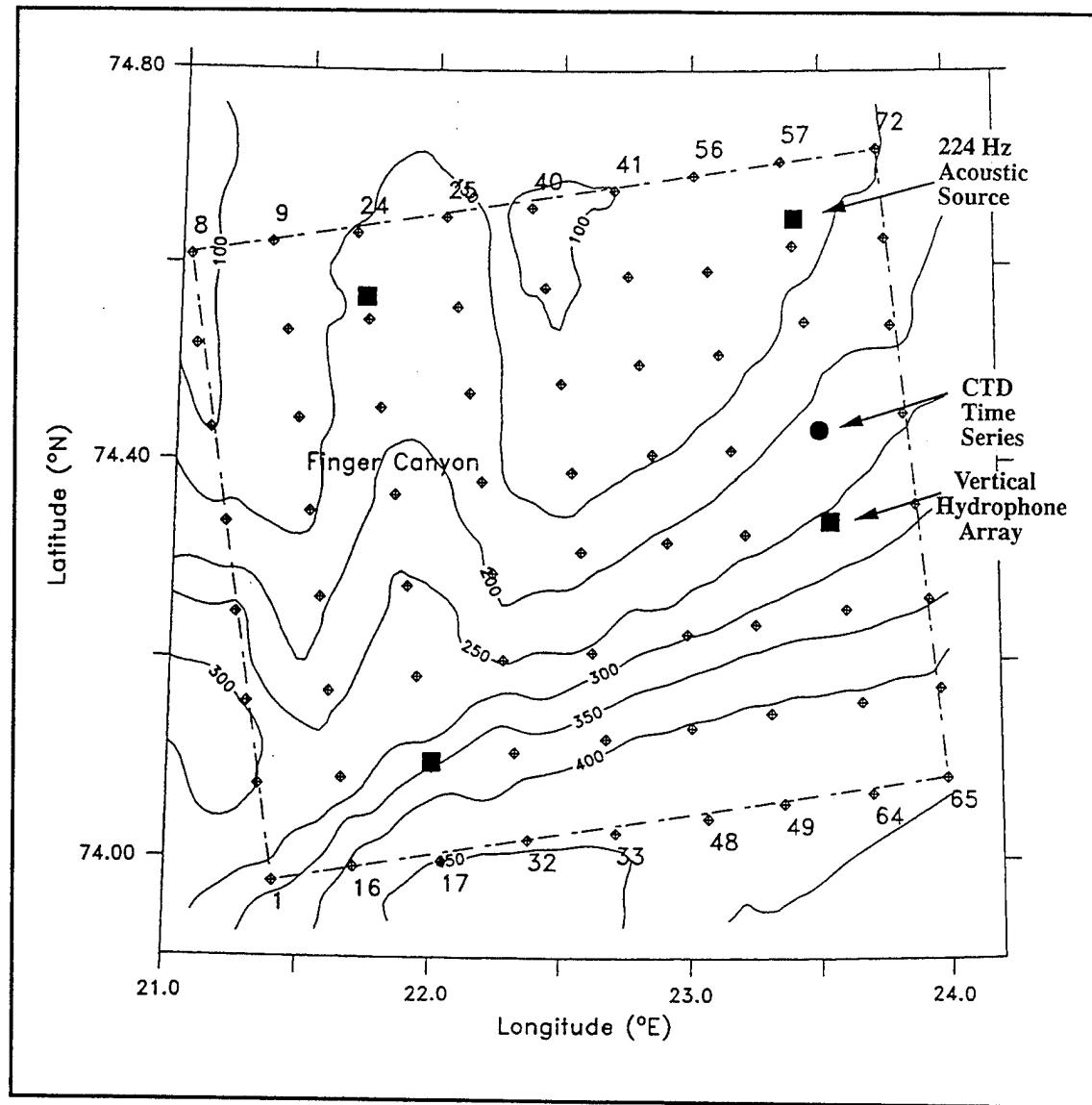
Figure 8. The experiment took place in a 70 by 80 km area. CTD stations were pre-defined with a 10 km spacing and labeled 1 through 72 preceding west to east. Each sampling of the stations is referred to as a grid run. Grid runs 1 and 4 were complete. The ■ symbol indicates current meter and tomographic mooring positions. The moorings are referred to by their location within the grid (i.e. , Northwest, Northeast, Southwest, and Southeast). The ● indicates the position of the CTD time series at the front. The bathymetry of the experimental area was derived from a compilation of ADCP data, CTD station depths, and Norsk Polarinstitutt Chart 7421. The eastern portion of the experimental area was over regular topography; the topography in the western section was steeper being dominated by Finger Canyon. Throughout the area the steepest bathymetric gradients were between the 300 - 400 m isobath.

dbar and then vertically averaged to 3 m increments and placed into a grid prior to vertical contouring. Density (σ_t) calculations were made from the 1 m vertical resolution data then averaged to 3 m. Table 2 summarizes the CTD deployment.

CTD Data Sets[a]	Time Period	Number of Standard Spaced Stations (10 km)	Number of Intermediate / Special Stations (spacing)	Number of Repeat Stations	Total Number of Stations
Grid 1	2030Z August 6 to 2300Z August 9, 1992	72	0	0	72
Grid 2	0610Z August 10 to 1050Z August 14,1992	47	6 (5 km)	5	58
Stationary Time Series	0600Z August 17 to 0800Z August18, 1992	0	27 (< 0.3 km)	0	27
Grid 3	2050Z August 21 to 0430Z August 23,1992	20	4 (5 km)	1	25
Grid 4	1445Z August 23 to 1550Z August 26, 1992	71	21 (5 km)	0	92

[a] 2.5 km spaced CTD stations are not included in this table

Table 2.   CTD Deployment during the Barents Sea Polar Front Experiment.

Four vector-averaging current meters (Aanderaa RCM-8) provided observations averaged at 10-minute intervals of current velocities at depths of 50 m and below with an accuracy of 5° and +/- 1 cm s^{-1} for speeds greater than 5 cm s^{-1}. Additionally, four vector-measuring current meters (two Neil Brown Acoustic Current Meters (ACM2's) and two Neil Brown SMART   Acoustic Current Meters (SACM's)) provided 10-minute average shallow water measurements at depths of 20-50 m.   A fifth Aanderaa meter failed on deployment. Table 3 lists the location and record lengths for all of the current meters as well as for the temperature sensors.

Mooring	Position	Start Time and Date	Duration (days)	Depth of Mooring (m)	Current Meters (Serial #)	Brankner or Other Temp. Sensors (Serial #)	Inst. Depth
Northwest	74°32.86N 21°43.54E	1400Z August 12	10.16	170	SACM 1173		19.4
						3664	29.5
						3659	39.2
					Aand.[a] 9254		49.3
					Aand.[b] 9263		159.9
Northeast	74°37.67N 23°24.14E	1600Z August 13	8.72	142	ACM 1169		22.1
						3363	32.1
						3754	42.1
					ACM 1170		52.0
					Aand. 9259		82.1
Southwest	74°04.67N 22°00.42E	0200Z August 11	12.26	380	SACM 1158		19.9
						3666	29.9
						3660	39.9
					Aand. 9258		50.0
					Aand. 9260		80.0
						3658	140.0
						3669	200.5
						sys3[c]	360.0

[a] Aand. = Aanderra Current Meter
[b] Aanderra 9263 speed rotor failed on deployment; the temperature record was available
[c] Tomographic Receiver Temperature Sensor (equivalent of thermistor on Aanderra Meters)

Table 3. BSPF Experiment Hydrographic Mooring Summary.

The RD Instruments self-contained Acoustic Doppler Current Profiler (ADCP) installed on the USNS BARTLETT operated at a nominal frequency of 300 kHz and provided a velocity accuracy (standard deviation) of 0.9 cm s^{-1} based upon the manufacturer's accuracy estimate for our configuration. The ADCP was configured to alternate between 8 m resolution "water-track" pulses and "bottom-track" pulses during a 3 minute ensemble averaging interval. Prior to ensemble averaging, velocities were corrected for tilt and converted to geographic coordinates. Thirty depth bins each of 8 m length were recorded for each ensemble. Water track data were converted to absolute

velocities using the ADCP bottom track velocity and corrected for gross errors (velocity "spikes") using a first-difference filter. The resulting velocities were then corrected for alignment and sensitivity errors (Joyce, 1989) using Global Positioning System (GPS) navigation data recorded with each ensemble (A. J. Plueddemann, personal communication, 1994). The bottom track mode was successful in depths of 400 m or less. ADCP bottom depths were found to be within a one or two meters of shipboard echosounder depths for water depths less than 325 m and were incorporated in the composite bathymetry. ADCP bottom depths from water deeper than 325 m were not used in further analysis.

An obvious feature of the front was its strong horizontal positional tie to the bathymetry within the experimental domain. Figure 8 depicts a contour field of the bathymetry for the experimental area based upon a compilation of CTD station depth taken from the ship's fathometer, ADCP bottom track data, and extracts from the Norsk Polarinstitutt Chart 7421 (1986). Finger Canyon, in the western part of the figure, is the obvious bathymetric feature within the experimental domain. The maximum bottom slope along Bear Island Trough in the region of the experiment varied from 1:65 near Finger Canyon to 1:300 in the eastern part of our region which is steeper than the average continental shelf gradient (1:500) but less steep than the average continental slope (1:20) (Bowden, 1983).

III. THE OBSERVED CONDITIONS

The measured currents and static fields of temperature, salinity and density define the salient features of the front in August 1992. Calculations of the geostrophic velocity from the temperature and salinity data relates the baroclinic currents to the observed currents.

Meteorological conditions during the period of observations were generally stable as a high pressure system dominated the region. Overcast conditions with low ceilings of 75 to 300 m lasted essentially the entire period. The mean air temperature was 7.7°C with little variation except on 12 August when the skies briefly cleared. At the start of the experiment, there were 20.8 hours of daylight and by the end of the experiment there were only 18.2 hours of daylight. Wind wave and swell height averaged less than 1.5 m. As a low pressure area approached the region, the strongest winds of 14 m s^{-1} out of the east-southeast were recorded on the 18th of August. A maximum wave height of 4 m was coincident with the passage of this storm. The consistency of the weather allowed interpretation of most variations in the observed conditions as primarily ocean-induced phenomena. Figure 9 depicts the meteorological observations recorded on the bridge of the USNS BARTLETT.

A. OBSERVED CURRENTS

1. The Tides

The overwhelming presence of the semidiurnal tidal signal in all the hydrographic measurements, coupled with the impact of tidal aliasing on the collection of CTD data, suggests a consideration of a tidal analysis as an initial step in the data analyses. Tidal components in the measured currents were deduced using the least squares method as detailed in Foreman (1978). The predominant barotropic species resolved by the analysis were the M2 and K1 species. Other less energetic internal tidal species (M3, M4, M6)

23
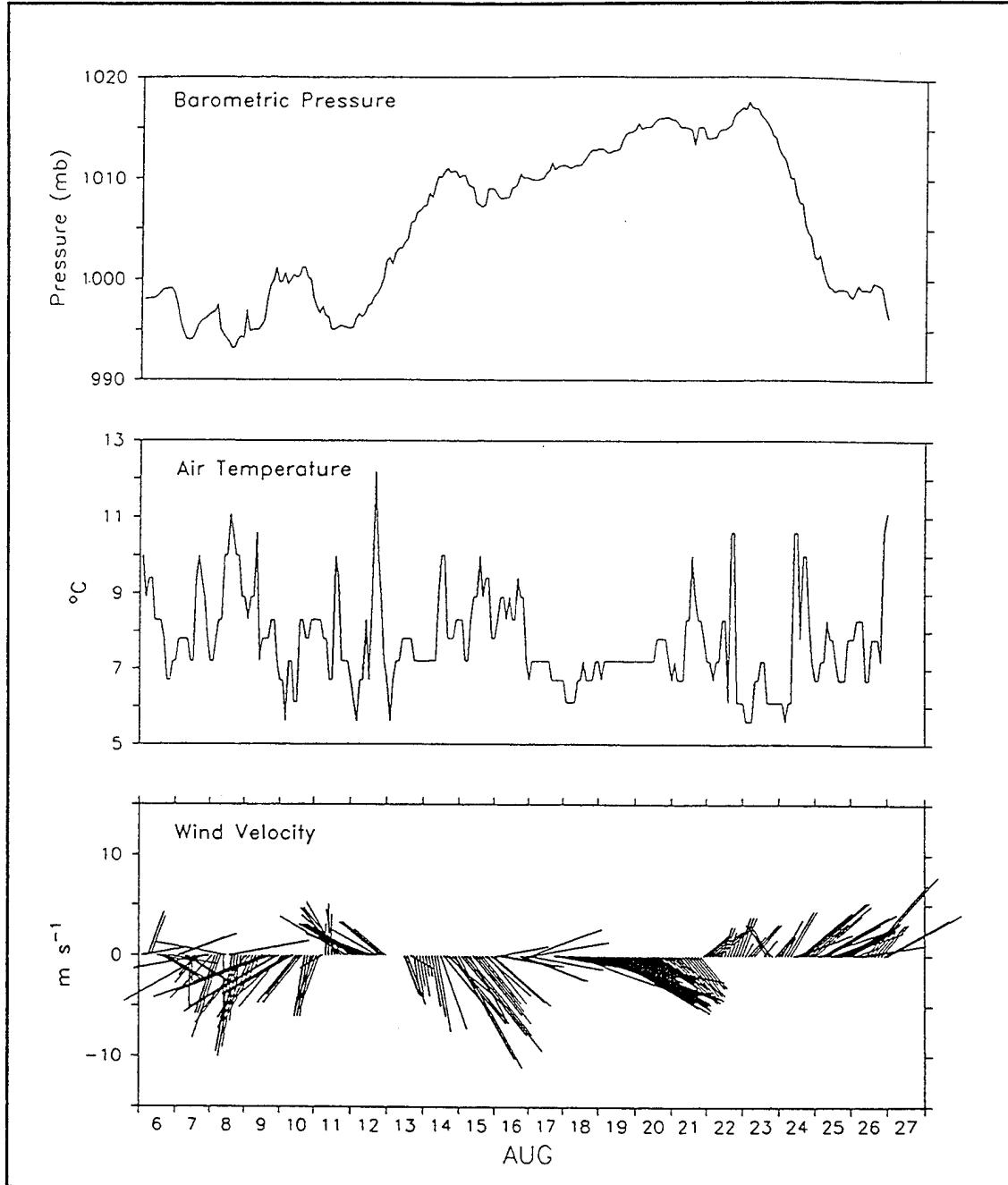
Figure 9. Observations of air temperature, barometric pressure and wind velocity recorded on the USNS BARTLETT highlight the meteorological conditions during the period observations were collected.

24

were identified in the analysis but their magnitudes were not significant relative to error considerations. Errors in the tidal fit were obtained by calculating the variance in tidal bands (e.g., diurnal, semidiurnal) from the spectra of the residual currents (difference between observed currents and calculated tidal currents) for both the zonal (u) and meridional (v) components following the techniques of Rosenfeld (1987).

Rosenfeld's techniques refine the error estimates to particular frequency bands vice treating the residual flow as white noise. This eliminates the assumption that the measured flow does not contain significant oscillations at non-tidal frequencies. The magnitude of the variance in a particular (tidal) frequency band reflects the error of the coefficients for the sine and cosine terms calculated from the least square fit. This error is carried into the subsequent calculations of phase, inclination and lengths of the semi-major and semi-minor axes for a particular tidal species associated with that frequency band. By relating the variance as a function of the four sine and cosine coefficients obtained in the Foreman results and assuming that the variance of the sine and cosine coefficients are equivalent while the covariance is zero, it is possible to calculate the error of these tidal ellipse parameters for a particular species which lies within that band.

The analysis of the variance in the semidiurnal frequency band is clouded by the fact that the critical latitude of 74°28.3'N passes through the experimental domain. At this latitude the M2 and inertial periods are identical. Since both the inertial motion and the M2 tidal ellipse exhibit clockwise rotations, a rotary spectra analysis is not useful in distinguishing the variance attributed to inertial motion. However the impact of inertial motion on these calculations is assumed small. The similarity of the magnitude of the variance in the semidiurnal band between the shallow meters and the deeper ones, later shown to be essentially isolated from wind-driven motion, supports this conclusion.

Initial estimates of the errors of the fitted currents to the observed values were considerable. The failure of the fit to include the principal solar semidiurnal (S2) species was due to the inadequate record length. The synodic period for the M2 and S2 species is ~14.77 days and the longest current meter record was 12.26 days. To reduce the error

25

of the tidal fit, the S2 species was inferred from an estimated ratio of M2 ellipse parameters to S2 parameters. Two techniques were employed to obtain the M2 to S2 ratio. First, a 'super-resolution' technique was employed, similar to that applied to tidal heights by Godin (1989), by assuming the currents were predominately tidal and had a high signal to noise relation. A validity of this assumption can be verified in an examination of the time series for the deepest meter on each mooring as seen in Figure 10. An M2 to S2 relation was obtained from the data through a relaxation of the Rayleigh criteria and used for the inference. The second technique was to use model data for the M2 and S2 species provided by Kowalik and Proshutinsky from their 14 km resolution Arctic tidal model specifically for each current meter location (Kowalik and Proshutinsky, 1994). Both techniques significantly reduced the error but the Godin technique provided the smallest errors based upon the estimated S2-M2 phase difference. Tables 4a through 4c summarize the results and calculated errors found for each current meter for the M2, S2, and K1 species. The calculated M2 tidal ellipses at 50 m are provided in Figure 11. Table 5 summarizes the vertically averaged tidal results and comparisons between other observations and tidal models. Note that the inclination of the major axis of the tidal ellipses are generally oriented parallel to the isobaths particularly at the SW mooring. This was true at all depths. The tidal ellipses also demonstrate a significant increase in tidal current amplitude for measurements made over the shelf.

The variability in tidal influence on the flow over the shelf compared to that in deeper water is also highlighted in the total variance explained by the Foreman tidal fit to the measured currents. The percent of total variance explained by the tidal fit is calculated by the ratio of the difference between the total variance and residual variance to the total variance of the current. Current fluctuations at the two shelf moorings indicated that ~ 93 percent of the total u velocity variance and ~ 85 percent of the total v velocity variance was explained by the tidal fit. In contrast, the three current meters in deeper water south of the front indicated substantially less tidal fluctuations, i.e., only ~ 49 percent of the total u variance and ~27 percent of the total v variance was explained by the
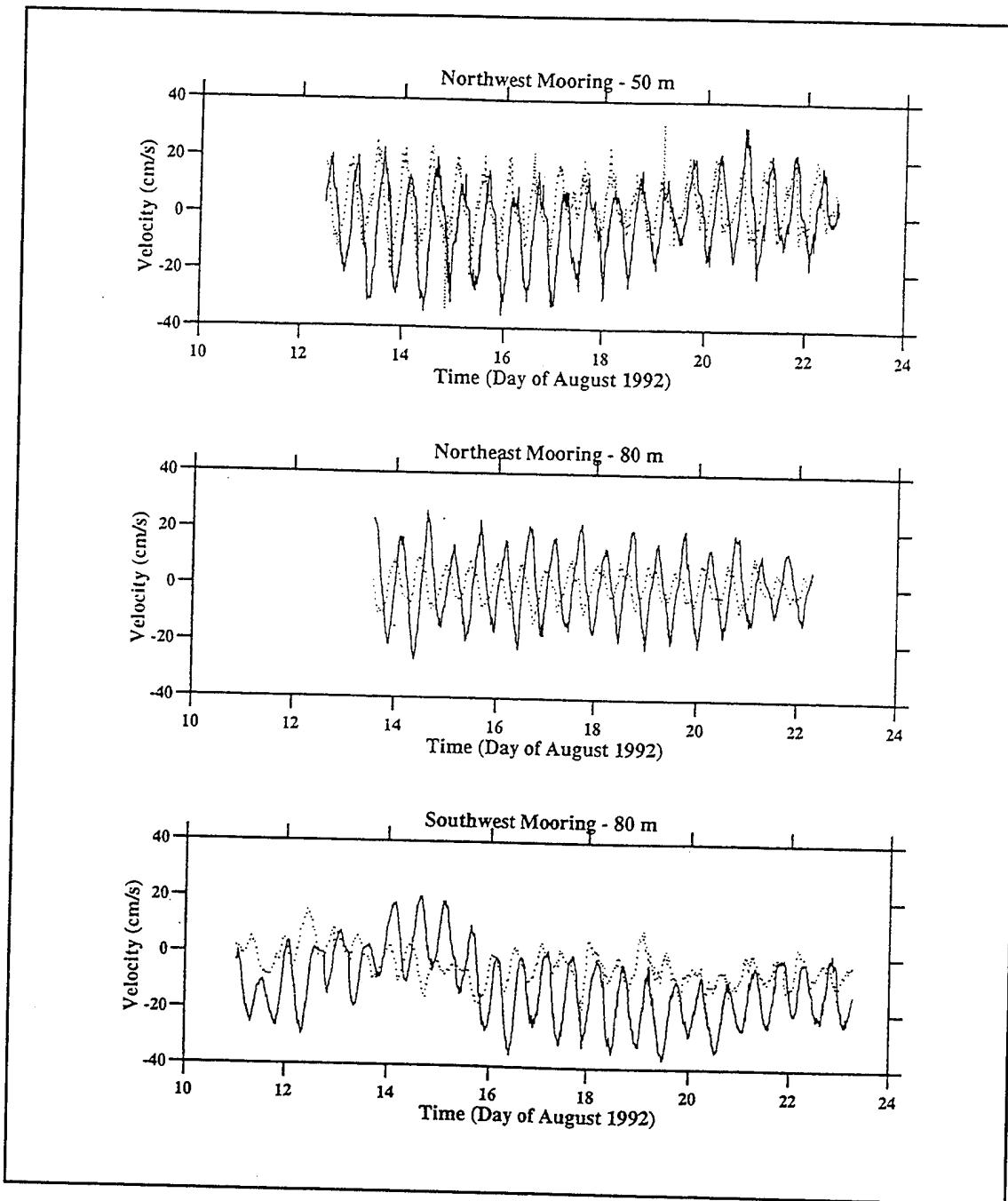
Figure 10. Time series of the *u* (solid curve) and *v* (dotted curve) components of the currents for the meters at 80 m on the NE and SW moorings and the meter at 50 m on the NW mooring show the strong tidal component in the currents.

Current Meter (Mooring)	Depth (m)	Major Axis (cm s⁻¹)	Error (cm s⁻¹)	Minor Axis (cm s⁻¹)	Error (cm s⁻¹)	Greenwich Phase (degrees)	Error (°)	Inclination(°) CCW from East Axis	Error (°)
SACM 1173 (NW)	19.4	5.9	0.2	-1.4	0.4	328.3	3.9	160.2	4.5
Aanderaa 9254 (NW)	49.3	2.9	0.1	-0.8	0.2	312.9	2.8	165.3	3.4
ACM 1169 (NE)	22.1	3.6	0.4	-0.9	0.3	331	6.3	148.5	5.3
ACM 1170 (NE)	52	3.5	0.7	-0.6	0.4	323.2	11.6	153.3	7
Aanderaa 9259 (NE)	82	3	0.1	-0.5	0.1	313.3	2.7	153.9	1.5
SACM 1158 (SW)	19.9	2.7	0.6	1.5	0	10.1	22.3	157.9	16.4
Aanderaa 9258 (SW)	50	3.4	0.2	2.6	0.2	56.7	12.1	190.6	12
Aanderra 9260 (SW)	80	3.4	0.4	2.4	0.4	354.6	12.1	133.4	19.5

Table 4a. K1 tidal species current analysis results.

Current Meter (Mooring)	Depth (m)	Major Axis (cm s⁻¹)	Error (cm s⁻¹)	Minor Axis (cm s⁻¹)	Error (cm s⁻¹)	Greenwich Phase (degrees)	Error (°)	Inclination(°) CCW from East Axis	Error (°)
SACM 1173 (NW)	19.4	24.8	2.3	-20	2.2	68	24.5	-2.6	4.5
Aanderaa 9254 (NW)	49.3	12.4	1.7	-7.4	1.9	62.9	20.3	17.1	16.3
ACM 1169 (NE)	22.1	16.9	0.5	-9.2	0.7	33	2.2	-1.5	3.6
ACM 1170 (NE)	52	23.7	2.6	-15.2	1.9	61.3	9.4	15.1	10.4
Aanderaa 9259 (NE)	82	10.9	0.6	-4.1	0.5	52.4	1.5	-5.4	3.4
SACM 1158 (SW)	19.9	6.5	3.8	-1	2.9	57.8	33	21.3	27.5
Aanderaa 9258 (SW)	50	9.1	0.9	-3.1	1	32.9	5.1	5.6	7.8
Aanderra 9260 (SW)	80	10	0.8	-3.7	0.6	41	4.4	3.1	4.8

Table 4b. M2 tidal species current analysis results.

28

Current Meter (Mooring)	Depth (m)	Major Axis (cm s⁻¹)	Error (cm s⁻¹)	Minor Axis (cm s⁻¹)	Error (cm s⁻¹)	Greenwich Phase (degrees)	Error (°)	Inclination(°) CCW from East Axis	Error (°)
SACM 1173 (NW)	19.4	9.2	0.6	-4.8	0.6	146.3	**	26.6	**
Aanderaa 9254 (NW)	49.3	8.6	1.8	-6.3	1.8	143.1	**	9.3	**
ACM 1169 (NE)	22.1	9.2	0.6	-4.8	0.6	146.3	**	26.6	**
ACM 1170 (NE)	52	13.3	1.9	-9.9	2.5	141.3	**	17.4	**
Aanderaa 9259 (NE)	82	7.8	0.6	-3.6	0.5	122	**	-5.4	**
SACM 1158 (SW)	19.9	4.5	2.8	-1.8	3.9	152.5	**	20.3	**
Aanderaa 9258 (SW)	50	6.7	1	-3.7	1	127.6	**	4.6	**
Aanderra 9260 (SW)	80	5.5	0.8	-3.1	0.7	115	**	3.8	**

Table 4c. S2 tidal species current analysis results.

tidal fit.   Examination of the current meter records reveals that lower frequency oscillations (synoptic scale) in the southern current meter records creates much of this contrast.

At all the moorings current meter records showed that the maximum calculated M2 species current was about four times larger than the K1 species current. Based upon the 'super-resolution' technique, the M2 component was inferred to be 1.5 times larger than the S2 species current. The M2 species was expected to be the dominant tidal component because this part of the Barents Sea was not subjected to the local amplification of the K1 tidal currents frequently observed over Svalbard Bank and in the vicinity of Bear Island as reported by Gjevik et al. (1994) and by Kowalik and Proshutinsky (1995).

The tidal analysis not only quantified the dominance and spatial variation of the semidiurnal tides relative to the front, but also provided some evidence for the existence of a baroclinic tide being generated over the slope.   The M2 tidal ellipses at the SW
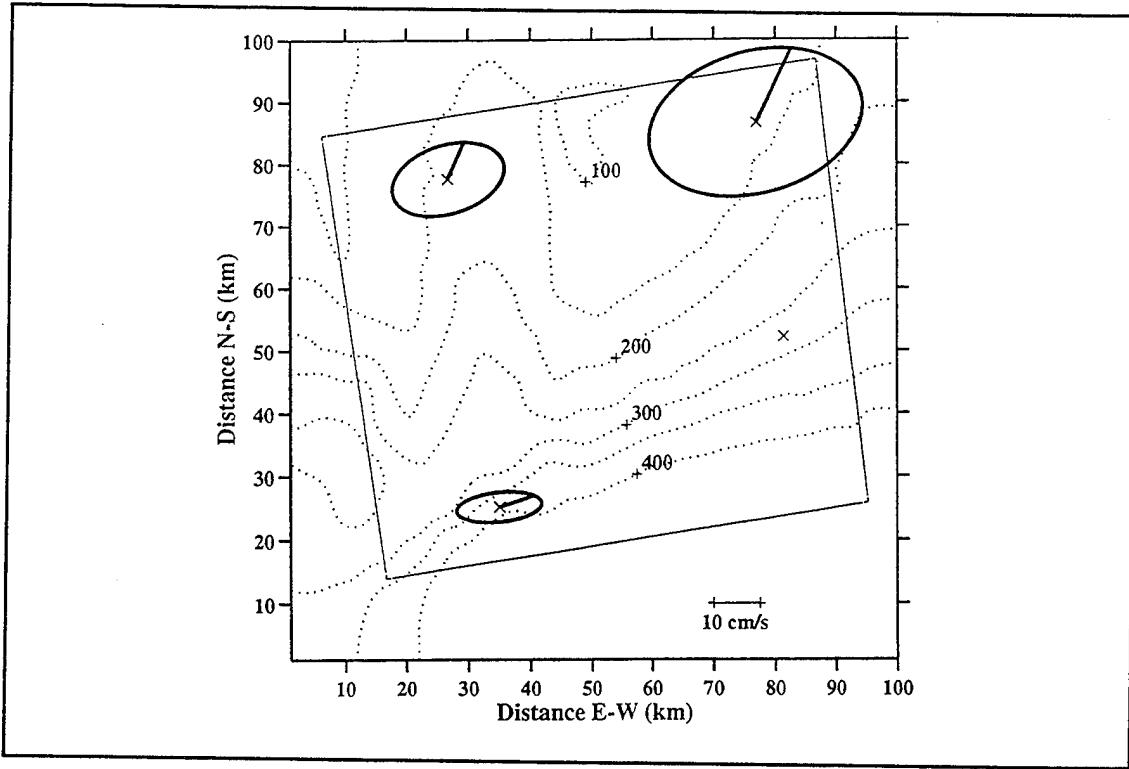
Figure 11. A plot of the M2 tidal ellipses for the deepest current meters at each mooring shows the increase in amplitude over the shelf at the shallow moorings. Notice that the ellipses at the NE and SW moorings are generally aligned with the bathymetry. The dark line from the center of the ellipse indicates the Greenwich phase relative to the time of maximum current. The experimental region was converted to local grid coordinates to correctly depict the ellipse orientation.

mooring demonstrated a nearly barotropic flow (Figure 12a). In constrast, over the shelf the tidal ellipses of the northerly moorings presented a baroclinic structure in major axis amplitude. Further evidence of the baroclinicity extending into the deeper slope water is seen in a least-squares tidal fit to the ADCP data collected at the 27-hour CTD time series in the frontal zone. Though the short record length only allowed the M2 species to be resolved, the fit to the data was deemed good based on the simple qualitative technique following Godin (1972). This evaluation of the fit merely comes through the visual examination of the residuals as a comparison of the variance of the residuals to the data (u: 4.7 to 157.0 cm^2 s^{-2}; v: 3.2 to 29.6 cm^2 s^{-2}). The effect of the sloping bottom on the

30

barotropic tide is seen by the depth dependence of the Greenwich phase and major axis inclination (Figure 12b). Huthnance (1989) reported that, though in general only a small amount of dissipation of the total tidal flow and related vertical mixing can be attributed to internal tides, the distribution can be localized and the effects important in specific areas (e.g., over the slope).

Study	KI Major Axis Amplitude	Greenwich Phase/ Rotation	M2 Major Axis Amplitude	Greenwich Phase/ Rotation	S2 Major Axis Amplitude	Greenwich Phase/ Rotation
NW Mooring Depth-Averaged[a]	2.9	313°/+	12.4	63°/+	8.6	143/+
NE Mooring Depth-Average[a]	3.4	333°/+	17.3	88°/+	9.5	159°/+
SW Mooring Depth-Average[a]	3.2	36°/-	9.4	65°/+	6.9	160°/+
Model NW Mooring[b]			20.3	85.5°/+	6	83.2°/+
Model NE Mooring[b]			20.6	84.5°/+	6.7	86.5°/+
Model SW Mooring[b]			12.4	84.3°/+	4.2	79.9°/+
Station 30[c]	3.4 2.7	- -	9.5 10.4	+ +	3.0 2.9	+ +
Mooring B$_L$[d]	~4.0	221°/-	~19.0	43°/-		

+ indicates clockwise rotation of the current vector, - indicates counter-clockwise

[a]   results of tidal current analysis of depth-averaged current meter velocities using Foreman's Tidal Current Analysis Programs

[b]   from model predicted tidal ellipses calculated specifically for experimental mooring positions by Kowalik and Proshutinsky using their 14 km Arctic Tidal model (see Kowalik and Proshutinsky, 1994)

[c]   Station 30 from Gjevik et al. (1994) is located just southwest of the SW mooring. Top line indicates observational data cited by Gjevik et al. and second line is their model prediction for the same location

[d]   Mooring B$_L$ from Huthnance (1981) is located 100 km south of experimental area

Table 5. Summary of tidal current amplitude and phase comparison

31
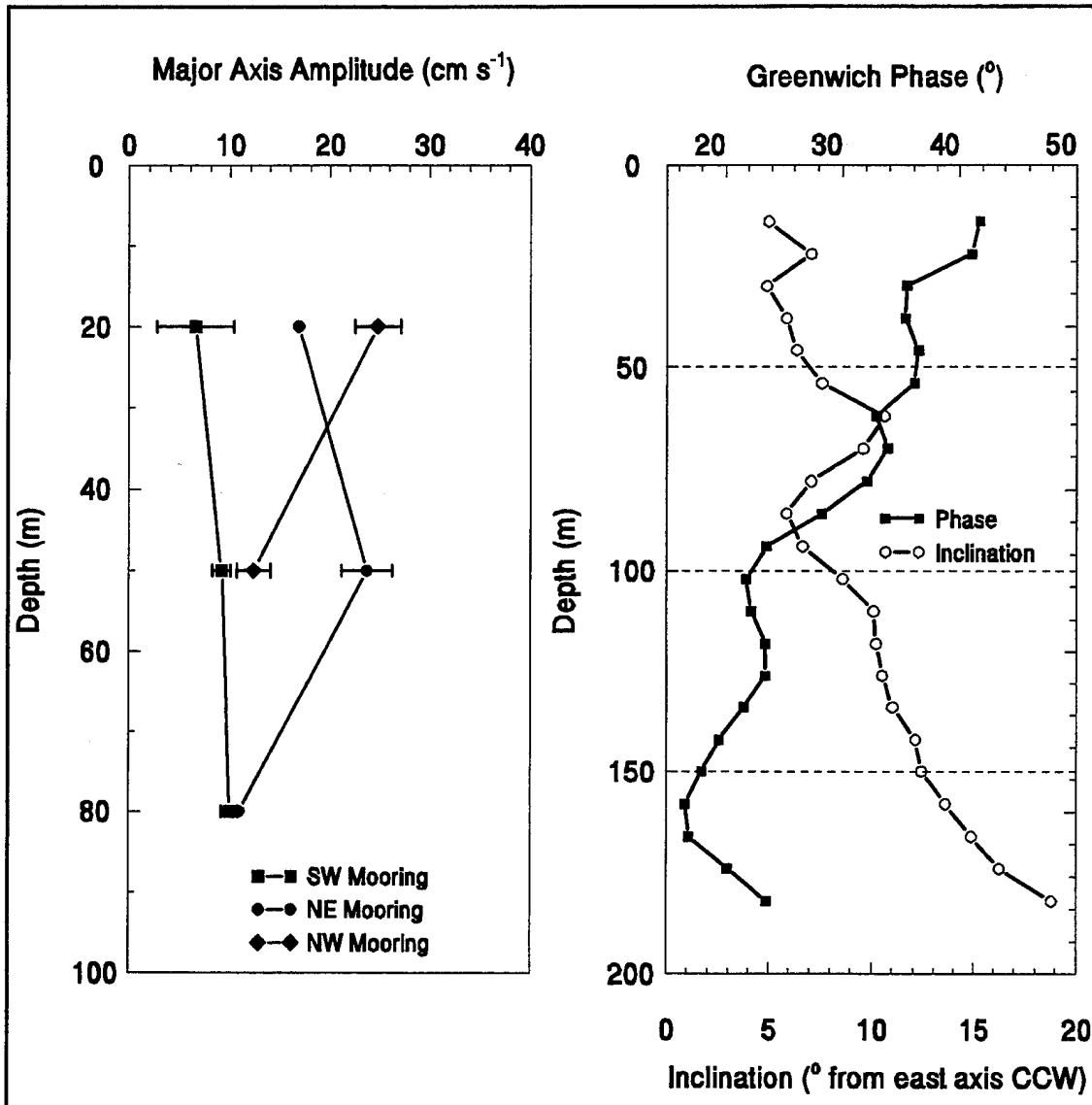
Figure 12 (a) A comparison of the M2 major axis amplitude with depth for each mooring shows the barotropic character of the tide at the SW mooring. Considerable vertical differences in amplitude are noted for the northern moorings suggestive of a significant baroclinic tidal component at these shallow water locations. Error bars indicate one standard deviation. (b) A plot of the phase and inclination of the M2 tidal fit to the ADCP data collected at the CTD time series shows the decrease in phase with depth and the counterclockwise rotation of the inclination with depth. Inclination is measured counterclockwise from positive x axis (east) . A similar plot for the amplitude shows that it is virtually constant except at the mixed layer.

2. Current Meters

In the examination of the time series of the measured currents, further distinctions in the flow relative to the front are found. Time-mean flows for all current meters are provided in Table 6. This average represents the remainder of the flow after short period tides have been averaged out but, due to the brevity of the records, still includes the effects of synoptic scale influences, long period tides, and seasonal influences as well as the long-term mean. South of the front the vector mean speed and the scalar mean speed are approximately the same, indicative of limited tidal influence on the mean horizontal flow. North of the front they are significantly different which indicates that tidal fluctuations dominate the mean horizontal flow at all depths over the shelf. The maximum scalar current speed of $\sim$ 60 cm s^{-1} recorded at the shallow meter on the NW mooring was $\sim$12 to 20 cm s^{-1} greater than the other current meter maxima.

Current Meter	Mooring	Moored Depth (m)	Scalar Mean Speed (cm s^{-1})	Vector Mean Speed (cm s^{-1})	Mean Direction
Neil Brown SACM 1173	NW	19.4	31.6	11.2	314.6
Aanderaa RCM-8 9254	NW	49.3	15	4.6	326
Neil Brown ACM-2 1169	NE	22.1	18.6	3.9	189
Neil Brown ACM-2 1170	NE	52	26.3	2.3	185
Aanderaa RCM-8 9259	NE	82.1	11.3	0.2	26.6
Neil Brown SACM 1158	SW	19.9	15	8.4	213.9
Aanderaa RCM-8 9258	SW	50	14.4	10.8	245.3
Aanderaa RCM-8 9260	SW	80	15.4	12	252

Table 6. Summary of current meter statistics

In plots of the progressive vector diagrams for deep meters on each mooring (Figures 13a - c), the distinction of the measured flow relative to the front is more readily observed. The elliptical tidal 'trajectories' are clearly evident in the diagrams from the northern moorings. A mean direction and scale of 'displacement' can also be observed for the northern moorings. At the Northeast mooring a net southerly 'displacement', though very small, is calculated (less than 1 km at 80 m). At the Northwest mooring a northwestward displacement with a larger net displacement (30 - 55 km) is observed. At the Southwest mooring , the west by southwest mean flow is quite apparent in the vector diagram while the elliptical tidally-forced 'trajectories' are not observed at this scale. The displacement at the Southwest mooring is on the order of 75 km over 12 days.

Figure 13c and Table 6 indicate that the deepest meter on the SW mooring demonstrated a southwestward mean direction. Similar mean vectors were evident for the mid-depth and shallow meters. These results are believed to be the first measured currents which are attributed to the return flow of warm Atlantic Water exiting the Bear Island Trough south of the front, such as reported by Novitskiy (1961) and Pfirman et al.(1994).

Mean vectors for both meters at the NW mooring reflect a northwestward flow [Table 6]. The deepest meter on the NE mooring indicated a near zero vector mean flow but at the shallower moorings (20 and 50 m) a small net southerly flow was evident. These very weak mean flows north of the front are interpreted to be part of the cold southwestward Bear Island Current being steered by the local bathymetry.

3. ADCP Measurements

Mean currents for the ADCP data were determined using the tidal removal technique described by Candela et al. (1992). Details of the tidal removal techniques and evaluation of residuals for this ADCP data set were completed by Harris et al. (1995). The technique, based on a least-squares fit, assumes the space/time grid of the ADCP data

34
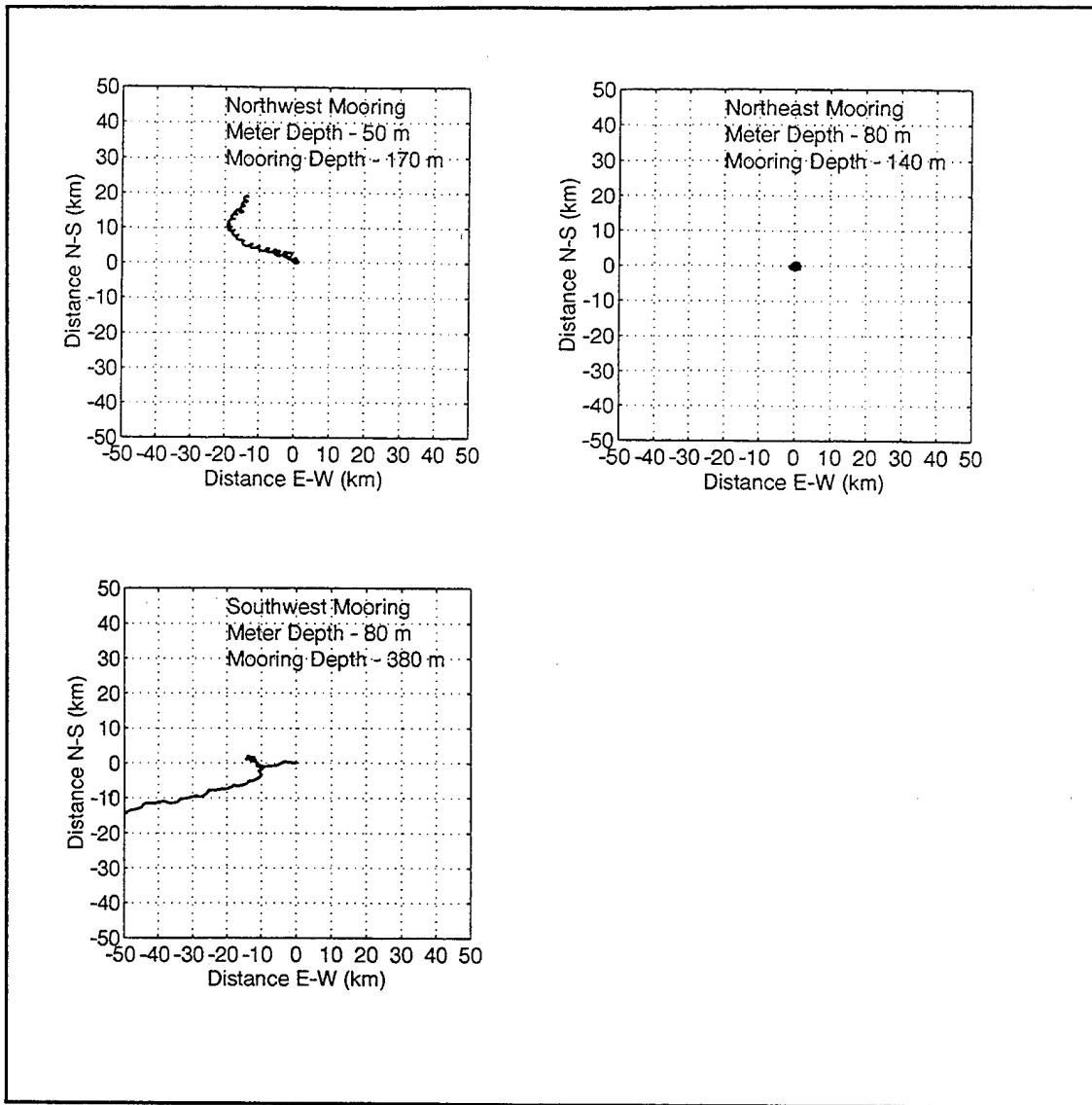
Figure 13. **Progressive vector diagrams for the (a) Northwest mooring 50 m (b) Northeast mooring 80 m (c) Southwest mooring 80 m. Progressive vector diagrams for the current meter provide not only an indication of mean direction but a sense of the character of the flow. An example is in (b) where the progressive vector diagram is plotted virtually as a single point which describes a**

can be modeled as a sum of harmonic functions at specified frequencies (the tidal constituents) and a temporally steady flow. Both the tidal currents and the steady flow may vary spatially. Prior to the model fit, ADCP data were averaged to either 1 hour in

35

time or 10 km in space, whichever occurred first. The best fit included harmonic functions at the frequencies of the M2, S2, and K1 tide, first order polynomials for the spatial variation of the tides, and second order polynomials for the spatial variation of the steady flow. The errors in the steady flow were estimated from the residuals of the model fit (Candela et al., 1992) and indicated that flows less than about 2 cm s^{-1} are not significant. The standard error of the model fit was found to depend upon the data density, model input data (whether moored data were included or not) and geographic location within the survey area. Evaluation of several model cases suggests that (3,2) cm s^{-1} for the (u,v) velocities is representative of the standard error in the subtidal field presented here.

The vertical average of the steady flow (subtidal) fields for the 25 m, 50 m and 81 m ADCP depth bins is shown in Figure 14. The ADCP data, as seen in this figure as well as the subtidal velocities from the other depth bins, indicate a significant southwest flow for locations deeper than the 300 m isobath. The magnitude of the southwestward flow near the SW mooring is somewhat less than the current meter mean (Table 6). This observation, combined with the current meter results, suggests that a southwestward barotropic flow characterizes the entire water column south of the front. In the eastern part of the study area the mid slope region (150 - 250 m) is characterized by a NE flow of about 4 cm s^{-1}. The weakening of this flow with the shallower water is consistent with the weak mean flow observed by the current meter at the NE mooring. In the center of the area, the ADCP data indicate a rapid current rotation from northeast to west. This is in reasonable qualitative agreement with the 50 m current meter mean at the NW mooring, although the ADCP current is weaker and more westward.

The analysis of the measured flow presents a structure surrounding the front that is essentially dominated by semidiurnal tides north of the front and containing a significant barotropic southwestward circulation south of the front. Evidence of a baroclinic structure to the tides was also found over the slope in the heart of the front itself. The southwestward direction of the flow south of the front observed in the current meters and

36
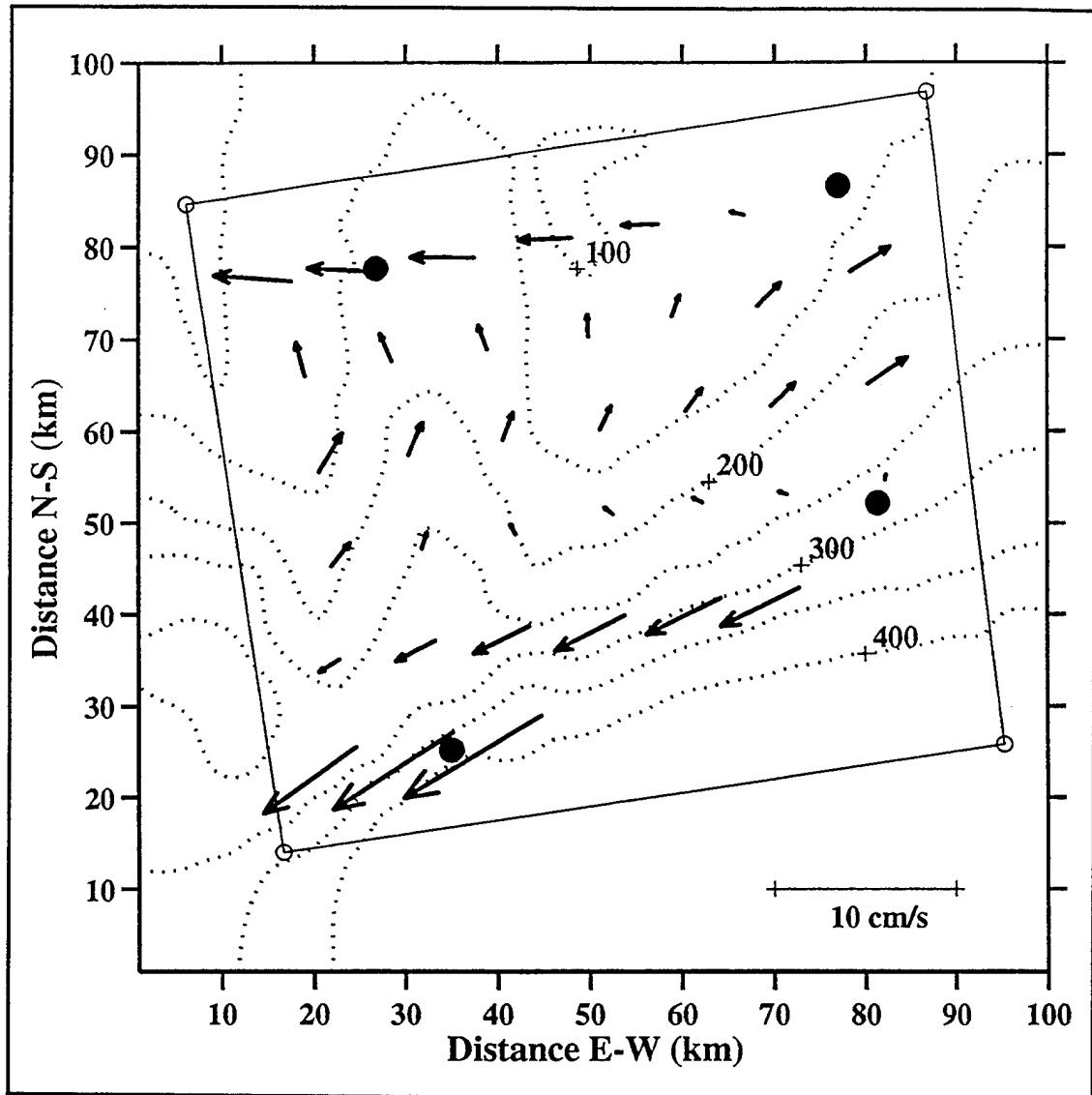
Figure 14. The averaged steady flow from the 25, 50 and 81 m ADCP depth bins is depicted at the hourly averaged positions (or at 10 km in spacing, whichever occurred first). The steady flow is the result of a least-squares fit of the observed ADCP velocities from the space/time grid represented by the cruise track to three tidal constituents (M2, S2, K1) and a steady flow (Candela et al., 1992). The tidal phase, amplitude and temporally steady flow are allowed to vary in space. The ● indicates the position of the hydrographic moorings.

ADCP data is consistent with a recirculation of NAW in Bear Island Trough. The persistence of the southwestward flow during the entire experiment over a wide domain

37

under varying wind conditions and directions suggests the flow was not the result of synoptic or mesoscale circulation influences.

B. OBSERVED HYDROGRAPHIC CONDITIONS

In the discussion that follows horizontal and vertical depiction of the BSPF are derived from the CTD observations. Each sampling of the station grid is assumed to be representative of a synoptic picture. True synopticity cannot be achieved as it took about 72 hours to sample the complete grid and about 7 to 8 hours to make a single cross-frontal line of stations. Interpretation of the data fields, therefore, requires consideration of interim forcing parameters which influence the synopticity of the survey (predominantly tides, but also winds and advection).

The two primary water masses meeting at the front, Norwegian Atlantic Water (NAW) and Barents Polar Water (BPW), were identified within the experimental area using the classification scheme from Hopkins (1991) [NAW (2° to 8°C and greater than 35.0 psu); BPW (-1° to 6°C and less than 34.4 psu)]. The BPW temperature range has been extended from that found in Hopkins to include the influences from summer warming. The series of cross-frontal T-S curves taken from the fourth occupation of the CTD grid, Figure 15, is typical of all cross sections. NAW (Station "64") was virtually isohaline beneath the mixed layer and was present at all depths in the southern stations. BPW (Station "57") was found to the north of the front beneath the mixed layer. At the stations immediately adjacent to the front (Stations "59" and "60"), the T-S mixing curves suggest the path the water masses follow when meeting and mixing at the front.

In order to spatially visualize how the two water masses meet at the front, a color-coded diagram of the parent water masses and the two regions of mixing, as identified from the TS plot, was constructed from eight CTD stations along the same cross section. This is a procedure similar to that of Steele et al. (1995) and is shown in Figure 16. The CTD data were divided by TS characteristics corresponding to regions on the TS curve. NAW is color-coded red and BPW is coded blue. The portion of the T-S

38
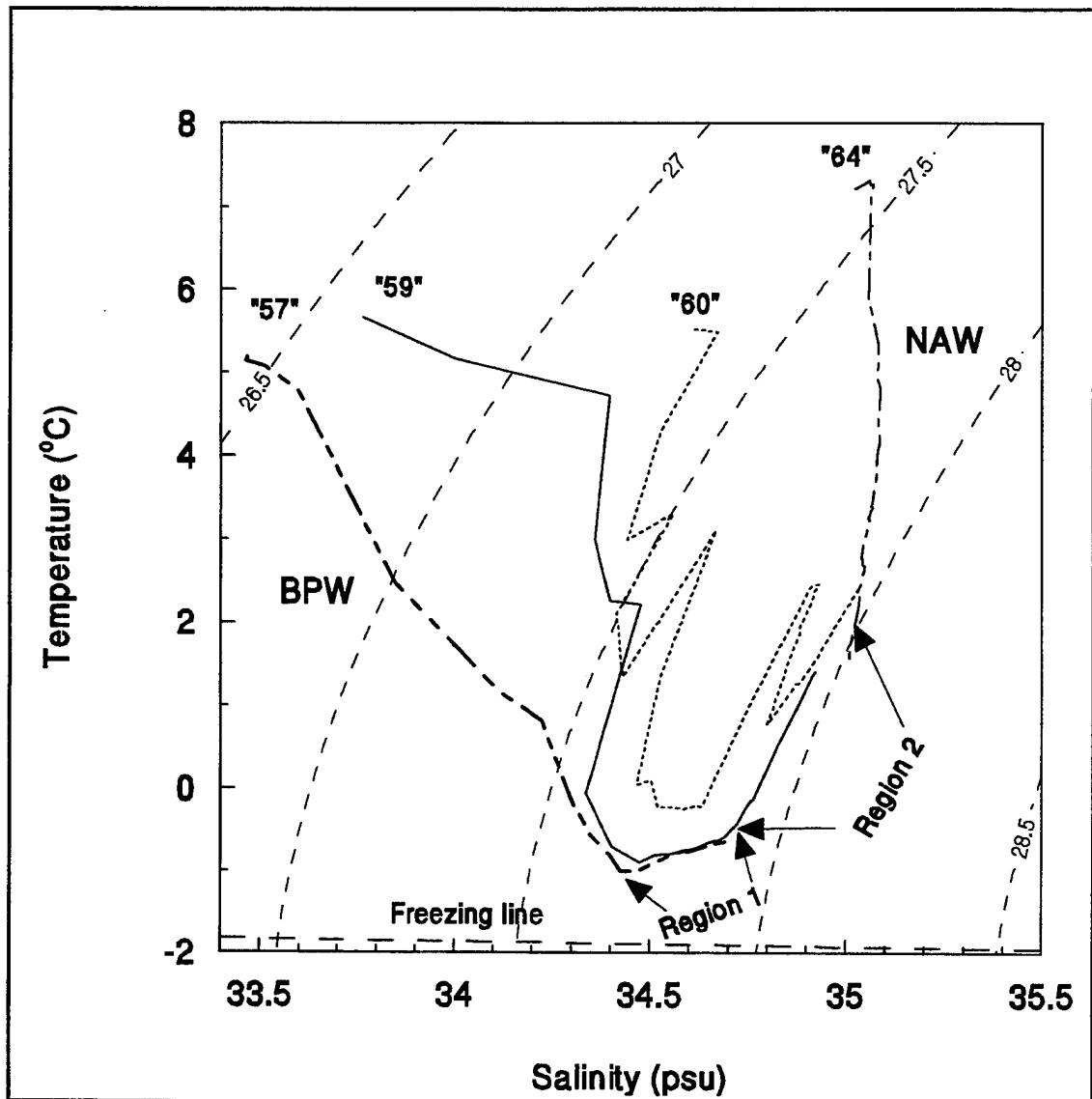
Figure 15. TS plot taken from four CTD stations along a cross section of the front indicates the primary water masses observed. The station positions from north to south, 57, 59, 60, and 64, are defined in Figure 8.

curve representative of diapycnal mixing is color-coded yellow and is labeled 'Region 1' on Figure 15. These water characteristics (~-0.5°C, 34.4 -34.6 psu) were found at the bottom of all the casts taken in the shallow water on Svalbard Bank (e.g., Station "57" - depth 110 m) and also found at mid column for those stations within 10 km of the front. Station "60" shows a warmer variant of this diapycnal mixing process representative of

stations on the southern boundary of the front. The portion of the TS curve which represents isopycnal mixing and labeled 'Region 2' in Figure 15 is color-coded green. The water characteristics in this region of the TS curve represent a significant cooling as well as a dilution of NAW as it mixes with the frontal water along isopycnals. Together, the green and yellow areas appear to be a manifestation of an upslope transport of NAW near the bottom and subsequent vertical mixing with the cooler fresher BPW water overlying it. Note that the highly localized frontal waters (e.g., stations 59 and 60) are not directly associated with either parent water and hence are not shaded. No mixing lines are seen connecting the TS water properties observed in the upper portion of the water columns. This also illustrates the minimal exchange of water mass characteristics observed across the front. Fine structure or interleaving of the water masses was confined to stations very near or at the front (< 10 km) (Station "60").

A vertical cross section between stations 57 and 64 of temperature, salinity, and density (σ_t) from the fourth transit around the CTD grid (Figure 17 a-c) is representative of all cross sections in the eastern two-thirds of the study area and reveals the general characteristics of the front. This cross section contains two additional stations near the front. These additional stations were taken on each cross-front leg during Grid 4 which increased the resolution in the vicinity of the front to 5 km. The front is easily delineated into vertical layers primarily due to the presence of the mixed layer warmed by summer solar insolation and freshened by summer ice melt on the northern side . The frontal surface manifestation is most clearly defined by the horizontal salinity gradient in the upper 20 -40 m. As salinity is the prime determinant of density within this still relatively cool mixed layer, a shallow density front corresponds to the salinity gradient. The maximum density difference across this shallow front was typically 0.8 kg m^{-3} at 10 dbar. The mixed layer depth as seen in the temperature cross section is seen to be ~ 10 m deeper on the southern side of the front than on the northern side. This is attributed to the decreased stratification on the southern side and the increased ability of the winds to mechanically mix deeper. Beneath the mixed layer and above 100 m, the front is defined
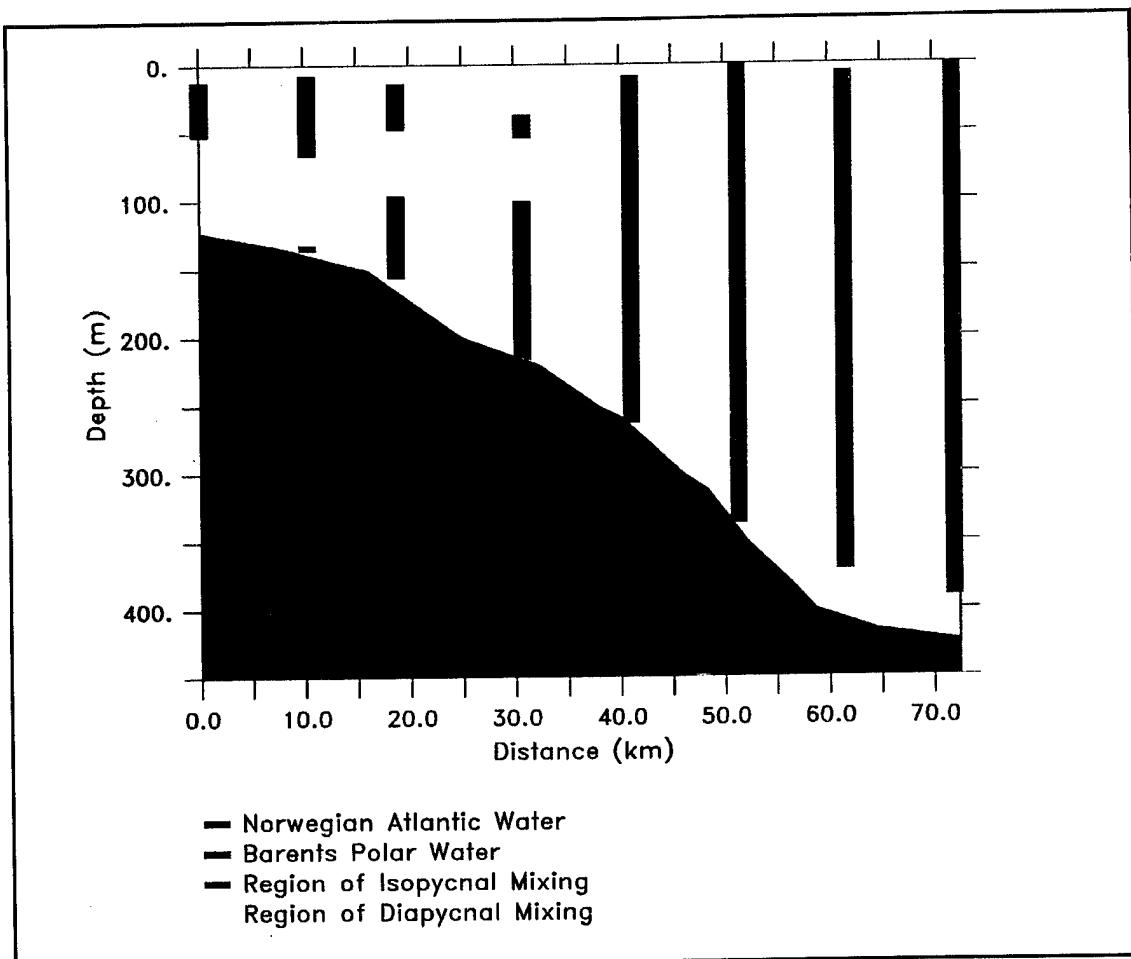
Figure 16. A color-coded plot of the parent water masses (NAW and BPW) and the two regions of the TS curve from Figure 15 portray the horizontal and vertical mixing paths at the BSPF.

by a horizontal temperature gradient. This shallow to mid-depth region at the front contained essentially all the fine structure associated with the front. Below 100 m the horizontal gradients are much weaker expanding the 'frontal zone' width, thought to be a result of bottom boundary layer and tidal mixing.

Note that the isopleths of temperature and salinity which define the front correspond to the convention of a retrograde front (Mooers et al., 1977) and are also consistent with previous depiction's of the frontal hydrography (Loeng, 1991). The horizontal scale as depicted from this cross section is ~ 10 km. However, it was

41

apparent from several other cross sections taken at sub-grid resolution that the 10 km station spacing undersampled the actual scale of the front. From stations taken at 2.5 km spacing, the scale of the maximum temperature and salinity gradients appears to be 3 km but finer resolution spacing may adjust this estimate.

The density field below the mixed layer portrays the barotropic nature of the front. Changes in temperature and salinity across the front are compensating in density resulting in nearly horizontal isopycnals. The maximum density difference at 80 dbar across the front from CTD grid 1 data was found to be only 0.24 kg m^{-3} while the median value was only 0.08 kg m^{-3}. Federov (1983) finds that typical density differences across ocean and coastal fronts range from 0.1 to 10 kg m^{-3}, a definition which further characterizes the relative weakness of the density signature of this front. Based upon several cross sections as well as 3-D visualizations of the CTD data, the 34.6 psu isohaline and the 2°C isotherm appear to be significant indicators of the summer frontal position at the surface and mid-depth, respectively. This differs from the 3°C isotherm suggested by Johannessen and Foster (1978) to define the frontal position. The maximum surface temperature gradient we observed was 0.11°C km^{-1} in the upper 10 m while it was 0.22 °C km^{-1} at 80 m. These values are similar to that (0.15 °C km^{-1}) reported by Johannessen and Foster (1978). The maximum salinity gradient observed in this experiment was 0.06 psu km^{-1} near the surface versus 0.02 psu km^{-1} at 80 m.

Plan views of temperature and salinity (at 8 and 80 m) from the first occupation of the entire CTD grid are presented in Figures 18 a-d. The primary surface front manifestation is in salinity as can be seen in Figures 18 a-b. In the eastern portion of the grid, the isohalines show a much stronger gradient than in the western portion. Similar plots from the other CTD occupations show little horizontal variation of the 34.6 psu isohaline in the eastern portion of the experimental area during the two week span of CTD observations. However, in the western section, the surface isohalines from different grid occupations appear either displaced to the north (into) or south (out of) Finger Canyon. Figures 18 c-d confirm the conclusions drawn from Figures 17 c -d, that at 80 m depth the
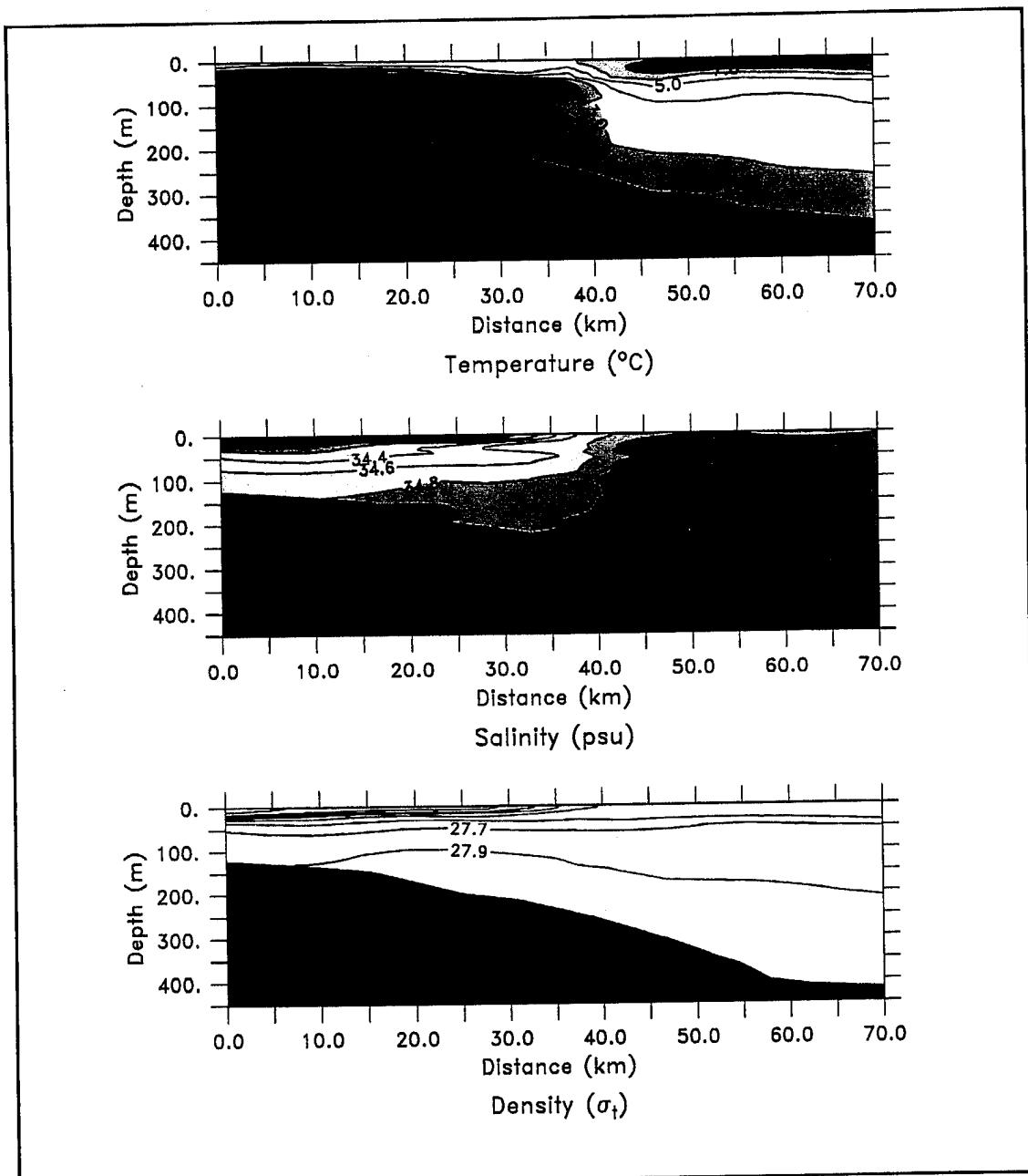
Figure 17. (a) A cross section of temperature shows the front as a strong temperature gradient below the mixed layer. Near the bottom the frontal zone is expanded due to bottom mixing. (b) The surface front is manifested by a strong salinity gradient as seen in the salinity cross section (c) A cross section of density (σ_t) shows a strong gradient at the surface associated with the salinity gradient but virtually no density difference below the mixed layer. The thermohaline structure is compensating in density below the mixed layer.

43

front is best defined by the temperature gradient. The horizontal fluctuation of the 2°C isotherm was identical to that of the salinity variation over the four CTD samples of the grid. Mesoscale circulation within Finger Canyon, which was not resolved in this experiment, is thought to exert a significant influence on the nearby hydrography. In general, the isopleths had regular gradients over the smoother topography in the eastern part of the survey area than in the vicinity of the canyon.

C. CALCULATED GEOSTROPHIC CURRENTS

The validity of the assumptions related to the derivation of the geostrophic method are indeed questionable when applied to a regime such as the BSPF experimental area. The depth of no geostrophic motion in this sloping bottom domain is not likely to be constant if, indeed, one actually exists. Frictional layers occupy a large portion of the deep water domain and most of the shallow water domain. These are manifested by well mixed layers typically extending ~ 40 m from the bottom and 20 - 30 m from the surface. Further evidence of frictional influences on the flow were seen in the observed transmissivity, collected simultaneously with the CTD data, in which relatively opaque plumes extended the water column within 100 m of the bottom near the base of the slope.

Additionally, tidal advection and internal wave activity effect the synopticity of the CTD data and thus the inferred geostrophic flow. A true "synoptic" picture of the density field is not achievable given the time scales of tidal and internal wave oscillations versus the ship sampling rate. As a tracer of tidal influence, the scale of frontal oscillation corresponding to the semidiurnal tidal periodicity was observed to be of similar magnitude to the CTD station spacing (5-10 km). Ray (1993) and Lynch et al. (1995) completed a comprehensive analysis of the current meter and temperature logger records as a means of characterizing the internal wave activity and its impact on acoustic propagation. Internal tide and internal wave amplitude spectra were produced from the temperature records under the assumption that most of the temperature fluctuations could be attributed to vertical motion, which also could be separated from the weakly correlated horizontal
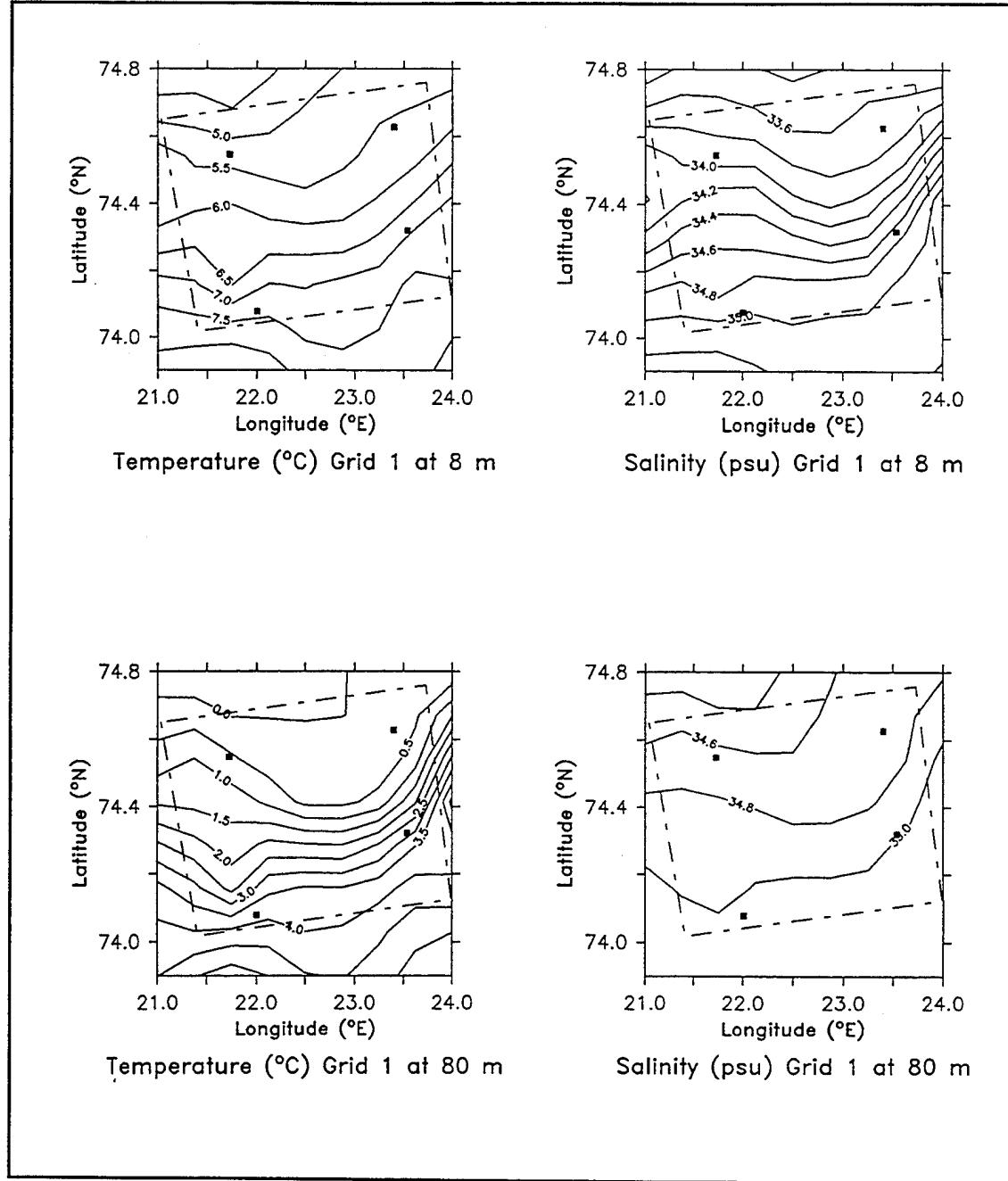
Figure 18. Four plan views of the experimental area provide the primary horizontal characteristics of the front. Depths of 8 m and 80 m were selected to allow contrast of the salinity and temperature gradients with depth. (a) temperature at 8 m CTD grid 1 (b) salinity at 8 m CTD grid 1 (c) temperature at 80 m CTD grid 1 (d) salinity at 80 m CTD grid 1

advective effects. Power spectra of the vertical displacement confirm the presence of a significant amount of energy in the internal tide and internal wave frequency bands at the front. The vertical scale of these high frequency oscillations ranged from 1 to 10 m.

The sum of the effects of tidal aliasing and internal waves were evident in the calculations of dynamic height. The dynamic height varied for a particular station from among the four different occupations of the grid ranging from .001 to .01 dyn m depending upon station location. The largest differences were found in stations near the front and to the north of the front. The standard deviation of the dynamic height for 27-hour CTD time series taken at the front was 0.003 dyn m.

Yet a geostrophic balance must be an essential element of a mean frontal picture. To arrive at some basis for examining a potential geostrophic field, several levels of no motion (80 to 300 dbar) were tried in calculations involving all stations in the grid as well as subsets of CTD stations based upon bottom depth and relation to the frontal location. After examining all the results, a level of no motion of 100 dbar was selected to depict the geostrophic velocity component based upon the following reasoning. As expected from the analysis of the static fields of density, essentially all calculations revealed that the geostrophic (baroclinic) component was restricted to the upper 50 m in the northern section of the experimental area. Lowering the depth of no motion of the deep water stations did not alter the magnitude nor character of the geostrophic results.

Figure 19, the surface dynamic topography of grid 1, shows the general south to north positive gradient in the dynamic height. Superimposed are the vector mean speed from each of the shallow (~20 m) current meters as a means of comparing the surface baroclinic field with the near surface measured currents. The surface geostrophic current vectors, interpolated for mooring location, are plotted with dashed lines for ease of comparison. Only at the NE mooring are these two vectors closely aligned reflecting the influence of the geostrophic flow at this location. At the SW mooring the two vectors illustrate the considerable difference between the dominant barotropic signal and the weaker geostrophic signal south of the front. At the NW mooring the measured current

46
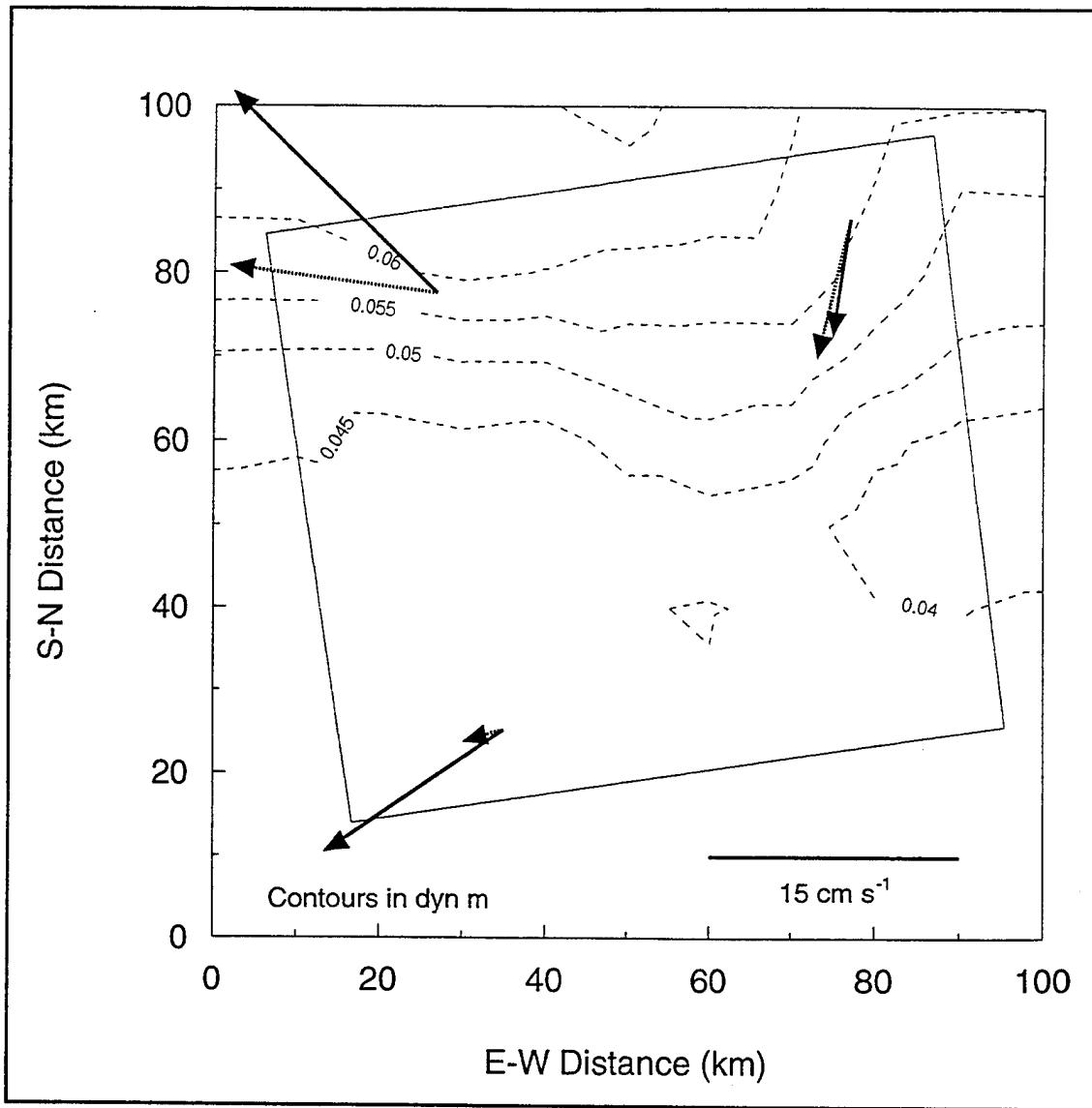
Figure 19. The dynamic height field (0/100 dbar in dyn m) from CTD grid 1 shows the alignment of the geostrophic flow along the front. Also portrayed are the vector mean speeds from each of the shallow (~20 m) current meters which are plotted as solid arrows on the grid of the experimental area. For comparison, the surface geostrophic current vectors, interpolated for mooring location, are plotted with dashed lines.

vector is similar in magnitude to the strong geostrophic flow but the direction is apparently influenced by the local topography or perhaps the measured flow is partially insulated from the mixed layer dynamics.

47

Pressure (dbar)

0.

20.

40.

60.

80.

5.   15.   25.   35.   45.   55.   65.

Distance North to South (km)
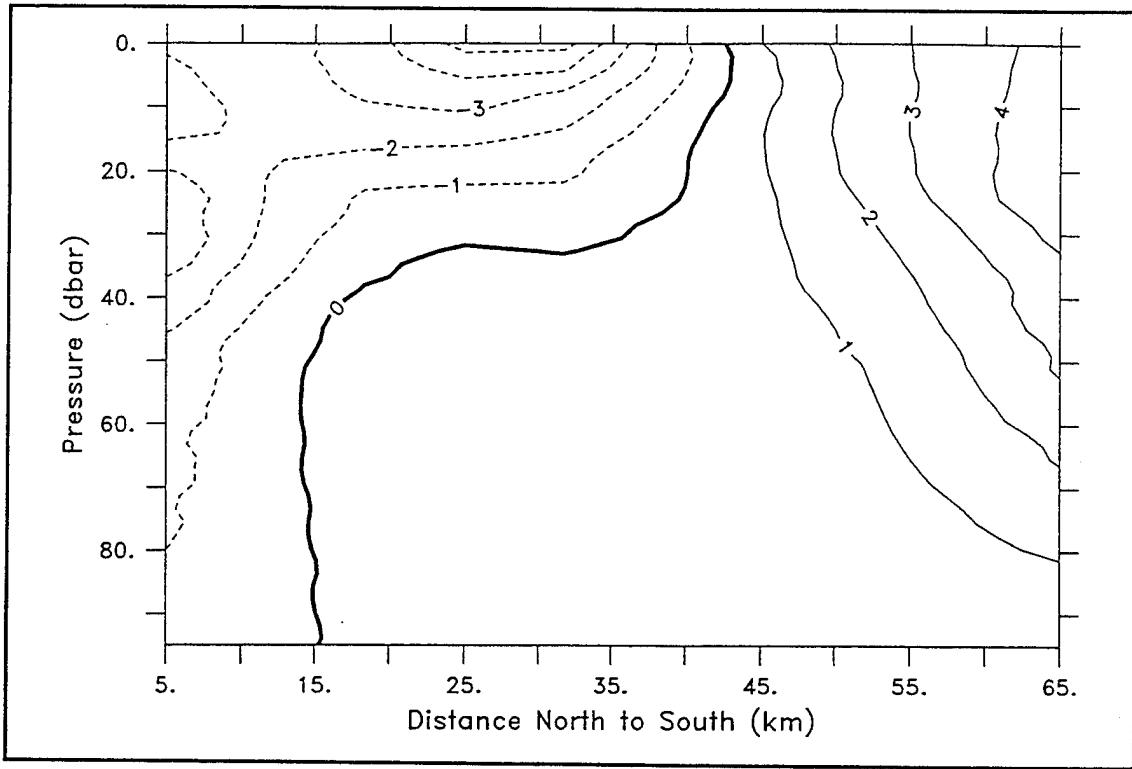
Figure 20. The geostrophic cross section from CTD grid 1, stations 57 to 64, highlights the shallow geostrophic jet associated with the surface layer baroclinicity. Solid lines indicate flow into the paper (eastward) and dashed lines indicate flow out of the paper (westward).

Figure 20 shows a representative geostrophic cross section from the first CTD grid run, stations 57 to 64. A shallow (< 20 m) baroclinic jet is observed coincident with the maximum horizontal surface salinity gradient. This westward flowing near-surface jet appears in all cross sections but its magnitude varies along the front (4 to 15 cm s^{-1}). An important feature in the southern part of all cross sections is a weak (~1-4 cm s^{-1}) baroclinic flow to the east. This eastward geostrophic component in the NAW agrees with previous depiction's of northeastward flow of NAW along the southern face of the front (Loeng, 1991), but the density gradients are weak, and the total flow is overwhelmed by a southwestward barotropic component.

The fact that the density gradients are "isolated" near the surface means that the geostrophic flow is useful in understanding the kinematics of the summertime mixed layer.

Mean surface currents agree reasonably well with the geostrophic currents. In contrast, the lack of density variability in the subsurface part of the front (i.e., the BPW - NAW boundary below the mixed layer) mitigates against geostrophic interpretations of flow in the region. The mean momentum balance beneath the mixed layer and south of the front appears to be governed by the barotropic forcing.

D. CALCULATED TIME AND SPACE SCALES

To better understand the processes involved at the BSPF and in preparation for the modeling study of the front, space and time scales at the experimental region were quantified from the observed data. These provide a first order range of the important scales which should be resolved in numerical modeling studies.

1. Horizontal Scales

The fundamental length scale of any oceanic flow which is strongly influenced by rotation is the Rossby radius of deformation (Δ_r) (Apel, 1987). The Rossby radius is determined by the ratio of the phase speed of the long or shallow-water wave to the Coriolis parameter f which is twice the angular rotation rate of the earth multiplied by the sine of the latitude. The phase speed for shallow-water waves reduces to $\sqrt{gH}$ from the dispersion relationship for wavelengths greater than 20H, where g is the acceleration due to gravity and H is the water depth. In a single layer system of depth H, this length scale is known as the barotropic or external Rossby radius of deformation. In a two-layer (or multi-layer) system gravity, which acts as a restoring force along the interface between layers, is reduced by a factor of the density difference between the layers to become the effective gravity g'. The internal shallow water gravity mode phase speed is then given by $\sqrt{g'h_u}$ where h_u is the thickness of the upper layer. The baroclinic or internal Rossby radius of deformation is then given by:

$$\Delta_r = \frac{\sqrt{g'H_u}}{f}$$

(3.1)

In a two-layer system effective gravity is calculated:

$$g' = \frac{\rho_2 - \rho_1}{1/2 \bullet (\rho_2 + \rho_1)} \bullet g$$

(3.2)

where ρ_1 and ρ_2 are the densities of the upper and lower layer. For a two layer system, this is termed the first mode or first baroclinic Rossby radius of deformation. Evidence from GEOSAT altimetery data has confirmed that the first baroclinic Rossby radius of deformation is the governing length scale for ocean dynamics and should be the corresponding length scale of ocean models (Semtner and Chervin, 1992).

From the BSPF data, calculations of this scale were made using the average temperature and salinity of the 4 CTD profiles made at station 69, selected for its proximity to the front and repeated sampling during the experimental period (see Figure 8). From an analysis of the corresponding baroclinic vertical modes solved from the corresponding Brunt-Vaisalla frequency profile, the first baroclinic mode interface was confirmed to be the mixed layer depth. The calculated first baroclinic Rossby radius of deformation at the front was found to be 3.56 km. Comparison with several other profiles along the front yielded similar results. This scale corresponds well to the horizontal scales of the temperature and salinity gradients and associated interleaving which were observed at CTD stations taken at 2.5 km spacing. The implications of this calculation in terms of model resolution and computational requirements are profound. An order of magnitude increase in horizontal resolution from the finest scale known numerical simulation models of the Barents Sea region would be required to resolve this scale and would result in a ~ 50 fold increase in computational load for a given domain.

2. Vertical Scales

As discussed in Section B, the mixed-layer depth, the region of strong-interleaving (30-100 m), and the more diffuse region from 100 m to the bottom provide a first order delineation of the various vertical layers at the front from examination of cross-sections. To further investigate the extent of natural layers found in the water column at each mooring, the vertical coherence of the temperature records at each mooring was investigated. Strong vertical coherence would indicate that either similar advective properties were acting within the layer encompassing the sensors (presumably at lower frequencies) or that the vertical amplitude of the internal tide/wave activity was of sufficient strength to effect the temperature record between a pair of meters. Unfortunately, the poor vertical resolution on the moorings prevented a resolution of internal wave activity at shallow depths, i.e., at the mixed layer depth, since only a single sensor was placed at the mixed layer depth.

Cross-spectra were computed using a Bartlett method FFT with a Hamming window. Only at the SW mooring did the temperature records (<50 m) show any significant coherence at the semidiurnal frequency. This argues for the minimal role of horizontal tidal advection in temperature changes in the homogenous regions north of the front. Further examination of the time series on the SW mooring (Figure 21) also reveals a wave in the temperature record below 80 m with approximately a 4.5 day period. While observational data indicate that this long-period wave is not meteorologically forced, it is unclear whether this effect is related to an alongshelf wave or eddy activity in the canyon.

At shallow depths (<40 m), the only common coherent feature was an oscillation at 7 cpd with zero phase lag. A comparison of the records at 50 and 80 m showed 1.5 cpd and 4 cpd coherent waves with several higher frequencies (> 10 cpd) also corresponding. The deep meters on the SW mooring (140 m and 240 m) were significantly coherent at 4, 8, and 10 cpd, attributed to internal tide and wave activity. The deep 360 m sensor on the current meter, just 20 m above the bottom was not coherent with any of the shallower sensors.

51
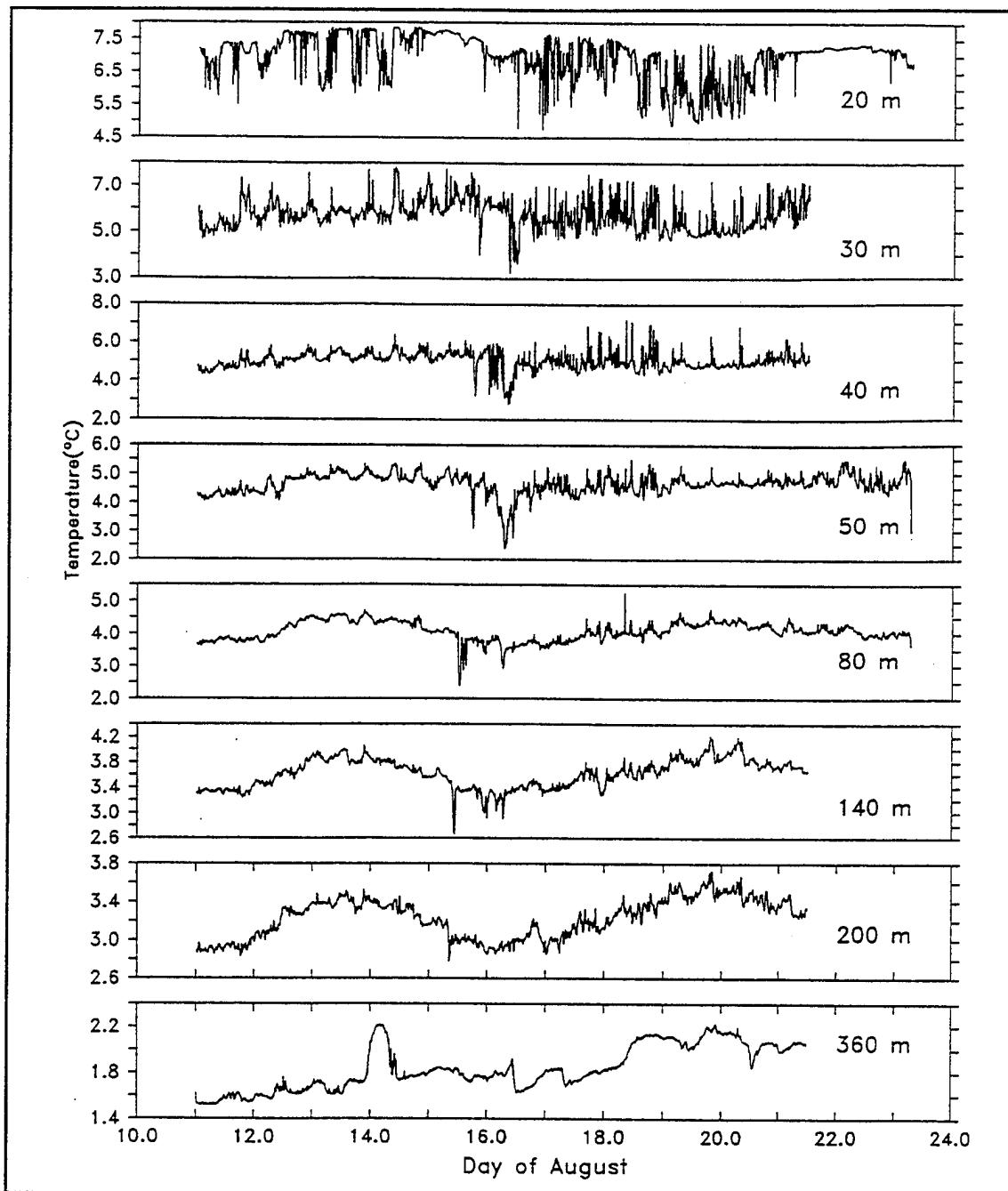
Figure 21. The time series of the 8 temperature records on the SW mooring shows the high frequency oscillations found in the data as well as some low frequency oscillations only observed at this mooring south of the front. [Semidiurnal period oscillation below 50 m and a 4.5 day period oscillation below 80 m].

52

At the NW mooring, only the meters at 20 and 30 m contain any significant vertical coherence which are at the diurnal period and at 3 cpd (the latter suggested to be internal tide phenomena).   Due to the presence of ACM type meters on the NE mooring, only three temperature records (30, 40 and 80 m) were available for comparison. All the meters were coherent at 3 cpd and the deeper two were also coherent at 12 cpd.

Summarizing the above results, only at the SW mooring, with 8 sensors spaced through the vertical, were distinguishable layers found from this analysis.   Coherent vertical temperature layers existed between the mixed layer and 40 m, between 50 and 80 m, and encompassing the 140 m and 200 m sensors.   Temperature changes in the mixed layer and bottom layer, containing the 360 m sensor, were found to be isolated from surrounding layers.

Also, the instantaneous profile from the instruments on the SW mooring appears to adequately represent the water column with the exception of the mixed-layer temperature as compared to a CTD profile with 1 m resolution taken adjacent to the mooring (Figure 22).   Model levels taken at these depths plus an additional layer at the mixed layer would likely prove adequate for a resolution of the dynamics.   However, examination of a typical station taken at the front (Figure 23) reveals vertical scales of the temperature and salinity interleaving < 10 m at depths between 20 - 100 m perhaps requiring 16 layers to represent the vertical structure in that region alone.

3. Time Scales and Summary

As revealed in Section A, the predominant time scales related to the energy of the currents were semidiurnal and diurnal; however, energy density spectra indicate that even higher frequencies contain significant energy. Energy density spectra for the individual temperature data show a broad range of significant frequencies depending upon horizontal relation to the front and depth from 0.2 to 20 cpd. A representative spectra for both the temperature and current data is provided in Figures 24a and b.
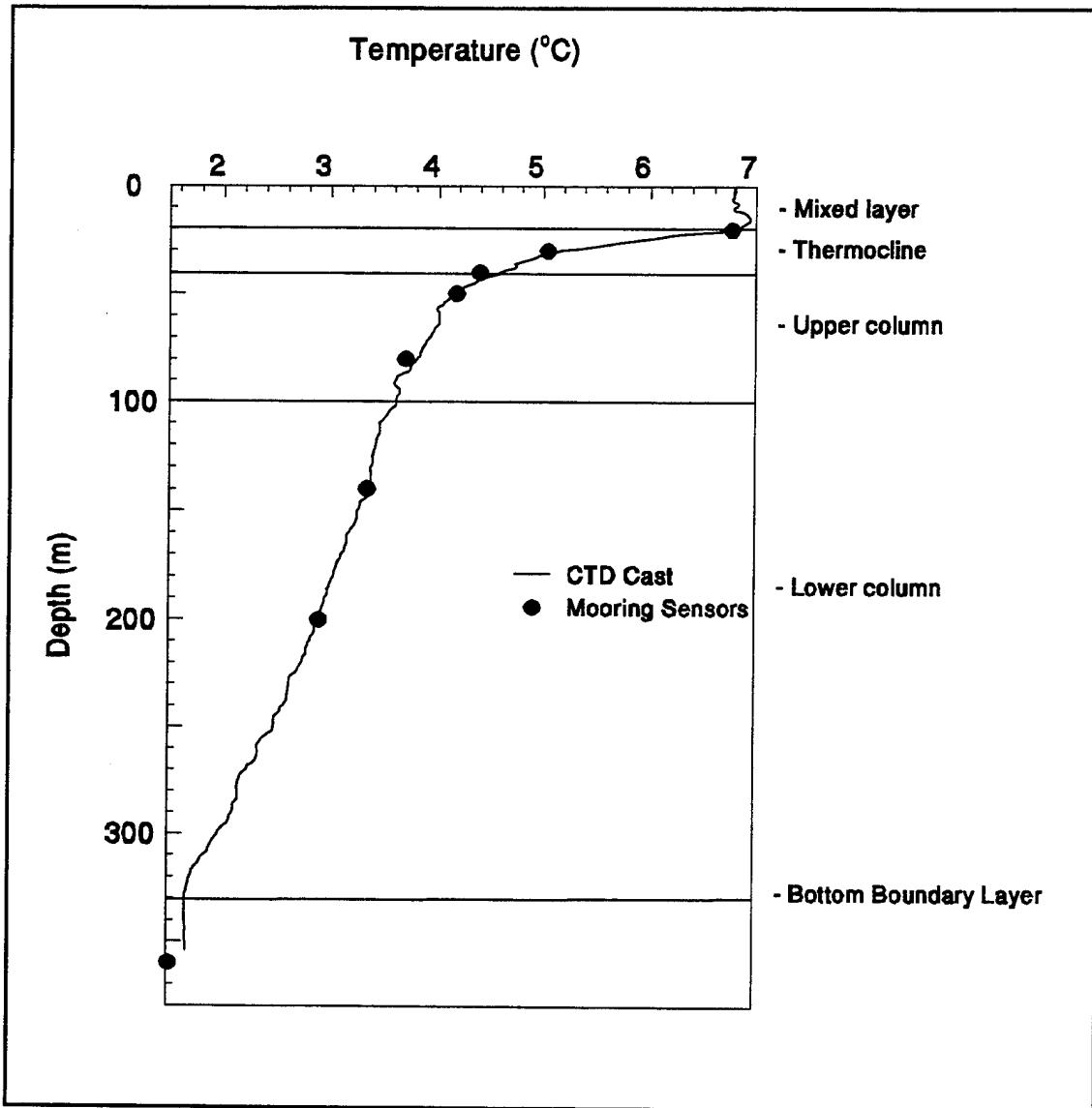
Figure 22. The temperature profile from the CTD cast taken at station 18 adjacent to the SW mooring on at 0520Z 11 August is well represented by with the corresponding temperatures taken from the sensors on the mooring. The layers identified from the vertical coherency analysis are labeled to the right.

Another measure of the temporal variability of the frontal scale was found by examining the autocorrelation function of the calculated dynamic height from the 27 hour CTD time series. The e-folding time of this function was between the 1 and 2 hour lags indicating a rather rapid change in the magnitude of the forcing for the geostrophic flow.
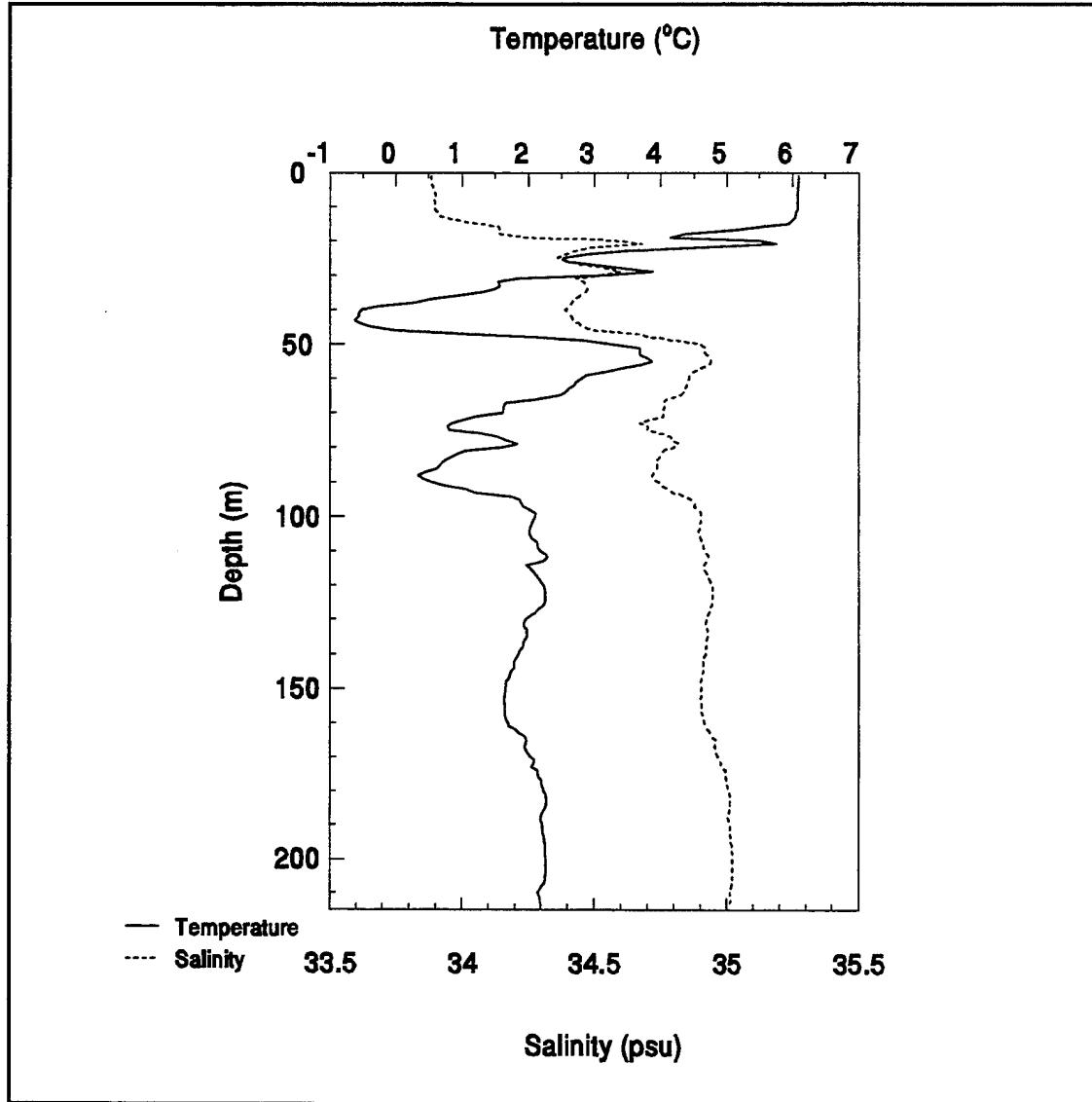
Figure 23. CTD profile taken at the front during the CTD time series highlights the area of strong interleaving between 30 and 100 m.

However, in terms of a model simulation, a time step can be adjusted to sample even the highest significant frequencies observed in the data. Balancing economy of the step, model stability and desired length of integration time to the natural frequencies observed in the data is a function of model design and generally not a limitation. From the data collected at the BSPF it is apparent that the minimum scale of these natural time
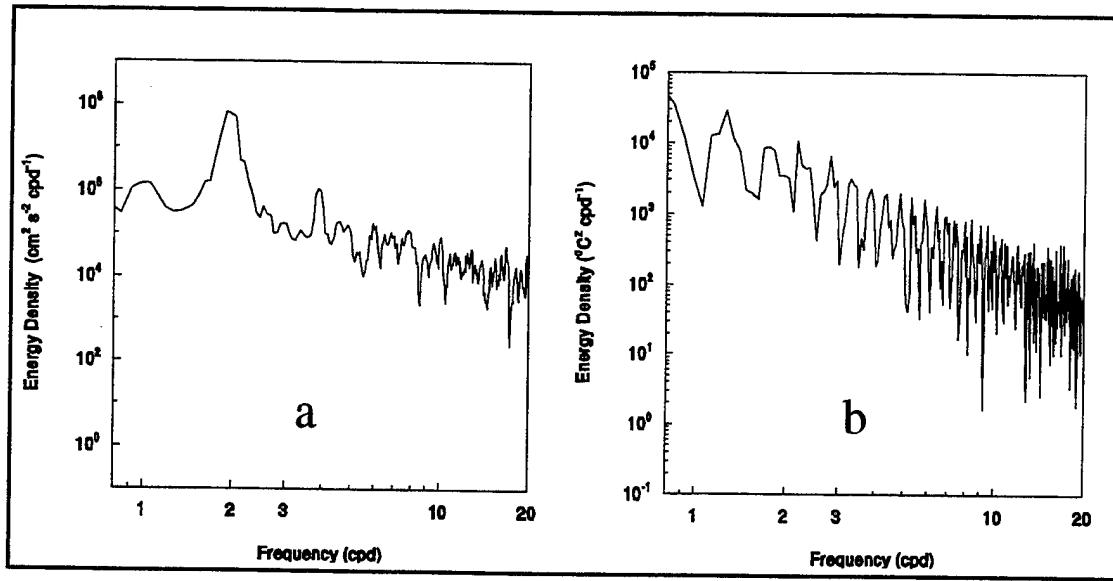
Figure 24. (a) Energy density spectra of the *u* velocity component, taken by the current meter at 54 m depth on the NW mooring, shows high frequency energy (particularly 4 cpd) aside from the significant diurnal and semidiurnal peaks. (b) Energy density from the temperature record from the sensor at 80 m on the SW mooring depicts a cascade of energy through many frequencies between 1 - 10 cpd.

periods at the BSPF is on the order of 1~2 hours. The fine spatial scales (~3.5 km) found in the observed data are more stringent requirements to the model design as discussed in Chapter VII.

The next chapter is dedicated to further examining the time and space scales and the associated phenomena found directly at the front from the data collected during the 27-hour CTD time series.

IV. OBSERVED FRONTAL STRUCTURAL DETAIL

Having described the important general hydrographic features observed at the front during the summer of 1992, data are now presented that relate tides, vertical mixing and internal waves to aspects of the vertical frontal structure and its horizontal variation. For this analysis the data from the 27-hour CTD time series and the tomographic temperature field are used.

A. VERTICAL STRUCTURE AT THE FRONT

On 17 and 18 August, a 27-hour CTD time series was conducted within the strongest part of the surface frontal zone in the eastern part of the experimental area in water 216 m deep (see Figure 8). Through the use of bow thrusters and GPS navigation, the ship drift was maintained to less than 300 m for the entire period.

Figures 25a and b depict the time series of temperature and salinity obtained from the hourly casts. Semidiurnal oscillations are evident at the base of the mixed layer depth. Additionally, higher frequency oscillations are detected at the mixed-layer boundary attributed to internal wave activity. Below 180 m depth, the temperature and salinity remain constant corresponding to the bottom mixed layer. The coolest water (BPW) is found at 50- 80 m depth but is discontinuous in the time series as the front oscillates horizontally with the tides. There is a noticeable but brief surface cooling during the early hours of the 18th which corresponds to the limited hours of darkness between sunset and sunrise (0049-0440Z).

The bottom-corrected ten-minute averaged ADCP current record during this 27-hour period is displayed in Figures 26a and b. The velocities have been rotated so that the v direction is purely cross-slope and the u direction is along-slope. One of the principal features observed is the correspondence of the warmer, more saline intrusions noticed in the CTD time series with the v velocity component consistent with the frontal
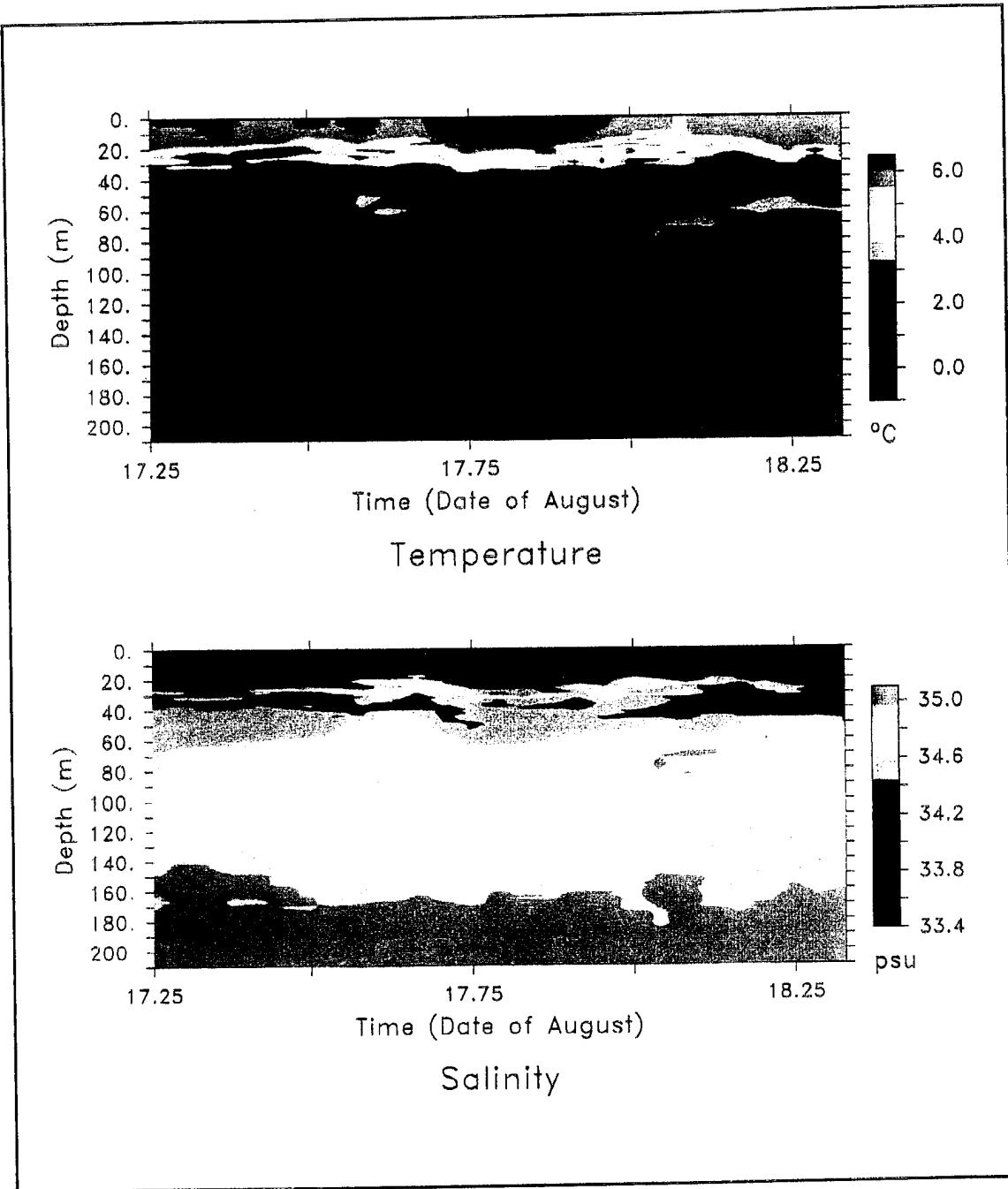
Figure 25. Contour plots taken from the CTD cast time series taken on 17 and 18 August 1992 within the surface frontal zone reveal the complex vertical structure found at the front. (a) temperature (b) salinity . The BARTLETT's drift was constrained to 300 m or less during the time series through the use of GPS navigation and bow thrusters.
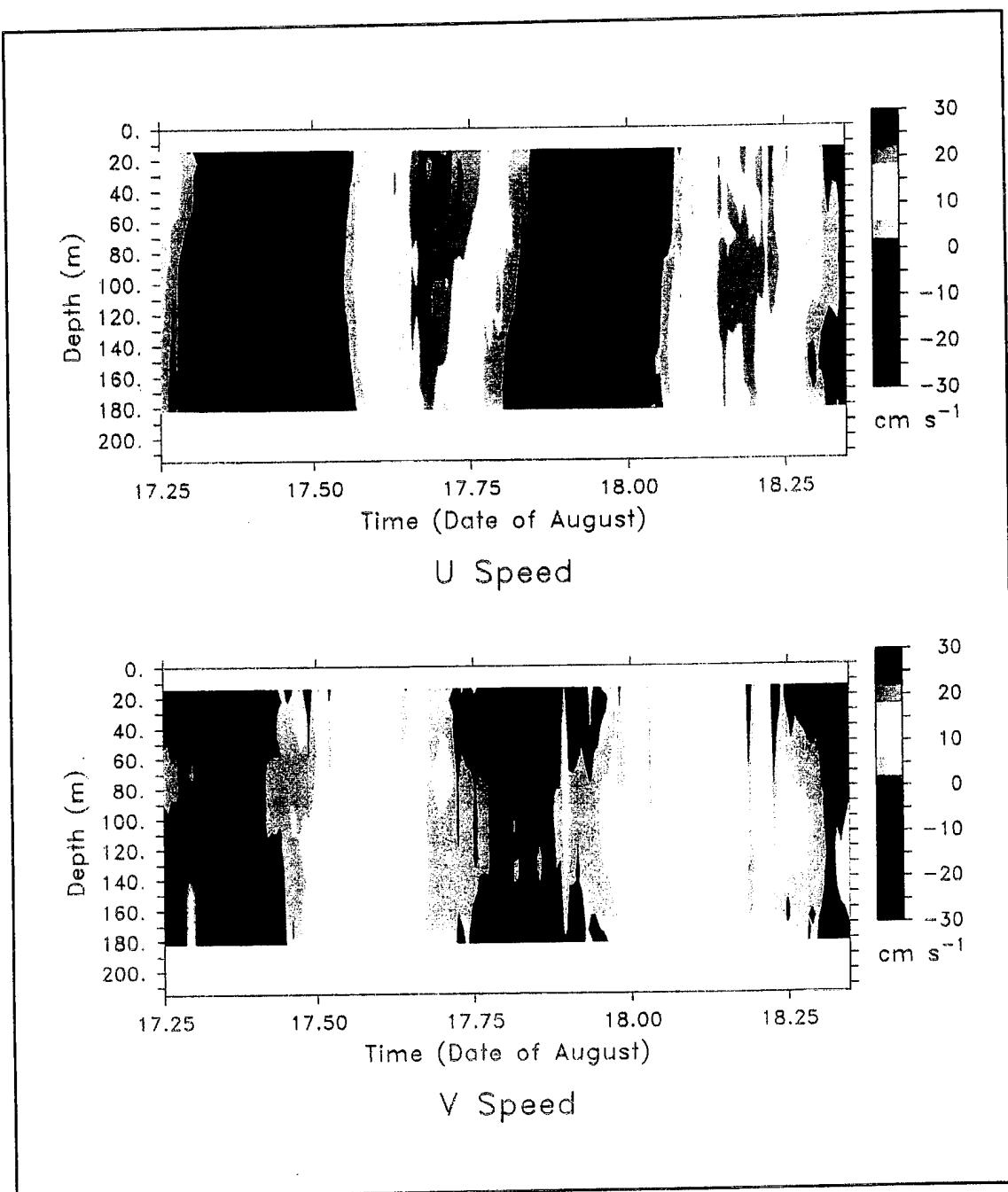
Figure 26. Significant vertical structure was also found in the ADCP velocities during the CTD time series. Contoured velocities have been averaged to 10 minute increments. (a) u velocity (b) v velocity .

gradients of temperature and salinity. Cross-correlations between the ADCP velocities at each depth bin and temperature and salinity were performed to further investigate this observation. The v velocity had a positive cross-correlation coefficient (r) with temperature greater than 0.5 in 14 of 22 ADCP depth bins (maximum r value at 86 m of 0.86 with CI_{95} : 0.73 - 0.94). Additionally the v velocity was positively correlated with salinity ($r > 0.5$) in 16 of the of the 22 ADCP depth bins (maximum r value of 0.69 at 86 m with CI95: 0.42- 0.85). In contrast the u velocity had a maximum correlation coefficient of 0.59 with temperature (> 0.5 in only 2 depth bins) and maximum correlation coefficient with salinity of 0.26. In all correlations the maximum coefficients were found between 60-100 m in the water column. This maximum correlation region is coincident with the region of strong stability and interleaving of NAW and BPW masses in the vertical structure as further discussed below.

Figure 27 is a plot of temperature from all the CTD casts during the time series and the mean density profile for the time period. From this plot the distinction between various layers is clear. The surface mixed layer can be seen extending to 20 m. Immediately below the thermocline is a highly stratified regime containing significant examples of interleaving that can be seen extending down to 100 m. From 100 m to 180 m there is an obvious decrease in the extent of the interleaving and gradual homogenization of the water column as depth increases and stratification decreases. A clearly observed bottom boundary layer about 40 m thick can be seen beginning at 180 m. Tidally-generated vertical mixing above the bottom boundary layer may account for the diffuse nature of the front below 100 m and the fact that interleaving in this region is less energetic.
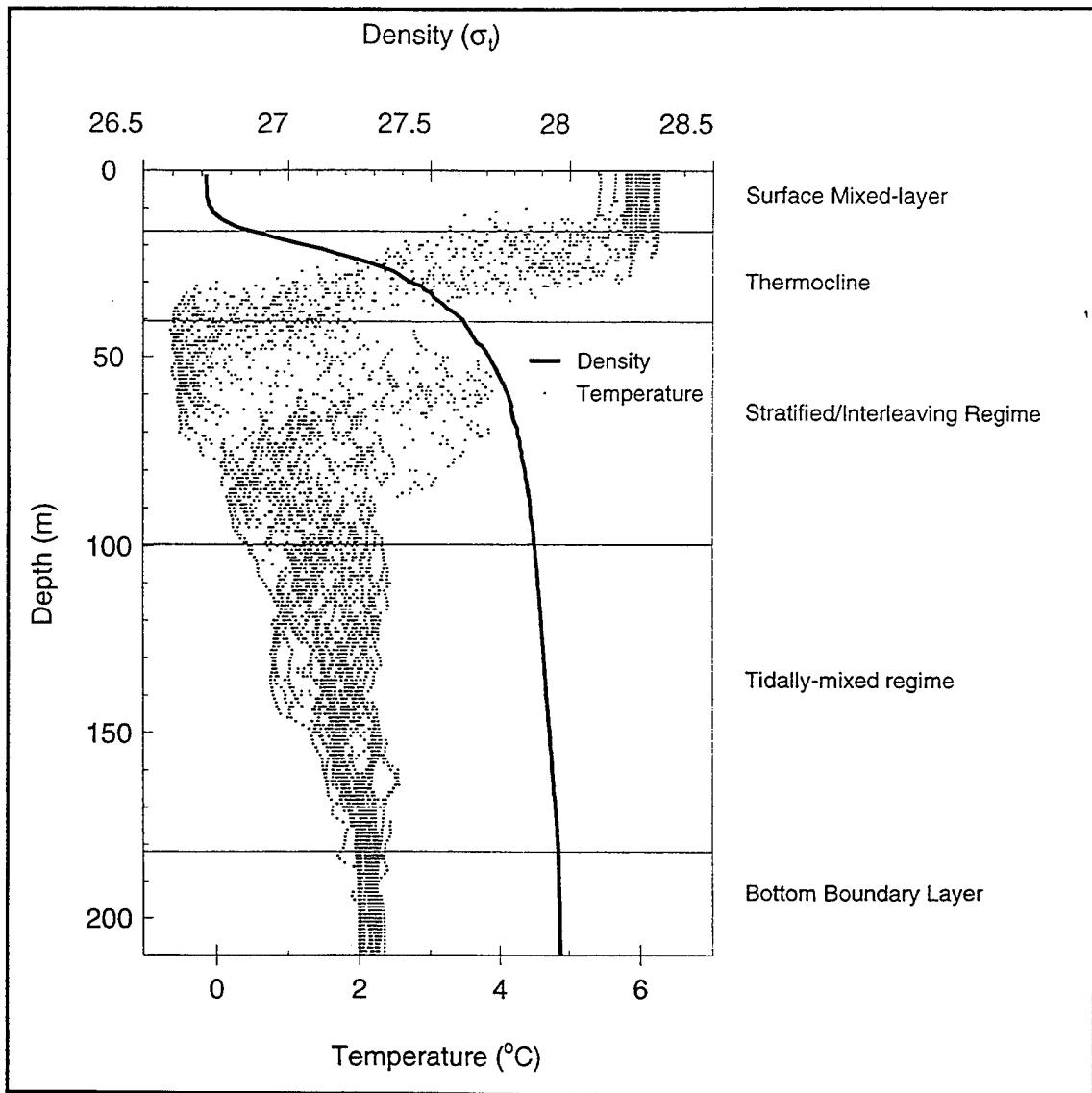
Figure 27. A plot of temperature versus depth for all CTD casts during the time series and a plot of the mean density profile distinguish the vertical structure found at the front. Five distinct zones can be identified: a surface mixed-layer, a highly stratified interleaving zone extending beneath the thermocline to 100 m, a region of vertical mixing, and a bottom boundary layer can be observed.

Investigation of the importance of vertical tidal mixing and its potential role in shaping the frontal structure of the BSPF was conducted using the data from the CTD and ADCP time series to calculate a time series of the gradient Richardson number profile given by:

$$Ri = \frac{N^2}{\left(\left(\frac{\partial u}{\partial z}\right)^2 + \left(\frac{\partial v}{\partial z}\right)^2\right)} \qquad (4.1)$$

In a weakly stratified column, a sufficiently strong baroclinic velocity structure can become unstable if, at somewhere in the flow, Richardson numbers values of 0.25 or less are found (necessary but not sufficient condition). Given adequate time for the amplitude of the instability to grow, the flow may become turbulent (Apel, 1987).

The observed ADCP velocity data were time averaged to 10-minute windows surrounding the CTD sample times for shear $\left(\frac{du}{dz}\right)$ calculations. The Brunt-Vaisala frequency (N), calculated from the CTD data as equation (4.2), was vertically averaged and smoothed over the 8 m ADCP depth bins.

$$N^2 = -\frac{g}{\rho}\frac{\partial \sigma_t}{\partial z} \ (\text{radians s}^{-1}) \qquad (4.2)$$

The Richardson number time series results are presented as a color contour in Figure 28. All Richardson numbers greater than 2, regions where strong stratification exists, were color-coded the same. The calculations do not extend into the surface mixed layer or bottom boundary layer due to the inherent boundary limitations of the ADCP. Between 20 and 100 m the strong stratification dominates the calculation. From 100 to 180 m the critical Richardson number (0.25) is periodically realized. While stratification is increasingly smaller in this regime, the shear is significant (maximum 0.01 s^{-1}). No regular periodicity was noted in the critical Richardson number which could be associated with an individual (u or v) velocity component.

To ascertain if the results could be attributed to the tidal flow, the calculation was repeated solely using the M2 tidal fit to the ADCP current data in each bin (see section 3.1) for formulating the shear term. A mean N2 profile from the entire time series was also employed. The results were similar with respect to the Richardson number and as

62
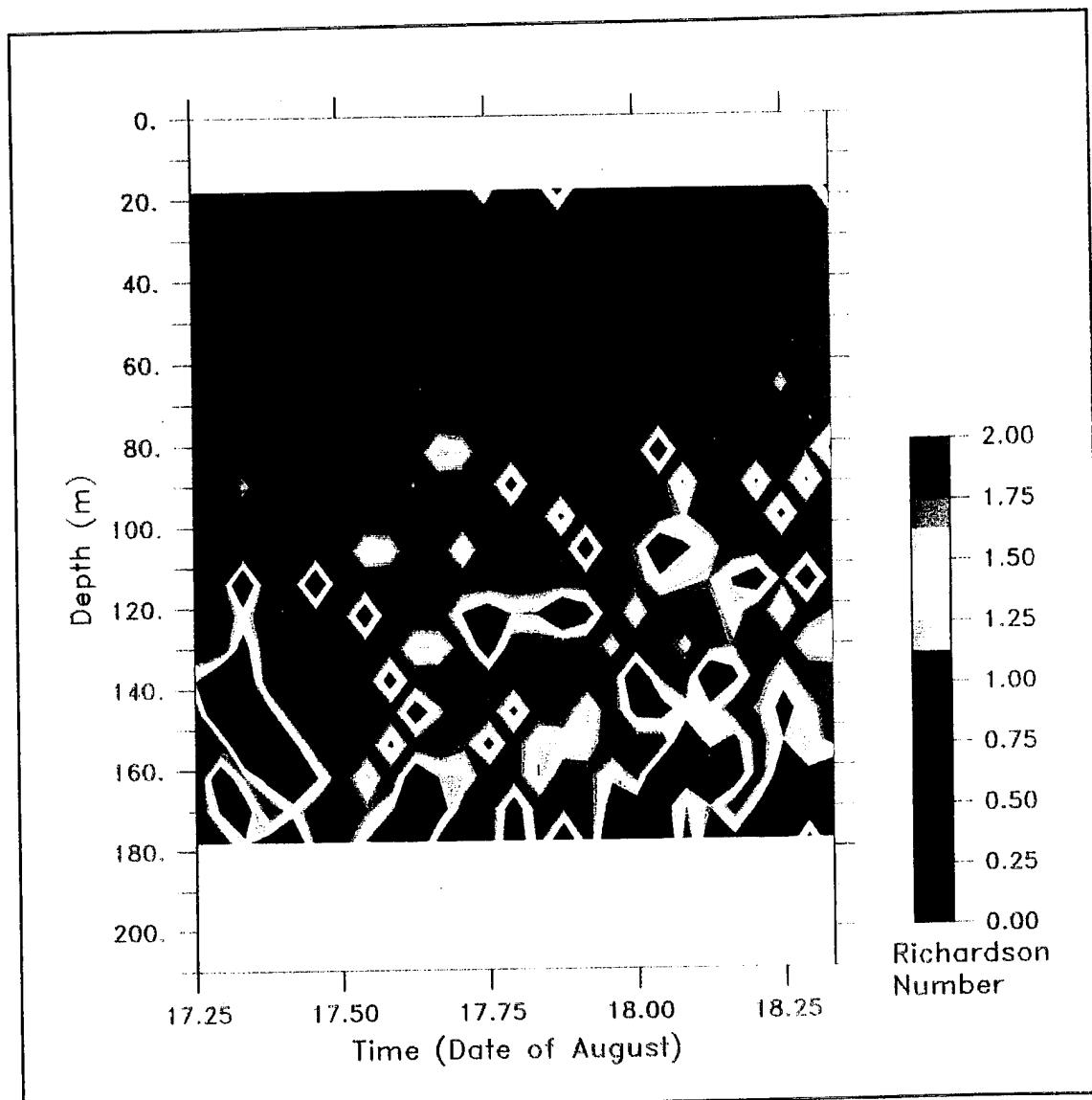
Figure 28. A color contour plot of a time series of the gradient Richardson number as produced from the analysis of CTD time series casts and ADCP data. Values greater than 0.25 indicate regions of laminar flow.

before some shear (maximum 0.004 s^{-1}) was found below 100 m. These results differed from that described above in that the regions of critical Richardson number were mostly confined to depths below 150 m (vice below 100 m). In Figure 12b it was previously noted that both the phase and inclination of the M2 tide varied with depth (while the amplitude was nearly constant). It is apparent that these vertical differences in phase and

inclination are responsible for the generation of this M2 shear. However, the vertical structure of the M2 tide alone is insufficient to explain the generation of all of the observed shear. Resolution of higher frequency internal tidal species would be necessary to fully attribute this phenomena to internal tides.

Interpretation of the implications of the critical Richardson number in this instance must be done with caution. What can be inferred is that if turbulent vertical mixing is present in the water column, it is most likely constrained to depths below 100 m and could be the result of baroclinic tides. Additional consideration still needs to be given on the time scales, growth rates and amplitudes of any instabilities which may generate turbulence and vertical mixing.

B. HORIZONTAL VARIATION

On 16 August, the tomographic part of the experiment began. The BARTLETT remained in the vicinity of the SE mooring, which contained the vertical hydrophone array, for four days to receive the tomographic data being telemetered back to ship via a wireless computer link. Using the 224 Hz bandpass source on the NE mooring, phase-encoded signals that correspond to short pulses after matched filtering were sent every 5 minutes. Space-time processing of the vertical array data allowed for resolving and tracking individual acoustic ray and mode arrivals. These were then compared to the predicted arrival structure. The differences in travel times were then used in an inversion to map a sound speed cross section at 5 minute intervals (Chiu et al., 1994, 1995a, 1995b). The sound-speed was then converted to temperature using an average salinity field for the cross section via inversion of a simple but robust sound speed equation (Coppens, 1981). Figures 29 a and b are temperature cross sections taken two hours apart as derived from the acoustic tomography. Additionally, sequential temperature cross sections generated at 5-minute intervals for a 13-hour period were converted into a
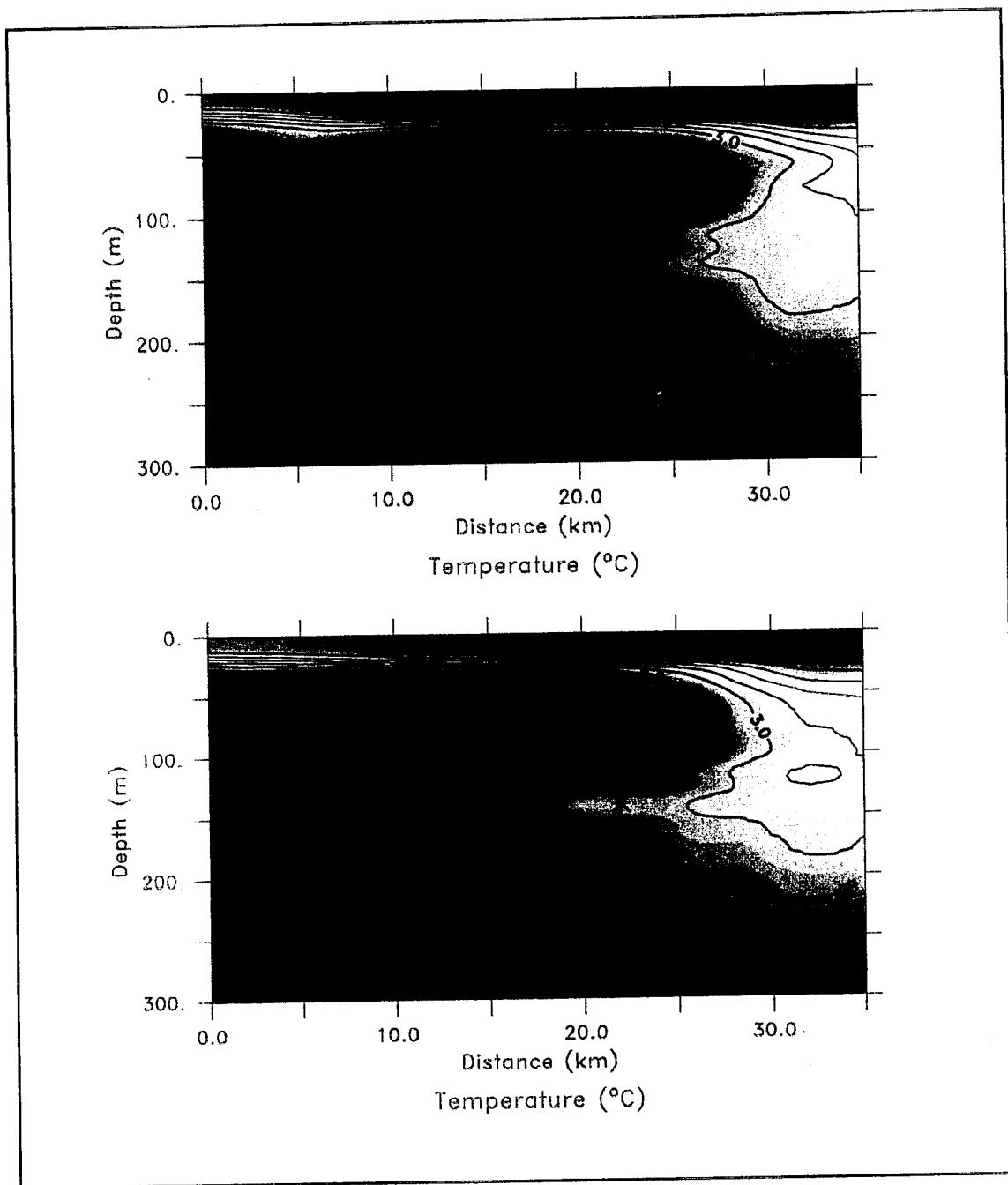
Figure 29. Acoustical tomographic images from the NE to the SE mooring taken ~ 1 hour apart provide a unique method to examine a synoptic cross section of the temperature structure. (a) at 2017Z 17 August 1992 (b) at 2212Z 17 August 1992. The * indicates the position of the time series displayed in Figure 30.

movie format and provided a graphic visualization of the mesoscale flow features which will be described below (also Chiu et al., 1994).

The temperature cross sections derived from the acoustic tomography achieve the synopticity that is absent from the CTD-derived cross sections. Several important features have been discovered from the movie and these multiple cross sections. First, internal waves can be observed vertically oscillating the mixed layer with an amplitude of ~ 10 m. The frontal position can be observed to oscillate horizontally with the tides with a displacement of ~ 5 km. Finally, and most interesting to this analysis, was the observation of filamented warm structures which push underneath the front at approximately 140-150 m depth, pinch off, and dissipate in about a two hour period. Although these observations are most clearly seen in a movie format, Figures 29 a-b represent a before and after shot of one of these filaments. The temporal passage of these warm boluses can be seen in Figure 30, a time series of temperature extracted from the data for a position 22 km south of the NE mooring and at 140 m depth (the * in Figure 29). The ~1.5 to 2-hour periodicity in the filamental structure is present throughout the 13 hour-long record.

To further investigate the origin of this phenomena, a vertical temperature time series for the same horizontal position (22 km south of the NE mooring) was taken from the tomographic data. This subset of the data was subjected to a principal component analysis (PCA) following Preisendorfer (1988) such that the temperature T can be represented as the sum of principal components $a_j(t)$ and eigenvectors $e_j(z)$ plus a residual term $\delta(z,t)$:

$$T(z,t) = \sum a_j(t) e_j(z) + \delta(z,t) \qquad (4.3)$$

The objective of the PCA was to separate the variance associated with these filaments into a simpler form from the complex field of the total variance found in the temperature data. Figure 31a represents the vertical eigenvector structure found in the data.

66
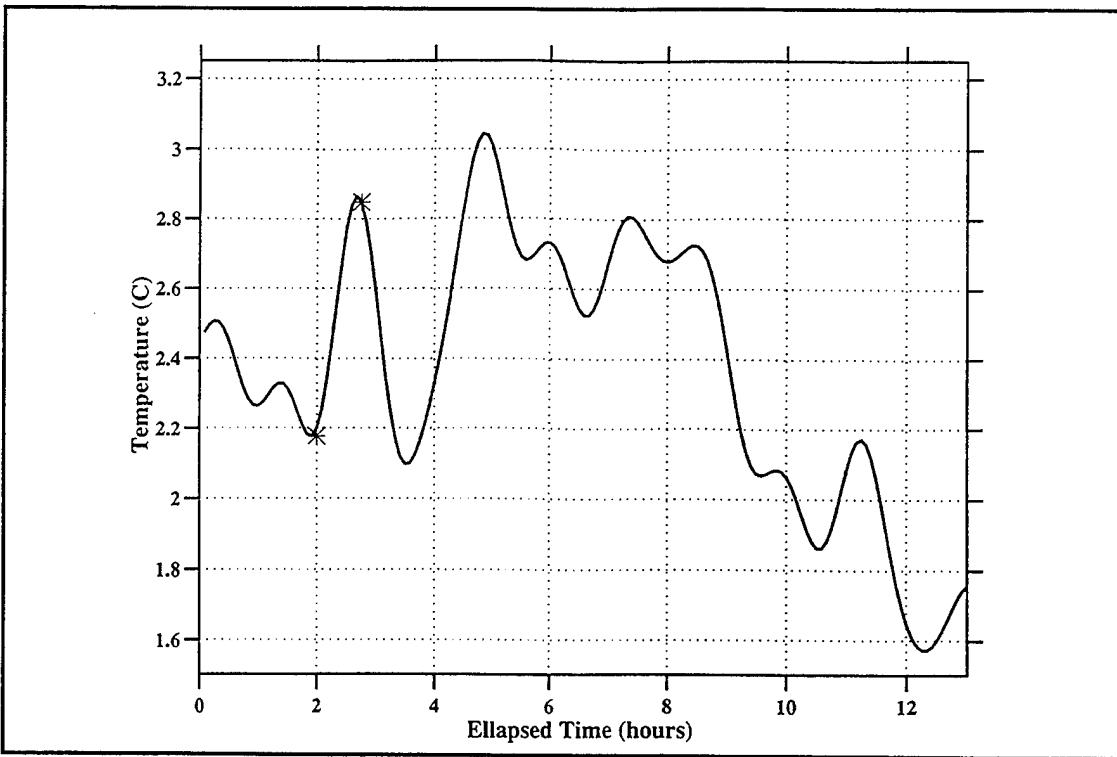
Figure 30. A 12 hour time series of temperature at 5 minute intervals at a point 22 km downrange from the NE mooring and at 140 m depth (position of the * in Figure 29) highlights the 1.5 - 2 hour fluctuations found in the tomography results. The stars (*) in this figure indicate the times of the images shown in Figure 29.

Mode 1 vertical structure corresponds to the variance associated with the semidiurnal period and represents ~70 percent of the total variance. The vertical structure of Mode 2 has predominant period of 18 hours and a broad energy peak around a 2-hour period. It represents 14 percent of the total variance. Mode 3 accounts for 8 percent of the total variance and its structure contains significant energy peaks at periods of 6 hours and 1.5 hours. Note that the vertical structures of both Modes 2 and 3 have peaks at ~140 m depth which correlates with the depth and the frequency of the filamental structures.

This position analyzed from this tomographic temperature time slice also corresponds to the location of the CTD time series within 3 km. The 10-minute averaged u and v velocities from the CTD time series were subjected to the same type PCA. Figure 31b is the vertical eigenvector structure contained in the v velocity data. Again,

67

the Mode 1 velocity structure is associated with the semidiurnal frequency and contains 94 percent of the total variance. Mode 2 is also similar to the temperature structure in that it is associated with periods of 18 hours and 2 hours but only represents 3 percent of the total variance. Modes 3 and 4 are just significant relative to a comparison with eigenvalues calculated from a random test matrix and each only represents ~ 1 percent of the total variance in the velocity structure. The energy density of the Mode 3 principal component contains peaks at periods of approximately 5 hours and 2 hours. Mode 4 of the velocity data also has a eigenvector amplitude peak at ~ 140 m and a significant energy density spectral peak also at a period of ~ 1.5 hours. The vertical structure of Modes 2 and 4 (Figure 31b) show the best correlation with the frequency and depth of the filamental structures near 140 m.

Combining these results it is possible to interpret that the vertical eigenvector structure and principal component frequencies found in the ADCP data correlate with the observed temperature structure derived from the tomography data. Even though the higher modes of the velocity field contain little energy, their existence at the frontal interface is believed significant relative to temperature advection. Suggesting an hypothesis for the forcing mechanism generating this high frequency phenomena is not so clear.

At 12-16 cpd, this oscillation is suggested to be above the range of internal tide frequencies (1-10 cpd) and into the internal wave frequency regime. Purely vertical displacements from high frequency internal wave oscillations cannot account for the apparent horizontal intrusions of warm water. The high correlation of v velocity and temperature at the front from the CTD time series and the general orientation of the frontal gradients mitigates against alongslope advection as an interpretation of these regular oscillations. Continuing analysis of the tomographic data and a current modeling study should lead to a better understanding of this observation. The presence of the these intriguing filaments identified by the tomography, however, may further assist in explaining the observed temperature and salinity structure in the vicinity of the front which
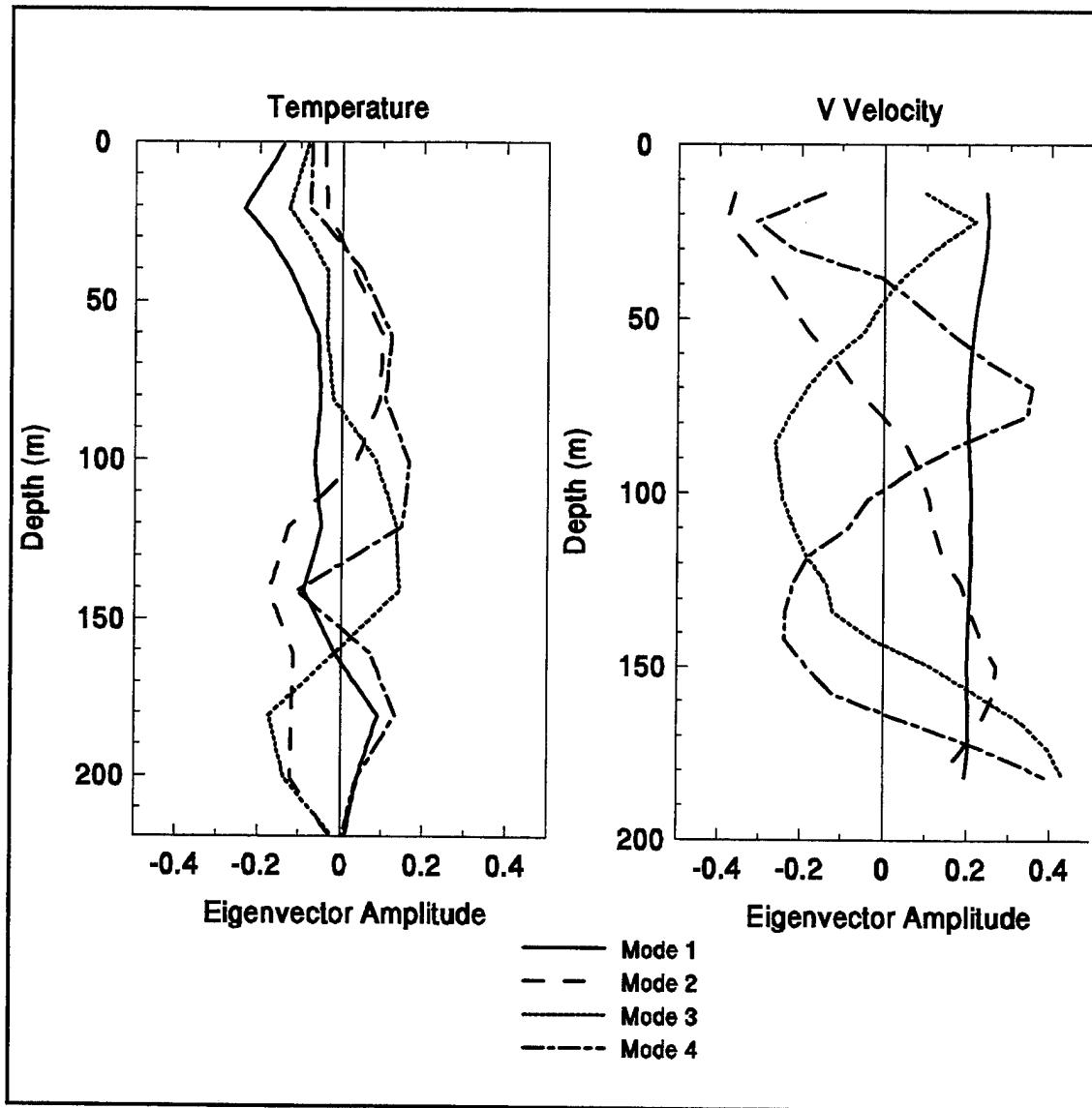
Figure 31. The vertical eigenvector structure as obtained from the principal component analysis of (a) subset of the tomographically derived vertical temperature time series (b) ADCP v velocity data at the location and time of the CTD time series. Correspondence of the modal amplitude structure is observed near 140 m.

shows the BPW at mid-depth extending out over the slope with warmer modified NAW found underneath nearly to the 100 m isobath (Figure 17).

V. OBSERVATIONAL IMPERATIVES

A. FRONTAL CLASSIFICATION

The BSPF has been found to possess many of the general characteristics attributed by Mooers et al. (1977) to a shelf-slope frontal system as presented in the introduction. These include: (1) cold fresh BPW water abutting warm saline Norwegian Atlantic Water on the slope, (2) position topographically constrained to the bathymetry of the slope on the northern side of Bear Island Trough, (3) interleaving at the frontal interface of BPW and NAW with salinity compensation which virtually eliminates a density contrast, (4) width scale of 3 km which is the same order of the computed internal Rossby radius of deformation (3.5 km) (5) M2 tidal ellipses at the front aligned with the bathymetry, (6) BSPF isopleths retrograde to the bathymetry, and (7) a frontal zone very active in the internal wave and tidal frequency bands. However, some aspects make the summertime BSPF unique.

Contrary to well-known examples of shelf-break fronts, such as off Georges Bank and the Mid-Atlantic Bight discussed by Gawarkiewicz and Chapman (1992), there was no significant alongshelf flow in the shallow water to the north of the front. Model experiments by Gawarkiewicz and Chapman demonstrated that such a flow would generate a buoyancy flux towards deeper water in the benthic layer which would eventually bend up to the surface at the shelf break generating and maintaining the front. Additionally, during the 22 days of the experiment no horizontal separation was observed in the vertical frontal layers described in Chapter III (e.g., the isopleths defining the surface salinity (density) front at the surface were continuous with the isopleths defining the strong temperature front below the mixed layer). In contrast, in the Mid-Atlantic Bight in the summer, the density expression of the shelf break front above the pycnocline often disappears (Burrage and Garvine, 1988). The observations in this experiment suggest that a depth-independent, quasi-stationary mechanism, such as the barotropic recirculation of NAW within the trough, defines the frontal location (Gawarkiewicz and

Plueddemann, 1995). This characteristic of a large steady current interacting with the bottom topography characterizing the frontal zone follows the description of a topographic-circulatory front given by Federov (1983).

The preceding arguments, and in light of the proposed importance of tidal mixing in particular sections of the front by Kowalik and Proshitunsky (1995), suggest that the BSPF is a hybrid of a shelf-slope frontal system. Figure 32 is a schematic frontal cross section representative of conditions, away from the influences of Finger Canyon, incorporating most of the conclusions made from the observations. The front is well defined in the summer by a surface salinity and a corresponding density gradient. The mixed layer can be seen to shoal as one looks northward across the front accompanied by increased stratification. Mean surface flows at the front itself appear to be governed by the near surface density gradient. Below the mixed layer the front is defined by a moderate temperature gradient. On the shelf side of the front the cold BPW can be seen extending out over the slope at mid depth. The currents on the northern side of the front (particularly below the mixed layer) are dominated by the semidiurnal tides with only weak mean flows, suggestive of the cold Bear Island Current, following the topography. Four distinct vertical layers are found at the front: (1) the mixed layer, (2) a highly stratified regime which also contains fine structure or interleaving, (3) a more diffuse regime above the bottom boundary layer which is proposed to be the result of aperiodic vertical mixing due to tidal shear, and (4) the benthic boundary layer (not depicted). The warm side of the front is dominated by the barotropic recirculation of NAW within Bear Island Trough. ADCP current measurements and analysis of TS properties indicate that NAW appears to move upslope and eventually underneath the mid-depth expression of the front. Superimposed on this movement are high frequency small scale boluses of warm saline water, revealed by the tomographic analysis, which carry pulses upslope. From a horizontal perspective (not depicted), the front is well-defined and relatively stable in position especially to the east of Finger Canyon.
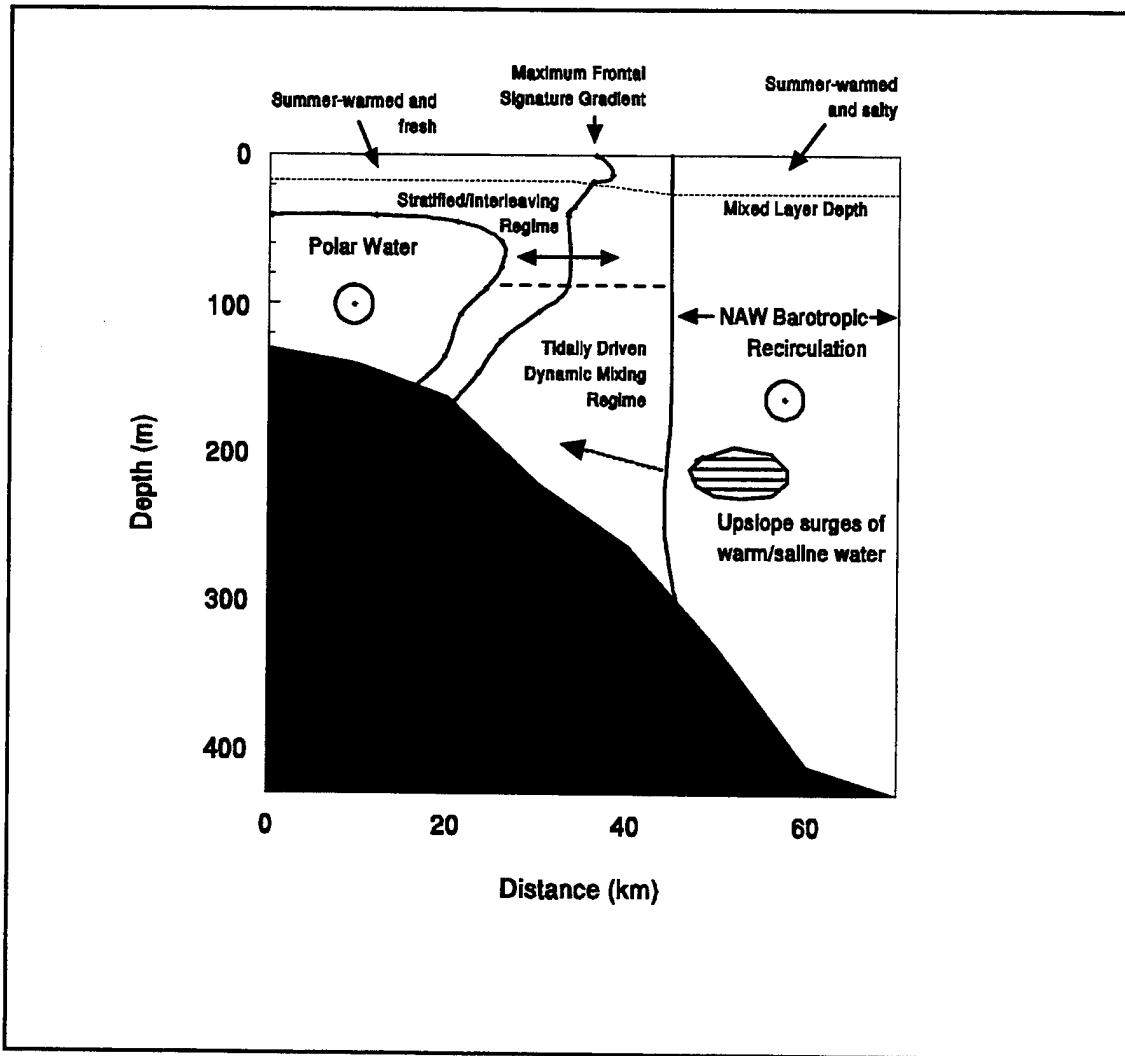
Figure 32. **A 2D schematic cross section of the summertime front is representative of the eastern section of the experimental area and summarizes many of the observations from the experiment.**

B.   COMPARISON OF FINDINGS WITH RELATED STUDIES

The proposed summertime schematic of the front differs from that of Loeng (1991) primarily in that the direction of the flow along the southern side of the front is westward, i.e., out of Bear Island Trough. Another difference is that a layer which could be distinguished as a 'transition layer' depicted by Loeng below the surface mixed layer was not observed in this data. Finally, the presence of the 'summer front' as shown by

Loeng was not observed. This latter difference could also be attributed to the limited horizontal extent of the experimental area onto Svalbard Bank itself.

Other more recent Barents Sea regional experiments and modeling studies have provided additional insight into the front beyond the resolution and scope of our data. T. McClimans (personal communication, 1994) used the laboratory model of the Barents Sea, described in Chapter I, to particularly investigate the BSPF features and dynamics. He found that the bottom slope acts to stabilize currents along the front. Additionally, topographic Rossby waves propagating westward induced local variability in the front as did topographic features (e.g., Finger Canyon) and were responsible for spawning cyclonic eddies. The record length of the data reported here was too short and spatially too coarse to resolve the flow in Finger Canyon or determine the presence of topographically-trapped Rossby waves. However, the current and temperature records at the SW mooring at the mouth of Finger Canyon suggest the passage of an anticyclonic eddy-like feature early in the experiment followed by a down-canyon flow of colder water. This feature, however, was too poorly resolved to be discussed further here. Eddies which may be associated with the mesoscale flow in the canyon likely perturb the frontal position in the immediate vicinity of the canyon and locally modify hydrographic parameters (Figures 10 and 21). Up and down canyon transports may increase cross-frontal transfer. Contrary to our brief observations, McClimans' model incorporates the flow of NAW to the northeast forming the frontal boundary. In his model NAW was partially cooled and freshened along the front and carried the resulting TS properties farther into the Barents Sea.

Gawarkiewicz and Plueddemann (1995) have recently modeled the circulation in the Bear Island Trough region using idealized bathymetry and mean flows as a process study. Their model was able to reproduce the basic flows and cross-shelf gradients of hydrographic variables observed in our data. In addition, their model was able to reproduce a barotropic southwestward recirculation of NAW inside Bear Island Trough trapped at the 260 m isobath. This isobath corresponds to the sill depth at the head of the trough which the NAW, carried by the Nordkapp Current, must cross prior to entering the

deeper regions and pockets of the eastern Barents Sea. With no significant mean BPW flow on the shelf in their model, the front dynamically represents a boundary between the barotropic recirculation and the cold BPW on the shelf (a topographic-circulatory front). In their model modification of the NAW along the front represents an advective and weak lateral diffusive balance.

Recent surface drifter data (Poulain et al., 1995) from the Barents Sea lends some support to the recirculation hypothesis. The circulation pattern suggested by the drifters is similar to that proposed by Gawarkiewicz and Plueddemann (1995). The drifters, which were drogued at 15 m, suggest that the major branch of the NAC which flows into the Barents Sea and forms the North Cape Current follows the 250-300 m isobath, close to the coast of Norway as seen in Figure 1. The drifter tracks diverge past 25°E and follow the other paths described in the literature such as the Murmansk Current and Novaya Zemlya Current. Another weaker and more northerly branch of the North Cape Current was identified by only a few drifters which entered directly into the Bear Island Trough. Once inside the trough, the paths of the buoys were highly circuitous and all the buoys had long residence times in the trough (order 1-2 months). Two of the buoys eventually proceeded to the east out of the trough and into the central Barents Sea during the fall and winter of 1994-1995. One buoy lost its drogue, exited to the west and rejoined the NAC as the West Spitsbergen Current. The long residence times of the drifters partially supports the presence of some recirculation in the trough.

The conditions of the BSPF in the summer of 1992 reported here, combined with the results of Gawarkiewicz and Plueddemann (1995) and the drifter data set of Poulain et al. (1995) have motivated the following modeling study into the circulation of Norwegian Atlantic Water in the Barents Sea and its relation to the Polar Front.

VI. THE MODELING PROGRAM

A.   BACKGROUND

The second objective of this research, to analyze the relation of the front to the regional oceanography, will be undertaken. The hypotheses on the recirculation of NAW inside Bear Island Trough, inferred from the observational data, will also be investigated more detail. Numerical simulation of the currents and water mass properties is the best tool to simultaneously achieve these tasks by providing the coverage, resolution, synopticity, and dimensionality not available from either direct observations or satellite data. Acoustic oceanographic tomography will in the near future provide another option for oceanographers to examine such problems.

1. Why the whole Arctic?

In planning the numerical experiments, a prime goal was to avoid the problem of specifying transports at open boundaries to the Barents Sea domain. As discussed in the introduction, transport estimates into and out of the Barents Sea are poorly known. To avoid contamination of results and reduce possible misinterpretations of the model predictions, the solution was to ensure the Barents Sea was well removed from any model boundaries. The major currents which carry the warm Atlantic Water to the Barents Sea are part of a global ocean conveyor belt circulation which transports heat poleward. These currents are an inherent part of the world's climate system (Broecker, 1991). However, by resolving the circulation in the Nordic Seas and Arctic Ocean, sufficient simulation accuracy is achievable. Observational density in the North Atlantic and southern portion of the Nordic Seas improves the quality of climatological averages used in initializing and forcing the model near these regions which in turn improves model performance in simulating these portions of the global current system. Treating the Arctic as a closed basin is an acceptable first order assumption as its connections to the Pacific

Ocean are estimated to be a transport of ~ 1.5 Sv (Semtner, personal communication, 1994; Aagaard and Greisman, 1975). The closed basin assumption was made for this study but inclusion of river discharge and specifying transports through Bering Strait will be included in follow-on sensitivity studies. Finally, the computational expense of using a hemispheric or global model was avoided to maximize the number of experiments and simulations for the given computer resources.

2. What to simulate?

Chapter V summarizes the observed scales and forcing observed at the BSPF in August 1992. The aim of the simulation is to replicate these scales and forcing mechanisms:

- time scale ~ 2 hours
- horizontal scale ~ 3.5 km
- vertical resolution ~ 10 m or less in the upper water column
- barotropic and baroclinic circulation
- semidiurnal tidal forcing

To compare model predictions with this unique data set, it was sought to simulate the summertime conditions of 1992 as best possible with the model.

The Barents Sea is essentially ice free in summer (Gloerson et al., 1992). However, it is not isolated from the influence of melted sea ice as was noted in the description of the front. Inclusion of sea ice in a numerical simulation of the Arctic is an essential element. The simulations reported here, however, are of an ice free Arctic Ocean because coupling and development of the sea ice model portion of the research is still in progress. A sense of the role of ice formation/melting can be achieved by restoration of the surface waters to climatological temperature and salinity data on a monthly basis to estimate the influences of sea ice on the oceanography.

Several grid resolutions were formulated, but with the finite relationship between time step, grid spacing, and required computational time, trade-offs ultimately became necessary to make the experiments tractable   The single greatest shortcoming of this modeling effort was the necessary compromise made in horizontal resolution.   Also, the high resolution forcing fields for such a projected broad domain at 5 km or less resolution were not available.   Compilation and interpolation from many data sets would be required to achieve realistic fields.   The final horizontal resolution of the model was ~18 km which does not resolve the fundamental scale of the baroclinic Rossby radius; however, combined with the 30 vertical levels it does represent the highest resolution model known for the entire Arctic region.

3. Collaboration

Given the human time scale of this modeling effort, I was grateful to be given the opportunity to join in a collaboration with Dr. Wieslaw Maslowski, Naval Postgraduate School, in this portion of my research.   We have used our combined efforts to develop this model to the point where the predicted fields were able to be studied in earnest in less than one-year, an accomplishment which was not achievable working alone.   Though our goals were entirely unique, the collaboration has benefited each of our research efforts. Dr. Maslowski's friendship, knowledge and insight are once again most thankfully acknowledged.

B.   MODEL CHARACTERISTICS

The model used for the simulations is the Semtner-Chervin General Circulation Model (GCM) with a free-surface (Semtner, 1974; Semtner and Chervin, 1988; Killworth et al., 1989; Killworth et al., 1991; and Semtner, 1995).   The model has its roots in the formulation of Bryan (1969) (Bryan and Cox).   The finite difference scheme, on an Arakawa B Scheme (Mesinger and Arakawa, 1976), solves the primitive equations on a

spherical coordinate system. Assumptions made in the equations are (1) thin shell (earth's radius much greater that the depth of the ocean) (2) hydrostatic assumption (3) Boussinesq approximation, and (4) Coriolis terms and viscous terms in the horizontal momentum equation including w (vertical motion) are neglected.

The system of equation reduces to seven basic model equations with seven unknowns as follows.

u and v momentum equations:

$$\frac{\partial u}{\partial t} + L(u) - fv = -\frac{1}{\rho_o a \cos \phi} \frac{\partial p}{\partial \lambda} + K_v \frac{\partial^2 u}{\partial z^2} + K_h \nabla_H^4(u) \tag{6.1}$$

$$\frac{\partial v}{\partial t} + L(v) + fu = -\frac{1}{\rho_o a} \frac{\partial p}{\partial \phi} + K_v \frac{\partial^2 v}{\partial z^2} + K_h \nabla_H^4(v) \tag{6.2}$$

Hydrostatic and Continuity equations for pressure (p) and vertical velocity w:

$$\frac{\partial p}{\partial z} = -\rho g \tag{6.3}$$

$$\frac{1}{a \cos \phi} \frac{\partial u}{\partial \lambda} + \frac{1}{a \cos \phi} \frac{\partial}{\partial \phi}(v \cos \phi) + \frac{\partial w}{\partial z} = 0 \tag{6.4}$$

The tracer equations for temperature (T) and salinity (S):

$$\frac{\partial T}{\partial t} + L(T) = D_v \frac{\partial^2 T}{\partial z^2} + D_h \nabla_H^4(T) \tag{6.5}$$

$$\frac{\partial S}{\partial t} + L(S) = D_v \frac{\partial^2 S}{\partial z^2} + D_h \nabla_H^4(S) \tag{6.6}$$

The Equation of State for density (ρ):

$$\rho = \rho(S, T, p) \tag{6.7}$$

The following variables and operators contained in the equations are defined below:

a = Earth's radius
Ω = Earth's angular rotation speed
(λ, ϕ, z, t) = (longitude, latitude, height, time)
ρ_o = mean density
$f = 2\Omega \sin\phi$ (Coriolis parameter)
(K_h, K_v) = (Horizontal, Vertical) eddy viscosity coefficients
(D_h, D_v) = (Horizontal, Vertical) eddy diffusivity coefficients

Advective Operator (defined for a dummy variable γ)

$$L(\gamma) = \frac{1}{a\cos\phi}\frac{\partial(u\gamma)}{\partial\lambda} + \frac{1}{a\cos\phi}\frac{\partial}{\partial\phi}(v\gamma\cos\phi) + \frac{\partial(w\gamma)}{\partial z}$$ (6.8)

Laplacian Friction Operator (used to define the biharmonic operator)

$$\nabla^2_H(\gamma) = \frac{1}{a^2\cos^2\phi}\frac{\partial^2\gamma}{\partial\lambda^2} + \frac{1}{a^2\cos^2\phi}\frac{\partial}{\partial\phi}\left(\cos\phi\frac{\partial\gamma}{\partial\phi}\right)$$ (6.9)

Biharmonic Friction Operator

$$\nabla^4_H(\gamma) = \frac{1}{a^2\cos^2\phi}\frac{\partial^2}{\partial\lambda^2}(\nabla^2_H\gamma) + \frac{1}{a^2\cos^2\phi}\frac{\partial}{\partial\phi}\left(\cos\phi\frac{\partial}{\partial\phi}(\nabla^2_H\gamma)\right)$$ (6.10)

The model boundary conditions are briefly summarized as follows. At the lateral walls a no-slip boundary is imposed such that $u = v = 0$. No flux of heat or salt allowed through the boundary. At the bottom, the flow is required to follow the slope of the bathymetry and no fluxes are allowed through the bottom. Bottom stress (τ_b) is a quadratic approximation as from using the bottom total velocity vector $\vec{U}$, a bottom drag coefficient (C_d) and the thickness of the bottom layer, d, in the form:

$$\frac{\vec{\tau}_b}{\rho} = \frac{C_d\vec{U}|\vec{U}|}{d^2}$$ (6.11)

81

At the surface, wind stress (τ_w), heat flux (Q_s) and salt flux (E) are specified. Also, the vertical velocity at the surface is allowed to be a function of the sea surface height η (free surface).

$$w = \frac{\partial \eta}{\partial t} \text{ at } z = 0 \tag{6.12}$$

By allowing a free-surface, the model is required to explicitly solve both the baroclinic and barotropic components of the motion. The barotropic motions are defined through the following equations which are recognizable as the shallow-water set of equations:

Barotropic momentum (U, V)

$$\frac{\partial U}{\partial t} - fV = -\frac{1}{a \cos \phi} g H \frac{\partial \eta}{\partial \lambda} + \nabla_H^4 U + X \tag{6.13}$$

$$\frac{\partial V}{\partial t} + fU = -\frac{1}{a} g H \frac{\partial \eta}{\partial \phi} + \nabla_H^4 V + Y \tag{6.14}$$

Free-surface hydrostatic relationship:

$$\frac{p_{surf}}{\rho_o} = g\eta(\lambda, \phi, t) \tag{6.15}$$

Continuity in terms of sea-surface

$$\frac{\partial \eta}{\partial t} + \frac{1}{a \cos \phi} \frac{\partial U}{\partial \lambda} + \frac{1}{a \cos \phi} \frac{\partial}{\partial \phi}(v \cos \phi) = 0 \tag{6.16}$$

82

where $-H$ is depth of the water column and the barotropic velocities are defined as:

$$U = \int_{-H}^{\eta} u\,dz$$

$$V = \int_{-H}^{\eta} v\,dz$$

The forcing terms for the barotropic field are defined as follows where F^u and F^v are the turbulent friction terms in equations (6.1) and (6.2) respectively:

$$X = -\frac{1}{a\cos\phi}\frac{\partial}{\partial\lambda}\left[\int_{-H}^{\eta} u^2 dz\right] - \frac{1}{a}\frac{\partial}{\partial\phi}\left[\int_{-H}^{\eta} uv\,dz\right] - \frac{1}{a\cos\phi}\left[\int_{-H}^{\eta} dz \int_{z}^{0} g\frac{\partial\rho}{\partial\lambda}dz\right] + \int_{-H}^{\eta} F^u dz \qquad (6.17)$$

$$Y = -\frac{1}{a\cos\phi}\frac{\partial}{\partial\lambda}\left[\int_{-H}^{\eta} uv\,dz\right] - \frac{1}{a}\frac{\partial}{\partial\phi}\left[\int_{-H}^{\eta} v^2 dz\right] - \frac{1}{a}\left[\int_{-H}^{\eta} dz \int_{z}^{0} g\frac{\partial\rho}{\partial\phi}dz\right] + \int_{-H}^{\eta} F^v dz \qquad (6.18)$$

The detail of the numerical implementation of the model are found in Killworth et al. (1989), but can be summarized as follows. The baroclinic velocities and tracer fields are integrated over one baroclinic time step, Δt (leapfrog in time). The terms X and Y are calculated as part of the baroclinic time step and are assumed to vary slowly in time. The barotropic motions, which vary much more quickly in time and include phenomena such as surface gravity waves, must be integrated over smaller time steps, $\Delta t'$. For long-term stability, Semtner (personal communication, 1994) has modified the approach of Killworth et al. (1989) by integrating the barotropic equations for time step n over $2\Delta t$ and averaging the resulting barotropic velocities which are coupled back to the baroclinic mode.

83

The scheme is as follows:

$$U_{avg} = \frac{1}{nb} \sum_{n}^{n+2\Delta t} U \quad \text{where} \quad nb = 2 \bullet \frac{\Delta t}{\Delta t'} \qquad (6.19)$$

The model uses a second-order accurate finite difference scheme and is flexible for use over small regional domains or for global applications. With the free-surface condition, smoothing of the real bathymetry is not required. The method has been optimized to run very efficiently on parallel-vector machines such as the Cray-YMP.

VII. MODEL DEVELOPMENT

The development of Semtner-Chervin GCM into a simulation model of the Arctic and Nordic Seas began with the establishment of the model grid and interpolation of the corresponding bathymetry for the region. Additional improvements to the model for use in the Arctic included insertion of an optimized equation of state for the colder temperatures, improving and tuning eddy diffusivity and viscosity coefficients, and determination of initial and forcing fields.

A. MODEL DOMAIN AND BATHYMETRY

The use of spherical coordinates in modeling the entire Arctic region fails at the North Pole due the convergence of the meridians to a singularity. To solve successfully the model equations, a polar model domain must exclude the Earth's poles by rotating the model grid off the pole. To achieve this rotation, a model grid was established which spans the equator with dimensions of 60 degrees by 50 degrees (361 by 301 grid points). Selection of the model spanning the equator was done to minimize the change in the meridional separation distance with latitude and thus providing a near uniform grid spacing. The real Arctic domain was then mapped into this model box by specifying the location of the North Pole within the domain to achieve the desired Arctic coverage (Figure 33a). The corresponding latitude and longitude for each grid point was then calculated (Figure 33b). The only variable in the model formulation which is sensitive to this model grid rotation on the globe is the Coriolis parameter. A true Coriolis parameter was calculated from the latitude which corresponds to the real Arctic domain for each grid point and was used in the integration.

Bathymetry for the model was collated from several sources. Interpolation of the ETOP5 data set from the NOAA National Oceanography Data Center to the grid points was used over most of the domain. Hand-gridded data sets from charted data for the Greenland Sea (provided by Dr. Wiesiek Maslowski), the Barents Sea (provided by Dr.

Andrey Proshintinsky), and the Central Arctic/Lomonsov Ridge (Parsons) were used in those particular regions to overcome known discrepancies in the ETOP5 data. Additional corrections for the Barents Sea were obtained from observations compiled and provided by Dr. Norm Cherkis, Naval Research Laboratory.

The vertical structure of the model was divided into 30 vertical layers of varying thickness and is described in Table 7. The gridded Arctic bathymetry was then mapped to the model levels. The shallowest ocean point was forced to have 2 vertical layers giving the minimum model depth of 45 m. The deepest bathymetry at ocean points was truncated to 4300 m from this technique. The final resulting model grid and corresponding bathymetry is provided in Figure 34.

Model Level	Layer Thickness (m)	Bottom Depth (m)
1	20	20
2	25	45
3	25	70
4	30	100
5	40	140
6	40	180
7	40	220
8	60	280
9	80	360
10	80	440
11	120	560
12	140	700
13 - 30	200	900-4300

Table 7. Vertical Structure of the Arctic Model.
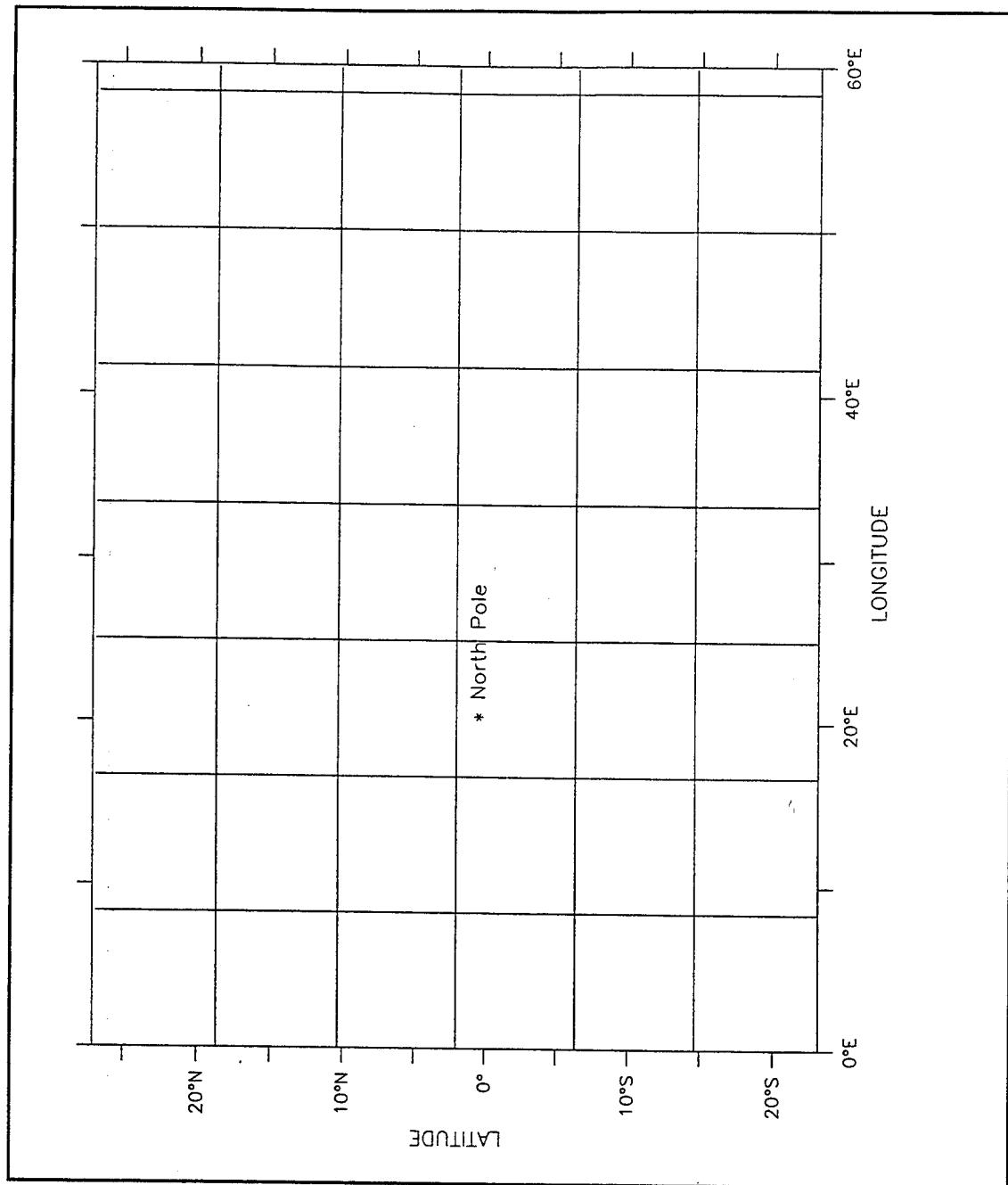
Figure 33a: The model grid as defined over the equator spans 60 degrees in a meridional direction and 50 degrees in a zonal direction. The * marks the position of the North Pole which was inserted.
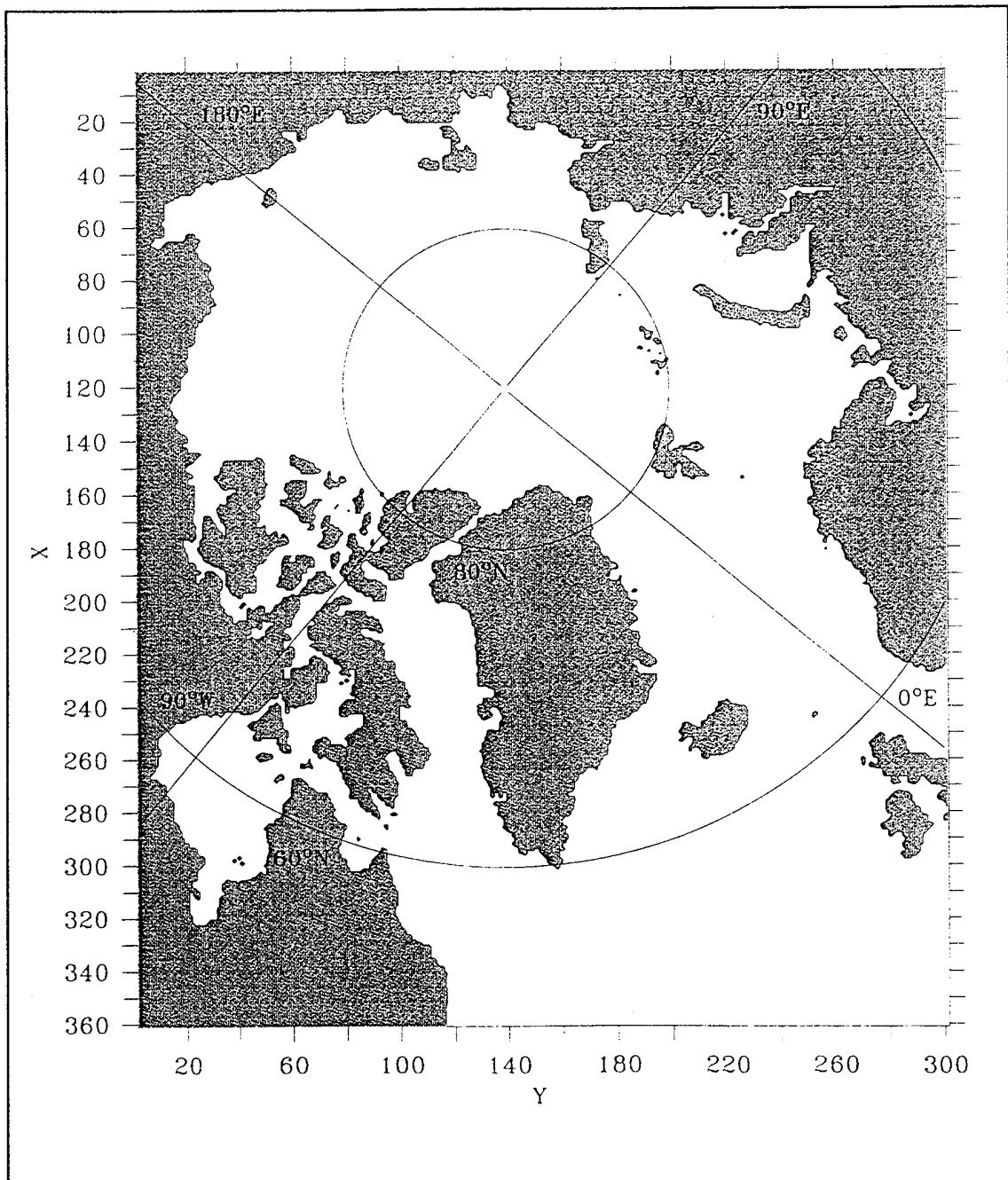
Figure 33b. The model grid after being mapped to the Arctic from the position of the North Pole at grid point (121,139). Contours are of real latitude and longitude calculated for each grid point. Land masses have been shaded gray.
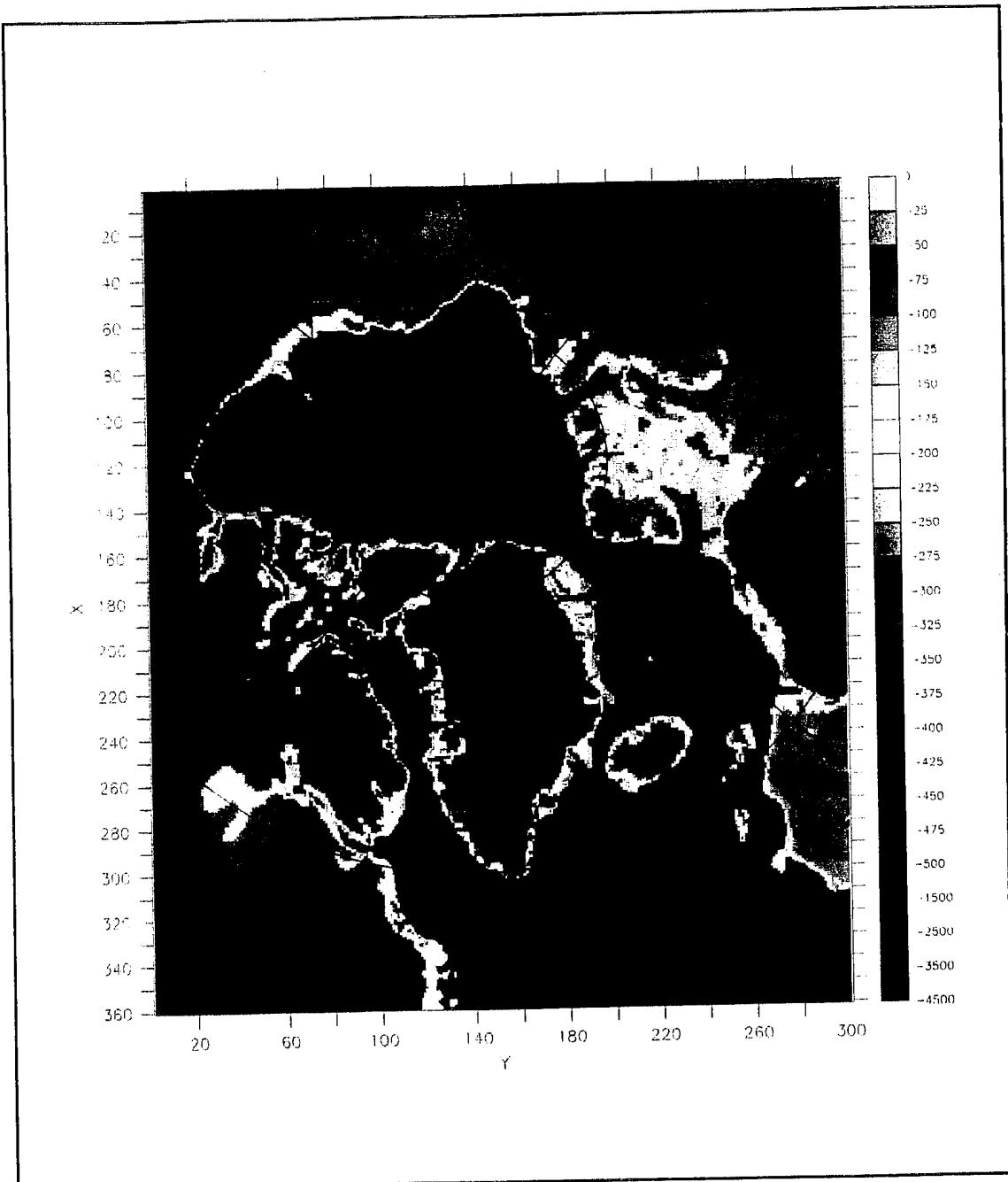
Figure 34: Contours of the model bathymetry (meters) after assignment of interpolated bathymetry to the specified model levels depicts the high resolution obtained through the use of 30 vertical levels.

B. FINDING AN EQUATION OF STATE

The version of the Semtner-Chervin formulation which was developed into the Arctic model contained a very computationally efficient equation of state (EOS) from Eckart (1958). However the accuracy of the Eckart EOS suffers in the extreme cold temperatures of Arctic waters. Simply inserting the full UNESCO Equation of State for Sea Water (1980) overcomes the accuracy problems but computational efficiency is lost.

An independent computational experiment was performed to select the best EOS for use in the model to provide maximum accuracy and computational efficiency. The EOS's evaluated in the experiment were the full UNESCO (1981), Eckart (1958) [EK], Bryan and Cox (1972) [BC], Friedrich and Levitus (1972) [FL] , and Mellor (1991) [ML]. The full UNESCO EOS is accepted as the accuracy standard.

EK is a rational quadratic equation in temperature and linear in salinity which predicts seawater density based upon a fit to scant laboratory data collected from very early this century (two salinities and four temperature points on each of various pressure isotherms). As will be demonstrated, this simple equation is still of sufficient accuracy over a large pressure range (0.05 kg m^{-3}) for many applications. FL use a polynomial fit to the Knudsen equation (Fofonoff, 1962) to efficiently derive seawater density. In the upper 2000 m a seven term polynomial is used which is cubic in temperature with a quadratic pressure correction. In the remaining deeper part of the water column, only a 5 term polynomial is used which is quadratic in temperature with a quadratic pressure correction.

BC use a 9 term cubic polynomial fit to the Knudsen equation with a slight variation. From a collection of global temperature and salinity points compiled from the NODC data base, they determined mid-point temperature (T_o), salinity (S_o), density (ρ_o) values at specific depths for the entire ocean. They then began their formulation by looking at the departures from these pressure specific midpoints [$S_o+\Delta S$, $T_o+\Delta T$, $\rho_o+\Delta\rho$]. The resulting polynomial, determined in a least squares fit to the Knudsen equation, provides the density departure from the midpoint at a particular depth. Coefficients for

90

the polynomial are then depth dependent since pressure is inferred (not explicit) in the formulation The technique used in this experiment differed from the original work of Bryan and Cox in that the temperature and salinity ranges were specified at selected model depths and that the least squares fit was made to the full UNESCO EOS. Additionally, the temperature and salinity ranges were taken from an interpolation to the model grid of the annual mean temperature and salinity found in the Levitus and Boyer (1994) and Levitus et al. (1994) climatological atlas. Finally, the resulting normalized densities were restored to real density by adding back the median density for that pressure (ρ_o).

ML found the most computationally inefficient part of the UNESCO equation of state was the pressure term.   Calculating just $\rho(S,\theta,0)$ was about a factor of 3 computationally faster that calculating the full density $\rho(S,\theta,p)$ where θ is potential temperature.   To obtain a pressure correction, he relied on the relationship that the adiabatic density gradient is proportional to sound speed squared $C(S,T,p)$:

$$\left(\frac{\partial \rho}{\partial p}\right)_{adiabatic} = \frac{1}{C^2} \tag{7.1}$$

ML then uses a sound speed term to account for the pressure correction such that :

$$\rho(S, T, p) = \rho(S, T, 0) + 10^4 \frac{p}{c^2}\left(1 - 0.20\frac{p}{c^2}\right) \tag{7.2}$$

where c is the speed of sound which is a function of potential temperature $c(S,\theta,p)$ (which is not true sound speed $c(S,T,p)$). The sound speed is calculated from a simple polynomial expression which is quadratic in pressure and temperature.

The experiment was comprised of two parts: speed and accuracy.   All computations were performed on a Cray YMP-EL98 at the Naval Postgraduate School. To perform the tests eight depths were chosen on which to perform the tests. At each depth a 100 by 100 was matrix was filled with equally spaced temperature and salinity

values spanning the minimum/maximum ranges determined from the annual Levitus and Boyer (1994) climatological atlas for the Arctic Model region. Table 8 describes the depths and *in situ* temperature and salinity ranges used in this experiment. All *in situ* temperatures were converted to potential temperature and used in calculating the potential density. The FL EOS contains an equation to restore pressure effects and uses *in situ* temperature before calculating the density. The BC coefficients were derived from a fit to potential density. The routines in each EOS subroutine were designed for maximum vectorization during computations and to mimic the calling structure used in the model.

Depth (dbar)	Minimum Temperature (°C)	Maximum Temperature (°C)	Minimum Salinity (psu)	Maximum Salinity (psu)
10	-1.76	16.69	18.41	35.68
60	-1.91	14.50	26.40	35.80
130	-1.98	12.94	29.09	35.75
550	-0.96	10.81	34.02	35.54
1090	-1.00	9.07	34.47	35.80
2090	-1.21	3.59	34.48	35.02
3090	-1.30	2.87	34.90	34.97
4090	-0.65	2.34	34.90	34.94

Table 8. *Depths and temperature and salinity ranges used in testing various EOS's. Note that the temperatures at 10, 60 and 130 m depth have been set to the freezing point. The methodology used in creating the Levitus and Boyer (1994) climatological data set allowed temperatures of -3°C to persist in the Arctic region.*

Figure 35 summarizes the speed tests based upon 10000 calls to each routine. Speed is given in average CPU time per call. The range of times covers two orders of magnitude. The UNESCO routine by far is the most computationally inefficient. ML reflects a speed increase of almost 10 times by use of the pressure effect simplification. The leaner polynomial equations used in FL, BC and EK show the tremendous
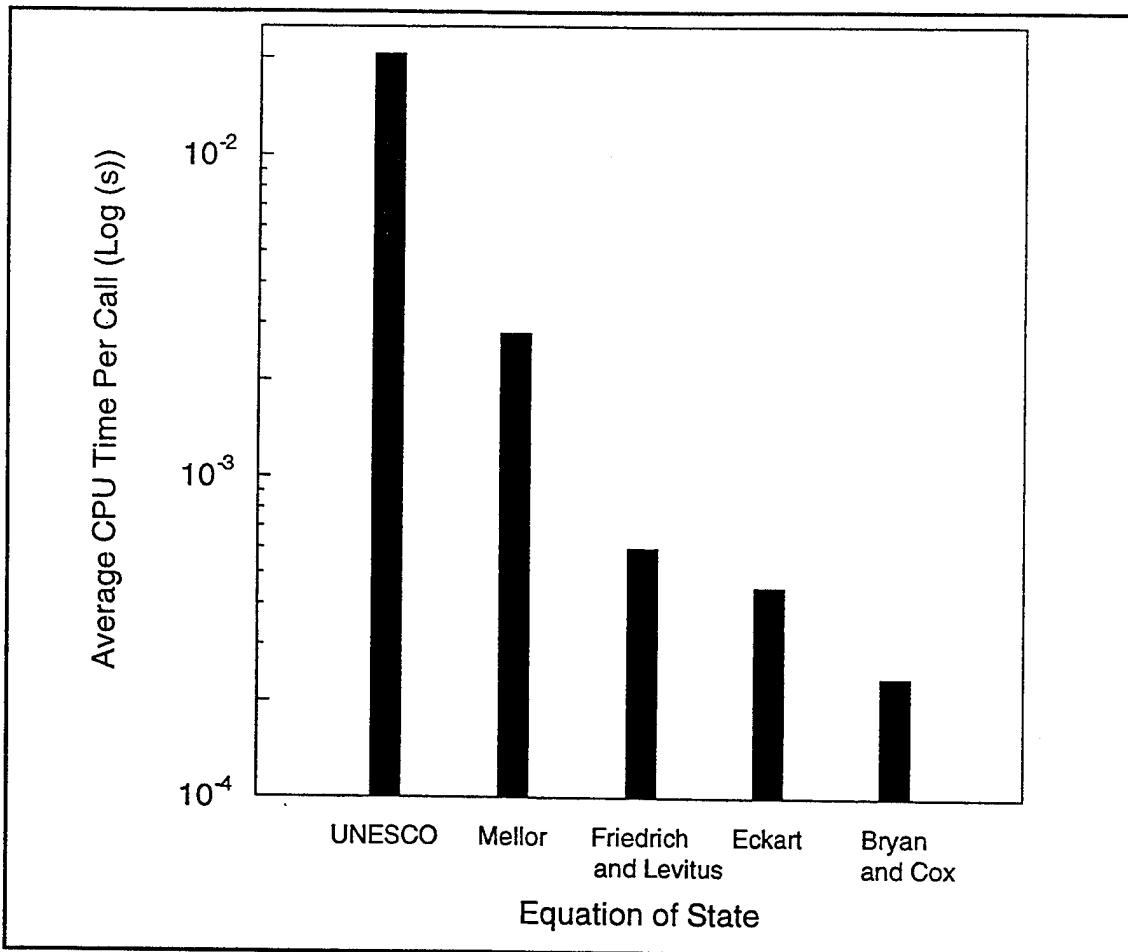
Figure 35. **A bar for each equation of state tested depicts the average CPU time per call over a sample of 10000 calls on a log scale.** **Each call to the routine performed 800 density calculations.**

computational advantage in using these formulations with the BC equation proving the most efficient in this experiment.

To couple accuracy with speed, plots were made of the difference fields from UNESCO for each equation of state tested. The plots, Figure 36a through 36h, are made in temperature and salinity coordinates with contours of differences in potential density made in real units (kg m^{-3}). Figure 36a represents the difference field at 10 dbars. The ML equation reflects the minimal impact of a 10 dbar pressure correction on the density and is essentially a duplication of the UNESCO calculation of $\rho(S,\theta,0)$. The

inaccuracies of EK at temperatures below zero are clear; however, its accuracy at median values cannot be discounted. The FL formulation shows a near constant bias of ~ 0.02 kg m^{-3} accept in cool or warm fresh water. The BC formulation appears accurate to within 0.002 kg m^{-3} over the entire range of temperature and salinity.

Increasing pressure has an adverse effect on the accuracy of all formulations except EK which maintains an error magnitude on the order of 0.05 kg m^{-3} throughout the water column. However, EK is clearly the most inaccurate for Arctic applications with large errors for cold and salty waters. The ML is most accurate consistently throughout the water column with BC and FL being second and third. At 3090 and 4090 dbar, the inaccuracies of the FL formulation switching to a 5 term polynomial at depths below 2000 m are evident in Figures 36g and 36h as the error magnitude essentially doubles.

To finally evaluate the balance between speed and accuracy, the error induced by density inaccuracies in the model must be evaluated. The model resolution tends to minimize the inaccuracies used in the various formulations. For horizontal velocities the model solves for the pressure gradient through the vertical integration of the hydrostatic equation for layer k:

$$\partial p = -g \int_{k-1}^{k} \rho dz \qquad (7.3)$$

Vertical model resolution (dz) varies from 20 m in the shallow levels to 200 m in the deeper levels. To perform scale analysis on the errors on the model calculations, the geostrophic velocity relationship was used:

$$u = -\frac{1}{\rho f} \frac{\partial p}{\partial y} \qquad (7.4)$$

Three representative density error magnitudes were selected (.001, .01, .1) from the accuracy tests and were doubled to account for maximum error from a finite difference estimation. Assuming ρ, f, ∂y constant, the error then associated with the

velocity calculation can be calculated through the pressure difference. Table 9 provided the simple error estimation from this scale analysis on the velocity.

Comparing the accuracy and speed of ML and BC in light of this scale analysis, the ML equation would be one order of magnitude more accurate both at shallow and deeper levels in velocity calculations but one order of magnitude slower. However, the BC formulation should still be accurate to the third decimal place in geostrophic velocity at the surface and the second decimal place at deeper levels.

Representative Density error (kg m^{-3})	Velocity error for dz = 20 m (cm s^{-1})	Velocity error for dz = 200 m (cm s^{-1})
0.0020	0.0010	0.0001
0.0200	0.0100	0.0010
0.2000	0.1000	0.0100

Table 9. Scale of geostrophic velocity errors associated with the EOS inaccuracies.

The last consideration on the density accuracy is its potential effect on the performance of the convective adjustment routine. This algorithm redistributes the buoyancy vertically in the water column to ensure stability through simple mixing of the vertical levels. Whether the temperature and salinity of two vertical levels are mixed depends on the density difference between the lower and upper level when density is calculated at the pressure of the upper level. The effect of the density inaccuracies on this comparison can be interpreted through the gradient of the density difference fields from UNESCO with respect to temperature or salinity. A large gradient would be associated with larger errors when comparing densities of different temperature and salinity values at the same pressure. The maximum gradients were found with respect to temperature for all four EOS's. At upper levels, the EK EOS has a maximum density difference gradient with respect to temperature magnitude of 0.03 (kg m^{-3} °C^{-1}). Similarly, FL, ML and BC are 0.01, 5 10^{-05}, and 0.003 kg m^{-3} °C^{-1}, respectively. At deeper levels all the equations had gradients on the order of 0.02 (kg m^{-3} °C^{-1}). An example of a convective adjustment

95
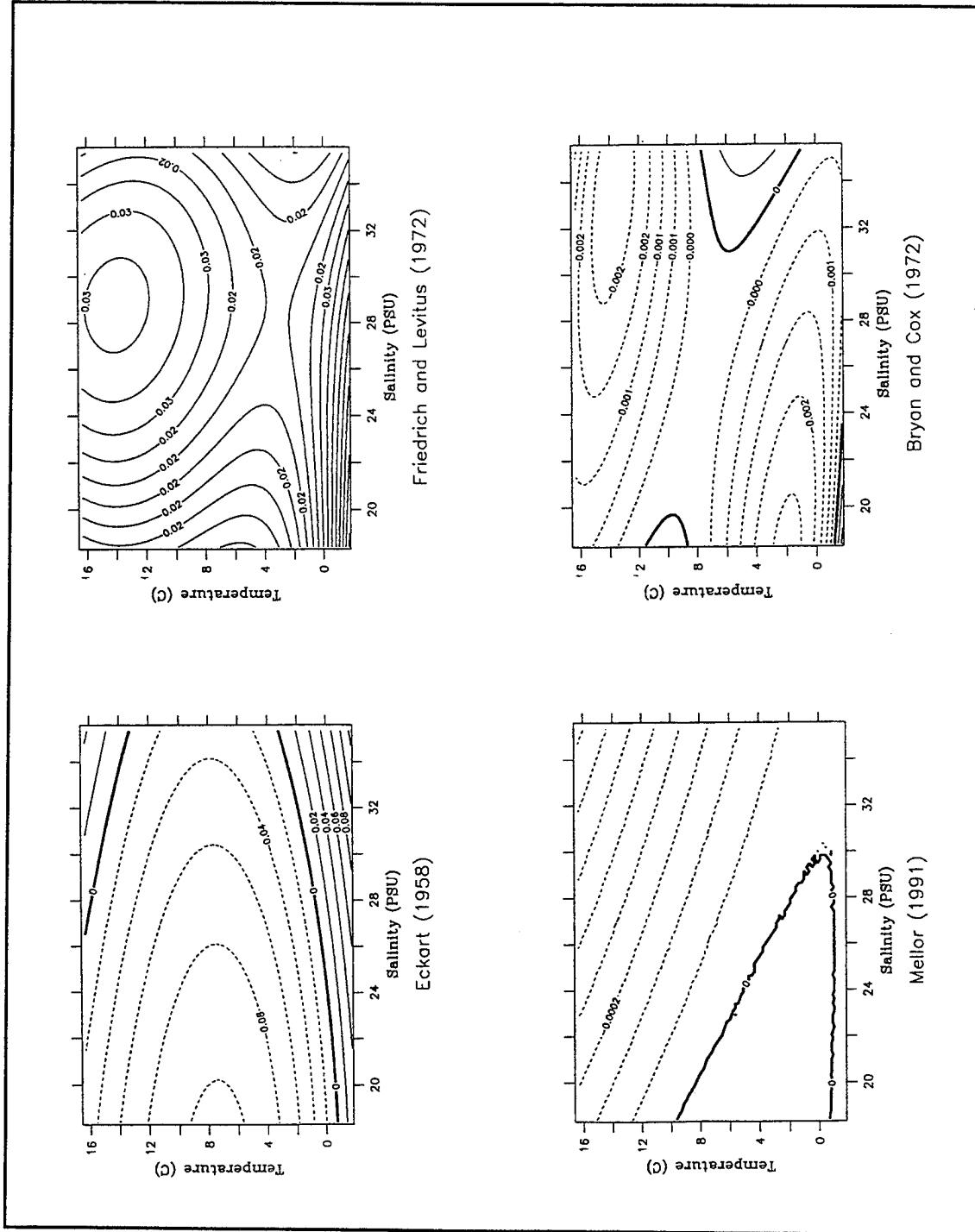
Figure 36a. The difference field from UNESCO EOS at 10 m for the four tested Equations of State show the Mellor (1991) equation to be most accurate.
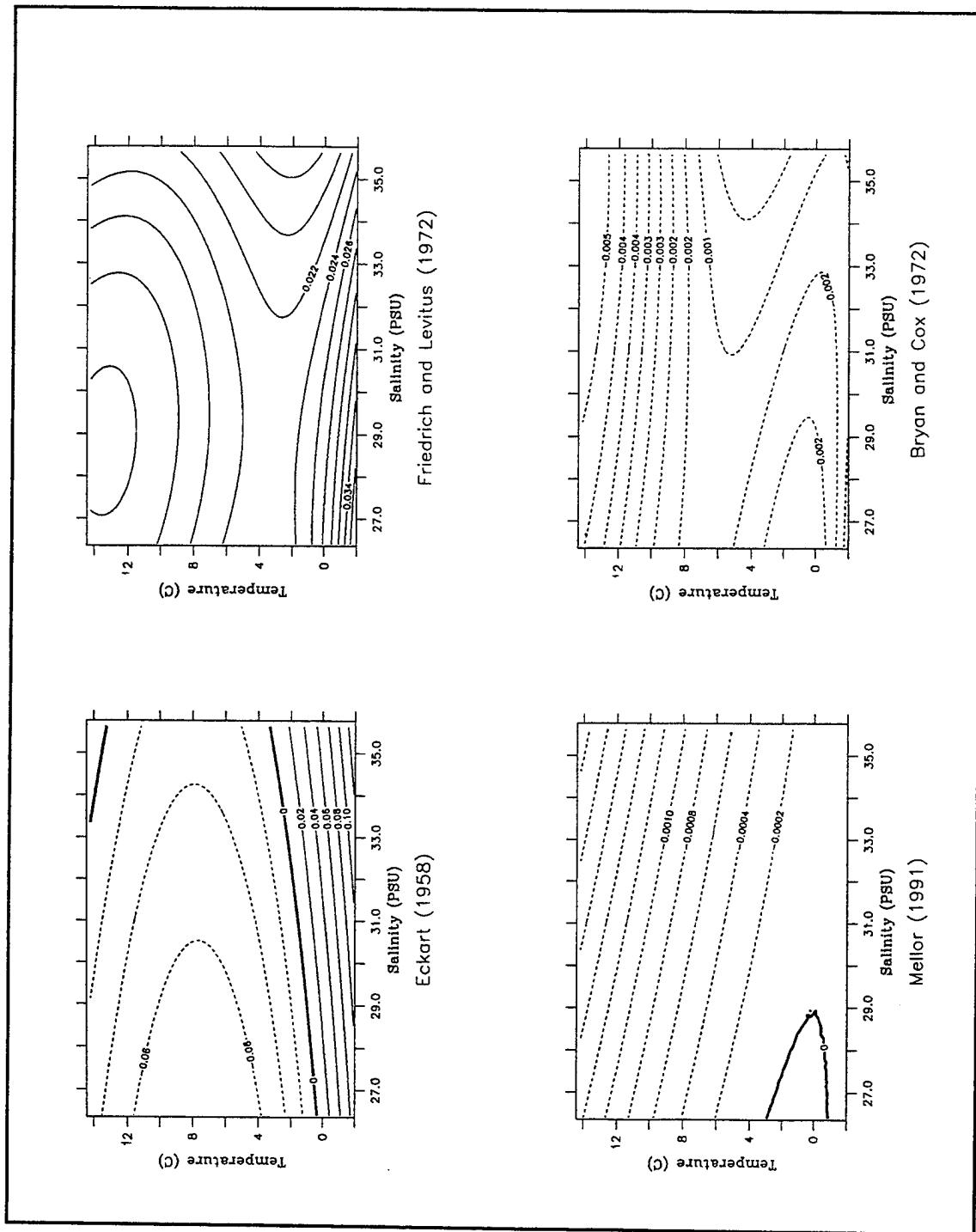
Figure 36b. The difference field from UNESCO EOS at 60 m.

97
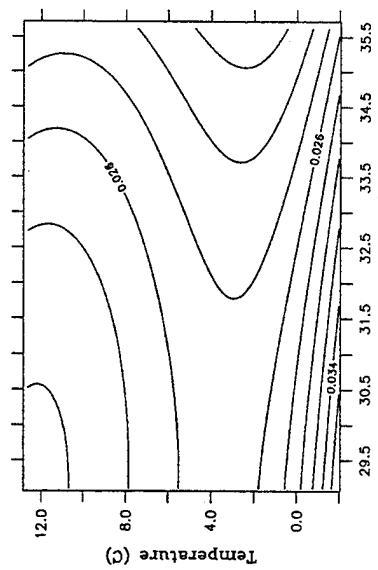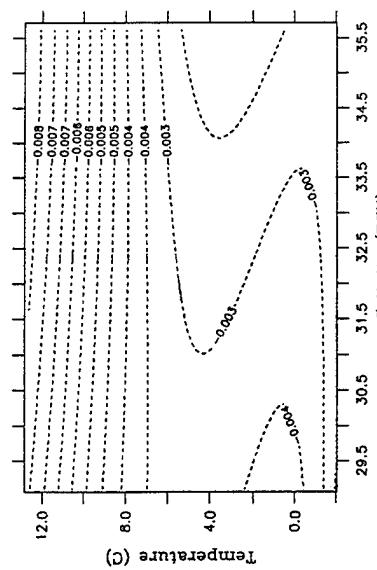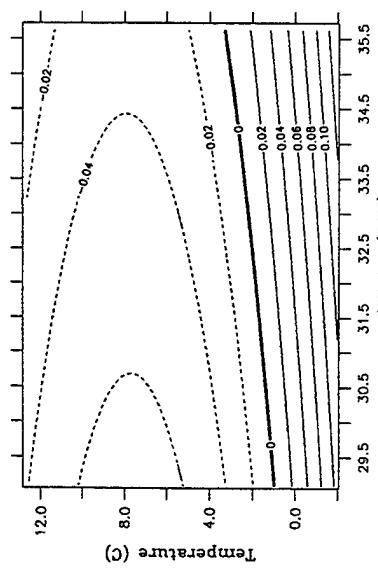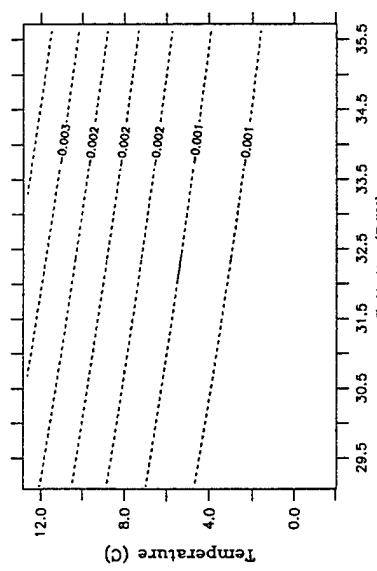
Figure 36c. The difference field from UNESCO EOS at 130 m.
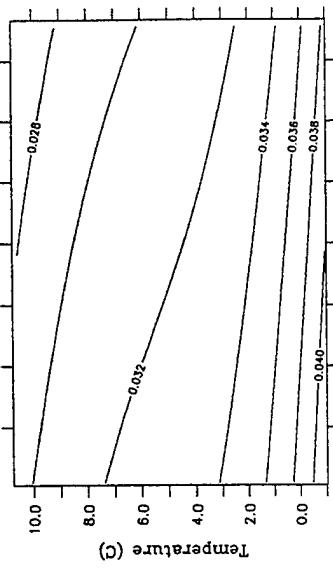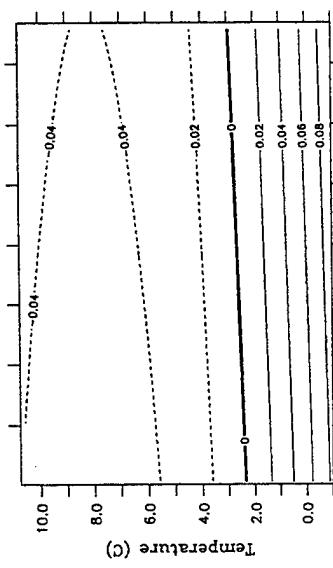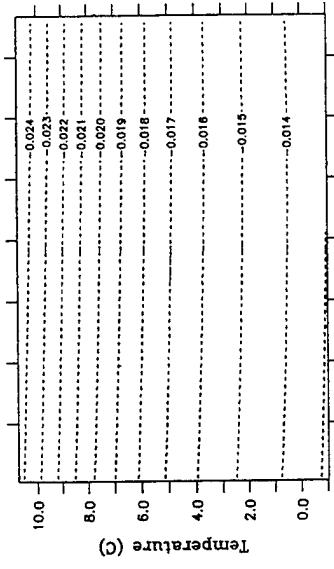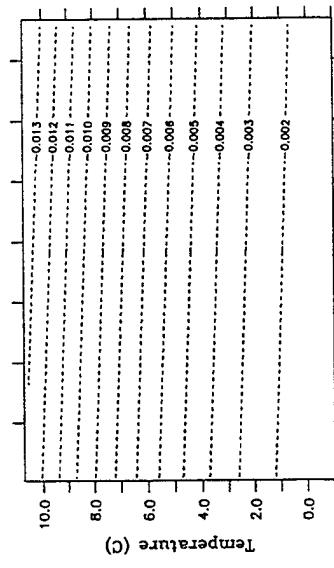
Figure 36d. The difference field from UNESCO EOS at 550 m.
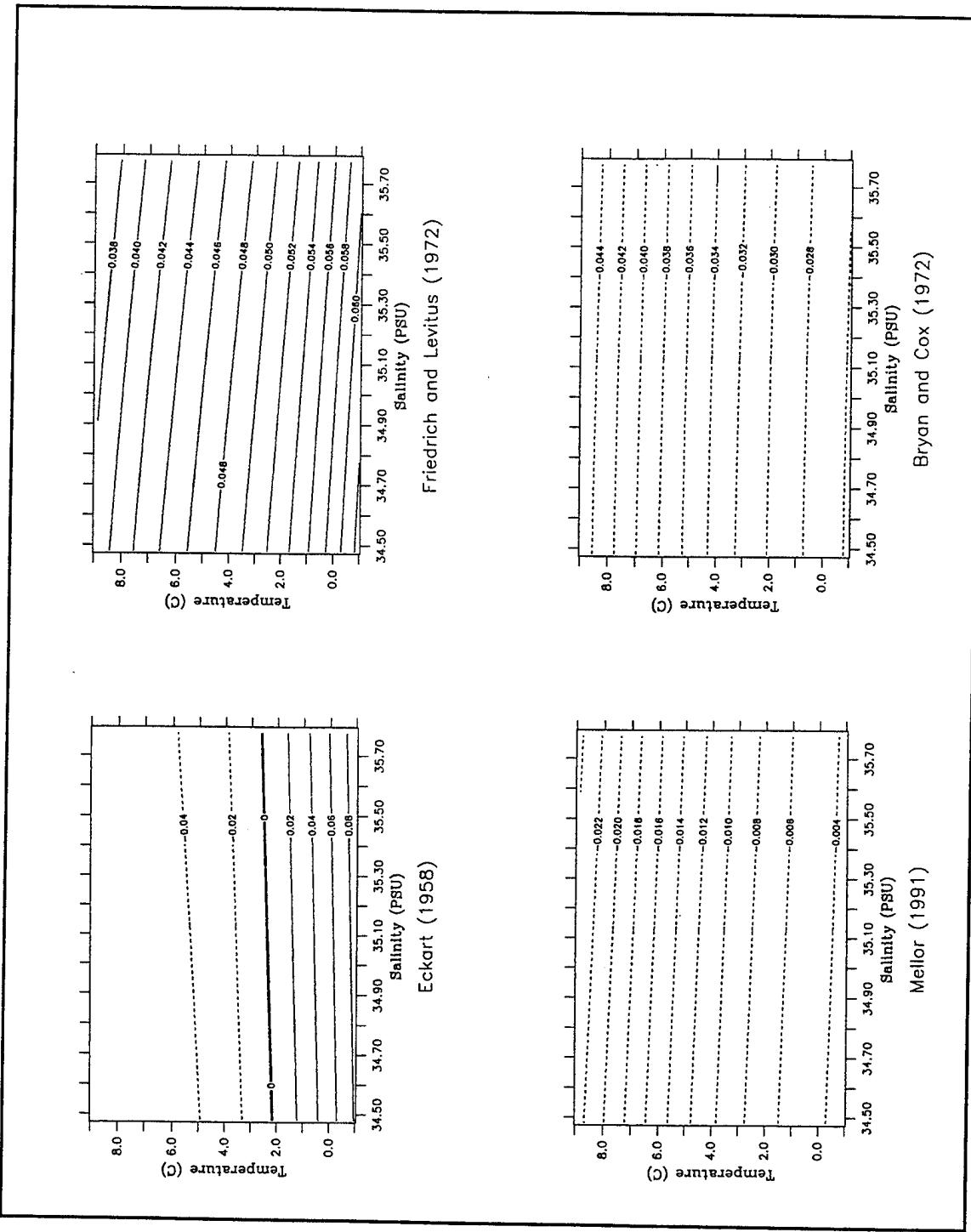
Figure 36e. The difference field from UNESCO EOS at 1090 m.
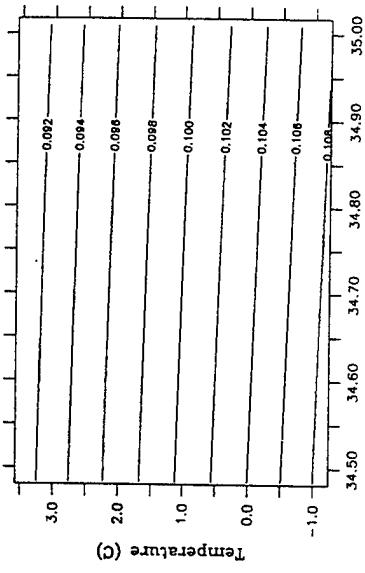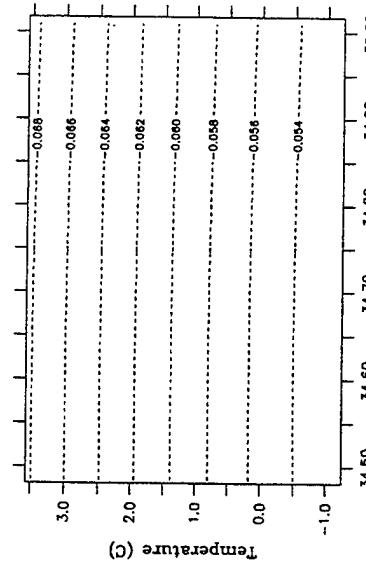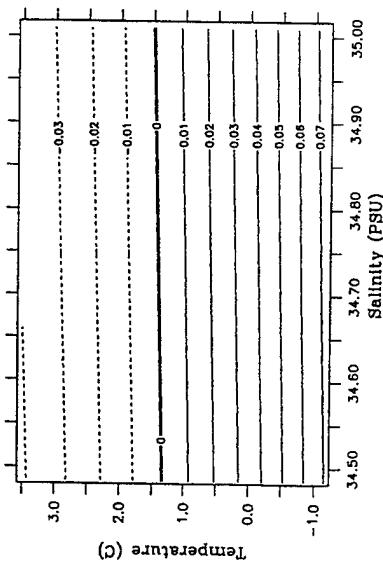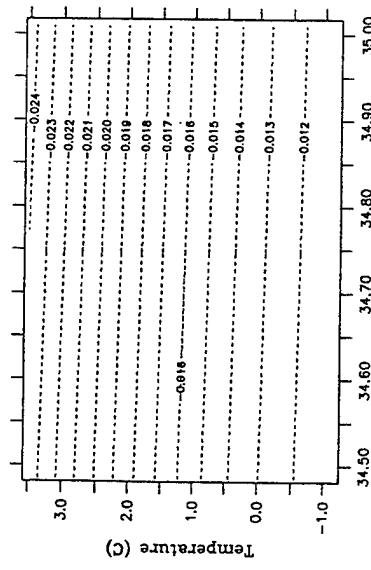
Figure 36f. The difference field from UNESCO EOS at 2090 m.
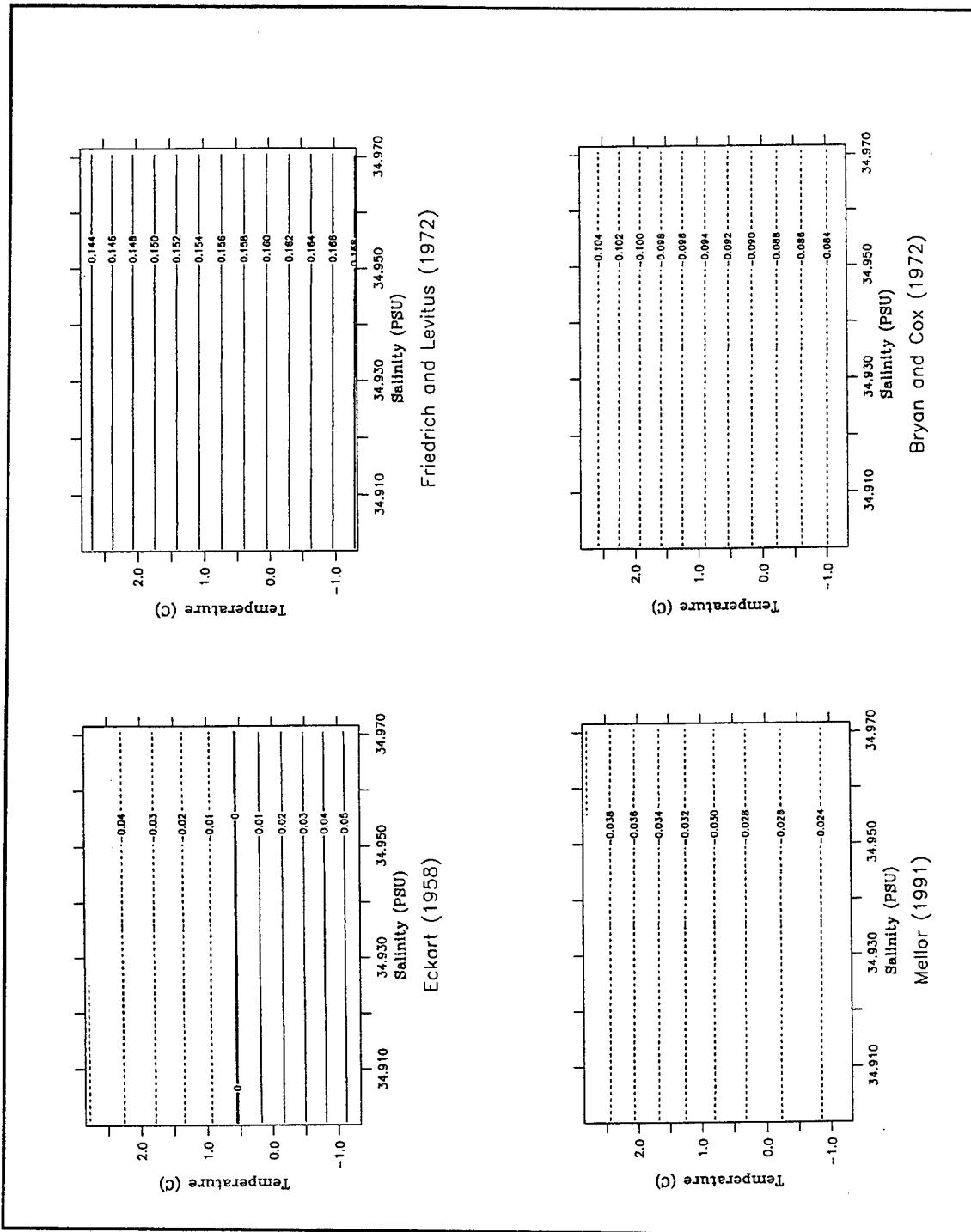
**Figure 36g. The difference field from UNESCO EOS at 3090 m.**
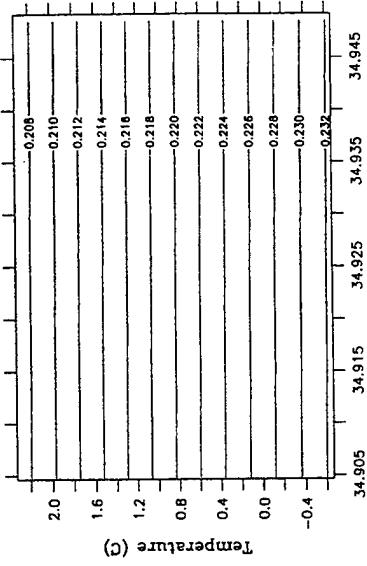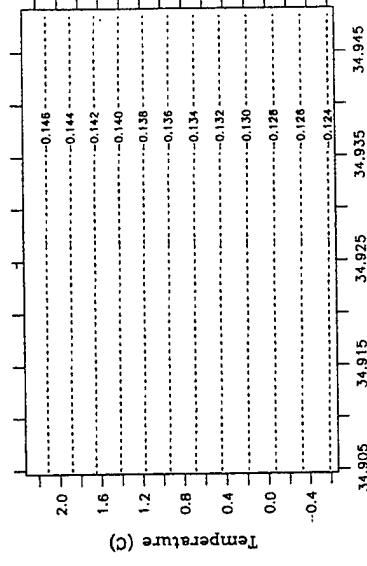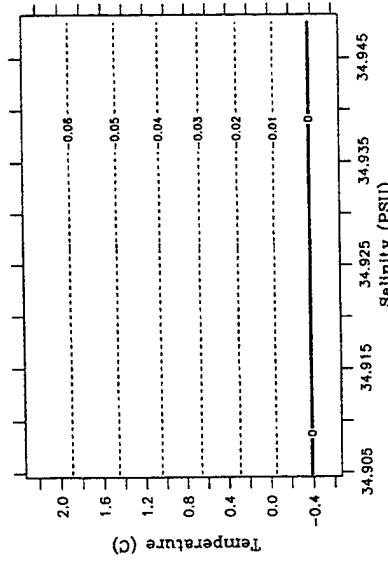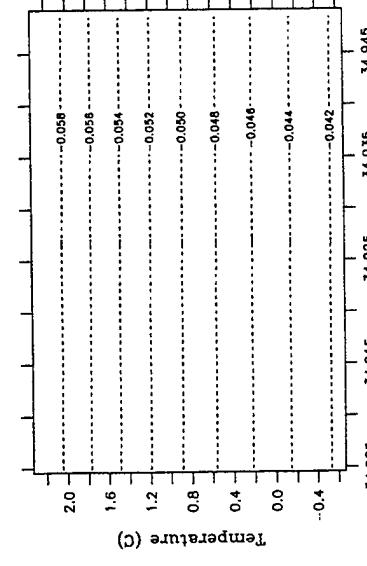
Figure 36h. The difference field from UNESCO EOS at 4090 m.

error due to density inaccuracies was found when testing the performance of the routine on a Eurasian Basin temperature and salinity profile extracted from climatology data. Most significantly, tests with EK EOS showed an erosion of the Arctic halocline through the convective adjustment mixing process when the other EOS's tested predicted the profile through the halocline would remain convectively stable.

On the basis of this experiment, the Bryan and Cox EOS was selected for use in the model experiments. The speed of the BC equation combined with minimal sacrifices of accuracy for derived model parameters were its key attributes. ML provides a substantial increase in speed and marginal loss of accuracy when compared to UNESCO and is ideally suited for models using isopycnal or sigma vertical coordinates where the BC formulation is incompatible.

C. VERTICAL AND HORIZONTAL MIXING PARAMETERIZATION

Selection of the coefficients for the horizontal and vertical viscosity and diffusivity terms (K_h, D_h, K_v, and D_v) in equations (6-1), (6-2), (6-3) and (6-4) is an inherent aspect to successful model simulation. The magnitude of these coefficients affect the amount of total kinetic energy, the distribution of that energy in frequency and space as well as the degree to which water masses mix. The assigned value of the coefficients serve to finish the parameterization of effects of turbulence or friction in the momentum and tracer equations in terms of a mean or known variable. The space and time scales of turbulence decrease ad infinitum preventing complete expression of all turbulence variables within a given number of equations. Turbulent or eddy parameterizations close the set of equations so that an equal number of unknowns and equations exist in the system.

The closure scheme used to account for the turbulent effects in the Semtner-Chervin GCM model equations represents a first order closure (Haltiner and Williams, 1980). The turbulent or frictional effects are parmeterized as an eddy viscosity or diffusivity (mixing length or K closure). Higher order closure schemes can better parameterize the effects of turbulence generation, mixing and dissipation but require

additional computer time and storage (Mellor and Yamada, 1982). Planned future improvements to the model include use of a higher order turbulence closure scheme. However, the real test of model turbulent closure schemes comes in comparison with observations.

Instantaneous vertical eddy viscosity and diffusion coefficients, K_v and D_v, in the 1/4 degree eddy-resolving global circulation model are derived following Pacanowski and Philander (1981) (Semtner and Chervin, 1992). It is a formulation based upon the empirical studies of Robinson (1966) and Jones (1973) using a neutral static stability coefficient and the bulk Richardson number. Stability in the water column used to calculate the Richardson number is predicted from the temperature gradient alone. In the very cold Arctic water, salinity is the prime determinant of density and the Pacanowski and Philander (1981) formulation, optimized for the tropics, would not be a suitable parameterization.

Two approaches to assigning values to the vertical coefficients were taken in model experiments. The first and simplest was assigning commonly used constant values to the coefficients (K_v = 10 cm^2 s^{-1} and D_v =0.3 cm^2 s^{-1}) taken from the literature (Böning and Budich, 1992). The second was using a modified Munk and Anderson (1948) approach with guidance adapted from Brooks (1994) and Endoh et al. (1981). The equations used in the formulations are as follows:

$$K_v = \frac{K_{vo}}{(1+10Ri)^{1/2}}$$

$$D_v = \frac{D_{vo}}{(1+3.3Ri)^{3/2}}$$

At each time step n, the coefficient values were updated following Brooks (1994) in the equation below where K_v and D_v from the above equations are presented as ϕ.

$$\phi^n = [\phi^{n-1}\phi]^{1/2}$$

The Richardson Number was calculated using the density gradient for stability (σ_t) from equation (4.1). The choice for K_{vo} and D_{vo}, the neutral static stability coefficients (Ri =0), were taken as 100 cm^2 s^{-1} and 50 cm^2 s^{-1}. The selection of these were consistent with values in Brooks (1994), Endoh et al. (1981) and Foo et al. (1981) which are coastal and continental shelf studies. Due to the large areas of continental shelf within the model domain and the increased vertical resolution, these values were deemed appropriate. Figure 37 presents the normalized functions described in equations (7.5) and (7.6) and relates their performance with respect to the Richardson number.

Horizontal viscosity and diffusivity are parameterized through used of the biharmonic friction operators. The fourth order derivatives allows the biharmonic friction to act on the small scales more strongly than that on the large scales as compared to the Laplacian friction formulation (Pond and Picard, 1982). By using the biharmonic friction, the overall friction placed on the mean flow and eddies necessary for numerical stability can be reduced and more realistic simulations should result.

Values for the biharmonic coefficients used in the models simulations were initially taken from commonly used values given by Böning and Budich (1992) which range from $-0.8*10^{19}$ to $-2.5*10^{19}$. Adjustments from these values were made to reduce the numerical noise seen in individual experiments and are provided in Chapter VIII.

D. MODEL INITIALIZATION

After model testing with homogeneous and horizontally homogeneous profiles of temperature and salinity, initialization fields from climatological data were constructed. Annual average temperature and salinity data from the Levitus and Boyer, (1994) and Levitus et al. (1994) climatological atlases, which are at 1° spacing and at 33 vertical levels, were first linearly interpolated to the model grid. In this step the 1° land points and bathymetry present in the atlas were maintained. The next step used a combination of horizontal averaging, vertical interpolation and planar interpolation to fill in the ocean
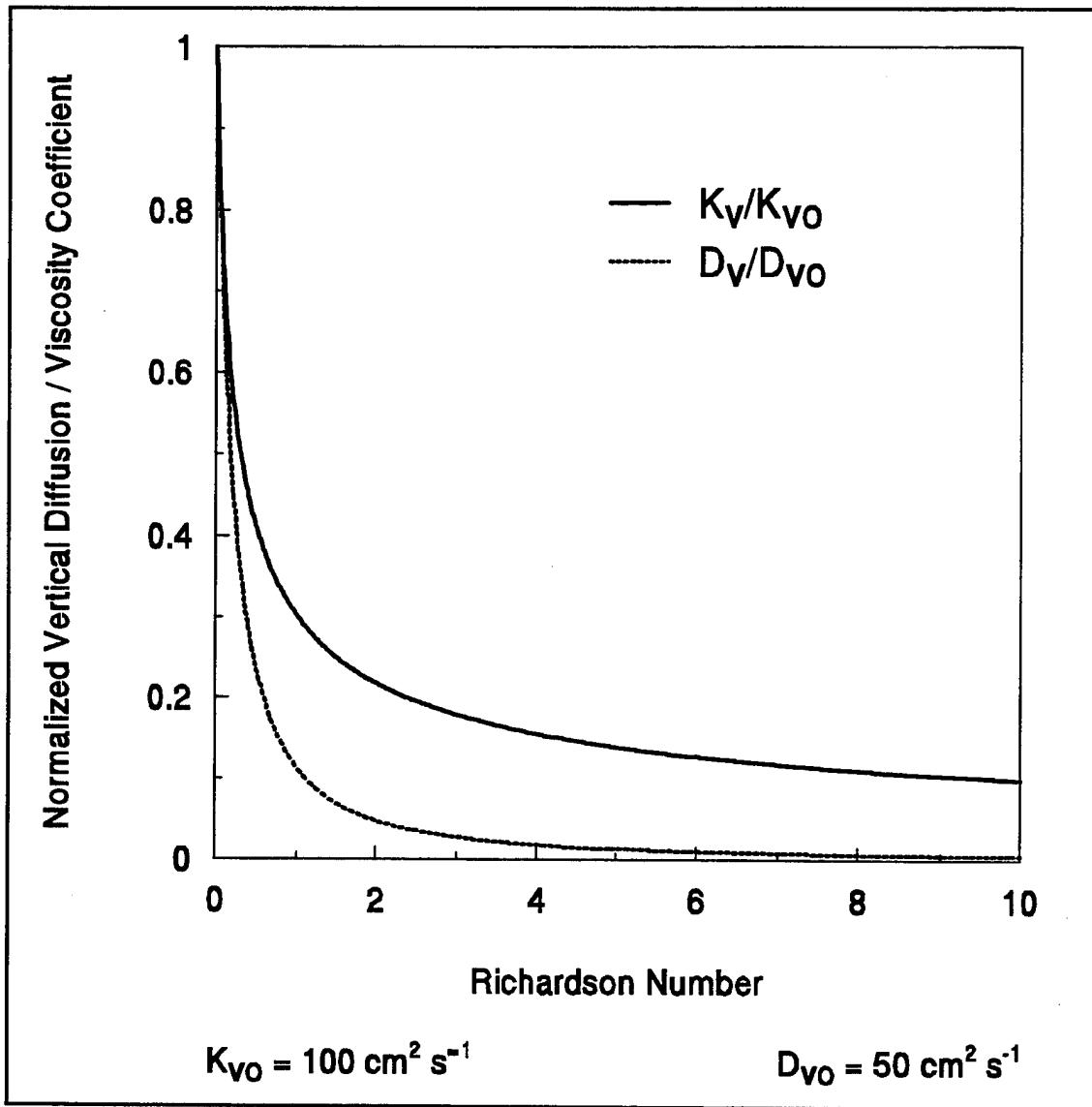
Figure 37. Normalized coefficients of vertical eddy diffusivity and viscosity are plotted with respect to the Richardson number. In regions of strong stability the vertical coefficients are extremely small but increase dramatically for Richardson Numbers less than 1.

points missing in the model grid from the first step. This three step procedure seem to provide acceptable temperature and salinity values for ocean points in such difficult areas as the Canadian Archipelago. Surface layer (10 m) temperatures and salinities from the

107

monthly climatological data fields were treated in the same manner in interpolating to the model grid.

Temperature data at each ocean point were tested for adherence to freezing point minima. The methodology of the construction of the climatological fields of temperature allowed a minimum temperature of -3°C to be recorded in the atlas (Boyer and Levitus, 1994). These temperatures are highly unrealistic given the corresponding salinity provided at the same point. To provide more realistic fields for initialization, these "supercooled" ocean points were reset to the freezing point. Finally all temperatures were converted to potential temperature for use in the model.

E. MODEL FORCING

Surface wind stress, heat flux, and salt flux compose the surface forcing fields available in the Semtner-Chervin GCM. Climatological wind stress data for 1992 from the European Center for Medium Range Weather Forecasting (ECMWF) was provided by Anthony Craig of the National Center for Atmospheric Research (NCAR). The u and v wind stress components are on a 2.5° grid and recorded at 0000Z and 1200Z for each day of the year. Two model forcing data sets were constructed from this data.

To form the two forcing fields, the wind stress data were averaged over an annual period and a three-day period. The averaged fields were interpolated to the model grid using a planar interpolation algorithm. Additionally the axes were rotated and the u and v windstress components were projected onto the model grid so that positive v pointed to the model North Pole and positive u pointed to east relative to the model pole. Figure 38 represents the annual average windstress fields in vector form. The northeasterly winds for 1992 across the Greenland and Norwegian Seas appear representative of long term average annual climatological fields (Trenberth et al., 1988).

In lieu of prescribing the heat and salt fluxes, the near surface layer (10 m) was restored to prescribed temperature and salinity conditions. For the experiments involving annual mean wind forcing, the surface layer was subjected to a 30-day restoring factor to

108
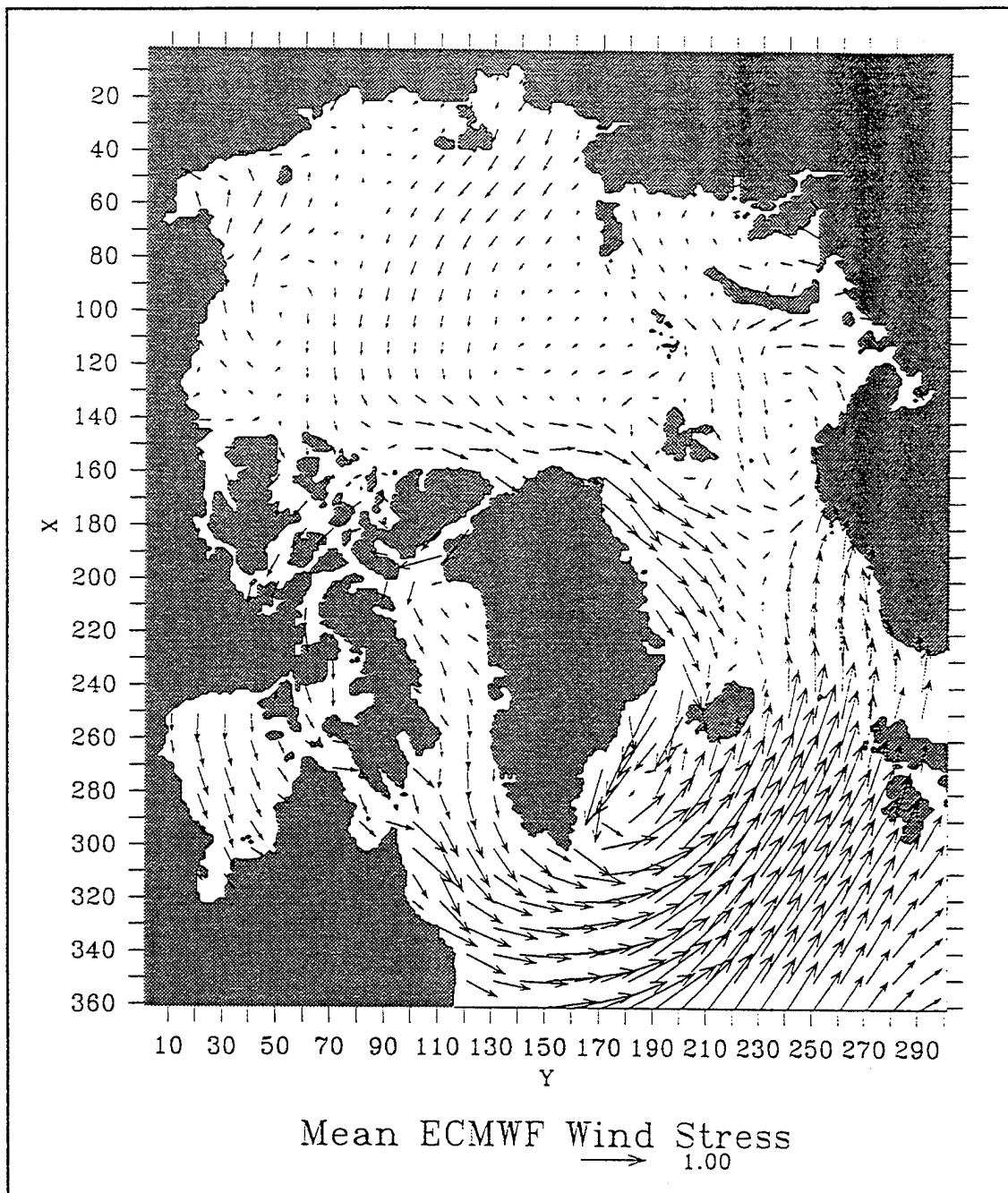
Figure 38. 1992 annual mean wind stress vectors have been interpolated and projected onto the model grid (dynes cm^{-2}). The predominant northeasterly flow across the Greenland and Norwegian Sea is consistent with long term climatological depictions.
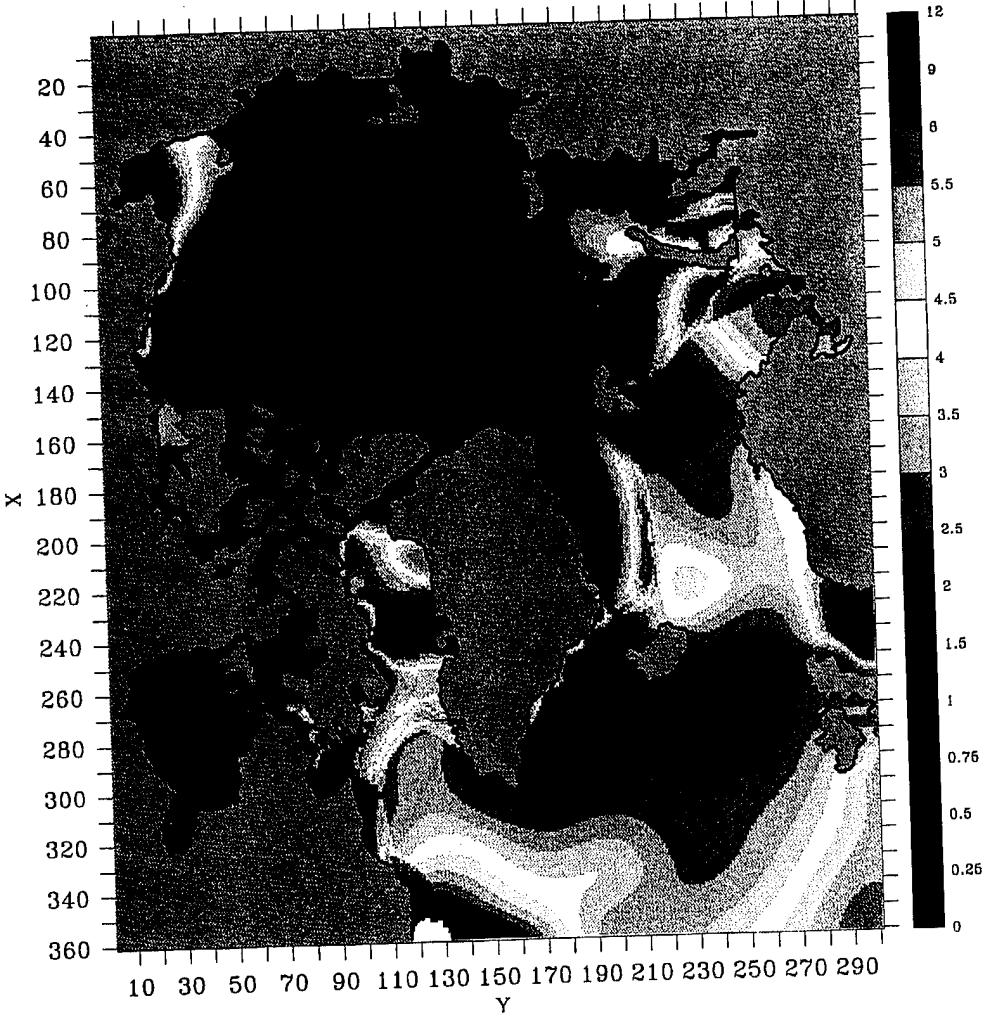
Figure 39a. The variance taken from the 12 monthly mean surface fields of temperature from the Levitus and Boyer (1994) climatological atlas shows the regions of the strongest variable surface forcing in the model. Units are °C².
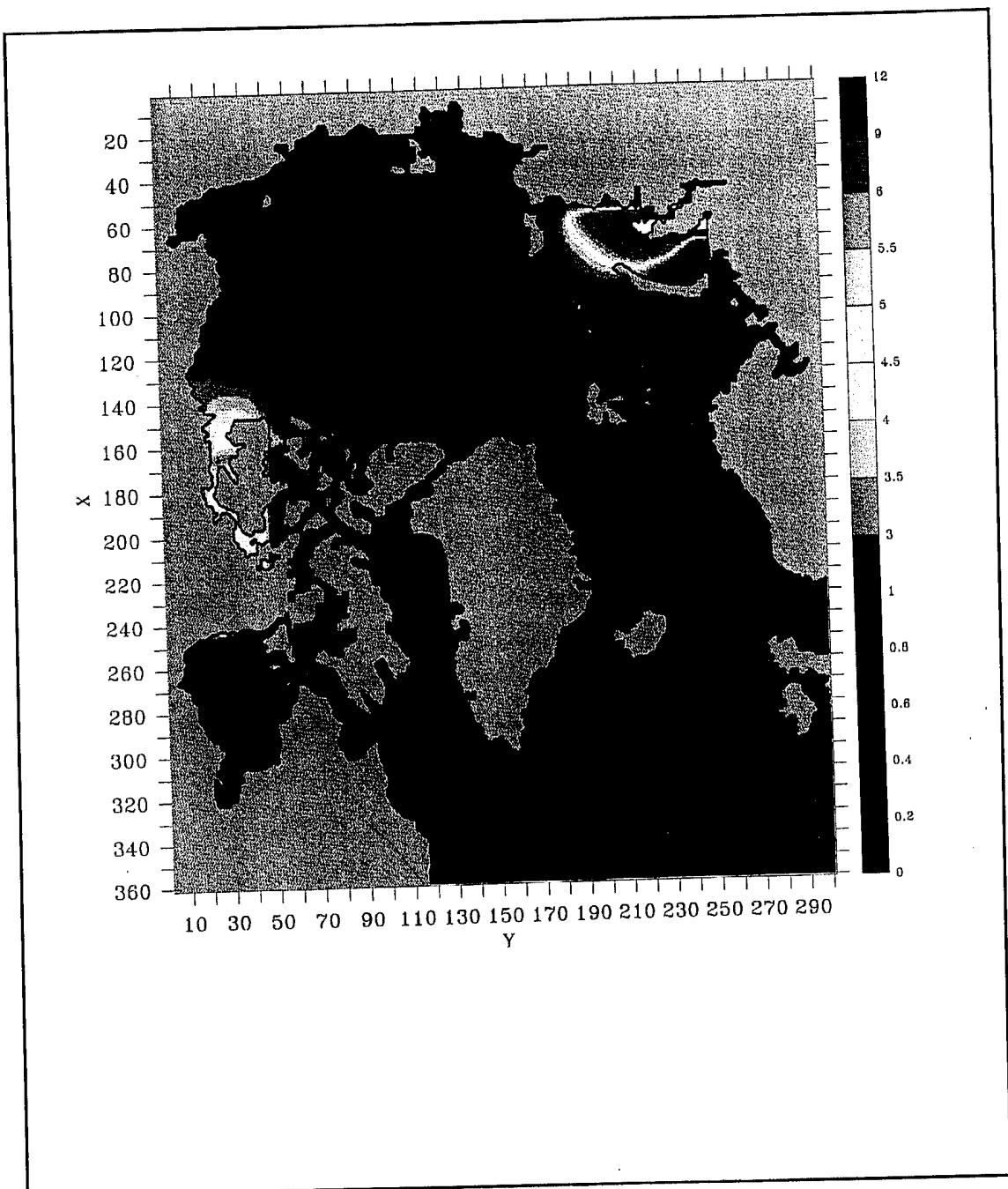
Figure 39b. An analogous variance plot for the monthly fields of salinity shows the importance of river runoff in the Arctic to the changes in surface salinity. Units are psu^2.

111

the annual surface temperature and salinity fields. For the experiment which used the set of 3-daily average wind stress fields, the surface layer was subjected to a 30-day restoring factor to monthly mean temperature and salinity for that particular month. Figures 39a and b represent the variance of the set of the monthly temperature and salinity fields used for the restoring. The regions which show the greatest variance in temperature are the Labrador Sea, the East Greenland Polar Front, and the Bering Strait. The summertime river runoff from the McKenzie, Ob and Lena Rivers provide the largest salinity variance in the model forcing.

VIII. THE MODELED CONDITIONS

Three numerical experiments were conducted to examine the predicted conditions for the Arctic Ocean and Nordic Seas. The first experiment used the annual averages of wind stress, temperature and salinity described in Chapter VII to provide the forcing for the model and was termed the annual forcing experiment. The second experiment used the annual forcing combined with semidiurnal tidal forcing using the M2 tidal solution from Schwiderski (1980) and was termed the tidal forcing experiment. The third experiment used the 3-day average 1992 wind stress fields and Levitus monthly mean temperature and salinity surface restoring for forcing as outlined in Chapter VII but without semidiurnal tides. This last experiment was termed the seasonal forcing experiment. Detailed results from the first experiment are presented and then contrasted with the second and third.

A. ANNUAL FORCING EXPERIMENT

The model was initialized with the interpolated annual mean temperature and salinity fields and the 1992 annual mean ECMWF wind stress was allowed to ramp up over 1 model day. Restoring to mean annual climatological fields of temperature and salinity was set to 30 days only at the surface for the entire model grid but at all model levels for locations within $3°$ of the model boundary in the North Atlantic and North Sea to better simulate the inflow into the interior domain. Biharmonic coefficients for viscosity and diffusion were both set at $-4.0 \cdot 10^{19}$. The Richardson-number-based vertical mixing scheme presented in Chapter 7 was utilized. The quadratic bottom friction coefficient was set to $-4.0 \cdot 10^{-3}$. The internal time step was set at 15 minutes and the external time step was set at 30 seconds. The model achieved a stable equilibrium after ~ 13 months of integration based on the total kinetic energy calculated for the system. The mean energy level is not a constant. A low amplitude, low frequency oscillation persists

113

about the mean which has been described as a vacillation between kinetic and potential energy by Cox (1987) and Böning (1989).

Figures 40, 41, 42, and 43 present the predicted mean fields of near surface (10 m) temperature, salinity, sea surface height, surface velocity for the entire model grid based on the average of fields from every third day from model year 1.5 to 2. The significant oceanographic features of the Arctic and Nordic Seas including the Norwegian Atlantic Current, West Spitsbergen Current, Beaufort Gyre, East Greenland Current and the Barents Sea Polar Front are predicted by the model when compared to Figure 44. However, an analysis spanning the entire domain of the model results, which are proving fruitful in adding to the understanding the Arctic Ocean circulation, is beyond the scope of the present discussion.

1. Temperature and Salinity Predictions within the Barents Sea Region

The signature of the BSPF is clearly evident the mean fields from the annual forcing experiment. Figure 45, a subplot of the Barents Sea from the entire Arctic domain, shows the mean predicted 10 m surface temperature and contours of salinity along with an outline of the experimental area. The horizontal coarseness of the model, however, has made the BSPF frontal signature more diffuse in both temperature and salinity than found in the observations which exemplifies the major weakness of these simulations. The maximum calculated gradients across the entire frontal region for the vertical layer 70 to 100 m were correspondingly less than the observed gradients across the experimental area (0.09 °C km^{-1} and 0.006 psu km^{-1} versus the observed 0.22 °C km^{-1} and 0.02 psu km^{-1}).

Figure 45 also provides evidence concerning the distribution of the primary waters masses within the Barents Sea (Barents Polar Water, Norwegian Atlantic Water and the Norwegian Coastal Water) [Norwegian Coastal Water defined as temperature > 2°C and salinity < 34.7 psu by Loeng, 1991]. Waters of Atlantic origin can be easily traced along a circuitous path, which is attributed to the irregular bathymetry in the Barents Sea,

114
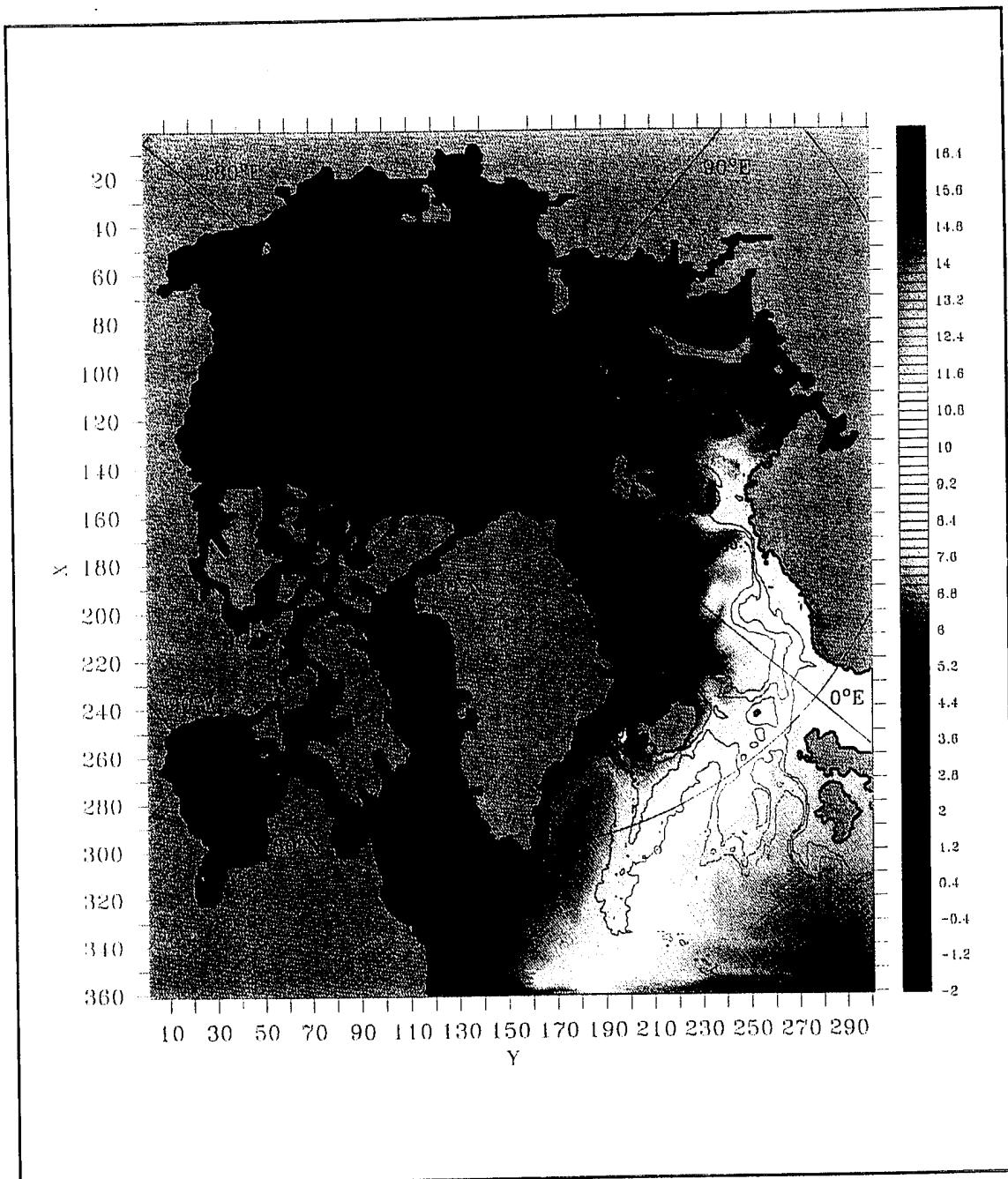
Figure 40. The mean predicted temperature field shows the influx of warm Atlantic water into the Nordic Seas and Arctic Ocean via the Norwegian Atlantic Current and West Spitsbergen Current.

115
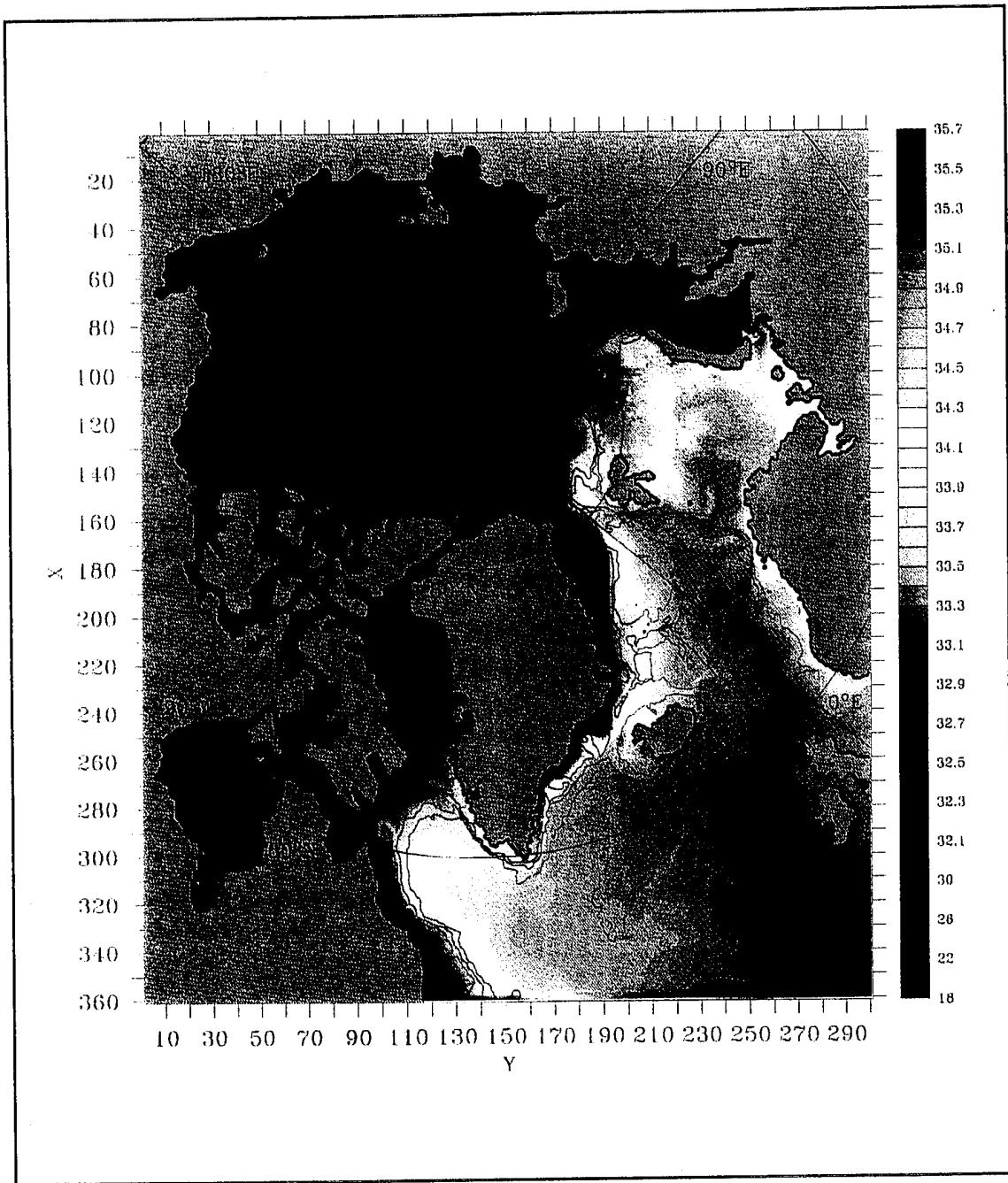
Figure 41. The contour of mean predicted salinty field shows the saline water carried by the Norwegian Atlantic Water north and the relatively fresh water carried by the East Greenland Current south.
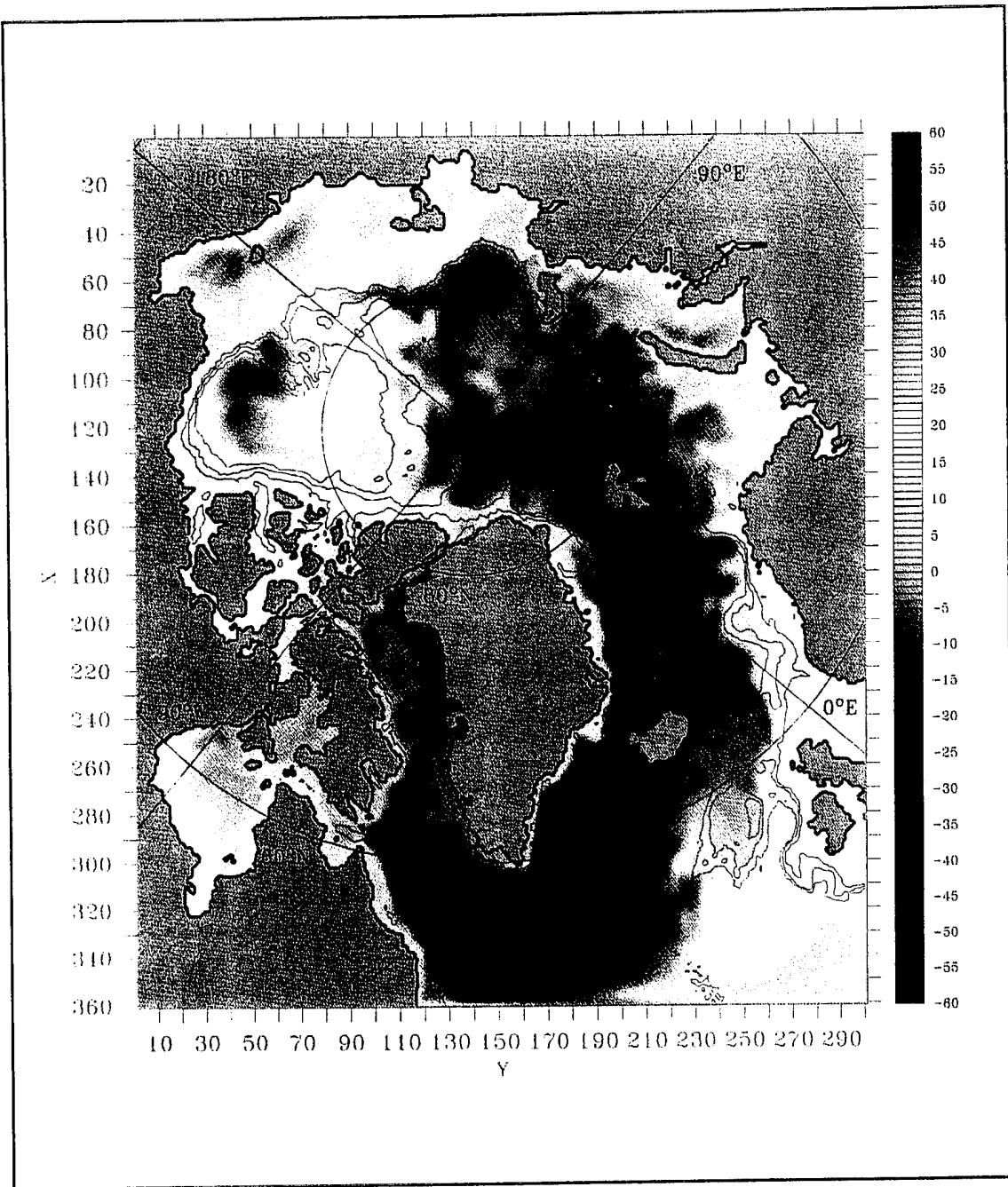
Figure 42. The predicted mean sea surface height field shows the relative low region in the center of the Greenland Sea supporting the cyclonic gyre.

117
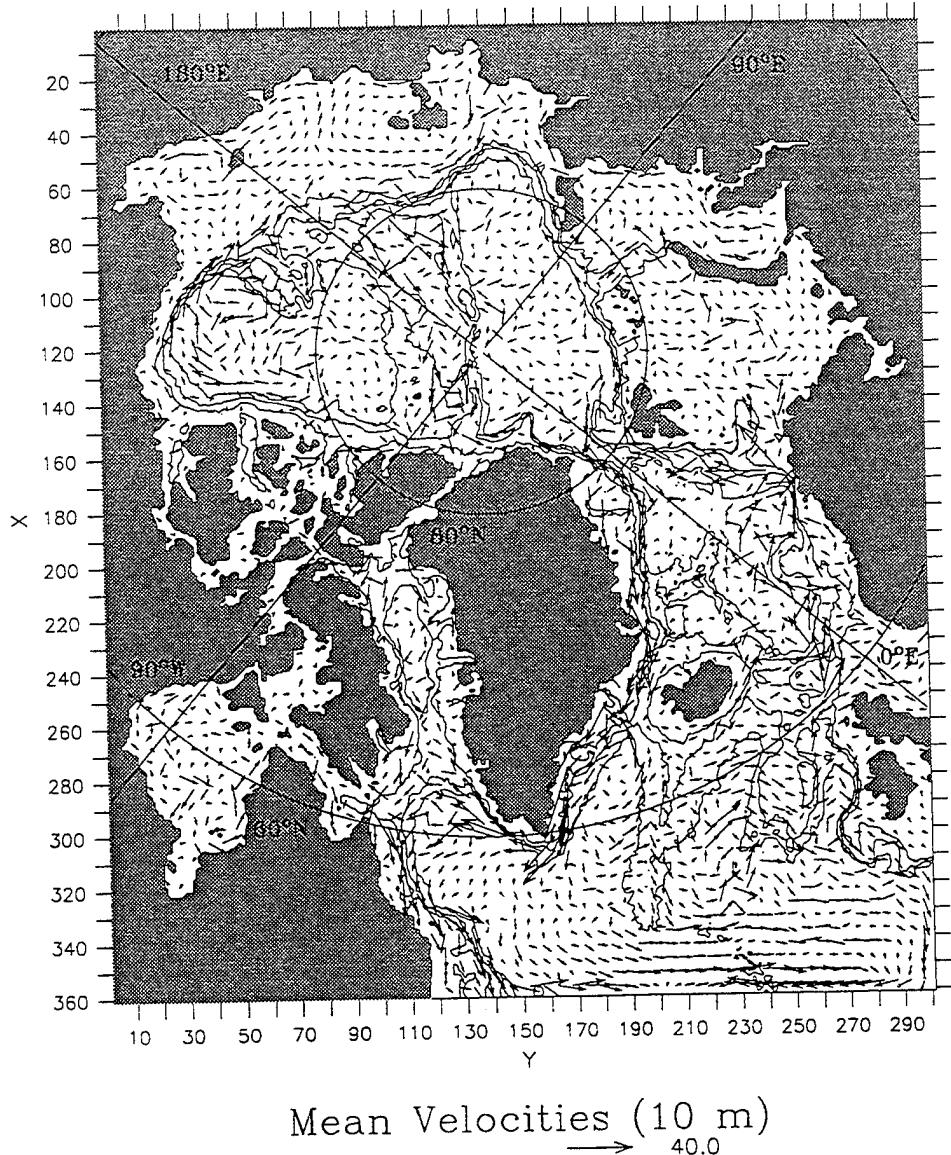
Figure 43. The mean velocity vectors overlaid on contours of bathymetry show the strong tie to bathymetric features of the major currents. Only every 5th vector is displayed. Units are cm s^{-1}.

118
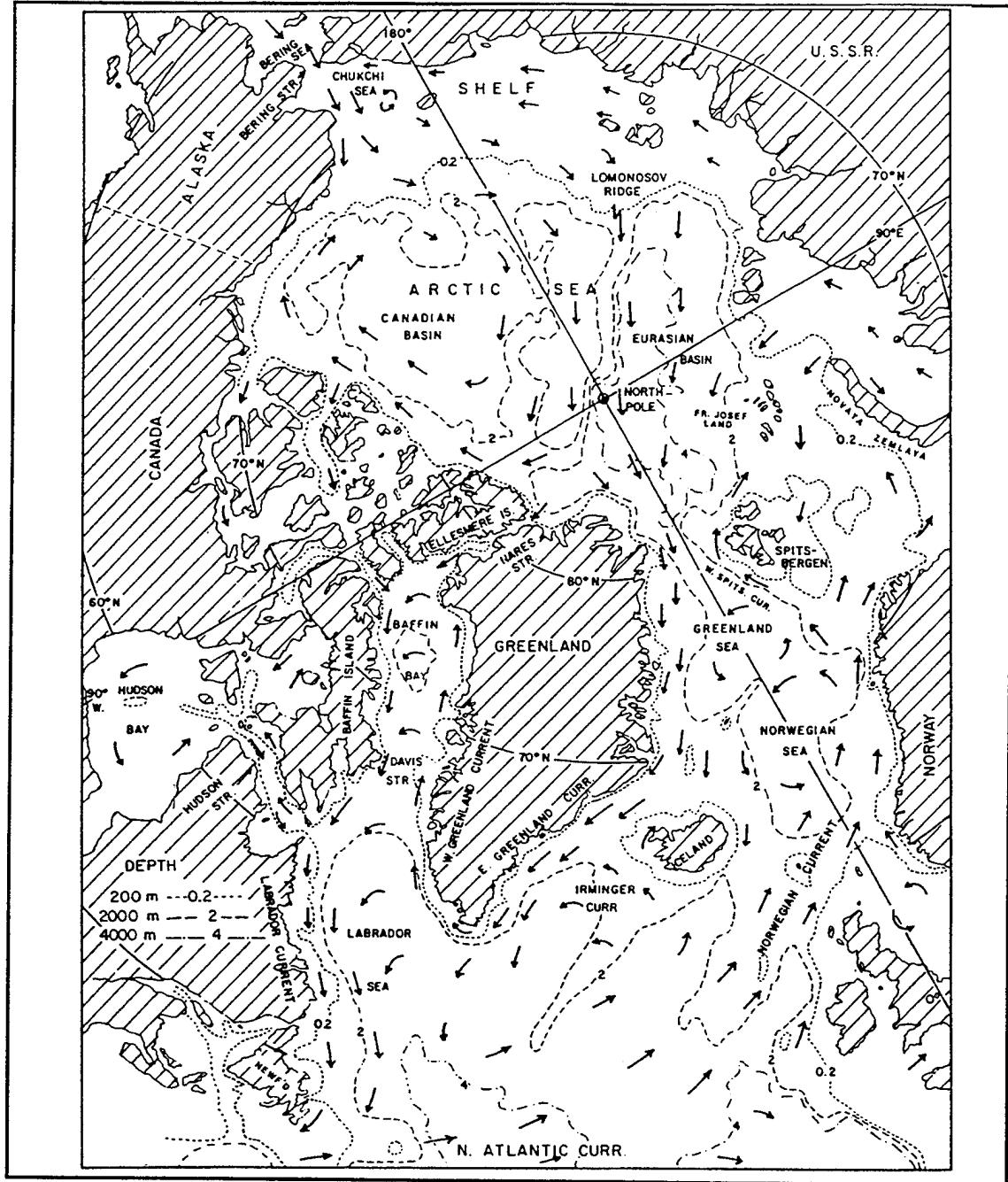
Figure 44. The surface currents of the Arctic Ocean and North Atlantic, depicted in this figure from Picard and Emery (1982), agrees sensibly with Figure 43.
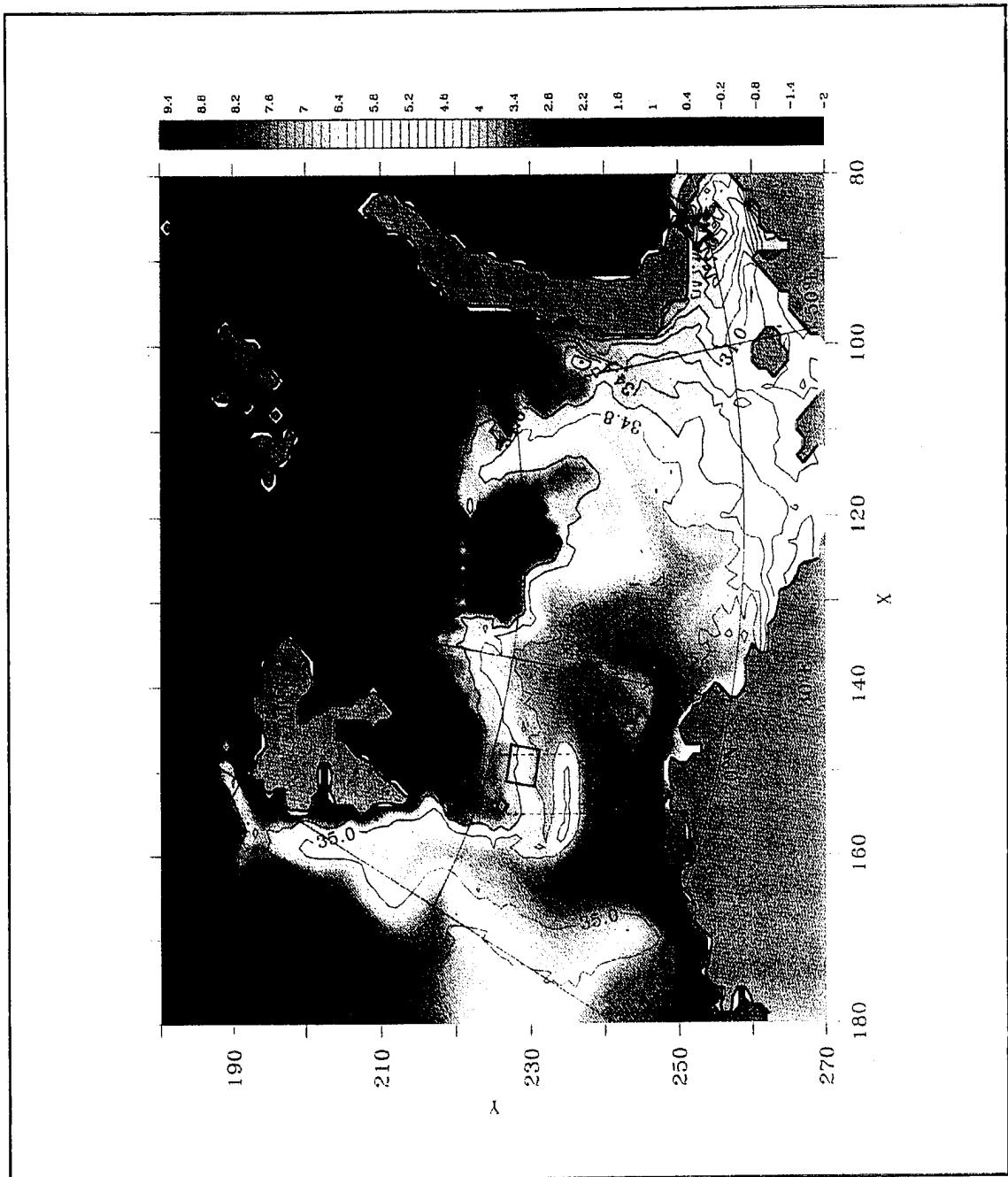
Figure 45. Shaded plot of model predicted surface temperture is overlayed with contours of salinity to shows the confluence of two principal water mass in the Barents Sea [Norwegian Atlantic Water and Barent Polar Water] and the distribution of Norwegian Coastal Water.

moving to the east and into the Kara Sea. This simulated distribution supports the proposed Barents Sea Branch of circulation into the Arctic Ocean described by Rudels et al. (1994) and as seen in Figure 3. The low salinity core of Norwegian Coastal Water can be traced as far eastward as the Kola Peninsula in the figure. Additionally, the coldest surface temperatures are seen between Franz Josef Land and Novaya Zemlya supporting the description by Loeng (1991) as that passage being the principal inflow source of PW into the Barents Sea.

A time mean cross section over the virtually the same Bear Island cross section as seen in Figure 2 from Nansen (1902) is presented in Figure 46. The isopleths which define the thermohaline structure within the Bear Island Trough are different than the summertime section shown by Nansen. The warm and saline NAW in the center of the trough described by Nansen is replaced in the model simulations by a narrow cool fresh core extending from the bottom of the trough upward to a narrow surface expression. The appearance of this anomalous surface expression is attributed to a combination of annual mean surface temperature restoring and the mean circulation pattern described in the next section. This cross section also identifies the cooler and fresher surface Norwegian Coastal Current immediately adjacent to the coast and the very warm and saline core of Atlantic Water entering at depth on the southern side of the trough in the model simulations.

A section across the BSPF of density (σ_t) calculated from model predictions corresponding to points within the experimental area is presented in Figure 47. The model simulations have replicated the barotropic nature of the temperature and salinity structure on the northern side of the front seen in the observations. However, the density difference across the front in the vicinity of the experimental area at the 70-100 m level, while still small, was typically 0.25 kg m^{-3} which was roughly twice the median observed value at the same depth. This enhanced density difference is also thought to being an artifact of the climatological surface restoring in the middle of the trough.
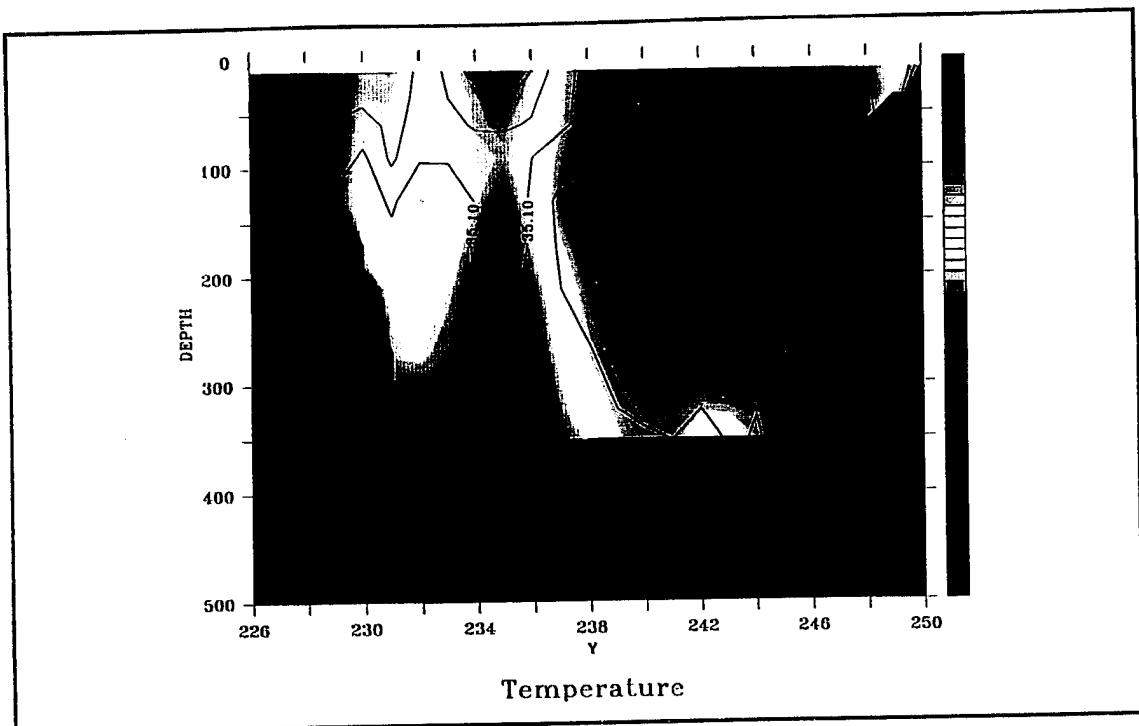
Figure 46. A North Cape to Bear Island cross-section of temperature (shaded) and salinity (contours) shows cool salty water at the trough bottom and a cool core in the central part of the trough in contrast to Nansen's historical depiction in Figure 2.
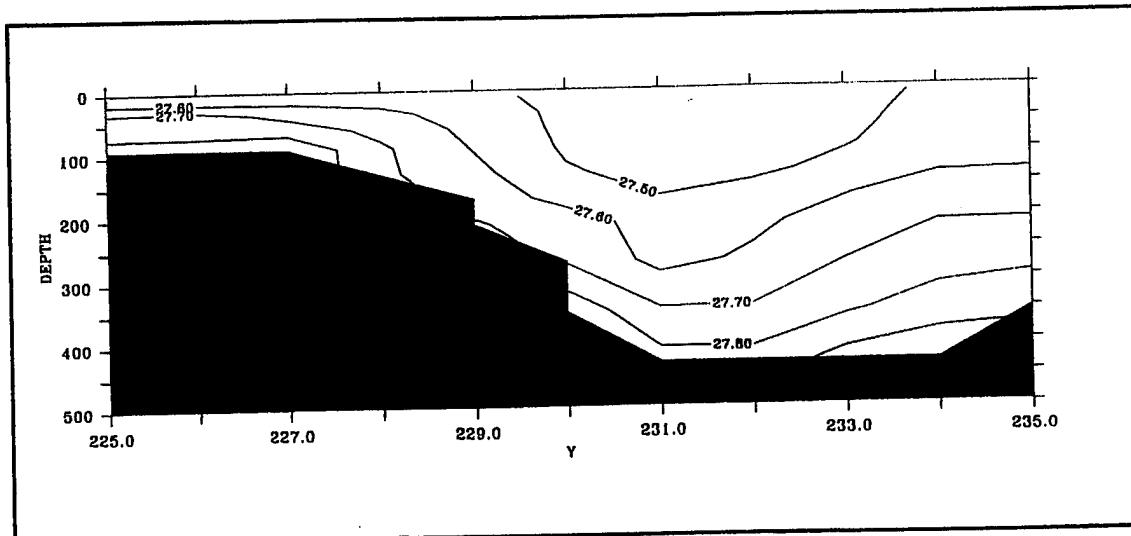
Figure 47. Cross-section of density (σ_t) taken along from the model grid points in the eastern portion of the experimental reflect that the model accurately simulates the barotropic nature of the front below the surface layer.

122

Contours of the dynamic height relative to 100 dbar with the corresponding surface geostrophic velocity vectors calculated from model predictions are presented in Figure 48. The overall gradient of dynamic height is small throughout the Barents Sea with associated geostrophic velocities generally less than 5 cm s^{-1}. Most features are associated with the topography where enhanced mixing over the shallow banks creates the density gradients with the more stratified waters in the troughs and depressions. The shallow 10 cm s^{-1} southwestward geostrophic flow found along the front in the observations is replaced in this simulation by a very weak northwestward flow. The cause of net reversal of the baroclinic surface jet along the front in model predictions is likewise the result of coarsely resolved climatological surface restoring which has the effect of adding buoyancy south of the front and subtracting it north of the front when contrasted to the observed conditions. However, the significantly stronger simulated total velocity provides a more complete picture of the circulation the Barents Sea.

2. Simulated Circulation within the Barents Sea Region

The mean surface current vectors for the Barents Sea region, shown in Figure 49, reveal one of the principal findings in these simulations -- a recirculation pattern of Norwegian Atlantic Water in the trough. Note that the core of this flow is parallel to the isobaths and strongly correlated to bathymetry within the trough. However, before examining the details of this circulation pattern, volume transports from model-predicted mean currents are calculated for the sections highlighted by dark lines in the Figure (labeled 1 through 6) and provided in Table 10.

Calculations through section 1 estimate a substantial 10 Sv of poleward volume transport which is comprised of Atlantic Water, recirculated Greenland Sea Gyre Water as well as NCW. For comparison, Worthington (1970) estimates a total of 8 Sv of Atlantic Water enters the Norwegian Sea between Iceland and Scotland. Through section 2 spanning the West Spitsbergen Current, the derived poleward volume transport
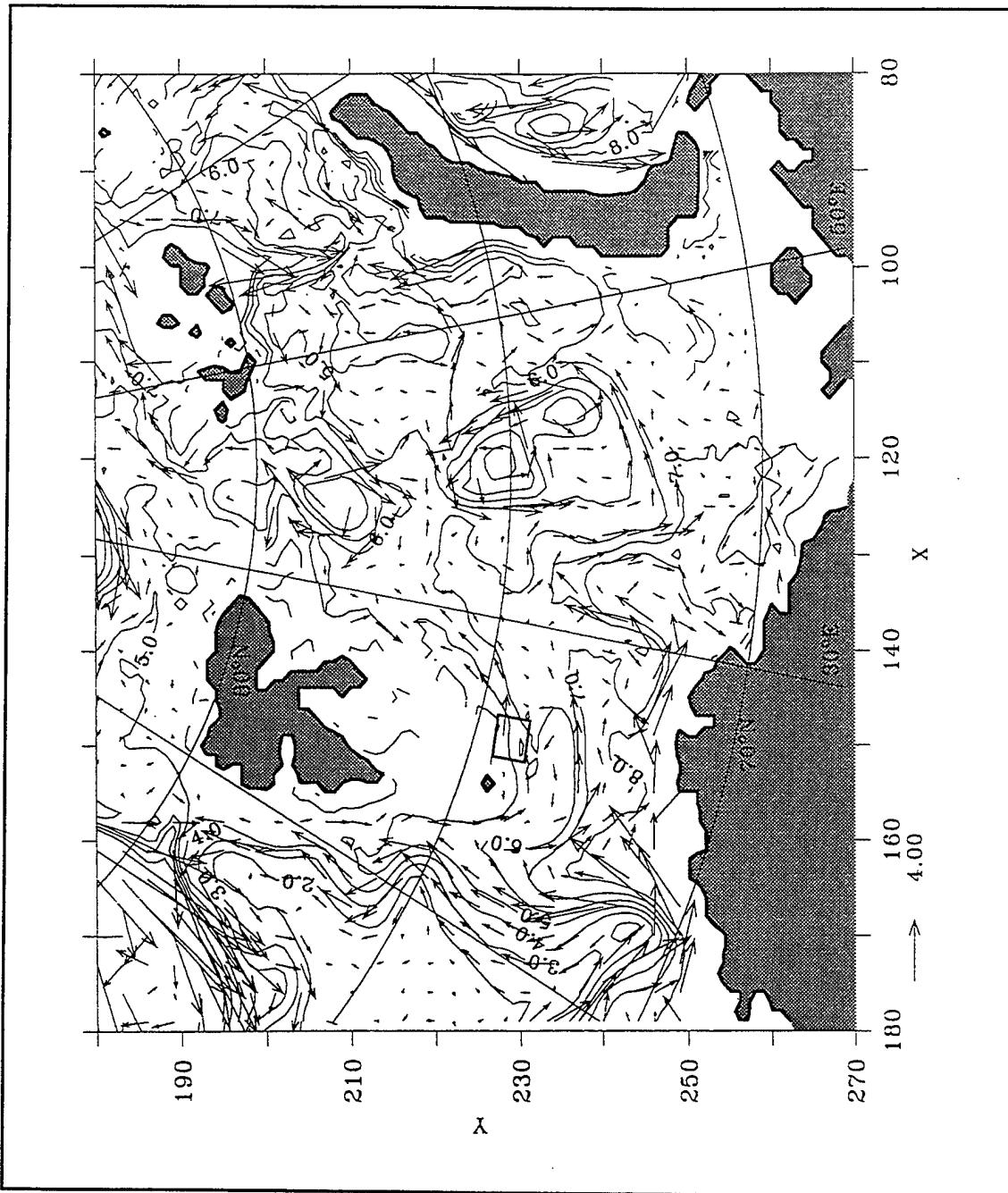
Figure 48. Contours of Dynamic Height and the corresponding geostrophic velocity vectors simulate the mean circulation pattern as presented in Figure 1. Units are cm s^{-1}.
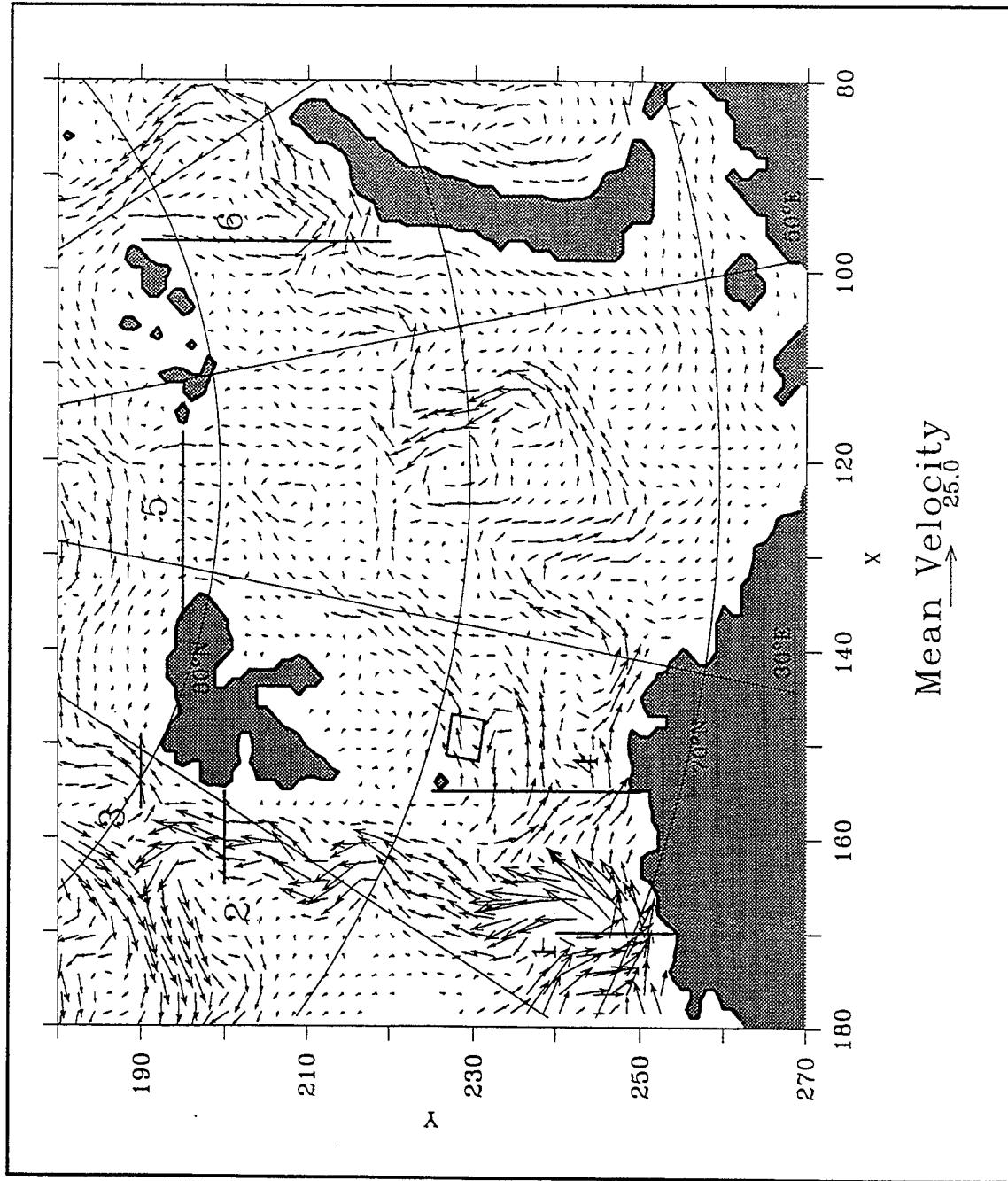
Figure 49. Mean surface current vectors depict a recirculation pattern of water entering the Bear Island Trough from the Norwegian Sea. Units are cm s⁻¹.

125

is ~ 7 Sv for this section which is south of the westward turning branch of the WSC. This value is nearly equivalent to that reported by Aagaard and Greisman (1975) which is the maximum estimate in a summary of transports reported by Rudels (1987). Rudels reported some estimates as low as 1.4 Sv. However, from calculations through section 3, only 3.6 Sv are estimated to actually enter the Arctic Ocean.

Source	Section Number	Volume Transport of Atlantic Water	
Norwegian Atlantic Current	1	10.0 Sv	
West Spitsbergen Current (before the westward turning branch)	2	6.6 Sv	
West Spitsbergen Current (80 N) (north of westward turning branch)	3	3.6 Sv	
		Volume Transport into the Barents Sea	Volume Transport out of the Barents Sea
Bear Island to North Cape	4	4.4 Sv	1.1 Sv
Spitsbergen to Franz-Josef Land	5	0.6 Sv	1.3 Sv
Franz-Josef Land to Novaya Zemlya	6	0.9 Sv	3.0 Sv

Table 10. Calculated volume transport for selected sections from the annual mean forcing experiment.

The net volume transport through section 4 which results from the difference between the inflow of the North Cape Current and Norwegian Coastal Current and the outflow of recirculated water, reveals ~3.3 Sv entering the Barents Sea which is generally 1 Sv higher than observed estimates (Loeng et al., 1993; Blindheim, 1989). From section 6, the net transport of 2.1 Sv through the Barents Sea into the Arctic Ocean via the Kara Sea compares very favorably with that reported by Loeng et al. (1993) and also Rudels (1987). This net transport reflects the difference between modified waters leaving the Barents Sea through the Barents Sea Branch (Rudels et al., 1994) and inflow of Polar Water via the Persey Current. To compensate the mass balance for this net throughput

difference between section 1 and 2, section 5 derived transports indicate a net of ~0.7 Sv is predicted to pass from the Barents Sea into the Central Arctic. This transport is the net flux considering the effects of the outflow of modified NAW and the inflow of Polar Water via the East Spitsbergen Current and NAW entering from the north which was carried around the north of Svalbard by the West Spitsbergen Current (Pfirman et al., 1994). This leaves an additional 0.5 Sv to leave the Barents Sea south of Novaya Zemlya towards the Kara Sea.

To return specifically to the examination of the flow of NAW within the trough, contours of potential vorticity are plotted for the region with an overlay of the depth-averaged velocity vectors (Figure 50). The potential vorticity theorem is provided in equation (8.1). This relation is derived from the horizontal momentum equations and fundamentally means that for an inviscid, horizontally homogenous fluid, a column of water will act to conserve the ratio of its absolute vorticity to the depth of the column. Here Π refers to the constant, f refers to planetary vorticity, $\left(\frac{\partial v}{\partial x} - \frac{\partial u}{\partial y}\right)$ is the vertical component of relative vorticity and H is the depth of the water column.

$$\Pi = \frac{f + \left(\frac{\partial v}{\partial x} - \frac{\partial u}{\partial y}\right)}{H} \qquad (8.1)$$

In an idealized model process study, Gawarkiewicz and Plueddemann (1995), as discussed in Chapter V, propose that the recirculation of NAW within Bear Island Trough is a response to this fundamental fluid dynamics theorem. As seen in Figure 50, this simulation not only supports their hypothesis, but provides the realistic flows into the region which achieve a magnitude of the recirculation similar to that observed (~ 10 cm s^{-1}).

Also apparent, just north of the recirculation within the trough in Figure 50, is a flow observed originating to west of Bear Island and directed to the east and northeast along lines of potential vorticity. Alone, the existence of this flow would be supportive of
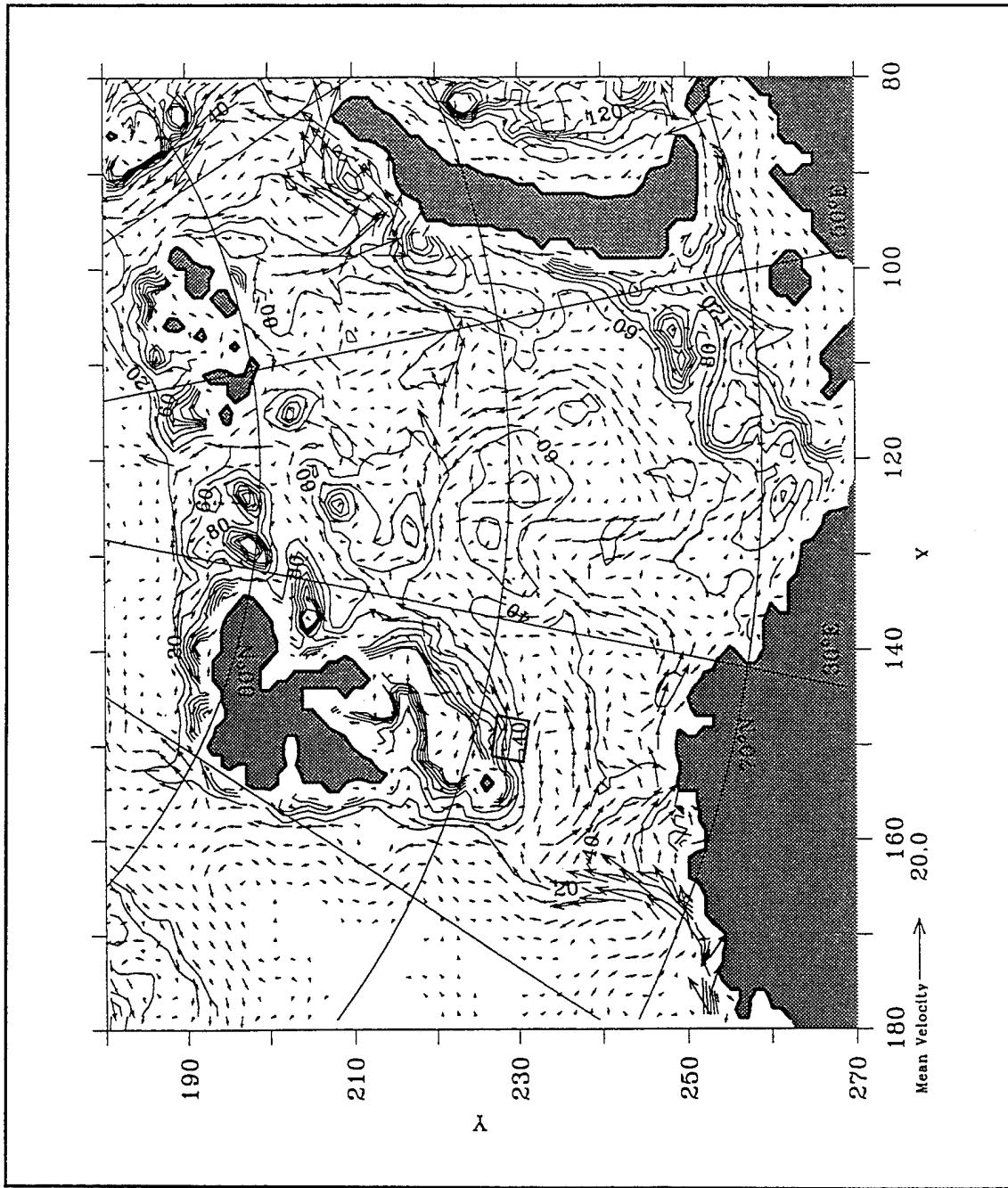
Figure 50. Calculated contours of potential vorticity are plotted with the vertically averaged mean velocity vectors shows the strong tendency of the flow to conserve this quantity within Bear Island Trough. Potential vorticity units are $(1 * 10^{-8})$ m^{-1} s^{-1}; velocity units are cm s^{-1}.
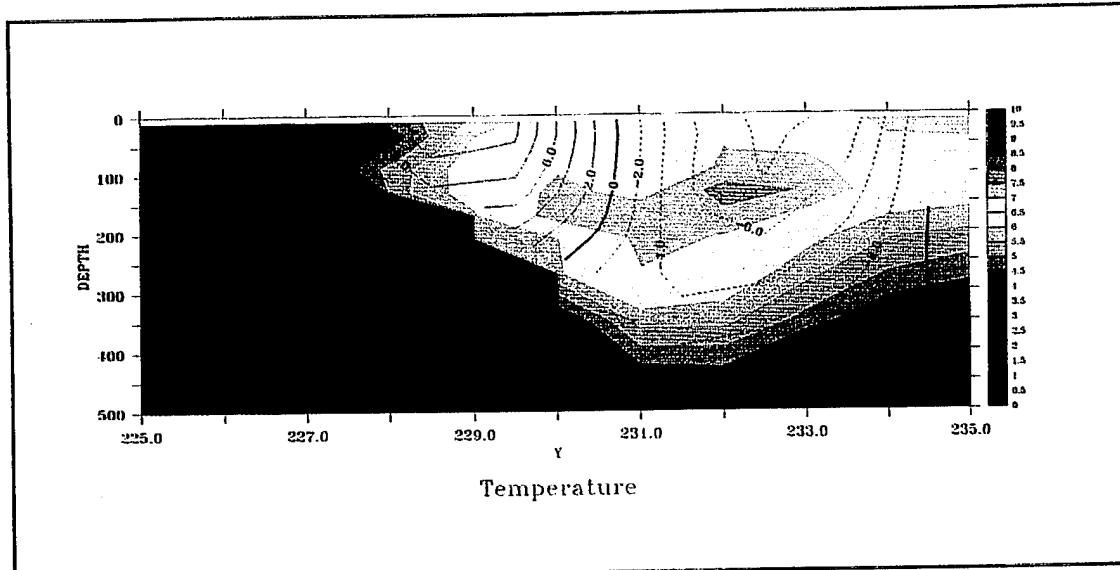
Figure 51. Contours of a vertical cross section of the alongslope velocity (cm s⁻¹) in a section from the eastern portion of the experimental area shows the recirculation (dashed lines) to be nearly vertically homogenous and along the 300 m isobath. The predicted temperature (°C) for the same section is shaded.

Loeng's (1991) description of the circulation adjacent to the front. Figure 51 is a cross-section of the velocity field overlaid on the temperature along the same section as Figure 47. This narrow eastward flow is confined between the 100 m and 250 m isobaths and associated with the frontal signature. The position of the westward flow along the trough is found deeper than the 300 m isobath. The relative vertical homogeneity of the NAW recirculation is also observed. The core of the northeastward flow appears to be advecting cooler (not BPW) frontal water to the east while the recirculation is centered over the core of the recirculating NAW. This trend is also supported in terms of salinity advection. Unfortunately the position of the northeastward flow relative to the position of the current meters in Figure 8 prevents observational verification. However, it must be noted that the detided ADCP data in Figure 14 do indicate an eastward component at these depths. The 300 m isobath defining the upslope extent of the southwestward recirculation is consistent with the reasoning offered by Gawarkiewicz and Plueddemann (1995) that the barotropic flow along the northern side of the trough should correspond to the isobath that also defines the sill depth at the eastern head of the trough (i.e., 300 m).

The concept of two opposing flows on the slope, both advecting waters of primarily NAW origin, appears unique to this simulation. However, the existence of the northeastward flow along the slope is consistent with other modeling studies and proposed schematics of the circulation. The increased horizontal resolution, compared to previous simulations, and the refined bathymetry contained within this simulation are believed responsible for resolving the recirculation pattern within the trough.

The relatively cool surface waters cited in Figure 46 in the center of Bear Island Trough can now be seen in light of this circulation pattern. In the simulations, NAW loops around the trough without a broad influx of warm surface waters into the center. In the absence of advection, modifications to waters in the center of the trough must occur through diffusion or surface heat fluxes. The narrow band of cooler water in the center of the trough likely represents a balance between diffusion and surface restoring to the cooler annual mean surface temperatures.

Finally, to examine the release of mean kinetic energy to eddy production within the Barents Sea, surface eddy kinetic energy is calculated for the region and presented in Figure 52. The horizontal eddy kinetic energy is given by:

$$EKE = \frac{1}{2}\overline{[(u'^2) + (v'^2)]} \tag{8.2}$$

where $u' = u - \bar{u}$ and $v' = v - \bar{v}$. The plot shows areas of higher EKE near the entrance to Bear Island Trough and along the southern slope of the trough which are also associated with regions of abrupt bathymetry features. The area in the vicinity of the eastern portion of the experimental area has a relatively low EKE, particularly in the shallower waters on Svalvard Bank. These relatively low values support the conclusions in the observations of a predominately stable barotropic flow dominating the currents. Other regions of higher EKE in the Barents can be seen near St. Anna Trough and along the coastal flow where the baroclinic balance dominates the flow.

Observations presented in Chapter III indicated that 50~90 percent of the measured current variance (equivalent to mean kinetic energy percentages) were of tidal
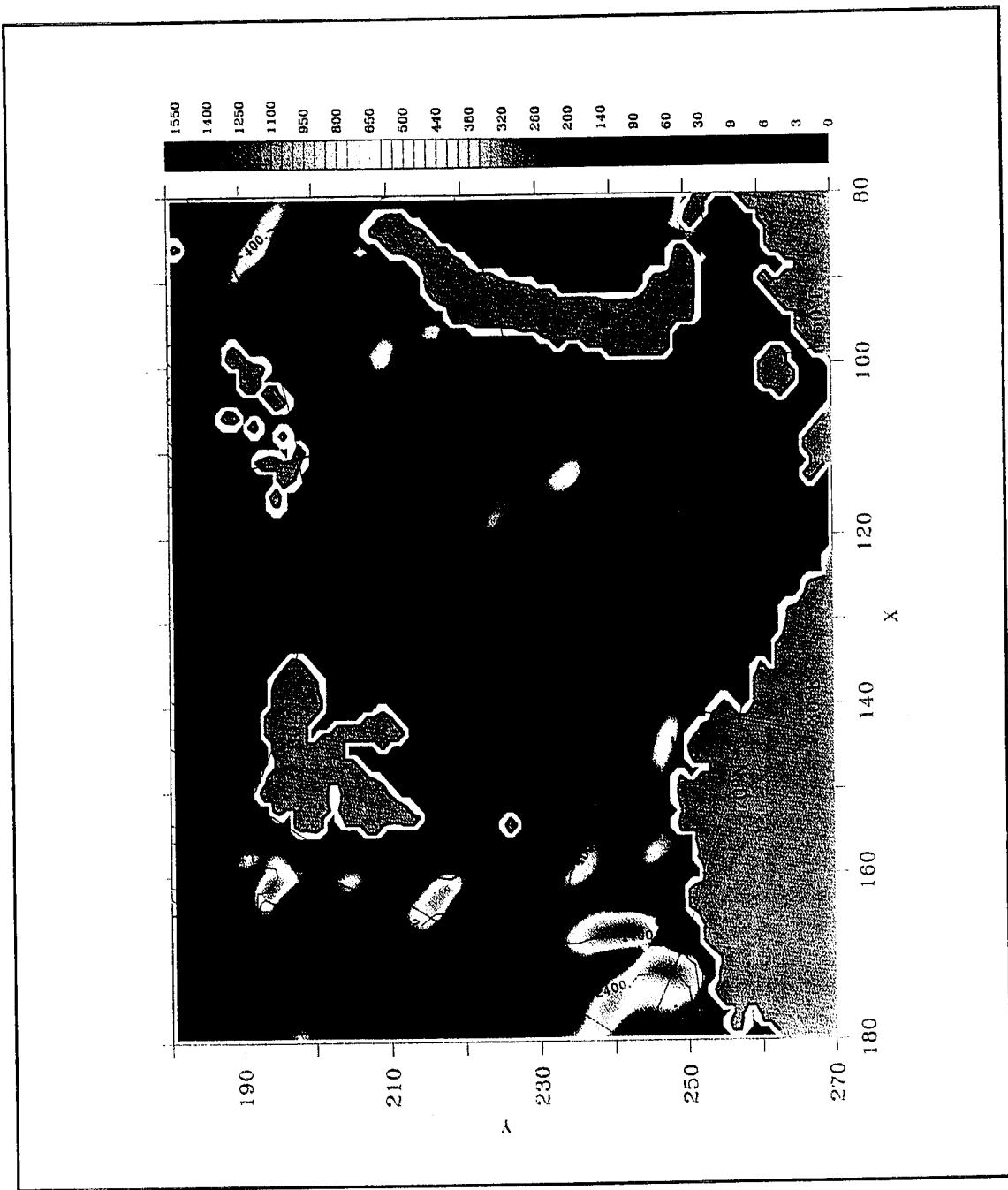
Figure 52. Contours of the near surface (0-50 m) eddy kinetic energy EKE (cm^2 sec^{-2}) for the Barents Sea indicate strong regions of EKE production on the southern part of Bear Island Trough, just east of Central Bank, and in the St. Anna Trough.

131

origin. Of the variance induced by the tides, semidiurnal frequencies accounted for 90-95 % of the tidal total percentage. The next section will repeat the above experiment with inclusion of semidiurnal tidal forcing to examine its effect on the BSPF and the regional oceanography.

B. TIDAL FORCING EXPERIMENT

From an examination of the literature, the following experiment is very probably the first large area regional 3D GCM to include tidal forcing along with the wind-driven and thermohaline circulation. To achieve a direct comparison to the annual mean forcing experiment, all constant friction coefficients, time steps, restoring and wind forcing were identical to those described in the previous section. The only differences between the experiments were the modifications made to the barotropic calculations to include the tides.

1. Modifications to the Model for Tidal Forcing

The modifications to the Bryan-Cox-Semtner primitive equation model to permit a free surface, described in Killworth et al. (1989) and Killworth et al.(1991), also outline changes necessary to allow tidal forcing within the barotropic calculations. Previous predictions of the sea surface height made by the non-tidal version of the present model and also in Semtner (1995) used a backward Euler numerical scheme (Mesinger and Arakawa, 1976) which was shown by Killworth et al. (1989) to damp the non-geostrophic barotropic motions. To permit tidal forcing, the numerical scheme is changed here to a backward-forward Euler scheme. However, the higher frequency, non-geostrophic motion (tidal motion) allowed by such a scheme appears as white noise when coupled to the baroclinic calculations. To achieve model stability, shorter external and internal time steps than would normally be used for a non-tidal model are required. The annual forcing

132

experiment proved stable when time steps up to 40 minutes for the internal mode and 40 seconds for the external mode were used. The shorter time steps of 15 minutes and 30 seconds, respectively, used in the previous experiment were based upon tidal model stability.

To incorporate tidal forcing, the barotropic momentum equations (6.13 and 6.14) are changed as follows:

$$\frac{\partial U}{\partial t} - fV = -\frac{1}{a\cos\phi}gH\frac{\partial}{\partial\lambda}(\alpha\eta - \beta\eta_{tide}) + \nabla_H^4 U + X \tag{8.3}$$

$$\frac{\partial V}{\partial t} + fU = -\frac{1}{a}gH\frac{\partial}{\partial\phi}(\alpha\eta - \beta\eta_{tide}) + \nabla_H^4 V + Y \tag{8.4}$$

All variables are as defined in Chapter VI with the exception of α, β and η_{tide}. The α and β terms reflect the corrections due to the effect of ocean loading and earth tide respectively. They are given by Schwiderski (1981) as $\alpha=0.69$ and $\beta=0.90$. The η_{tide} term can be included in one of two forms in the model. The most common form in large area or global 2D tidal models to express η_{tide} as the equilibrium tide (or when $g \cdot \eta_{tide}$, it is termed the astronomical tidal generating potential) at each grid point. This type of forcing is known as body forcing. Following Newton's (1676) solution and as expressed by Schwiderski (1980), the semidiurnal equilibrium tide is given by:

$$\eta_{tide} = K\cos^2\phi\cos(\sigma t + 2\lambda + \chi) \tag{8.5}$$

where K is the amplitude of the equilibrium tide, ϕ is the latitude, λ is the longitude, σ is the frequency of the equilibrium tide, and χ is the astronomical argument of the equilibrium tide. Table 11 gives the values for these constants for the M2 principal lunar semidiurnal tide.

The second form of the forcing can use a predetermined solution from another tidal model or observation for the amplitude and phase at specific latitude and longitude

points to force the tides at the boundary (or interior point) of the model. This form of the tidal solution is given as:

$$\eta_{tide} = \xi(\phi, \lambda)\cos(\sigma t + \chi - \delta(\phi, \lambda)) \qquad (8.6)$$

where $\zeta(\phi,\lambda)$ is the tidal amplitude and $\delta(\phi,\lambda)$ is the Greenwich phase in radians.

Variable	Value	Expansion	Expression
K	24.2334 cm		
σ	$1.40516 \cdot 10^{-4}$ s^{-1}		
χ	$2h_o - 2s_o$		
		h_o = mean longitude of the sun at Greenwich midnight	$279.69668 + 36000.768930485 \cdot T + 3.03 \cdot 10^{-4} \cdot T^2$
		s_o = mean longitude of the moon at Greenwich midnight	$270.434358 + 481267.88314137 \cdot T - 0.0011334 \cdot T^2 + 1.9 \cdot 10^{-6} \cdot T^3$
		T	$[27392.500528 + 1.0000000356 \cdot D] / 36525$
		D	$d + 365(y\text{-}1975) + Int[(y\text{-}1975)/4]$
		d	d= day number of year
		y	$y \geq 1975$ = year number
		Int	Int[x] = integral part of x

Table 11. M2 Tidal Constants for astronomical forcing (from Schwiderski, 1980).

Using a mathematical-emperical global ocean tide model, Schwiderski (1979) has determined these values on a 1° global resolution for the M2 tide (as well as essentially all the other major tidal constituents). The values of amplitude and Greenwich phase at 1° resolution were interpolated to the model grid using a local planar interpolation algorithm.

To test the various forms of forcing (body forcing, boundary forcing, or combination) on the time step and model friction parameters, a horizontally homogeneous but vertically stratified profile of temperature and salinity was initialized throughout the

134

model domain. All other forcing was set to zero and the model was integrated with the tidal forcing for 180 days to obtain a stable tidal solution. The stability of the solution was determined using a method suggested by Proshutinsky (personal communication, 1995) by monitoring the change in model total kinetic energy which has been averaged over a tidal cycle. The energy level generally appeared to be stable after ~ 130 days. Validation of the accuracy of the solution (M2 amplitude and phase over the predicted domain) for the first order effects of the semidiurnal tides sought in this experiment was achieved primarily through comparisons to the M2 solution of Kowalik and Proshutinsky, (1994) (see Figures 6a and 6b). Kowalik and Proshutinsky (1994) describe extensive observational comparison and validation to their solution.

The use of body forcing alone at each grid point in the model generated a solution which appeared correct in phase but was too low in amplitude. Proshutinsky (personal communication, 1995) confirmed the conclusions of Gjevik et al. (1994), that to achieve the proper resonance and propagation of the M2 tide into the Arctic Ocean, forcing of the solution from the North Atlantic boundary is not only necessary and but is also generally sufficient. Experiments were made with various forms of including the Schwiderski solution on the boundary and the inclusion of the body forcing in addition to it. Since the North Atlantic boundary of the model is closed, it was found to be necessary to expand the region of boundary forcing to be within several degrees of the boundary to achieve proper propagation of the tides into the Arctic Ocean and Nordic Seas. The final solution for these experiments contained the Schwiderski solution within 8° of the closed North Atlantic boundary, no body forcing, with time step and friction parameters as follows: time step: 15 min internal and 30 s external; biharmonic horizontal viscosity and diffusion: $K_h=D_h=-4 \cdot 10^{19}$; bottom friction: $C_d=2.65 \cdot 10^{-3}$. Note that these are the parameters used for the experiment described in Section A and those utilized in this experiment with one exception. Previous tests of the model without tidal forcing examined surface stress, bottom stress and stability in such high flow areas as the Denmark Strait and led to the use of $4.0 \cdot 10^{-3}$ as the value for the bottom friction drag

coefficient. Use of this coefficient in tidal experiments typically reduced the tidal amplitude ~ 4 cm over much of the predicted tidal domain as compared to the use of $2.65 \cdot 10^{-3}$. Also, the values for the biharmonic coefficients used in the tidal forcing experiment, and therefore the annual forcing experiment, are higher that the typical values cited by Böning and Budich (1992) in the previous chapter but were found necessary for stability in the tidal forcing experiment.

Lastly, it is believed that increased tidal prediction accuracy can be achieved over this formulation by either opening the North Atlantic model boundary or coupling to a 3D global GCM with tidal forcing. (Both techniques were beyond the scope of this research).

2. Tidal Analysis

One technique to arrive at the stable amplitude and phase of the tide at model grid points is to test the predicted amplitude and phase for convergence to a steady solution. Schwiderski (1980) assumed model convergence to a steady solution when the amplitudes varied less than 2 cm and Greenwich phases varied less than 2°. In a 3D model with thermohaline and wind forcing this technique is not tractable due to the aperiodic, non-tidal forcing on the sea surface height.

To arrive at a solution in these experiments, model sea surface height predictions were examined by the data analysis programs of Foreman (1978). Model predictions of the height for each grid point were saved at hourly intervals and the Foreman program was modified to sequentially compute the least squares fit tidal solution at all grid point locations (vice a single station). Since M2 was the only tidal species included in the forcing, the sample size for the solution was typically 100 hours.

Figure 53 is the solution obtained from the Foreman analysis for the horizontally homogeneous initialization and optimal tidal parameters discussed in the previous section. A comparison of this figure to Figure 6a reveals that tidal amplitudes appear to have been adequately simulated (within 10 cm) over essentially all of the predicted domain. The main region of difference between the two solution appears to be over Frobisher Bay,
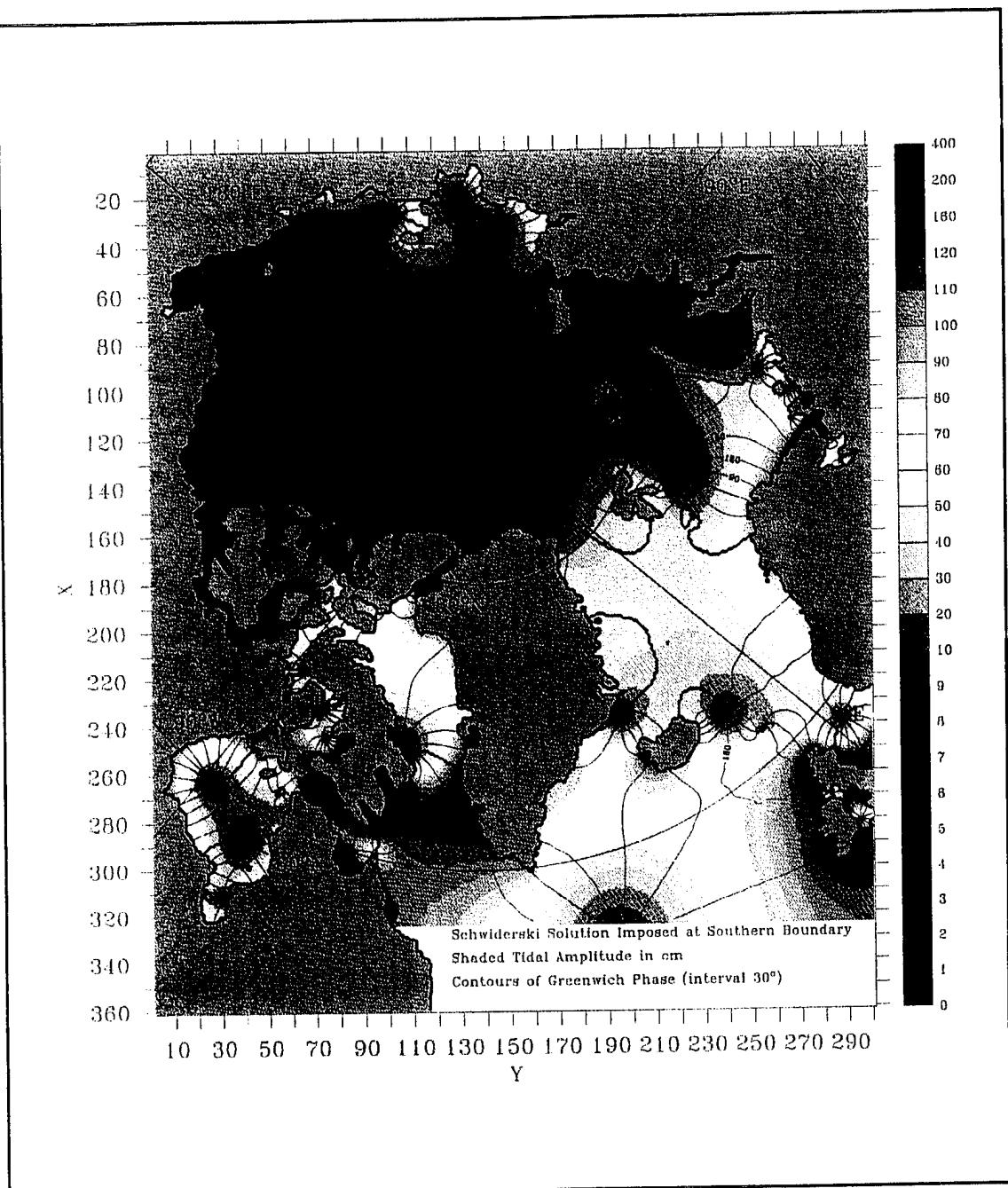
Figure 53. The M2 tidal solution for the horizontally homogeneous initialization after 180 days of integration agrees substantially with Figures 6a and 6b.

137

Hudson Strait, Cumberland Bay and Davis Strait. The amplitudes in those areas in Figure 53 are somewhat larger than that seen in Figure 6a, particularly in Frobisher Bay. These differences may actually be significant; however, it should be noted that the solution shown in Figure 6a contains but does not depict amplitudes greater that 120 cm. Comparison of Figure 6b with Figure 53 shows that this model has replicated the location of all the amphidromic points of the Kowalik and Proshutinsky solution and has generally replicated the position of the corresponding cophase lines. Continued detailed validation of the complete tidal solution with observations is planned. However, it is believed that the solution depicted in Figure 53 is at least a first order approximation of the M2 tide in the Nordic Seas and Arctic Ocean.

The mean annual forcing experiment with tides was started after 1 year integration without tides to first allow the mean flow field to develop. The model was then integrated for an additional year to allow the tidal solution to stabilize and to provide comparison of average fields with those obtained in the previous experiment. Figure 54 is the same solution after the two years of integration with added thermohaline and wind forcing but with the aforementioned increase in the bottom drag coefficient. With the exception of the decreased amplitudes by ~ 4 cm, which was demonstrated to be a function of the bottom drag coefficient, the tidal solution is stable when compared to Figures 6a, 6b and 53. Comparison of the effects due to the addition of the M2 tide with the annual forcing experiment is now possible and described below.

3. Temperature and Salinity Difference Fields and Inferred Mixing

The total model volume integrated kinetic energy increased by approximately a factor of 2 when compared to the annual mean forcing experiment. What type of work does this increased energy perform? Recent proposals suggest that the tidal motions, aside from their purely oscillatory nature, do contribute a significant amount of energy to mixing processes on the ocean shelves which affect the entire ocean thermohaline structure (Semtner, personal communication, 1995). Figure 55 is the contour plot of the
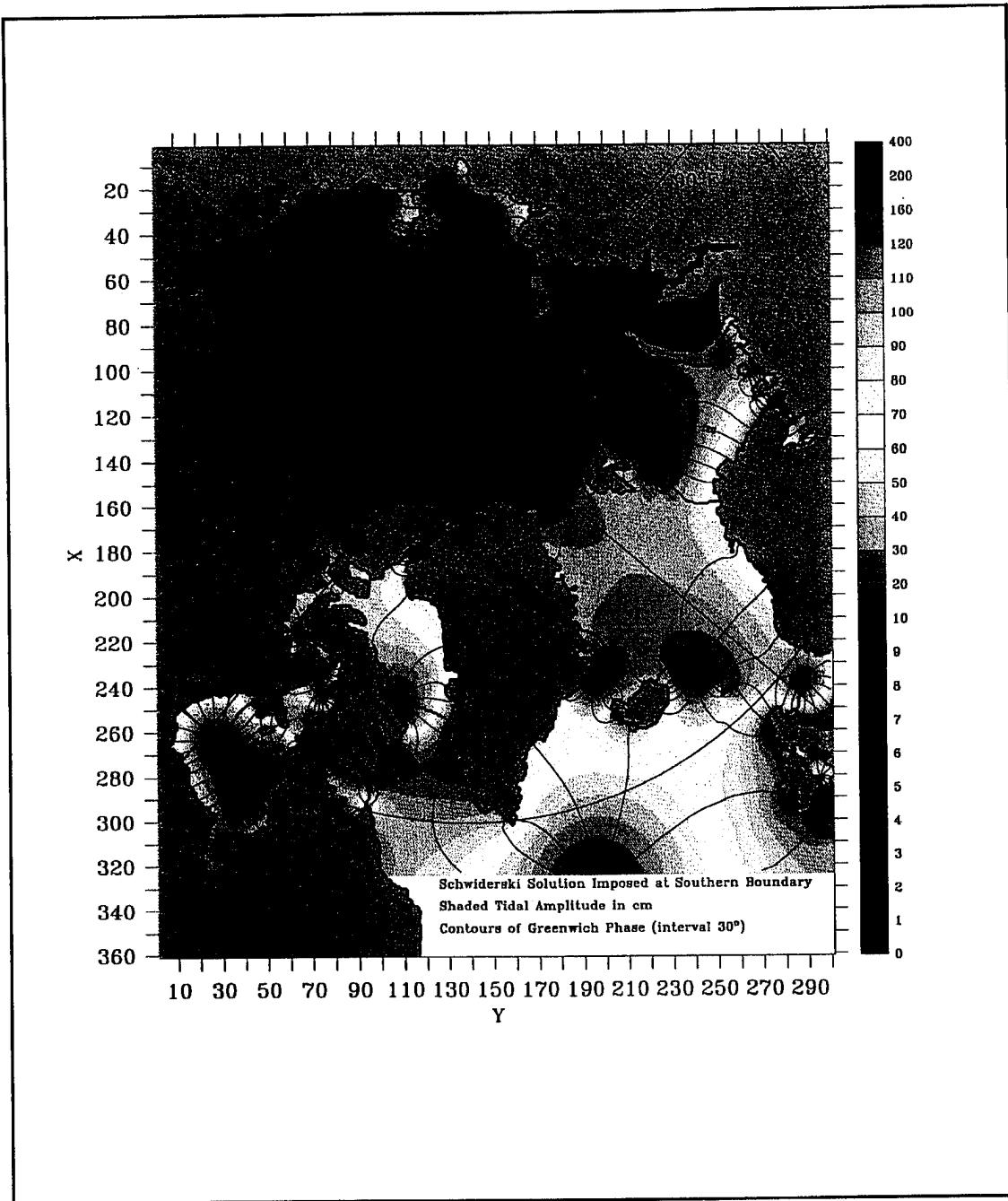
Figure 54. The M2 tidal solution after 1 year of integration with annual forcing (annual mean wind stress and surface restoring). Prior to forcing with the tides the model was allowed to spin-up for 1 year with the annual forcing, An increase in bottom friction necessary to provide stability in Denmark Strait reduced the amplitudes by ~ 4 cm over the Nordic Seas. The solution, however, still correlates well with the solutions in Figures 6(a-b) and 53.

139
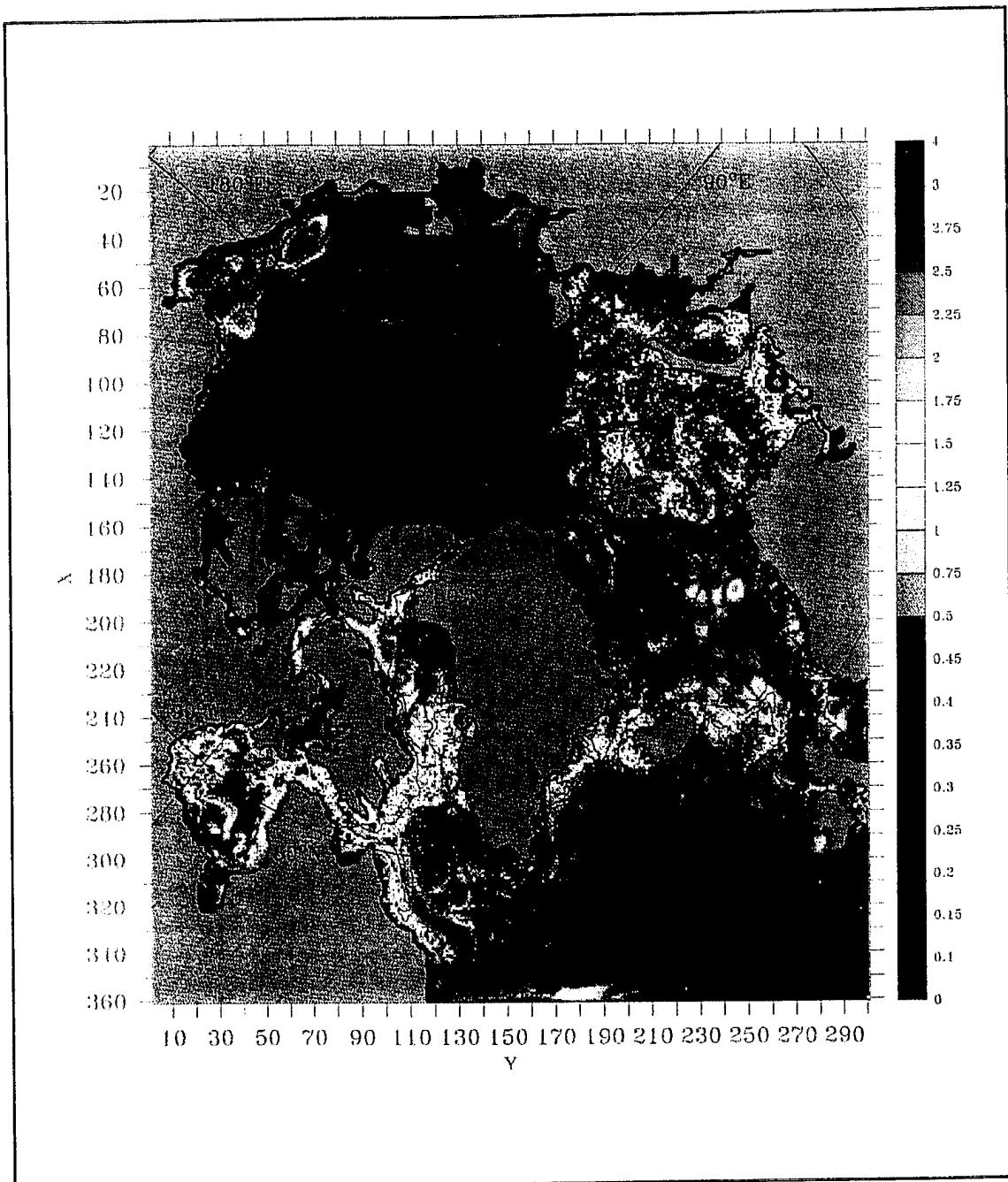
Figure 55. Contours of the maximum temperature difference in the water column (0 - 4300 m) between mean temperature fields in the tidal forcing experiment and the annual forcing experiment shows the regions of strong tidal mixing on the shelves and slopes of the Arctic Ocean and Nordic Seas.

maximum difference in temperature between the mean temperature fields from the tidal forcing experiment and the annual forcing experiment found over the entire water column. The regions of larger absolute difference found over the shallow seas, shelves and other topographic features suggest that some of the tidal energy is converted into mixing processes. Further promising analysis on the basin scale impact of this finding is in progress.

In a close-up of the Barents Sea as seen in Figure 56, the maximum difference fields found in the water column between 0 - 2000 m indicate that the largest magnitudes are found over the shallow banks and topographic features. The magnitude of the differences were typically 0.5°C but, as seen in the figure, some differences were as large as 3°C. The differences in surface salinity (not shown) corresponded to the regions of temperature difference and were typically 0.2 psu but as large as 0.8 psu. These simulated differences are consistent with mixing due to internal tides generated over these features The net effect in the vicinity of the experimental area was to mix away the cool and fresh surface restoring artifact in the middle of Bear Island Trough and to enhance the temperature and salinity differences across the front. In summary, the tides in these simulations, do appear to generate a significant amount mixing within the Barents Sea.

4. Effects of Tides on the Mean Current Structure

Mean current vectors from the tidal forcing experiment were subtracted from the mean current vectors from the annual forcing experiment. This residual flow can be interpreted as the tidally induced residual flow or the net effect of the tides on the mean flow and is plotted in Figure 57. A purely tidal residual flows is found by averaging the currents over a tidal period vice the long term average used here. The residual flows shown here, however, are in generally consistent in direction and magnitude with the purely tidal residual flows reported by Harms (1992) within the Barents Sea.

The magnitude of the anticyclonic residual circulation around Bear Island in these simulations was enhanced in the vicinity of Bear Island. Other important features are the
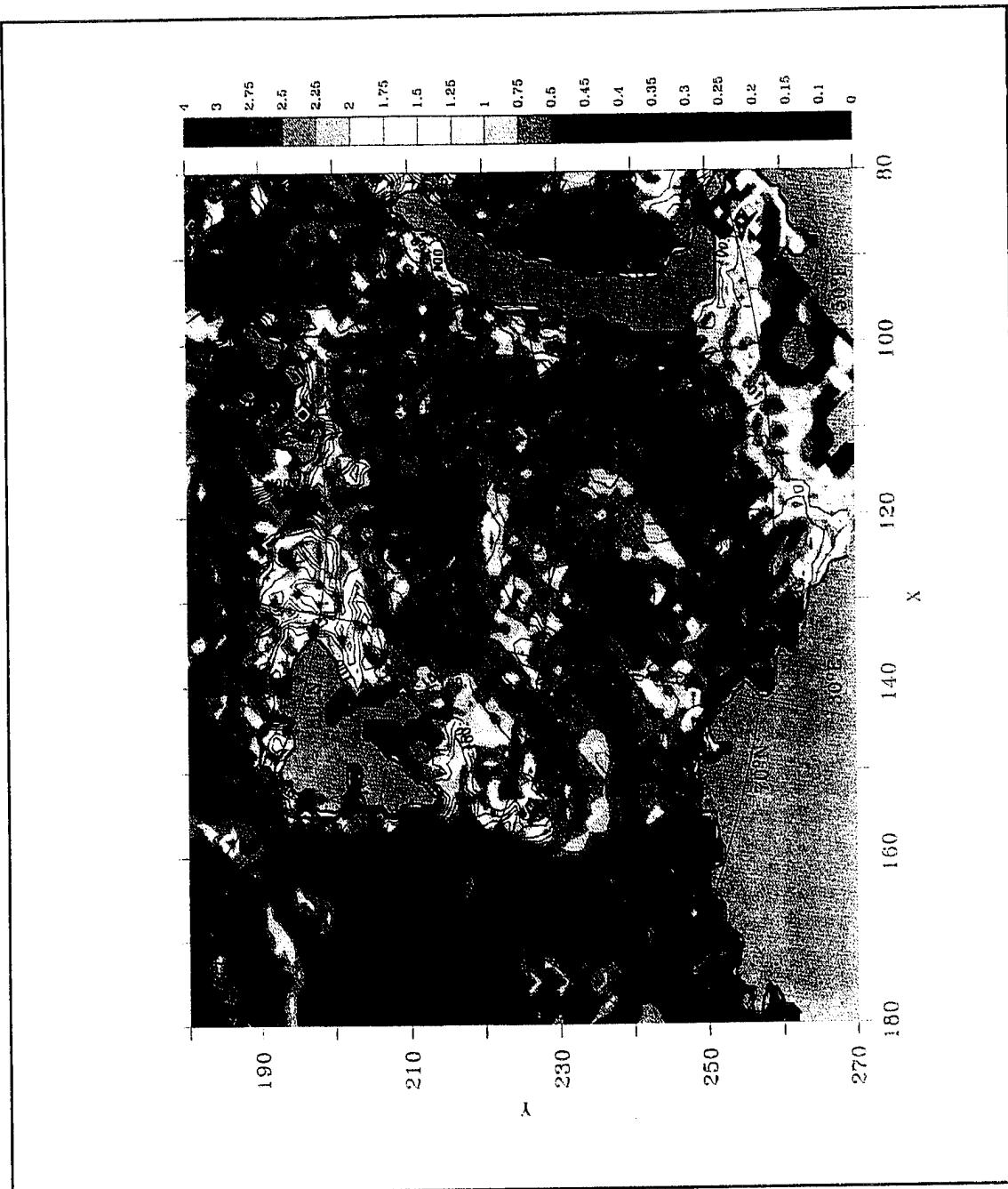
Figure 56. The maximum temperature difference in the water column (0-2000 m) between the mean temperature fields from the tidal forcing experiment and the annual forcing experiment indicates the significance of tidal mixing throughout the Barents Sea.

142
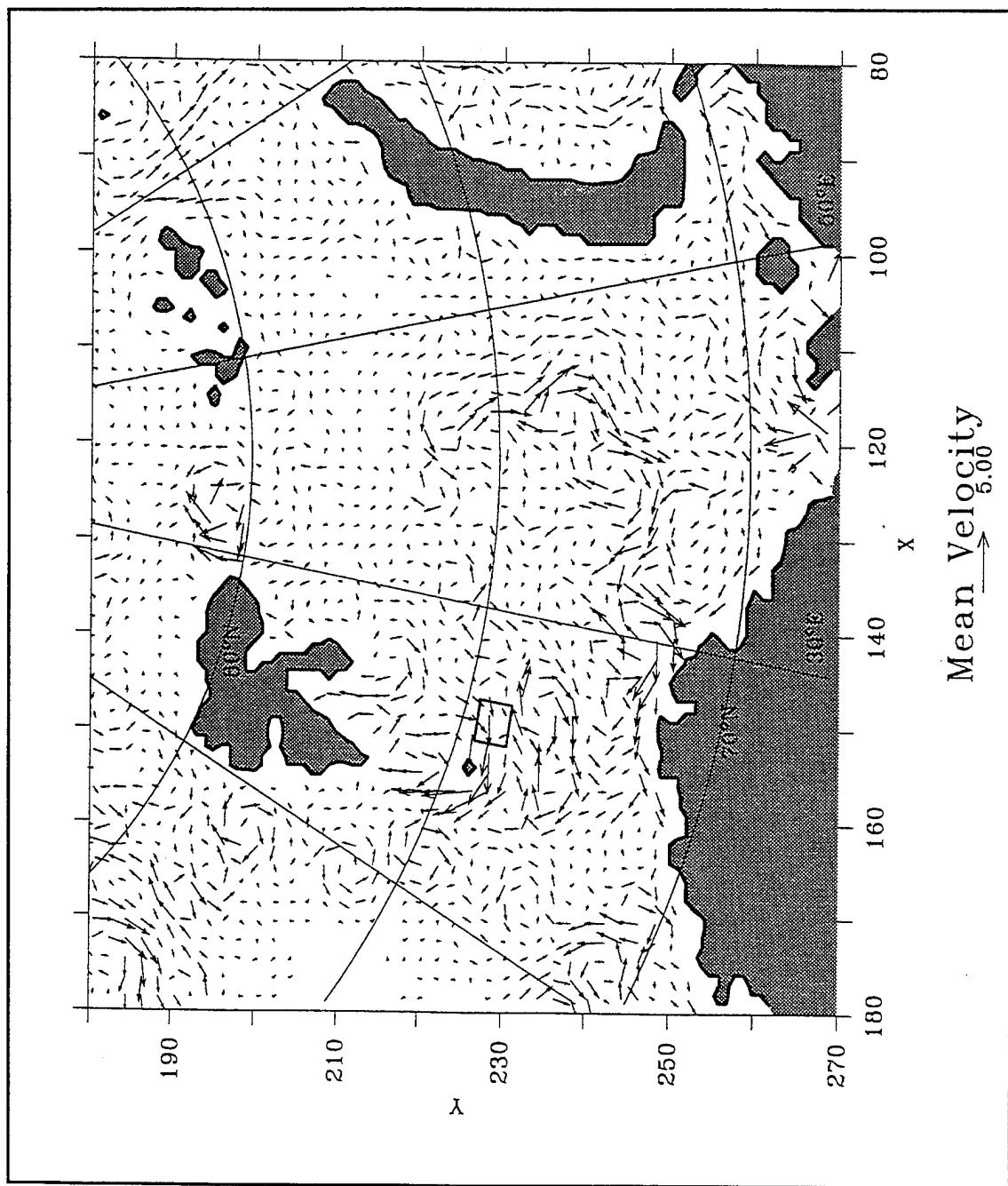
Figure 57. The difference between the mean surface velocity fields (10 m) of tidal forcing experiment and the annual forcing experiment provides an estimation of the tidally induced residual flow. Enhanced anticyclonic circulation around Bear Island, Kvitoya and Central Bank indicates the strong interaction between the tides and the topography.

143
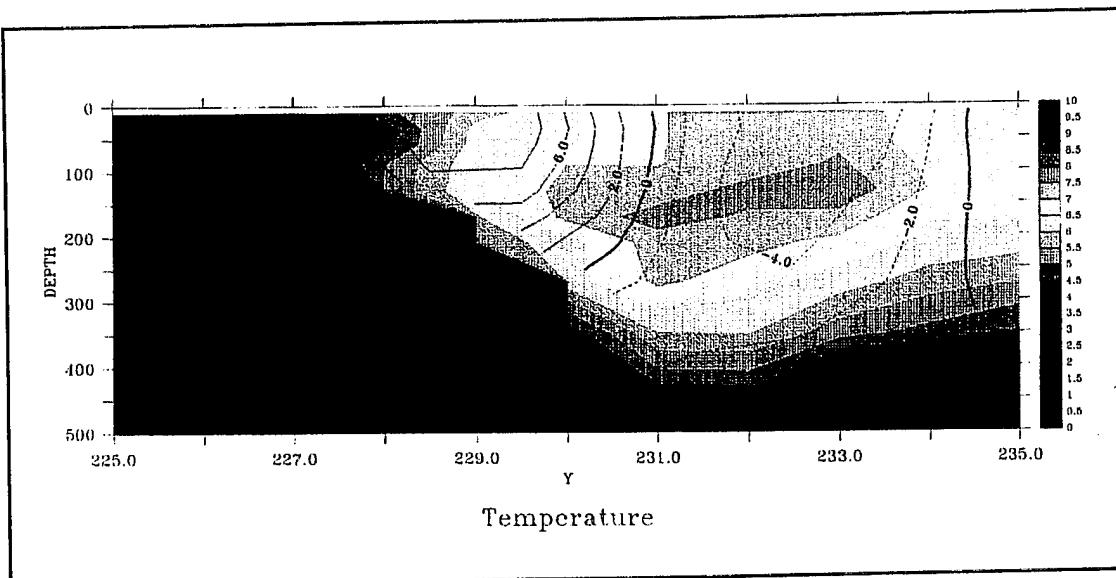
Figure 58. The same cross section in temperature and velocity as seen in Figure 51 shows the net reduction in the core velocities of the northeastward flow along upper part of the slope and in the southwestward recirculation deeper than 300 m. Note also the temperature is substantially more mixed near the bottom on Svalbard Bank which resembles the structure seen in the observations.

net reduction of the flow into the North Cape Current and the reduction of the northeastward flow along Svalbard bank discussed in the annual forcing experiment. This reduction in the flow effectively reduces the transport into the Barents Sea by ~0.4 Sv. Also, the prominent anticyclonic flow around the shallow bathymetry corresponding to location of Kvitoya enhances the unidirectional transports estimated through this region but maintains the same net transport. The same effect on the volume transports is observed between Franz Josef Land and Novaya Zemlya. The balancing flow required through the passage south of Novaya Zemlya into the Kara Sea is thus reduced to 0.1 Sv.

The effect of the tidal flow at the front is seen in Figure 58 which is identical to the cross section (Figure 51) for the annual forcing experiment. The opposing flows on the slope of the trough are present in both experiments but the maximum core velocities have been reduced by ~ 4 cm s^{-1}. Also the temperature structure on the northern side of the front is substantially different and shows the formation of a cold tongue extending out over the topography (in this simulation a warm ~3°C, which will be discussed in the next

144

chapter) with complete mixing to the bottom on Svalbard Bank. This temperature structure is very similar to the structure found in the observations (Figure 17). This simple comparison provides evidence that the tides are an essential element in simulating the frontal features at the BSPF.

C.   SEASONAL FORCING EXPERIMENT

To examine the effects of high frequency winds and seasons on the BSPF and circulation within the Barents Sea, the 1992 ECMWF wind stress fields (averaged over every 3 days for the year) and the monthly mean Levitus data, described in Chapter VII, were used for model forcing. This experiment was integrated with the high frequency forcing for 7 model years after an initial spin-up for one year. The model time step, viscosity and diffusivity constants were all different for this experiment. The model time step was set to 40 minutes for the internal mode and 40 seconds for the external mode. Vertical viscosity and diffusivity (K_v and D_v) were held constant at 10 cm^2 s^{-1} and 0.3 cm^2 s^{-1} vice being a function of the Richardson number. Horizontal biharmonic viscosity and diffusivity (K_h and D_h) were both set to -2.0 $\bullet$ 10^{19}. Fields for the following analysis were taken from August of the sixth year of integration.

1.   Summertime Difference Field of Temperature and Salinity

Figure 59 shows the difference fields of surface (10 m) temperature from the annual forcing experiment and the mean conditions for August of the simulation year in the seasonal forcing experiment. The magnitude of the differences were substantially larger than the tidal forcing comparison due to the seasonal change in surface temperature restoring. Magnitudes of the salinity change (not shown) were also on the order of 0.8 psu. The primary feature at the BSPF seen in this figure is reduction of the surface signature at the front by net warming on the northern side and a net cooling on the southern side. This effect is consistent with the observed weak temperature gradient at
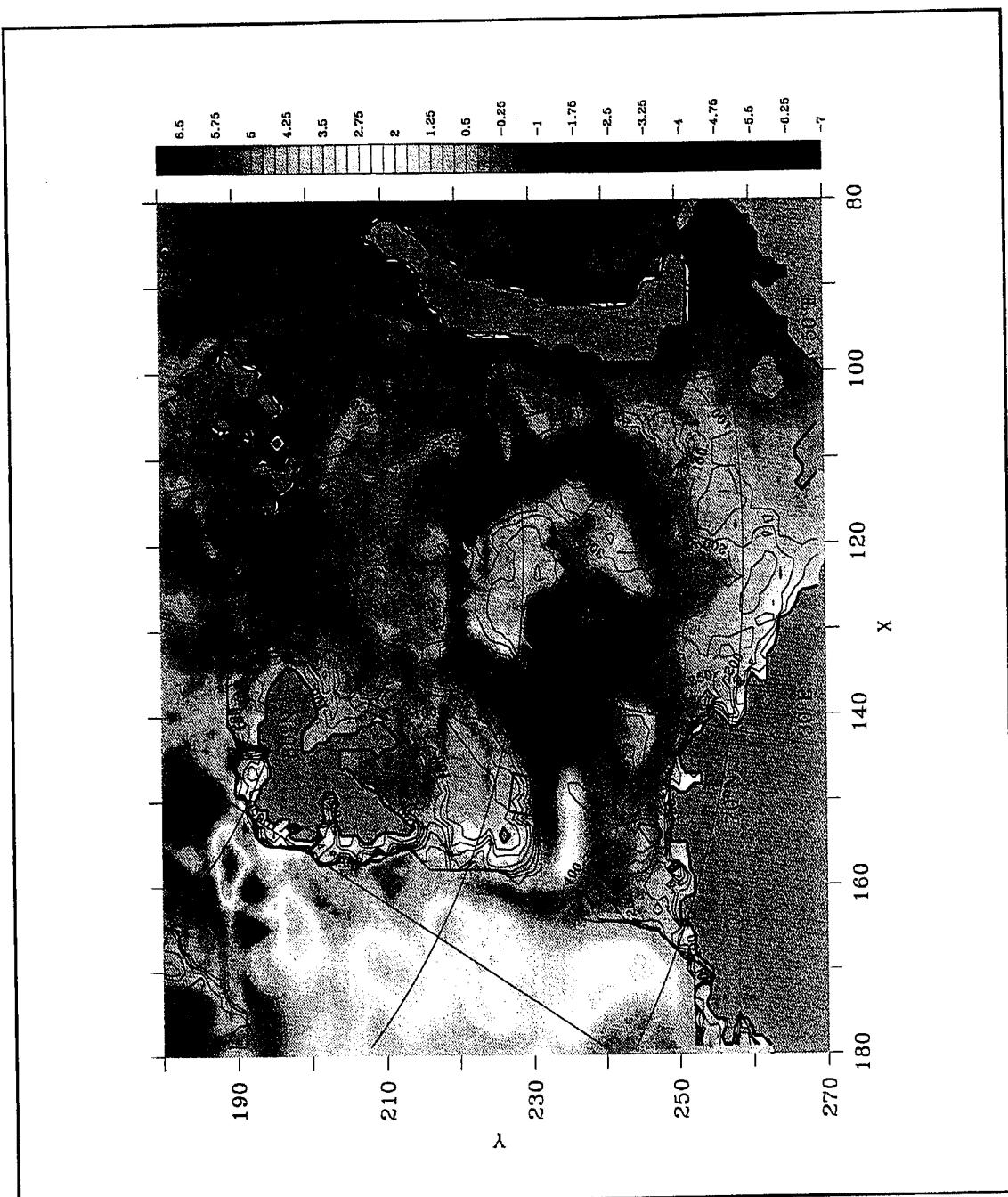
Figure 59. The surface (10 m) difference field between the mean temperature fields for August derived from the seasonal forcing experiment and the annual forcing experiment displays the effect of summer warming inherent in the simulation through the use of restoring the surface layer to the monthly mean climatology of Levitus and Boyer (1994).

146

the surface. Also, the anomalous cool surface feature within Bear Island Trough seen in Figure 45 also has been corrected with this forcing.

However, in Figure 60 (a-c), a comparison of the frontal cross section in salinity for the 3 experiments, another weakness in the use of coarse climatological surface conditions for restoring is found. The Levitus et al. (1994) climatology reflects a net freshening of the surface salinity in summer for the Barents Sea (the effects of summer ice melt); however, their 34.6 surface isohaline incorrectly extends nearly to the Norwegian Coast. A summertime fresh water lens, instead of ending at the BSPF as seen in the observations, now extends across the front as seen Figure 60c. The advantages of the high resolution of the model in the vicinity of the front to better simulate the surface layer in this experiment are lost due to this improper forcing. However, examination of the circulation provides evidence of the seasonality of the flows contributing to the BSPF.

2. Seasonality in Transport

Figure 61 is the time series of the net monthly averaged transports from the sixth year of integration into the Barents Sea through sections 4, 5 and 6 found in Figure 49. Also depicted is the outflow from the Barents Sea through section 4. Before proceeding further, note that these transports are based upon 1992 wind forcing data alone and may not be indicative of results from other years due to the frequently observed interannual variability.

The net averaged transport through section 4 reaches a local minima in April, July, and October. Maxima are achieved in the winter months of December and January which reflects the strong global poleward heat flux in the winter. The highest frequency of the presence of low pressure systems spawned from the Icelandic Low and the maximum recorded wind speed for the Nordic Seas are observed during these months (Gathman, 1986) which was also reflected in the ECMWF wind stress forcing.

Ranges for the net transport into the Barents Sea in the Bear Island to North Cape transect (section 4) vary from ~5 Sv in winter to a minimum of ~1.75 Sv in the late spring

147
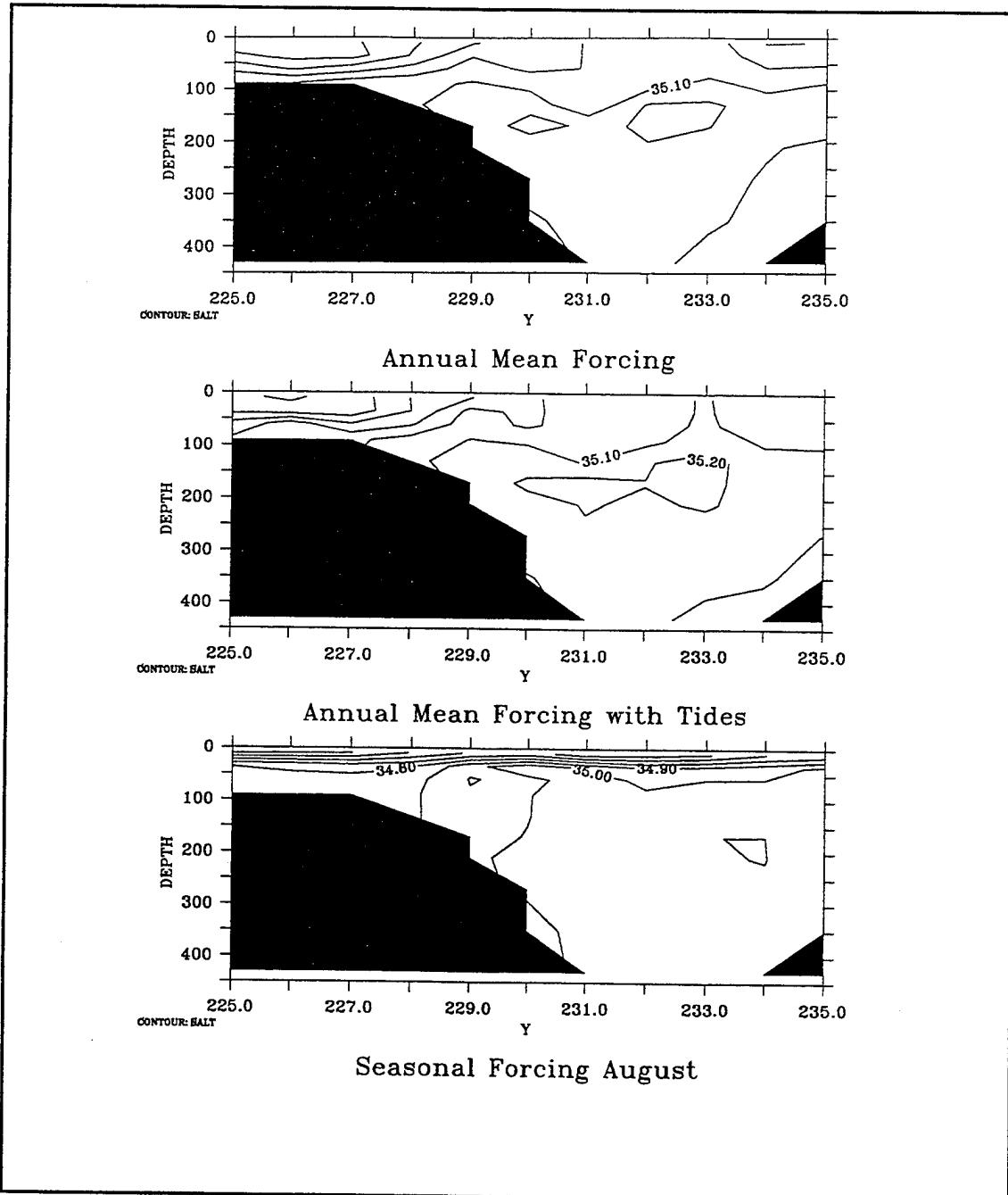
Figure 60. A comparison of mean salinity cross sections between the three modeling experiments (a) annual forcing experiment (b) tidal forcing experiment and (c) seasonal forcing experiment (August) is used to highlight the problems of coarse forcing fields. Figure 60c shows the problem of the using the coarse monthly mean climatology to freshen in the summer surface layer as the fresh layer extends past the position of the front.

148
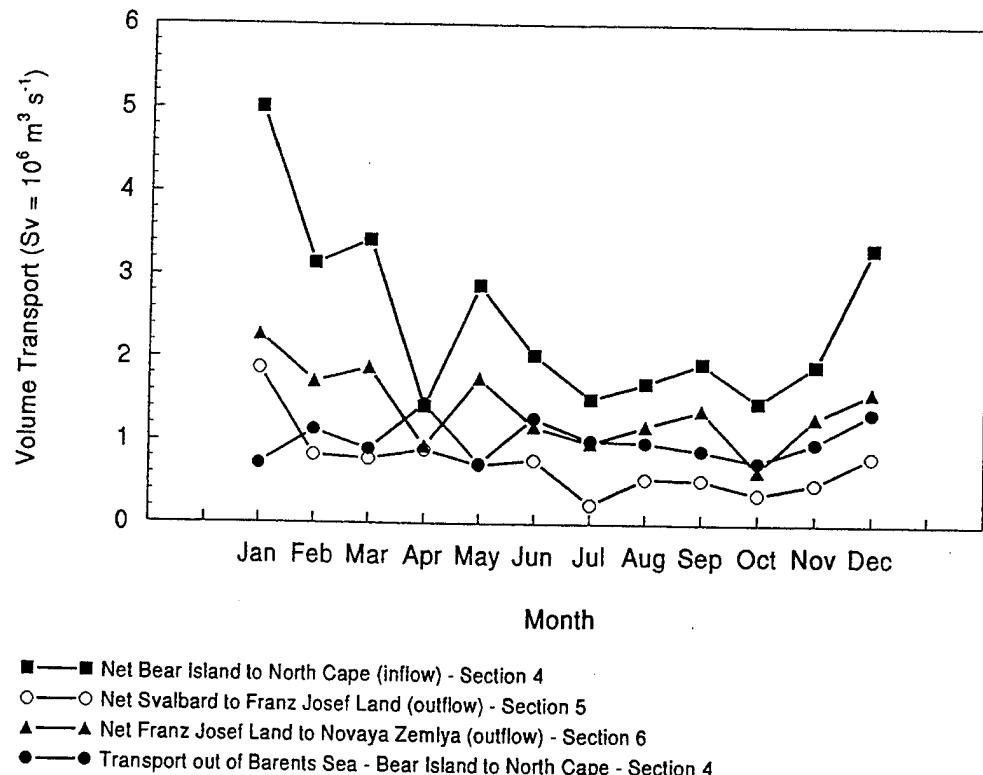
Figure 61. A time series of the monthly mean net volume transports calculated from the seasonal forcing experiment for sections 4, 5, and 6, as seen in Figure 49, shows a strong seasonal signal. The transport between sections 4 and 6 is closely correlated. Also depicted is the transport out of the Barents Sea through section 4 which is essentially constant for the entire year.

and early fall. Note the close correspondence of the transport out of the Barents Sea through the Franz Josef Land to Novaya Zemlya transect (section 6). This close correspondence reflects the strong connection between the flows through sections 4 and 6 which are connected by the Barents Sea Branch (Rudels et al., 1994). The net transport in section 5 is less than 1 Sv for most of the year (a net outflow) with a maximum in January and a minimum in July.

149
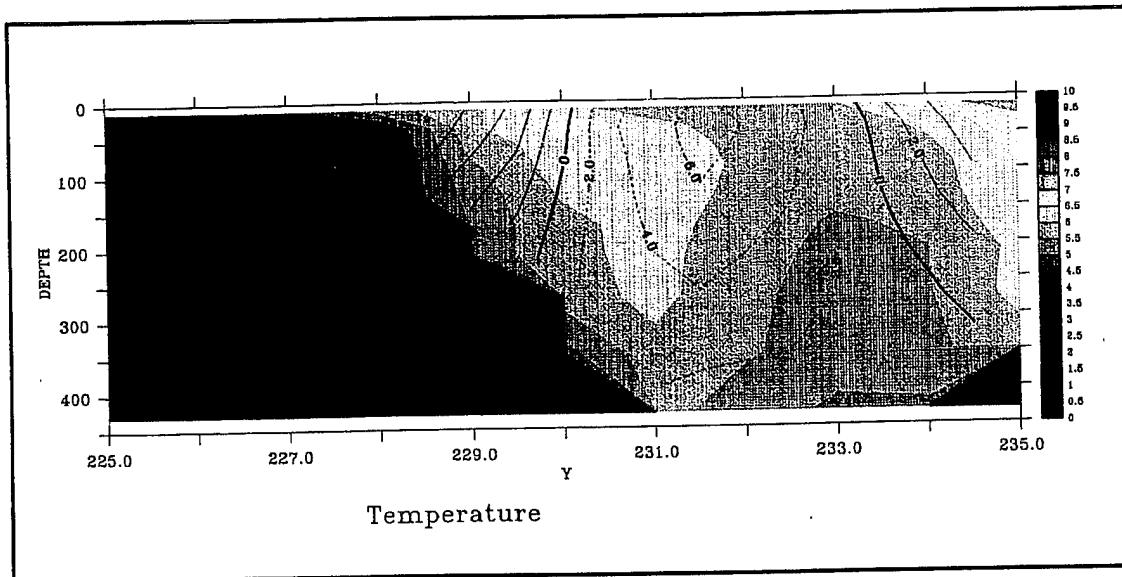
Figure 62. Contours of temperature and the alongslope velocity for same cross section as Figures 51 and 58 is displayed for the seasonal forcing experiment. The recirculation within the trough and the northeastward flow up on the slope is also predicted in this experiment. The consistency of these flows under a variety of forcing supports the barotropic nature of the circulation.

The lack of a strong seasonal cycle in the recirculation within the Bear Island Trough can be seen the same figure as the volume transport out of section 4. The average transport of about 1 Sv varies much less than the net transport which is governed by the inflow. This lack of strong seasonal variability is attributed to most of the increased wintertime volume transport occurring in the upper layers in response to wind forcing. The strong wind forcing overcomes the topographic steering and pushes water deeper into the Barents Seas. The track history of the of the drogued drifter data of Poulain et al. (1995) discussed in Chapter V supports this hypothesis.

3. Effects of Seasonal Forcing at the Front

Finally, in Figure 62, temperature and the alongslope velocity contours are provided for the same section as seen in Figures 51 and 58. Again the opposing flows along the slope defining the northeastward topographically steered circulation and the

150

recirculation in the trough are evident in this experiment. However, the temperature structure is much more homogeneous with 4°C water found to the bottom over the Svalbard Bank. Observations indicate that near bottom temperatures should be less than 2°C. The core temperature of ~7°C seen in the recirculation flow in the previous two experiments is ~6°C here. It is apparent that the increased cross-frontal mixing associated with this experiment has homogenized the frontal signature. The reason for the homogenous conditions along the front in this experiment and the generally warmer waters to the north of the front in contrast to the previous experiments and observed data will be discussed in the next chapter.

IX. A SYNTHESIS OF MODELED AND OBSERVED CONDITIONS

A.   COMPARISON

Chapters III and VIII have independently examined the observed and modeled conditions in the Barents Sea and at the BSPF. While some similarities and differences between the different approaches to studying the BSPF have been mentioned, a few more comparisons are now presented to aim towards a synthesis of fundamental features revealed by this work.

1. Temperature and Salinity Structure

A large portion of understanding the Barents Sea and the Polar Front is revealed in mapping the meeting of the contributing water masses. Figure 63a is the T-S diagram compiled from all temperature and salinity observations taken during the entire fourth CTD grid occupation. Figures 63b through d are the predicted temperature and salinity values from all grid points within the experimental area from the mean fields of the three modeling experiments discussed in the previous chapter. The obvious distinction between the observations and modeling predictions is the absence of the cold and fresh BPW water mass. All the modeling experiments predict the temperature and salinity characteristics of NAW, with the results from the annual forcing and the tidal experiment (Figures 63b and c) most closely resembling the observed NAW characteristics. The model predictions seem to capture only a part of the frontal mixing that actually occurs within the confines of the experimental areas as seen in the observations. The seasonal forcing experiment, Figure 63d, appears unique in that it is much more homogenous with most points occurring within a limited range (salinity greater than 35.0 psu. and temperature between 4°C and 7°C).   Also the anomalous surface fresh layer discussed in the previous chapter and seen in Figure 60c can be seen. A water mass suggestive of BPW is present in the model simulations but is obviously
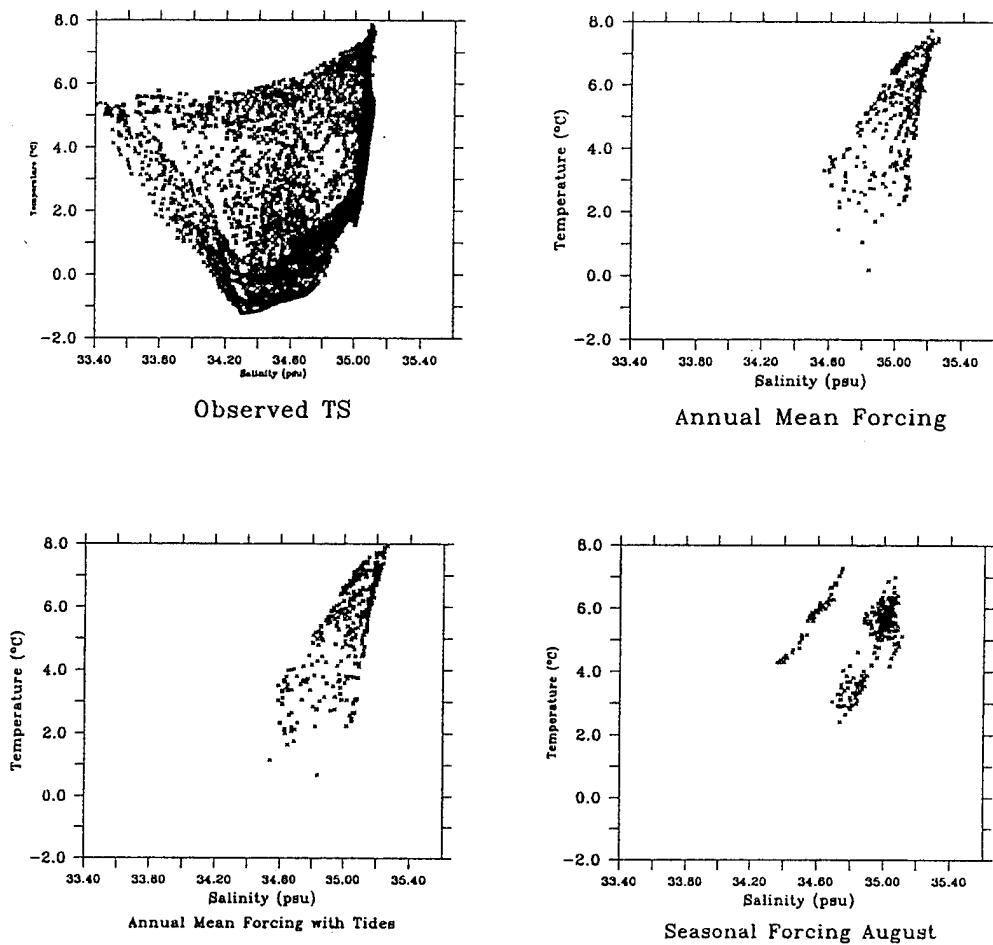
Figure 63. A comparison of T-S diagrams taken from values inside BSPF experimental area from (a) observed values during the 4th CTD grid occupation (b) the annual forcing experiment predictions (c) tidal forcing experiment predictions and (d) the seasonal forcing experiment predictions shows that the presence of BPW is missing in all of the modeling experiments.

154
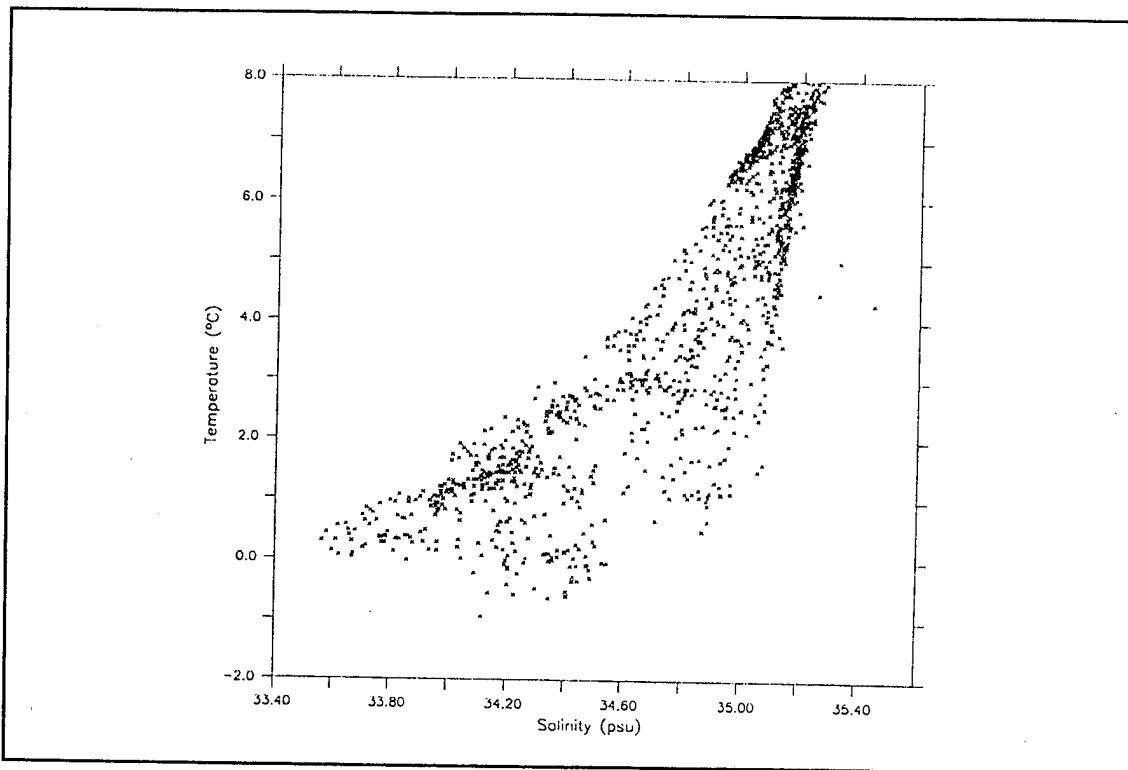
Figure 64. T-S diagram made from predictions from the tidal forcing experiment over an area extending from Bear Island Trough to 77°N shows the characteristics of BPW. The front in the model simulations has been diffused over a much larger area than is observed.

displaced from where it should be. The meeting of the frontal water masses has been spread out over a much larger region as can be seen in Figure 64 which collects the model temperature and salinity points from the tidal forcing experiment but is extended from Bear Island Trough to 77°N along 30°E longitude. The T-S correlation now includes BPW. However, the plot does not reflect the characteristics of the warmer and fresh summer melt layer because the mean annual surface restoring does not reflect this contribution.

Correspondingly, the accuracy of the model in reflecting the observed temperature and salinity fields at 10 and 45 m is poor. Figures 65a through d show the predicted salinity at 10 m from the three model experiments compared with the observations from the first CTD grid occupation at the same depth. The annual forcing and tidal forcing

155
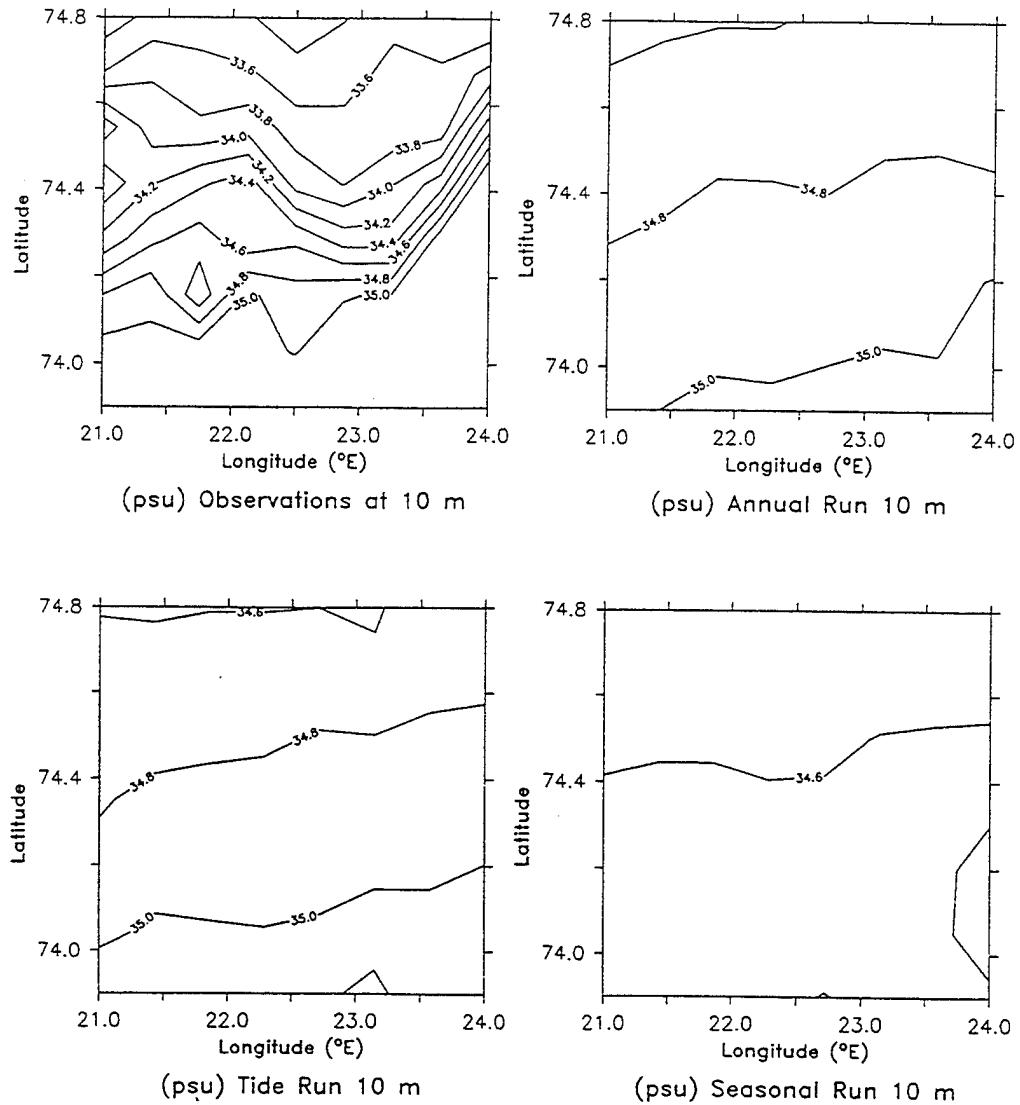
Figure 65. A plan view of the surface salinity (10 m) taken from the CTD observations made in the first grid occupation (a) is compared with the model predictions from the (b) annual forcing experiment (c) tidal forcing experiment and (d) seasonal forcing experiment.

experiments reflect a much more diffuse front in salinity at the surface with the frontal signature essentially absent in the seasonal experiment. Figures 66a through 66d make a similar comparison over an expanded domain with the temperature fields at 45 m. All three model experiments have warmer water at this depth in the experimental area than was seen in the observations south of the front and warmer water likewise north of the observed frontal position. In all three modeling experiments, the cooler BPW is seen to the northeast of the experimental area on Svalbard Bank.

Has the modeling failed in producing an understanding of the temperature and salinity at the front? The answer is found in examining the reason behind the inaccuracies of the model results. Cold, fresh BPW is not being advected southward from the northern Barents Sea to the observed position of the Polar Front. Pfirman et al. (1994) have identified the flows carrying the BPW (Persey Current, East Spitsbergen Current and Hopen - Bear Island Current) as waters with temperature minima at 50 to 100 m depth. Cross sections of model predictions at the northern extent of the Barents Sea (~79°N) agree substantially with the depth, location and temperatures from the observations presented by Pfirman et al. As the flow precedes south in model simulations, the signature of this cold core is no longer coherent and has been substantially mixed away below 75°N. This is clearly seen in Figures 67 and 68 which are contours of the minimum temperature and salinity found in the water column between 0 and 300 m. This cold fresh core can be traced in both figures crossing 30E and moving southwest to an area just south of Svalbard where it dissipates.

A broad examination of the density structure reveals that the stratification of the upper water column is not as strong as seen in the observed summertime profiles. This decreased stratification allows wind induced mixing to penetrate deeper into the water column. This type of mixing is referred to as mechanical mixing which is parameterized in the model through the vertical friction coefficients and instantaneous convective adjustment. The source of this decreased stratification and susceptibility of the model to increased vertical mixing is attributed to two conditions present in the model simulation. First, the weakness of using coarse climatological fields for surface restoring, which has
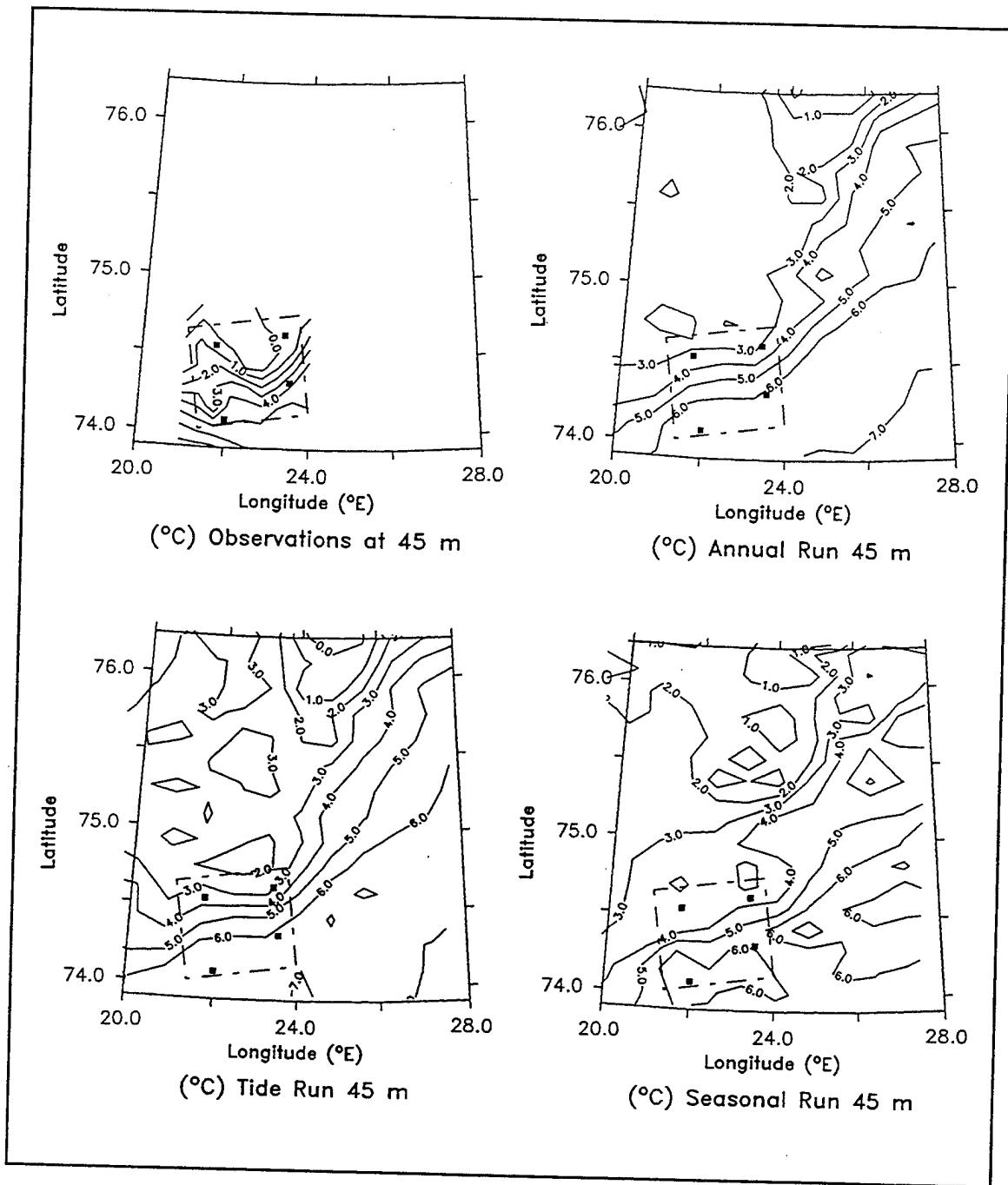
Figure 66. A plan view of the temperature at 45 m made from the CTD observations in the first grid occupation (a) is compared with the model predictions from the (b) annual forcing experiment (c) tidal forcing experiment and (d) seasonal forcing experiment for the same area and depth.
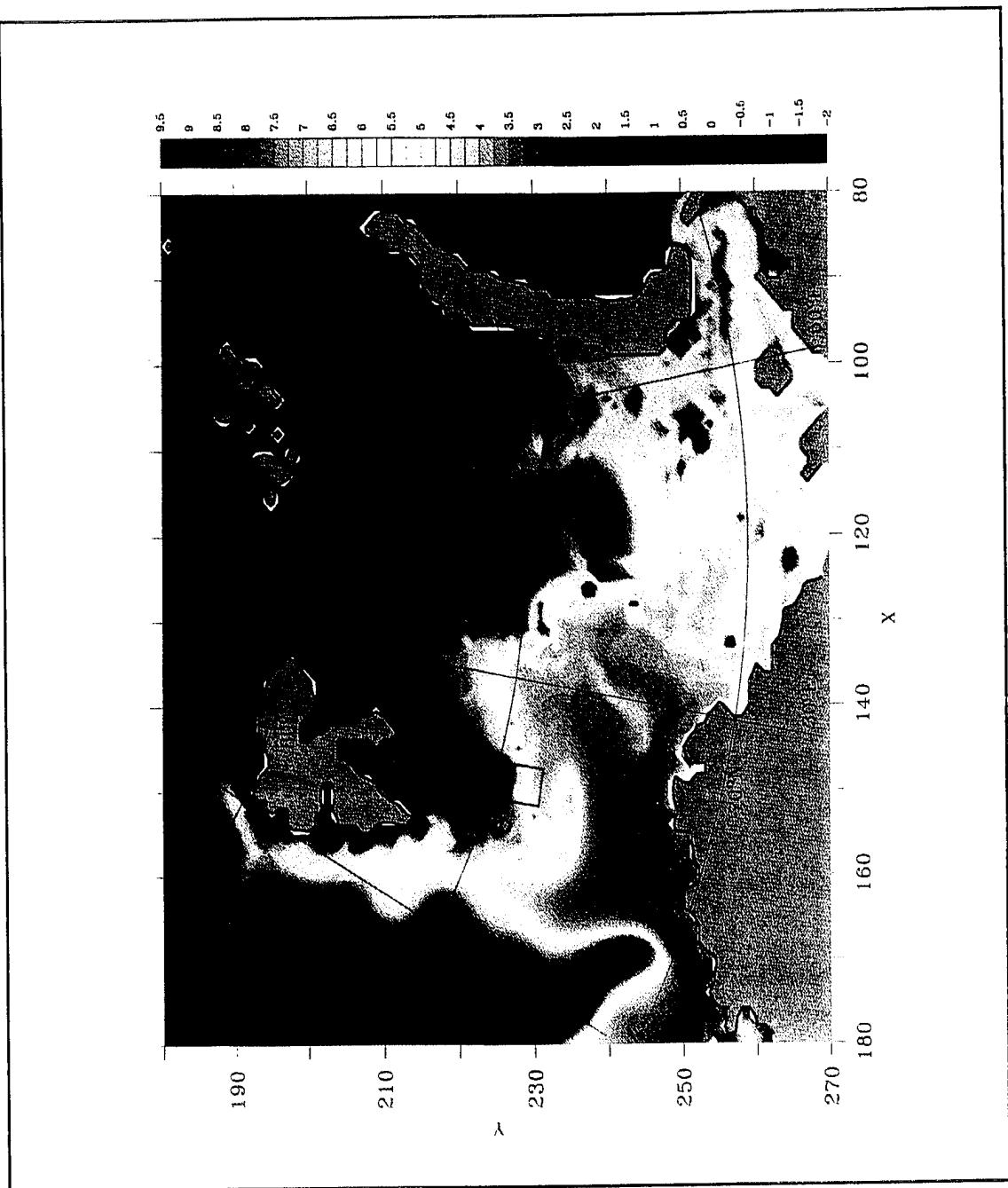
Figure 67.   Contours of the minimum temperature found in the water column between 10 to 300 m taken the tidal forcing experiment traces the cold core of BPW along the Hopen-Bear Island Current southeast of Svalbard as far south as 75°N with very little signature remaining at the experimental area.
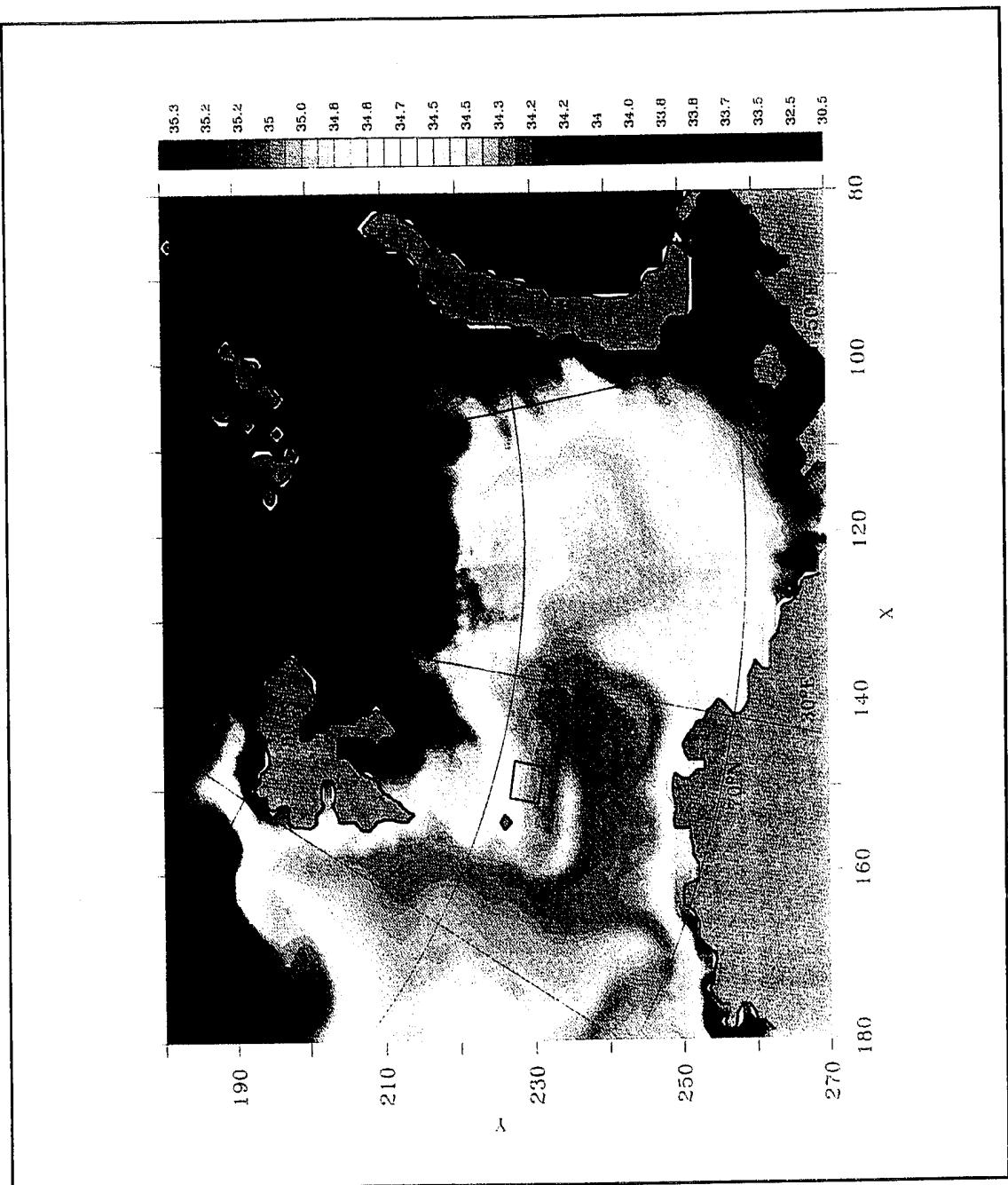
Figure 68. Similar to Figure 66, the contours of the minimum salinity found in the water column from 10 - 300 m indicates the fresher core of BPW has been substantially diffused by 75°N along the same path southeast of Svalbard.

been previously mentioned, is clearly borne out in frontal regions such as the BSPF which are not resolved in the climatology. Buoyancy is added or subtracted to the water without physical relation to the topographically restrained position of the front. Assessment of the annual climatological fields reveals generally that the surface is too warm for winter simulations and too salty for summer simulations midway into the Barents Sea. The monthly climatological salinity fields do show a summertime freshening from melt water influence but this freshening is spread over too broad an area as mentioned in Chapter VIII. It also should be noted that this climatological summer freshening is still too salty to be truly identified as melt water as it is still greater than 34.2 psu over much of the Barents Sea. In summary, the weakness of using surface fluxes obtained through restoring climatological conditions is manifested by the spurious placement or subtraction of buoyancy into the simulation.

The second reason for the model's susceptibility to increased vertical mixing is the lack of ice cover in winter, particularly in the Barents Sea. In wintertime, the water column becomes mostly neutral in stability throughout the northern Barents Sea as the surface waters are cooled and ice forms (Midttun and Loeng, 1987). This neutral stability does not infer homogeneity as warm salty NAW still penetrates into and generally beneath the cooler but fresher BPW (excluding the formation and presence of Barents Sea Bottom water in winter). Also, as pointed out in Chapter VIII, storm frequency and wind speed are at a maximum in the Barents Sea in the winter which serves as a passage for most winter storms which enter the Arctic region (Serreze and Barry, 1988). Without an ice cover acting to damp the wind's influence on the ocean surface, mechanical mixing can also prevail to homogenize the water column in the Barents Sea. As personally observed, even when the ice edge is pushed back by winter storms and the surface exposed to winds in the Barents Sea, the ice quickly reforms as a thin surface layer of frazil or nilas ice and the ice edge returns to a typical mean position at the BSPF on a synoptic time scale. It is this lack of ice cover during the winter wind stress conditions in the seasonal forcing experiment which is proposed to have created the very diffuse and nearly homogeneous conditions seen particularly in the Barents Sea.

Without either deep layer climatological restoring or realistic surface fluxes in the region, expectations for the model to regenerate and simulate the observed conditions in the Barents Sea in the summer must be low.

This analysis of the model's inaccuracies has actually provided a better understanding of an essential feature of the temperature and salinity structure of the BSPF in summer. The presence of a highly stratified surface layer is necessary to allow the mid-depth cold BPW to penetrate through the Barents Sea to the front without being mechanically mixed away. Secondly and related, though the ice edge is typically hundreds of kilometers away in the summer, it appears necessary that the ice edge must extend to the frontal position the previous winter in order to provide the source of the fresh melt water layer. The highly temporal and spatially fine features associated with the BSPF are not found in or easily replicated using ocean climatology.

2. Mean Velocities

Figure 69 is a plot of the depth-averaged currents in the 0-100 m layer from the tidal forcing experiment plotted on the scale of the experimental area. In comparing these predictions with the subtidal flow derived from the ADCP measurements in Figure 14 two distinctions are clear. First, the model predicted northeastward flow over the slope between 150 and 300 m appears too strong, broad and extends even to the northern part of the experimental area. Secondly, the west-southwestward recirculation is only prominent deeper than 400 m in the simulation as compared to the observed ADCP velocities which show a clear recirculation as shallow as 300 m. This latter difference is believed to be the result of the vertical averaging (cross sections in Figures 51, 58 and 63 all show the isotachs prograde to the bathymetry). Also, the steepest topography gradients are between the 300 and 400 m isobaths as seen in Figure 8 but these isobaths lie between the model grid points. A steeper and better resolved slope would likely steer the simulated currents more realistically.
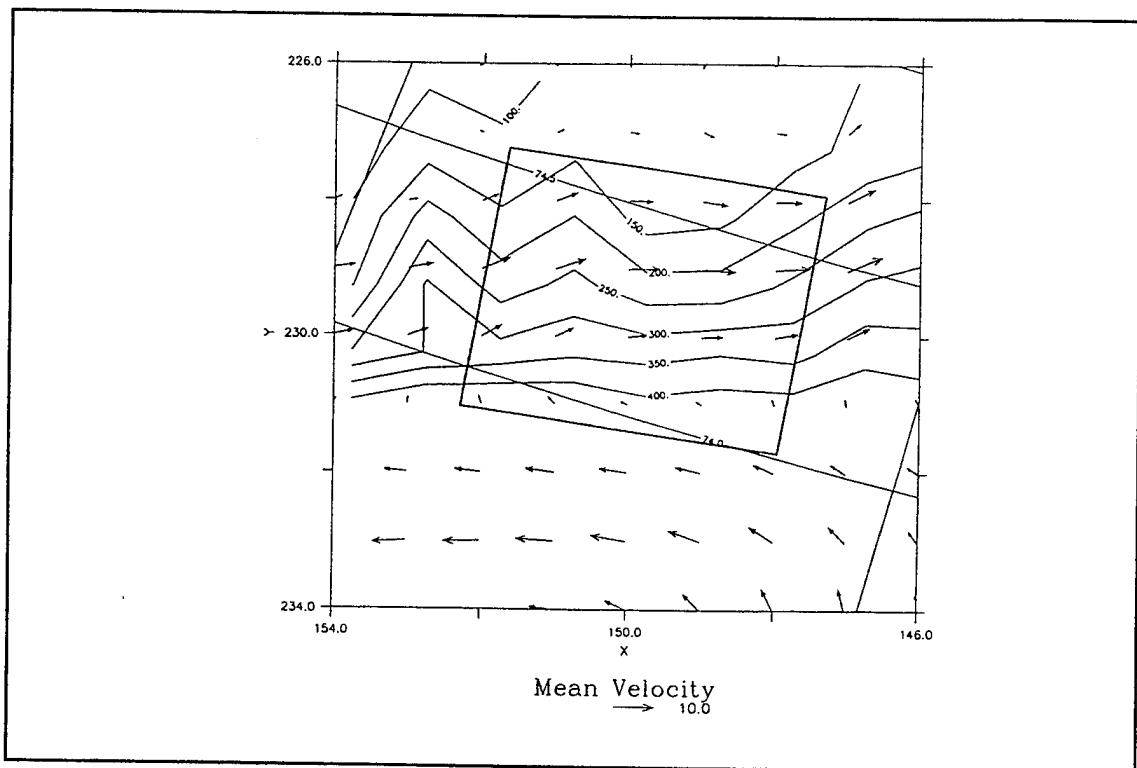
Figure 69. Depth-averaged velocity vectors (0 - 100 m) from the mean current fields predicted in the tidal forcing experiment are shown in relation to the experimental area. The recirculation of NAW strongest in grid points south of the experimental area and broad northeastward flow is seen passing through much of the shallow region. Refined grid resolution and bathymetry would likely improve the predicted positions of these flows along the slope.

The prediction and location of the northeastward flow was consistent in all three modeling experiments. As pointed out in the previous chapter, in light of the position of this simulated flow in relation to the fixed current meters, its existence cannot be discounted by the observations and is actually supported by the ADCP measurements. However, the extent of this flow onto the shelf, particularly in the vicinity of the NE mooring and considering the very weak mean currents measured there, makes the horizontal span seen in this figure suspect. Again, better model resolution and bathymetry might confine the predicted flow to a much narrower region . This flow was not predicted by the geostrophic calculations made from the observational data and was only weakly present in the calculations made from the model predictions. Thus, this

163

flow, if its existence is verified, will likely be barotropic and the implications are twofold. First, by positioning alone, this current would appear to buffer the mixing between the BPW and the recirculated NAW. Second, from model simulations, it appears to advect intermediate frontal waters (vice NAW) back into the Barents Sea. The implications for derived water mass formation in the Barents Sea, specifically the formation of Arctic halocline water, as discussed by Steele et al. (1995) are stimulating for further observational investigation.

B. A SYNTHESIS

A synthesis of the findings from the observed and modeled conditions in terms of balances at the front and relationship of the BSPF to the regional oceanography is now presented.

1. Principal Balances at the BSPF

The Barents Sea Polar Front is the focal point for the meeting of waters of Atlantic and Arctic origin in the Barents Sea along the steep northern slope of Bear Island Trough. Strong mixing of BPW and NAW across the front in summertime was not observed. The isopleths defining the front were seen to be retrograde to the bathymetry. The properties of the frontal waters at mid-depth (20 - 100 m), a region strong interleaving, are believed to a manifestation of a horizontally advective-vertically diffusive balance. The horizontal scale of the frontal signature in summer within this mid-depth regime is on the order of 3 km which corresponds to the first baroclinic Rossby radius of deformation. The corresponding vertical scale of the front, determined from the interleaving structure, was less than 10 m. In the lower portion of the water column, tidal and bottom mixing are attributed to diffuse the frontal signature with mixed waters appearing underneath the cold BPW extending up and onto Svalbard Bank. The

density contrast across the front is minimal as the characteristics of BPW and NAW were found to be compensating in density.

The front was found to move horizontally at the period of the semidiurnal tide which also defined the most energetic time scale in velocity and temperature. Observations indicate that the tides also excite higher frequency internal tides around the front. Additionally frequencies in the internal wave regime as high as 16 cpd were detected in the temperature and velocity data. The high frequency horizontal oscillations detected in the acoustic tomography are proposed to contribute to the observed frontal structure.

The position of the front, which is strongly tied to the topography, appears to be controlled by the recirculation of NAW along the 300 m isobath inside Bear Island Trough. This barotropic flow conserves its potential vorticity as it enters and proceeds around Bear Island Trough. Simulations indicate that the strength of this southwestward flow leaving Bear Island Trough appears nearly constant throughout the year. This consistent flow would help explain the perennial position of the front along Bear Island Trough. Simulations indicate the BSPF region has generally low eddy kinetic energy and geostrophic calculations confirm that baroclinic balances appear to be second order near the front.

2. Regional Oceanography

The surface signature of the front in summertime is seen in a shallow salinity gradient. This gradient exists because of the melting of the wintertime sea ice cover on the northern side of the front in the warm summer months. The advection of cold BPW towards the front from the northern Barents Sea, by the Persey and East Spitsbergen Currents, appears to be sensitive in model simulations to the amount of near surface vertical stratification. The amount of near surface stratification is tied to the presence of the fresh melt water layer. Without an adequately represented summertime melt layer or

the preceding wintertime ice cover, the signature of BPW at the position of front is lost due to increased mixing.

Tidal residual flows and tidal mixing on the shallow banks and around numerous topographic features is proposed to be an inherent part of the oceanography inside the Barents Sea. Tidally induced residual flows had the effect of reducing the simulated net volume transport into the Barents Sea by 0.4 Sv making it closer to observed estimates. Comparison of the simulations with and without tidal forcing showed marked changes in temperature and salinity throughout the entire Barents Sea when tides were included. The observed temperature structure on the shallow Svalbard bank more closely resembled model simulations which included tidal forcing when compared to simulations without tides.

The seasonal forcing experiment indicated that in wintertime a net volume transport of NAW into the Barents Seas increased from ~ 2 Sv to ~5 Sv. As previously discussed, the net volume transport along the front and out Bear Island Trough remained essentially constant. This predicted increased wintertime volume transport was traced through the Barents Sea and into the outflow between Frans Josef Land and Novaya Zemlya. This substantial wintertime increase in volume transport provides more evidence on the importance of the Barents Sea Branch (Rudels et al., 1994) on providing modified Atlantic Water to the Arctic Ocean oceanography.

X. CONCLUSIONS AND RECOMMENDATIONS

A. CONCLUSIONS

An extensive hydrographic data set was collected during an experiment held in August 1992 in the vicinity of the Barents Sea Polar Front. The front was found to be strongly tied to the topography within the experimental domain. Due to the uniform warming of the surface waters on either side of the front by summer heating, the surface expression of the front was observed as a surface salinity gradient, the result of summer ice melt. This surface salinity gradient also defined a shallow density front. The 34.6 psu isohaline was found to be a good indicator of the frontal position. Beneath a shallow mixed layer (~ 20 m) the front was defined by a moderate temperature gradient coincident with the 2°C isotherm; however, the thermohaline structure was compensating in density providing a barotropic character to the front. Below 100 m, the structure of the front was more diffuse which was attributed to vertical mixing due to shear in the tidal flow. The isopleths which define the maximum temperature/salinity gradients characterize the front as retrograde. The local hydrography around Finger Canyon modifies the circulation within the canyon and the frontal position over the canyon. The frontal position to the east of the canyon was found to be quasi-stationary; its horizontal position was laterally oscillated by the tides approximately +/- 5 km. There were no observations which indicated a horizontal exchange of water mass properties across the front greater than 10 km.

Analysis of the kinematic structure through geostrophy showed a shallow westward geostrophic jet associated with the surface density signature. South of the front, current meter and ADCP data showed a barotropic southwestward flow of warm NAW water with a speed of ~ 10 cm s^{-1}. This southwestward flow is attributed to the recirculation of the North Cape Current within the Bear Island Trough. This is believed to be one of the first measured observations associated with this recirculation. North of the front and over the shelf associated weak mean flows were present which were

associated with the cold southwestward Bear Island Current being steered by local bathymetry.

Acoustic tomographic images of a sound speed cross section across the front showed warm filaments originating south of the front to move upslope, pinch off, and dissipate with a ~1.5 hour periodicity. A forcing mechanism for this observation was undetermined though it was suggested to be of internal wave origin.

To examine the relation of the BSPF to the regional oceanography, an advanced, high resolution (1/6° and 30 vertical levels) Arctic Ocean and Nordic Seas model was developed as a part of this research from the Semtner-Chervin General Circulation Model (GCM) with a free-surface. Significant modifications to the model formulation for density calculations and vertical mixing were made to improve the Arctic simulations.

Three numerical experiments were conducted to simulate conditions in 1992. Results from an annual mean forcing, annual mean forcing coupled with semidiurnal tidal forcing and seasonal forcing were analyzed for salient features of the BSPF and its relation to the regional oceanography. All three numerical experiments predicted the recirculation of NAW within Bear Island Trough supporting the observed circulation pattern. This recirculating flow is proposed to control the horizontal position of the front.

The unique 3D tidal forcing experiment highlighted the significance of including tides in shallow sea simulations. Significant changes in the temperature and salinity structure due to tidal mixing were seen throughout the Barents Sea when compared to simulations without tides. Overall, the resultant T-S structure more closely resembled the available observations. Additionally, the predicted mean transport into the Barents Sea was reduced by 0.4 Sv in the tidal experiment making it closer to estimates based on observations. This was attributed to the effect of the tidally induced residual flow.

Model predicted net transports through the Barents Sea support the strong connection proposed by Rudels et al. (1994) of the Barents Sea Branch carrying a significant amount of modified Atlantic Water to the Arctic Ocean.

168

Finally, modeling predictions indicate that the coherent advection of BPW to the known frontal summertime position is contingent upon strong surface stratification of the upper layers from the summer ice melt. Thus presence of sea ice over the Barents Sea in the preceding winter is a necessary condition even for a summertime simulation.

B. RECOMMENDATIONS

Recommendations to improve follow-on observational work in the Barents Sea and numerical simulation studies can be made as a result of this research and are provided below. The modeling effort, which began as a part of this research, is still continuing. Work on many of the suggested improvements is already in progress.

- A high resolution (~ 5 km) survey of the currents across the northern slope of Bear Island Trough should be made to (1) verify the southwestward recirculation seen in these observations, and (2) investigate the presence of the northeastward flow seen the ADCP data, model predictions and other depictions of the regional circulation. Additionally, long-term current measurements are also needed to provide more conclusive estimates on the seasonal cycle of the transport through the Barents Sea and the importance of the Barents Sea Branch to the transport of Atlantic Water into the Arctic Ocean. These measurements could be obtained through traditional moorings but the results presented in this research indicate a 3-D acoustic tomographic survey would also provide the needed data The benefits from using the tomographic approach would include the corresponding temperature data as well as information on the high frequency phenomena noted in this research.

- Observations on the measured circulation cited in the literature in the northern Barents Sea between Svalbard and Frans Josef Land is sparse. Ice cover makes this a difficult area to survey much of the year. Correspondingly,

there very few conclusions on the connection and transfer between waters and tracers in the Barents Sea and the Arctic Ocean in this region. A survey of this region is needed to better understand this passage to the central Arctic.

- Inclusion of sea ice in the model is a necessity, especially for the accuracy of a summertime simulation away from the ice edge. The goals of coupling the ocean model to the sea ice model, aside from accurately simulating the sea ice, are to more accurately specify heat fluxes and salt fluxes at ocean grid points as well as to end the reliance on climatological restoring.

- Other major and minor improvements recommended to the basic model include:

    - Increase the vertical resolution in the upper 200 m.

    - Continue efforts to increase the horizontal resolution to the scale of the baroclinic Rossby radius, i.e. ~ 3 km.

    - Improve the turbulent closure scheme.

    - Incorporate a fourth order advective scheme.,

    - Reconfigure the model to run on a massively parallel machine.

- The tidal version of the model should be coupled to a 3D high resolution global model with tidal forcing to improve the quality of the tidal solution and to avoid contamination of the solution at the closed boundary. This technique is recommended as opposed to merely specifying open boundary conditions.

- Finally, the observational work needs to proceed hand-in-hand with the modeling effort. At the risk of preaching to the choir, this research has demonstrated more can be learned from using both approaches to understanding the oceanography of a region than either in isolation.

LIST OF REFERENCES

Aagaard. K. and P. Greisman, Toward new mass and heat budgets for the Arctic Ocean, J. Geophys. Res., 80(27), 3821-3827, 1975.

Apel, J. R., Principles of Ocean Physics, pp. 634, Academic Press, London, U.K., 1987.

Aukrust, T. and J. M. Oberhuber, Modeling of the Greenland, Iceland and Norwegian Seas with a coupled sea ice - mixed layer - isopycnal model, J. Geophys. Res, 100, 4771-4789, 1995.

Blindheim, J., Cascading of Barents Sea bottom water into the Norwegian Sea, Rapp. P. -v-Réun. Cons. int. Explor. Mer, 188, 49-58, 1989.

Böning, C. W., Influences of rough bottom topography on flow kinematics in an eddy-resolving circulation model, J. Phys. Oceanogr., 19, 77-97, 1992.

Böning, C. W., and R. G. Budich, Eddy dyanmics in a primative equation model: sensitivity to horizontal resolution and friction, J. Phys. Oceanogr., 22, 361-381, 1992.

Bowden , K. F., Physical Oceanography of Coastal Waters, pp. 302, Ellis Horwood Ltd., West Sussex, U.K., 1983.

Boyer, S. P., and S. Levitus, Quality control and processing of historical oceanographic temperature, salinity and oxygen data, NOAA Tech. Rep. NESDIS 81, Dept. of Comm., NOAA, Washington, D. C., 1994.

Brooks, D. A., A model study of the buoyancy-driven circulation in the Gulf of Maine, J. Phys. Oceanogr., 24, 2387-2412, 1994.

Broecker, W. S., The great ocean conveyor, Oceanography, 4, 79-89, 1991.

Bryan, K. A numerical method for the study of the circulation of the world ocean, J. Comput. Phys., 4, 347-376, 1969.

Bryan, K. and M. Cox, An approximate equation of state for numerical models of ocean circulation, J. Phys. Oceanogr., 2, 510-514, 1972.

Burrage, D. M, and R. W. Garvine, Summertime hydrography at the shelfbreak front in the Middle Atlantic Bight, J. Phys. Oceanogr., 18, 1309-1319, 1988.

Candela, J., R. C. Beardsley, and R. Limeburner, Separation of tidal and subtidal currents in ship-mounted acoustic doppler current profiler observations, J. Geophys. Res, 97, 769-788, 1992.

Chiu, C. S., J. H. Miller, J. F. Lynch, Inverse techniques for coastal acoustic tomography, in Theoretical and Computational Acoustics - Volume 2, edited by D. Lee and M . H. Schultz, pp. 917-931, World Scientific Publishing, River Edge, New Jersey, 1994.

Chiu, C. S., J. H. Miller, W. W. Denner, and J. F. Lynch, Forward modeling of the Barents Sea tomography vertical line array data and inversion highlights, in Full Field Inversion Methods in Ocean and Seismo Acoustics, edited by O. Diachok, A. Caiti, P. Gerstoft, and A. Schmidt, pp. 237-242, Kluwer Academic Publishers, Dordrecht, The Netherlands, 1995a.

Chiu, C. S., J. H. Miller, and J.F. Lynch, Forward coupled-mode propagation modeling for coastal acoustic tomography, J. Acous. Soc. Am., in press, 1995b.

Coppens, A. B., Simple equations for the speed of sound in Neptunian waters, J. Acous. Soc. Am., 69(3), pp. 862-863, 1981.

Cox, M. D., An eddy-resolving numerical model of the ventilated thermocline: Time dependence, J. Phys. Oceanogr., 17, 1312-1314, 1987.

Chiu, C. S., J. Miller, R. Bourke, J. Lynch, R. Muench, Acoustically derived images of the Barents Sea Polar Front, EOS, Trans. AGU, 75(3), p. 118, 1994.

Dickson, R. R., L. Midttun, and A. I. Mukhin, The hydrographic conditions in the Barents Sea in August-September 1965-1968, in International O-group fish surveys in the Barents Sea 1965-1968, edited by O. Dragesund, pp. 3-24, Int. Coun. Explor. Sea. Cooperative Res. Rep., Ser. A. , 18, 1970.

Eckart, C., Properties of water, Part III, Amer. J. Sci, 256, 225-240, 1958.

Endoh, M. C., C. N. K. Mooers, and W. R. Johnson, A coastal upwelling circulation model with eddy viscosity depending upon Richardson Number, in Coastal Upwelling, Coastal and Estuarine Sciences, No. 1, edited by F. A. Richards, AGU, Washington, D.C., pp. 203-208, 1981.

Federov, K. N., The Physical Nature and Structure of Ocean Fronts, 333 pp., Springer-Verlag, New York, 1983.

Fofonoff, N. P., Physical properties of sea water, in The Sea, Vol 1, 864 pp,. Interscience, New York, 1962.

Foo, E.-C., C. Rooth, and R. Bleck, A two-dimensional diabatic isopycnal model of a coastal upwelling front, in Coastal Upwelling, Coastal and Estuarine Scienes, No. 1, edited by F. A. Richards, AGU, Washington, D.C., pp. 193-202, 1981.

Foreman, M. G. G., Manual for tidal currents analysis and prediction, Pacific Marine Science Report 78-6, 70 pp., Institute of Ocean Sciences, Sidney, B.C., 1978.

Friedrich, H. and S. Levitus, An approximation to the equation of state for sea water, suitable for numerical ocean models, J. Phys. Oceanogr., 2, 514-517, 1972.

Gathman, S. G., Climatology, in The Nordic Seas, edited by B. Hurdle, pp. 1-18, Springer-Verlag, New York, 1986.

Gawarkiewicz G., and A. J. Plueddemann, Topographic control of thermohaline frontal structure in the Barents Sea Polar Front on the south flank of Spitsbergen Bank , J. Geophys. Res., 100(C3), 4509-4524, 1995.

Gawarkiewicz G. and D. Chapman, The role of stratification in the formation and maintenance of shelf break fronts, J. Phys. Oceanogr., 22, 753-772, 1992.

Gloerson, P., W. Campbell, D. Cavalieri, J. Comiso, C. Parkinson, and H. Zwally, Arctic and Antarctic Sea Ice, 1978-1987, NASA SP S11, NASA, Washington, D.C., 1992.

Gjevik, B., E. Nost, and T. Straume, Model simulations of tides in the Barents Sea, J. Geophys. Res, 99(C2), 3337-3350, 1994.

Godin. G., The analysis of tides and currents (review), in Tidal Hydrodynamics, edited by B. B. Parker, pp. 675-709, John Wiley and Sons Inc. , New York, 1991.

Godin, G., The Analysis of Tides, pp. 264, University of Toronto Press, Toronto, 1972.

Hakkinen, S. and G. L. Mellor, Modeling the seasonal variability of the coupled Arctic ice-ocean system, J. Geophys. Res., 97, 20,285-20,304 , 1992.

Haltiner G. J., and R. T. Williams, Numerical Prediction and Dynamic Meteorology, pp. 447, John Wiley and Sons, New York, 1980.

Harms, I. H., A numerical study of the barotropic circulation in the Barents and Kara Seas, Cont. Shelf Res., 12(9), 1043-1058, 1992.

Harms I. H. and J. O. Backhaus, Application of the Hamburg Shelf Ocean Model to winterly watermass formation in the Barents and Kara Seas, Tellus, accepted, 1994.

173

Harris, C. L., A. J. Plueddemann, R. H. Bourke, M. D. Stone and R. A. Pawlowicz, Collection and analysis of shipboard ADCP data from the Barents Sea Polar Front Experiment, WHOI-95-03, Woods Hole Oceanographic Institution, 1995.

Hibler III, W. D. and K. Bryan, Ocean circulation: its effects on seasonal ice simulations, Science, 224, 489-492, 1984.

Hibler III, W. D. and K. Bryan, A diagnostic ice-ocean model, J. Phys. Oceanogr., 17, 987-1015, 1987.

Holland. D. M., and L. A. Mysak, An investigation of the general circulation of the Arctic Ocean using an isopycnal model, submitted to Tellus, 1995.

Hopkins, T. S., The GIN Sea, a synthesis of its physical oceanography and literature review, 1972-1985, Earth Sciences Reviews, 30, 175-318, 1991.

Huthnance, J. M., Large tidal currents near Bear Island and related tidal energy losses from the North Atlantic, Deep-Sea Research, 28A, 51-70, 1981.

Huthnance, J. M., Internal tides and waves near the continental shelf edge, Geophys. Astrophys. Fluid Dynamics, 48, pp. 81-106, 1989.

Johannessen, O. M. , Brief overview of the physical oceanography, in The Nordic Seas, edited by B. Hurdle, pp. 103-127, Springer-Verlag, New York, 1986.

Johannessen, O. M., and L. A. Foster, A note on the topographically controlled oceanic polar front in the Barents Sea, J. Geophys. Res, 83, 4567-4571, 1978.

Jones, J. H., Vertical mixing in the equatorial undercurrent, J. Phys. Oceanogr., 3, 286-296, 1973.

Joyce, T. M., On in situ "calibration" of shipboard ADCP's, J. Atmosph. Oceanic Technol., 6, pp. 169-172, 1989.

Killworth, P. D., D. Stainforth, D. J. Webb, and S. M. Patterson, A free-surface Bryan-Cox-Semtner model, Report No. 270, 163 pp., Insitute of Oceanographic Sciences Deacon Laboratory, Surrey, U. K. 1989.

Killworth, P. D., D. Stainforth, D. J. Webb, and S. M. Patterson, The development of a free-surface Bryan-Cox-Semtner ocean model, J. Phys. Oceanogr., 21, 1333-1348, 1991.

Kowalik, Z., and A. Y. Proshutinsky, The Arctic Ocean tides, in The Polar Oceans and Their Role in Shaping the Global Environment: The Nansen Centennial Volume, Geophys. Monogr. Ser., Vol 85, edited by O. M. Johannessen, R. D. Muench, and J. E. Overland, pp. 137-158, AGU, Washington, D.C., 1994.

Kowalik, Z., and A. Y. Proshutinsky, Topographic enhancement of tidal motion in the western Barents Sea, J. Geophys. Res, 100(C2), 2613-2637, 1995.

Levitus, S., R. Burgett, and T. Boyer, World Ocean Atlas, 1994: Volume 3, Salinity, NOAA Atlas NESDIS 3, NOAA, Washington, D.C., 1994.

Levitus, S. and T. Boyer, World Ocean Atlas, 1994: Volume 4, Temperature, NOAA Atlas NESDIS 3, NOAA, Washington, D.C., 1994.

Levitus S., Climatological atlas of the world ocean, NOAA Professional Paper 13, NOAA, Washington. D. C., 1982.

Loeng, H., V. Ozhigan, B. Ådlandsvik, and H. Sagan, Current measurements in the northeeastern Barents Sea, ICES Statutory Meeting, pp. 22, 1993.

Loeng, H., Features of the physical oceanographic conditions of the Barents Sea, Polar Research, 10(1), 5-18, 1991.

Lynch, J. F., J. Guoliang, R. Pawlowicz, D. Ray, C.S. Chiu, J. Miller, R. Bourke, R. Parsons, A. Plueddemann, R. Muench, Acoustic scattering from shallow water internal waves and internal tides in the Barents Sea: theory and experiment, J. Acous. Soc. Am., in press, 1995.

McClimans, T. A., and J. H. Nilsen, Laboratory simulation of the currents in the Barents Sea, Dy. Atmos. Oceans, 19, 3-25, 1993.

Mellor. G. L., and T. Yamada, Development of a turbulence closure model for geophysical fluid problems, Rev. Geophys. Space Phys., 20, 851-875, 1982.

Mellor, G. L., An equation of state for numerical models of oceans and estuaries, J. Atmos. Ocean. Tech., 8, 609-611, 1991.

Mesinger, F., and A. Arakawa, Numerical methods used in atmospheric models, Volume 1, pp. 64, GARP Publication Series 17, WMO-ICSU Joint Organizing Committee, 1976.

Munk W. H., and E. R. Anderson, Notes on a theory of the thermocline, J. Mar. Res., 7, 276-295, 1948.

Midttun, L., and H. Loeng , Climatic variations in the Barents Sea, in The Effect of Oceanographic Conditions on Distribution and Populations Dynamics of Commercial Fish Stocks in the Barents Sea, edited by H. Loeng, pp. 13-27, Proc. 3rd Soviet-Norwegian Symp, 26-28 May 1986, Institute of Marine Research, Bergen, 1987.

Mooers, C. N. K., C. N. Flagg, and W. C. Boicourt, Prograde and retrograde fronts, in Oceanic Fronts in Coastal Processes, edited by M. Bowman and W. Esaias, pp. 43-58, Springer Verlag, Berlin Heidelberg New York, 1978.

Nansen, F., The oceanography of the North Polar Basin, in The Norwegian North Polar Expedition 1893-1896, Vol. III, edited by F. Nansen, pp 1-427, Greenwood Press, New York, 1969 (reprint, orginally published in 1902 by Longmans, Green and Co.).

Newton, I, Philosophiae Naturalis Principia Mathematica, London, 1676.

Nost, E., Calculating tidal current profiles from vertically integrated models near the critical latitude in the Barents Sea, J. Geophys. Res. , 99, 7885-7901, 1994.

Novitskiy, V. P., Permanent currents of the northern Barents Sea, Trudy Gosudarstvennogo Okeanograficheskogo Instituda, Engl. Transl., 64, 1-32, 1961.

Pacanowski, R. C. and S. G. H. Philander, Parameterization of vertical mixing in numerical models of tropical oceans, J. Phys. Oceanogr., 11, 1443-1451, 1981.

Perry, R. K., Bathymetry, in The Nordic Seas, edited by B. Hurdle, pp. 211-234, Springer-Verlag, Berlin-Heidelberg-New York, 1986.

Pfirman, S. L., D. Grabitz, and T. Gammelsrød, The northern Barents Sea: water mass distribution and modification, in The Polar Oceans and Their Role in Shaping the Global Environment: The Nansen Centennial Volume, Geophys. Monogr. Ser., Vol 85, edited by O. M. Johannessen, R. D. Muench, and J. E. Overland, pp. 77-94, AGU, Washington, D.C., 1994.

Pickard, G. L., and W. L. Emery, Descriptive Physical Oceanography: An Introduction, 4th Ed., pp. 249, Pergamon Press, Oxford, U.K., 1982.

Pingree, R. D., and D. K. Griffiths, Tidal fronts on the shelf seas around the British Isles, J. Geophys. Res. , 83, 4615-4622 , 1978.

Pond, S. and G. L. Pickard, Introductory Dynamical Oceanography, 329 pp. , Pergamon Press, Oxford, U. K., 1982.

Poulain, P. -M., A. Warn-Varnas, and P. P. Niler, Near surface circulation of the Nordic Seas as measured by Lagrangian drifters, J. Geophys. Res., in press, 1995.

Preller, R. H, and P. Posey, The Polar Ice Prediction System -- a sea ice forecasting system, NORDA Report 212, Naval Research Laboratory, Stennis Space Center, MS, 1989.

Preisendorfer, R., Principal Component Analysis in Meteorology and Oceanography, pp. 425, Elsevier Pub. Co., N.Y., 1988.

Ranelli, P. H., and W. D. Hibler, III, Seasonal Arctic sea ice simulations with a prognostic ice-ocean model, Annal of Glaciology, 15, 45-53, 1991.

Ray, D. S., Acoustic travel time perturbations due to internal tide and internal wave field in the Barents Sea, M.S. thesis, 73 pp., Mass.Inst. of Technol./Woods Hole Oceanogr.Inst., August 1993.

Robinson, A. R., An investigation into the wind as to the cause of the Equatorial Undercurrent, J. Mar. Res, 24, 179-204, 1966.

Rosenfeld, L. K., Tidal band current variability over the northern California continental shelf, Tech. Rep. WHOI 87-11, 237 pp., Joint Program Woods Hole Oceangr. Inst/Mass.Inst. of Technol., 1987.

Rudels, B., On the mass balance of the Polar Ocean, with special emphasis on the Fram Strait, Norsk Polarinstitutt Skrifter, 188, 53 pp., 1987.

Rudels B., E. P. Jones, L. G. Anderson, and G. Kattner, On intermediate depth waters of the Arctic Ocean, in The Polar Oceans and Their Role in Shaping the Global Environment: The Nansen Centennial Volume, Geophys. Monogr. Ser., Vol 85, edited by O. M. Johannessen, R. D. Muench, and J. E. Overland, pp. 33-45, AGU, Washington, D.C., 1994.

Schwiderski E. W., Tides, in The Nordic Seas, edited by B. Hurdle, pp. 191-209, Springer-Verlag, New York, 1986.

Semtner, A. J., An oceanic general circulation model with bottom topography, Tech. Rep. 90 pp., Dept. of Meterol., Univ. of Calif., Los Angeles, 1974.

Semtner, A. J., Numerical simulation of the Arctic Ocean circulation, J. Phys. Oceanogr., 6, 409-425, 1976.

Semtner, A. J., A numerical study of sea ice and ocean circulation in the Arctic, J. Phys. Oceanogr., 17, 1077-1099, 1987.

Semtner A. J. and R. M. Chervin, A simulation of the global ocean circulation with resolved eddies, J. Geophys. Res. , 93, 15,502-15,522, 15,767-15775, 1988.

Semtner A. J. and R. M. Chervin, Ocean circulation from a global eddy-resolving model, J. Geophys. Res. , 97, 5493-5550, 1992.

Semtner, A. J., Very high resolution estimates of the global ocean circulation, suitable for carbon-cycle modeling, in Proceedings of the Snowmass Global Change Institute on the on the Global Carbon Cycle, Office of the Interdisciplinary Earth Studies, Boulder, CO, in press, 1995.

Serreze, M. C. and R. G. Barry, Synoptic activity in the Arctic Basin, 1979-1985, J. Climate, 1, 1276-1295, 1988.

Simpson, J. H., The shelf-sea fronts; implications of their existence and behavior, Phil. Trans. R. Soc. Lond., A302, 531-546, 1981.

Slagstad, D., K. Stole-Hansen, and H. Loeng, Density driven currents in the Barents Sea calculated by a numerical model, Modeling, Identification, and Control, 11, 181-190, 1990.

Steele, M. J. Morison, and T. Curtin, Halocline water formation in the Barents Sea, J. Geophys. Res., 100(C1), 881-894, 1995.

Tantsiura, A. I., About the currents of the Barents Sea, Trudy Polyvar. Nauchno-issled, Inst. Morsk. Ryb. Knoz. Okeanogr., 11, 35-53, 1959.

Trenberth, K. E., J. Olson, and W. Large, A global ocean wind stress climatology based on ECMWF analyses, NCAR Tech. Note 338+STR, NCAR, Boulder, CO, 1989.

UNESCO, Tenth rep. of the joint panel on oceanographic tables and standards, UNESCO Tech. Pap. in Marine Science No. 36, 25 pp., UNESCO, Paris, 1981.

Worthington, L. V., The Norwegian Sea as a mediterranean basin, Deep Sea Res., 17, 77-84, 1970.

178

INITIAL DISTRIBUTION LIST

1. Defense Technical Information Center   2
   Cameron Station
   Alexandria, VA 22304-6145

2. Library, Code 013   2
   Naval Postgraduate School
   Monterey, CA 93943-5002

3. Professor Robert H. Bourke   2
   Chairman, Department of Oceanography, Code OC/Bf
   Naval Postgraduate School
   Monterey, CA 93943-5000

4. Professor Albert J. Semtner   1
   Department of Oceanography, Code OC/Se
   Naval Postgraduate School
   Monterey, CA 93943-5000

5. Associate Professor Ching-Sang Chiu   1
   Department of Oceanography, Code OC/Ci
   Naval Postgraduate School
   Monterey, CA 93943-5000

6. Associate Professor Peter Chu   1
   Department of Oceanography, Code OC/Cu
   Naval Postgraduate School
   Monterey, CA 93943-5000

7. Professor Kenneth L. Davidson   1
   Department of Meteorology, Code MR/Ds
   Naval Postgraduate School
   Monterey, CA 93943-5000

8. Professor Robert L. Haney   1
   Chairman, Department of Meteorology, Code Me/Hy
   Naval Postgraduate School
   Monterey, CA 93943-5000

9.   Professor Roland W. Garwood   1
         Department of Oceanography, Code OC/Gd
         Naval Postgraduate School
         Monterey, CA 93943-5000

10.   Professor Edward B. Thorton   1
         Department of Oceanography, Code OC/Tm
         Naval Postgraduate School
         Monterey, CA 93943-5000

11.   Associate Professor Mary L. Batteen   1
         Department of Oceanography, Code OC/Bv
         Naval Postgraduate School
         Monterey, CA 93943-5000

12.   Assistant Professor Jeffery D. Paduan   1
         Department of Oceanography, Code OC/Pd
         Naval Postgraduate School
         Monterey, CA 93943-5000

13.   Assistant Professor P. -M. Poulain   1
         Department of Oceanography, Code OC/Po
         Naval Postgraduate School
         Monterey, CA 93943-5000

14.   Research Assistant Professor Newell Garfield   1
         Department of Oceanography, Code OC/Gf
         Naval Postgraduate School
         Monterey, CA 93943-5000

15.   Research Assistant Professor Leslie K. Rosenfeld   1
         Department of Oceanography, Code OC/Ro
         Naval Postgraduate School
         Monterey, CA 93943-5000

16.   Research Assistant Professor Julie McClean   1
         Department of Oceanography, Code OC/Mn
         Naval Postgraduate School
         Monterey, CA 93943-5000

17. Research Assistant Professor Wieslaw Maslowski   1
     Department of Oceanography , Code OC/Ma
     Naval Postgraduate School
     Monterey, CA 93943-5000

18. Research Associate Professor Yuxia Zhang   1
     Department of Oceanography , Code OC/Zh
     Naval Postgraduate School
     Monterey, CA 93943-5000

19. Mike Cook   1
     Department of Oceanography , Code OC/Ck
     Naval Postgraduate School
     Monterey, CA 93943-5000

20. Pete Braccio   1
     Department of Oceanography , Code OC/Bc
     Naval Postgraduate School
     Monterey, CA 93943-5000

21. Robin Tokmakian   1
     Department of Oceanography , Code OC/Bc
     Naval Postgraduate School
     Monterey, CA 93943-5000

22. LCDR Emil Petruncio, USN   1
     Department of Oceanography
     Naval Postgraduate School
     Monterey, CA 93943-5000

23. University of Rhode Island   1
     Department of Ocean Engineering
     Attn: Professor James H. Miller
     211 Sheets Building
     Narragansett, RI 02881

24. Commanding Officer   5
     Naval Atlantic Meteorology and Oceanography Center
     Attn: LCDR Arthur R. Parsons, USN
     9141 Third Street
     Norfolk, VA 23511-2394

25. Oceanographer of the Navy   1
    Naval Observatory
    34th and Massachusetts Avenue NW
    Washington, DC 20390

26. Commander   1
    Naval Meteorology and Oceanography Command
    Stennis Space Ctr, MS 39529-5000

27. Commanding Officer   1
    Naval Oceanographic Office
    Stennis Space Ctr, MS 39522-5001

28. Office of Naval Research   1
    Attn: ONR 322 / Dr. Thomas B. Curtin
    800 North Quincy Street, Ballston Tower One
    Arlington, VA 22217-5660

29. Naval Research Laboratory   1
    Code 7322
    Attn: Dr. Ruth H. Preller
    Stennis Space Center, MS 39529

30. Naval Research Labora tory   1
    Marine Meteorology Division
    Attn: Pedro Tsai
    7 Grace Hopper Ave, Stop 2
    Monterey, CA 93943-5002

31. Dr. James F. Lynch   1
    Department of Applied Ocean Physics and Engineering
    Woods Hole Oceanographic Institution
    Woods Hole, MA 02543

32. Dr. Albert J. Plueddemann   1
    Department of Physical Oceanography
    Woods Hole Oceanographic Institution
    Woods Hole, MA 02543

33. Dr. Robin D. Muench   1
Earth and Space Research
1910 Fairview E., #102
Seattle, WA 98102-3699

34. Dr. Rich Pawlowicz   1
Institute of Ocean Sciences
PO Box 6000
9860 West Saawich Rd
Sydney, British Columbia
Canada V8L 4B2

35. Dr. Thomas McClimans   1
SINTEF-NHL
Klaebuveien 153
N-7034 Trondheim, Norway

36. Dr. O. M. Johannessen   1
Nansen Environmental and Remote Sensing Center
Edvard Griegsvei 3A
N-5037 Solheimsvik, Norway

37. Dr. Harald Loeng   1
Institute of Marine Research
PO Box 1870 Nordnes
5024 Bergen, Norway

38. Professor Bjorn Gjevik   1
University of Oslo
Department of Mechanics
PO Box 1035
Blindern, Oslo 3, Norway

39. Dr. Zygmunt Kowalik   1
Insititute of Marine Science
Room 108 O'Neill Bldg
University of Alaska
Fairbanks, AK 99775-7220

40.   Dr. Andrey Yu. Proshutinsky   1
        Insititute of Marine Science
        Room 110 O'Neill Bldg
        University of Alaska
        Fairbanks, AK 99775-7220

41.   Dr. Peter Killworth   1
        Southampton Oceanography Centre
        Empress Dock
        European Way
        Southampton,UK   S014 3ZH

42.   Dr. Jean-Claude Gascard   1
        Univ Paris. 6
        LODYC Tour 14-2C
        4 Place Jussieu F-75252
        Paris, Cedex 05, France

43.   Professor Knut Aagaard   1
        University of Washington HN-10
        Polar Science Center
        Seattle, WA 98195

44.   Dr. Robert Chervin   1
        NCAR/CGD
        Mesa Laboratory
        PO Box 3000
        Boulder, CO 80307-3000

45.   Anthony Craig   1
        NCAR/CGD
        Mesa Laboratory
        PO Box 3000
        Boulder, CO 80307-3000

46.   Steve Hankin   1
        Pacific Environmental Marine Laboratory
        7600 Sand Point Way NE., Bldg 3
        Seattle, WA 98115-0700

47. Dr. James Wilson   1
     Neptune Sciences Inc.
     3834 Vista Azul
     San Clemente, CA 92674

48. Dr. Michael Steele   1
     University of Washington
     Applied Physics Laboratory
     1013 NE 40th Street
     Seattle, WA 98105-6698

49. Dr. Ingo Harms   1
     Institutt fure Meereskkunde
     Universitaet Hamburg
     Troplowitzsir .7
     22529 Hamburg
     Germany

50. Dr. Laurence Padman   1
     College of Oceanography
     Oregon State University
     Corvallis, OR 97331-5503